ABSTRACT

Title of Dissertation:	ELECTROMAGNETIC INTERFERENCE REDUCTION USING ELECTROMAGNETIC BANDGAP STRUCTURES IN PACKAGES, ENCLOSURES, CAVITIES, AND ANTENNAS
	Baharak Mohajer Iravani, Doctor of Philosophy, 2007
Dissertation Directed By:	Associate Professor Omar M. Ramahi, Mechanical Engineering Department Electrical and Computer Engineering Department

Electromagnetic interference (EMI) is a source of noise problems in electronic devices. The EMI is attributed to coupling between sources of radiation and components placed in the same media such as package or chassis. This coupling can be either through conducting currents or through radiation. The radiation of electromagnetic (EM) fields is supported by surface currents. Thus, minimizing these surface currents is considered a major and critical step to suppress EMI.

In this work, we present novel strategies to confine surface currents in different applications including packages, enclosures, cavities, and antennas. The efficiency of present methods of EM noise suppression is limited due to different drawbacks. For example, the traditional use of lossy materials and absorbers suffers from considerable disadvantages including mechanical and thermal reliability leading to limited life time, cost, volume, and weight. In this work, we consider the use of Electromagnetic Band Gap (EBG) structures. These structures are suitable for

suppressing surface currents within a frequency band denoted as the bandgap. Their design is straight forward, they are inexpensive to implement, and they do not suffer from the limitations of the previous methods.

A new method of EM noise suppression in enclosures and cavity-backed antennas using mushroom-type EBG structures is introduced. The effectiveness of the EBG as an EMI suppresser is demonstrated using numerical simulations and experimental measurements.

To allow integration of EBGs in printed circuit boards and packages, novel miniaturized simple planar EBG structures based on use of high-k dielectric material ($\varepsilon_r > 100$) are proposed. The design consists of meander lines and patches. The inductive meander lines serve to provide current continuity bridges between the capacitive patches. The high-k dielectric material increases the effective capacitive load substantially in comparison to commonly used material with much lower dielectric constant. Meander lines can increase the effective inductive load which pushes down the lower edge of bandgap, thus resulting in a wider bandgap. Simulation results are included to show that the proposed EBG structures provide very wide bandgap (~10GHz) covering the multiple harmonics of of currently available microprocessors and its harmonics.

To speed up the design procedure, a model based on combination of lumped elements and transmission lines is proposed. The derived model predicts accurately the starting edge of bandgap. This result is verified with full-wave analysis.

Finally, another novel compact wide band mushroom-type EBG structure using magneto-dielectric materials is designed. Numerical simulations show that the

proposed EBG structure provides in-phase reflection bandgap which is several times greater than the one obtained from a conventional EBG operating at the same frequency while its cell size is smaller. This type of EBG structure can be used efficiently as a ground plane for low-profile wideband antennas.

ELECTROMAGNETIC INTERFERENCE REDUCTION USING ELECTROMAGNETIC BANDGAP STRUCTURES IN PACKAGES, ENCLOSURES, CAVITIES, AND ANTENNAS

By

Baharak Mohajer Iravani

Dissertation submitted to the Faculty of the Graduate School of the
University of Maryland, College Park, in partial fulfillment
of the requirements for the degree of
Doctor of Philosophy
2007

Advisory Committee:
Associate Professor Omar M. Ramahi, Co-chair/Supervisor
Professor Victor Granatstein, Chair/Advisor
Professor Issak D. Mayergoyz
Associate Professor Bruce Jacob
Professor Amr Baz

Dedication

To my great family especially my dear mother Hilda and my dear father Parviz

To my lovely and supportive relatives

To the memories of my beloved grandparents and aunts

Acknowledgements

I am grateful to the Lord for his mercy and blessings. He is giving me the chance of progressing and understanding a little from infinite logics existent in this world. I would like to thank my family especially my parents, relatives, and friends for their sincere love, ultimate support, and continuous encouragement in every step of my life. I would like to offer my thanks to Prof. Omar Ramahi for supervising and guiding me during different stages of my Ph.D. research. He was aggressive to make me fruitful, modest to make me confident of my knowledge and logic, pushing to make me hit the top, consultant to choose the best way, advisor to suggest ideas in situations in which I had been stuck, and decent to give me chance to develop my own ideas. I would like to thank Prof. Victor Granatstein, Prof. Issak Mayergoyz, Prof. Bruce Jacob, and Prof. Amr Baz for serving on my defense committee. I am thankful to Dr. Granatstein for accepting to be my official advisor at the last stage of my doctorate study. I am grateful to Prof. Zaki for advising me one year, who provided me great opportunity to achieve theoretical and practical experience about microwave components. I would like to thank Dr. Mahmoud EL Sabbagh for his support and advice both during the early steps of my research at University of Maryland and the last steps at University of Waterloo, Canada. I am thankful to Dr. Mehdi Kalantari at University of Maryland for his helpful discussions and encouragements. I would like to thank Mr. Jay Pyle in Machine Shop at Institute for Research in Electronics and Applied Physics (IREAP), University of Maryland, for his advice and help in building different microwave components. I am thankful to Ms. Maria Hoo for her help at office of Graduate Studies, Department of Electrical and

Computer Engineering, University of Maryland. I would like to thank my friends Dr. Shahrooz Shahparnia, Dr. Mohammad Haeri Kermani, Dr. Telesphor Kamgaing, Dr. Lin Li, and Dr. Xin Wu in Electromagnetic Compatibility and Propagation Lab at University of Maryland for their support, discussions, and cooperation. My thanks are due to my friends Dr. Yunchi Zhang and Mr. Mohamed Fahmi in Microwave Lab at University of Maryland, Dr. Jorge Alfonso Ruiz Cruz at Universidad Autonoma de Madrid/ Spain, and Mr. Seokjin Kim at University of Maryland for their help, support, discussions, and guide. Finally, I would like to thank my friends Mrs. Leila Yousefi, Mr. Samer Abdullah, Mr. Muhammad Boybay, and Mr. Ali Kabiri in Electromagnetic group at University of Waterloo for being supportive.

Table of Contents

List of Tables

List of Figures

Chapter 1 : Introduction

1.1. Background on Electromagnetic Noise

Electromagnetic Interference (EMI) adversely affecting electronic devices is a critical challenge facing designers of electronic equipment operating at low threshold voltage levels. These challenges are intensified by increase in system speed and integration driven by commercial imperatives to increase functionality while reducing space and power consumption, resulting in inexpensive hardware, wide range of functionality with longer battery life. EMI can be generated from or attributed to different hardware stages including the device, the chip, the package, the printed circuit board (PCB), the interconnects, the components, the chassis, and the peripherals. Mitigation of noise in all system levels is necessary due to strict requirements in new design technologies. It is important to note that in addition to disrupting interference due to unintentional radiation, EMI is also of concern when using intentional radiators (i.e., antennas) placed in close proximity of each other, or that share common reference planes. Continuous advances in communication and electronic circuits increase the need for complicated systems with several electromagnetic sources that operate in the same environment such as array of antennas or several electronic circuits located in different compartments in chassis. The proximity of these radiating sources increases the probability of interference, or mutual coupling between them.

The most common type of noise in high speed packages is simultaneous switching noise (SSN). SSN, also referred to as voltage bounce or delta-I noise, is caused by the switching of transistors between two different logic levels. When switching takes place, a surge of current travels between power and ground planes causing a voltage drop between them and a voltage drop across segments of the power plane itself. These voltage drops are directly proportional to the current switching rate and the effective inductance of current paths. SSN was studied extensively in the past decade [1]-[4]. The propagating wave between metallic layers of laminated substrate acting as parallel plate waveguide which is supported by traveling current on planes can interfere with other via passing through or connected to these planes. When the traveling wave reaches the edges, it will partially radiate out and the rest will reflect back inside the package. The radiated wave from package can interfere with the other electronics located in the same media. Another design artifact that exacerbates the noise induced by switching is the natural resonance of the package itself. If the natural resonant frequencies of the package encompass the switching frequency or the clock frequency and its harmonics, then the potential for further disturbance to the reference voltage levels increase and equally important, the potential for EMI increases. The resonant frequencies of the package may be pushed out of the band of interest if the package size is reduced. However, such a solution is not viable as higher integration is demanding larger size packages.

Packages are designed to provide structural and mechanical integrity and EM shielding to insure proper functionality of the integrated circuit (IC). A package is an intermediate stage which transfers input/output (IO) signals between IC and PCBs

through the connections such as pins and balls. The EMI noise with the external/internal sources can lead to currents that flow through the interconnects all over the package. Therefore mitigation of noise at the early stage such as IC package level becomes critical considering the increasing demands to produce electronic devices with higher speeds, compact size, longer life-time batteries, and higher functionality. As a result, it is necessary to develop new designs for IC packages. In between packaging techniques of microprocessor which is the heart of most electronic devices are developing fast. In typical modern processor architecture, the L2 cache memory and microprocessor chip are packaged together to speed up the CPU execution time. The forthcoming generation of processors will have several parts of chipsets integrated in the same package [5], thus resulting in complex integrated circuits and highly dense power dies.

Package integration is expected to reduce the cost and the complexity of interconnects. However, higher density and faster processors lead to higher levels of electromagnetic noise. If the noise is not managed effectively such that it remains below acceptable levels, then the performance can be compromised and the potential for the device to electromagnetically interfere with other independent devices increases. Therefore, one of the key challenges for package designers is noise mitigation at every stage of the system. In fact, design for electromagnetic noise management becomes one of the key imperatives in the design process.

Enclosures and chassis which are designed to provide structural and mechanical integrity are also intended to provide EM shielding to insure proper functionality of the system. The mechanism of coupling between internal

electromagnetic sources and the external electromagnetic environment takes place either by direct penetration of electromagnetic fields through openings or through induced currents on conducting surfaces. Once currents exist on the internal surface of an enclosure, they travel to the external surface through openings such as apertures, seams, gaskets, etc. Once currents reach external surfaces, they travel and penetrate other cavities sharing the same surface, thus creating fields in these so-called victim cavities. Therefore, designs for enclosures and chassis managing electromagnetic noise are necessary.

1.2. Problems and Challenges

EMI can be generated from or attributed to different hardware stages including devices, chips, packages, printed circuit boards (PCB), interconnects, components, chassis, and peripherals. To minimize EMI, which could mean either reducing radiation from the equipment or increasing the immunity to external electromagnetic stimuli; various strategies are applied that are typically specific to each of these level. Electromagnetic noise or interference can be mitigated using one or more of several strategies. These strategies include, but are not limited to, isolation of critical components, shielding, grounding, matching, filtering, addition of lossy materials and absorbers and finally the possibility of redesigning the circuitry of the victim device or the circuitry of the source of EMI [6]-[17]. Eliminating the source of EMI is clearly desirable, but does not necessarily translate or equate to reduction in the susceptibility of the device to external sources. In fact, strong interference can occur at frequencies different from the frequencies corresponding to the device

switching speed (and its significant harmonics), which makes the containment strategies even more challenging.

The techniques proposed to reduce coupling noise between cavities as a constitutive part of the cavity-backed antennas include: placement of lossy materials and absorbers between the radiating elements, change in antenna configurations (E-plane or H-plane), increasing the distance between radiating elements, cutting a slit on the common surface or a combination of these methods [6]. However, while lossy materials have desirable electromagnetic features, mechanical and thermal properties can severely limit their applicability. Additionally, cost can be a detrimental factor as these materials need to be engineered to work over specific frequency bands. Also the other mentioned methods are not efficient, as they lead to increase in size and weight, or change in the setup and structure of system.

The problem of mitigating noise in IC packages remains a major challenge. In [18], a solution based on stitching via and retreated power planes was introduced to reduce package radiation. Most noise mitigation strategies presented in the literature, however, were applied to PCBs. In [9], [12] dissipative and lossy materials were used to damp down the noise level. Yet, the thermal and mechanical factors can limit the reliability and the applicability of this method. In [13], decoupling capacitors were applied which are effective for suppressing noise from DC to a few hundred mega hertz. In [14], [15], embedded capacitance was studied. In this method, decoupling level depends on the limitations in the fabrication techniques, such as: limitation in using different dielectric materials or minimum isolation distance between two metallic layers (minimum dielectric thickness between two consecutive layers).

Generally, by using embedded capacitance methodology, EM waves within the entire frequency band are still guided. Therefore, the application of this method completely depends on the level of noise tolerance in electronic circuits. In [16], power islands method, which isolates the source of noise from susceptible components, was used. Efficiency of this method depends on the level of components' density and topology. In [17], via stitching was used. It is an effective method in reducing emission from PCB package and coupling to periphery. Efficiency of this method which increases the dimension of board depends on the size requirements and fabrication techniques. The concept of using electromagnetic bandgap (EBG) structures for suppressing SSN and EMI was introduced in [3], [19]-[25]. EBG structures consist of dielectric substrate with periodic metallic patterns. They are designed to function as band-stop filters. This method is effective in that band-stop or bandgap is located in a range from few hundred megahertz to above. The bandgap is a function of the dimensions and the materials of both metallic patterns and substrate [26]-[28]. In [4], [19]-[25], an additional layer of metal for patches of the EBG structure is sandwiched between two layers of the package. Each patch is connected to one of these two metallic layers through a via. Recently, new planar EBGs were proposed to reduce fabrication cost. In these structures, the patterns were etched on one of the metallic layers instead of having additional third layer and vias [29]-[31]. Although, these new planar EBGs reduced the fabrication cost, their size was impractical for numerous applications and for use in suppressing noise in IC packages. More recently in [20], [32], an EBG structure suitable for use in IC packages was proposed. While the size of the EBG structure introduced in [32] was suitable for IC packages, it provided a narrow

bandgap which has to be fine tuned to coincide with a specific switching frequency, clock frequency, or higher-order harmonics.

In enclosures, the integrity of shielding compromised with size and number of apertures designed for airflow and heat dissipation [33]. To reduce EMI in enclosures, absorbers and lossy materials [8], [11] and combination of lossy materials and dual perforated ventilation screens [10] have been used. Although, lossy materials have desirable EM features their mechanical and thermal properties can severely limit their applicability. In addition, cost can be a detrimental factor as these materials need to be engineered to work over specific frequency bands. Also, designs with dual aperture screens change the size and weight of enclosure. In other methods implemented to reduce EMI, designers change the dimensions of box or openings till natural resonances of box and openings do not coincide with clock frequency of system and its significant harmonics. Generally, methods which change the dimension and weight and others which apply additional materials may add cost and size to enclosures.

Challenges with the present methods of noise reduction can be summarized as follows: 1) geometry dependence; 2) material dependence; 3) no guarantee of effectiveness in the microwave region; 4) presence of reliability issues. All these limitations and drawbacks in the methods of noise suppressions in the PCBs, the packages, the enclosures, the cavities, and the antennas are showing that the problems related to EMI noise suppression are not solved yet! In the following chapters, new solutions for EMI noise reduction in stages including: the packages, the enclosures, the cavities, and the antennas will be proposed and studied.

This dissertation is organized as follow. In 0, the EBG structures are introduced. Then, we study the characterization of EBG structures for applications where they are exposed to open media (they are not confined in closed media such as embedded EBGs in parallel plate waveguide). Also, we investigate the relationship of the suppression band versus different constituent materials and structures of EBG.

In Chapter 3, the concept of miniaturization of EBG structures using very high-k materials for mushroom- and planar-type structures is discussed. These novel EBGs are characterized. Also, we discuss the modeling of the proposed planar EBG structures. The developed model is providing efficient initial start in the design procedure.

The SSN and EMI noise suppression in IC packages using very high-k material is discussed in Chapter 4. We study analytically and numerically the limitations of using high-k materials in EM noise suppression in packages.

In Chapter 5, we discuss the new applications of EBG structures under two categories as follows: 1) EM noise reduction and 2) design of low profile antennas. In this chapter, the potential of EBG structures in suppressing EMI noise in enclosures and chassis, cavities and cavity-backed antennas, and packages are demonstrated. We assess the performance in enclosures and chassis numerically, in cavities and cavity-backed antennas numerically and experimentally, and in IC packages numerically.

The design of novel EBG structures using magneto-dielectric materials applied in the design of low profile wideband antennas is discussed in Chapter 5. Finally the conclusions and the future work are presented in Chapter 6.

Chapter 2 : Electromagnetic Bandgap Structures

In this chapter, we present different methods to characterize EBG structures. We will study numerically the effect of different design parameters on the suppression bandgap. The data obtained in this chapter will be used in subsequent chapters in different case studies to develop the concepts and to validate the efficiency of the proposed methods.

2.1. EBG Structures

EBG structures operating in the high frequency and the microwave frequency bands are periodic or quasi-periodic patterns created by metallic inclusions in dielectric or magnetic material [26]-[28]. In the literature, the EBG structures have been referred to as high-impedance surfaces (HIS), metallo-dielectric material, negative materials, and other designations. In this study, we adopt a simple structure of mushroom-type EBG patterns represented generically by the schematic shown in Figure 2.1. These structures are characterized by periodic metallic patches connected to a common ground (or reference) plane through shorted stubs or plated through-holes (commonly referred to as *vias*). In essence, the EBG structures are comprised of a Frequency Selective Surface (FSS) positioned on top of a conductor-backed material with vias positioned between the FSS and the metallic backing, hence electrically shorting them together. The material between the patches and the ground plane can be dielectric, magnetic, or combination of the two. In this study, we consider the metallic patches to be square. However, this choice does not diminish the

generality of our study as other designed topologies of similar size can be ptimized to achieve higher suppression. Design parameters of the EBG structure under study are illustrated in Figure 2.1. These parameters include the size of individual patches, the gap between adjacent patches, the diameter of stubs (*vias*), the thickness, and the material of the substrate. The geometrical features of the structure and the material of the substrate are directly related to the frequency range of the stop band.

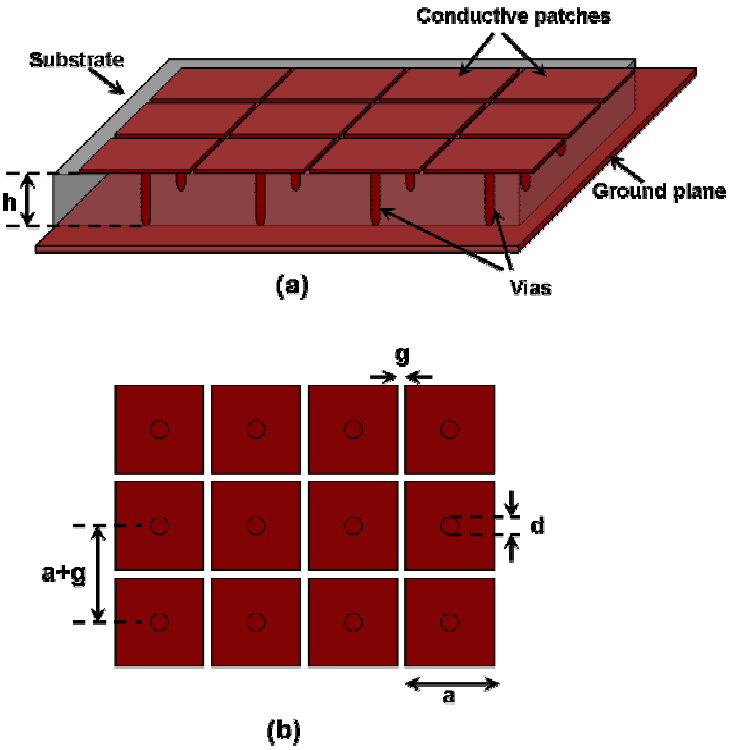

Figure 2.1. Square patch mushroom-type EBG structure (a) Perspective view. (b) Top view. Relevant design parameters are shown on the diagrams.

A major property of the EBG structure is the suppression of surface waves as originally postulated and experimentally demonstrated by the ground breaking work of Sievenpiper et al. [26]-[28]. This fundamental property of EBG structures makes

them play a highly critical role in the field of EMI/EMC and signal integrity. In effect, the EBG structure acts as a medium with either effective negative μ_r or effective negative ε_r occurring within a specific frequency band. In fact, EBG structure could be viewed as a plasma medium resonating over a band of frequencies which can be produced inexpensively using PCB technology.

2.2. Characterization of EBG Structures

The frequency bandgap of EBGs is directly related to the geometrical parameters and material parameters of the host medium. The EBG structures are essentially electrically-small resonators. Within the bandgap where they provide wave suppression, their size is much smaller than the wavelength. Analytical formulation of a precise relationship between the effective bandwidth (bandgap) and the geometrical and material parameters is difficult. In [34], [35], the authors have obtained circuit models for EBGs embedded in power planes. However, for the cases of EBG structures used in open systems, as in this study, we could not find any analytical expressions or accurate circuit models to give a reasonably accurate prediction of the bandgap. Therefore, and until a highly accurate closed-form analytic expression is developed, the stop band of an EBG structure may be generated directly or indirectly using numerical simulation tools. There are different numerical techniques to extract the frequency stop band of a structure which vary in complexity and efficiency. Using the scattering parameters (S-parameters) to characterize the bandgap is the most direct method while the dispersion diagram [36], [37] is the indirect one.

2.2.1. Scattering Parameters

In this method the bandgap can be specified by extracting the S-parameters numerically between two ports placed across the EBG structure as shown in Figure 2.2. For this purpose full-wave EM simulators such as Ansoft HFSS [38] can be used. EBG structure with specific bandgap can be designed using this method by trial and error procedure. This method is the most direct one because not only it characterizes the location of the bandgap, the bandwidth, and the center frequency but also, it provides the attenuation level of the signal at different frequencies.

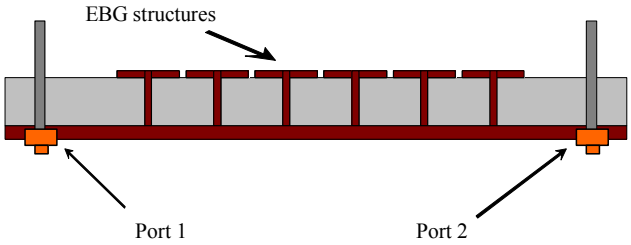

Figure 2.2. A schematic showing the simulation setup used to extract the bandgap of an EBG structure using scattering parameters. In this setup S_{21} represents the power delivered at port 2 when port 1 is excited.

2.2.2. Dispersion Diagram

In this method, the bandgap is specified by extracting the dispersion diagram which describes the propagation characteristics of an infinitely periodic structure composed of EBG patches. Dispersion diagram is numerically extracted using full-wave solver, by considering a single patch (unit cell) and applying periodic boundary condition (PBC) on the sides of the cell to mimic the presence of the cell in a inifinite

array of periodic structure, and absorbing boundary condition (ABC) or perfectly matched layer (PML) on the top open wall as shown in Figure 2.3 (a) [36].

Dispersion diagrams show the relationship between wave numbers and frequency. These diagrams present the propagating modes and the bandgaps that can potentially exist between such modes (in a periodic structure at a given frequency of operation, many modes propagating in different directions may be excited) [37]. Brillouin, in his theory of wave propagation in periodic structures [39], states that for any periodic structure there are certain vectors (i.e., directions) in the unit cell of the periodic structure that constitute a boundary region of propagation called irreducible Brillouin zone. According to that theory, deriving the propagating modes in the direction of these vectors suffices to cover all possible directions of wave propagation within the lattice. Therefore, the problem of deriving the propagating modes excited at a certain frequency reduces to finding such modes only in the directions of the vectors of the irreducible Brillouin zone. For the type of structure considered in this work, the border of the irreducible zone is illustrated in Figure 2.3 (b) and it consists of the direction pointing from Γ to X, from X to M and from M back to Γ.

Therefore, in light of Brillouin theory, a dispersion diagram will consist of three regions. In each region, we consider the paropagation wave vector β which is translated into a phase shift between the sides of the unit cell shown in Figure 2.3 (a). This translation allows the derivation of dispersion diagram using traditional eigenmode solver based on full-wave analysis. In these simulations, the structure of unit cell and the required phase shifts (shown as Phase 1 and Phase 2 in Figure 2.3 (a)) are given to the simulator. The simulator calculates the frequencies of

propagating waves that would generate such phase shifts. For a wave propagating in the *x*-direction with no *y* variation, Phase 1 is varied between 0 and 180^0 and Phase 2 is kept constant at zero degree. This corresponds to the Γ to X direction. The X to M direction corresponds to Phase 1 being constant and equal to 180^0 and Phase 2 varying from 0 and 180^o. This represents the second region in the dispersion diagram. The third region is represented by the M to Γ direction in which both phases are equal and changing from 180^o back to 0. For wave propagation in free space, as there is no dispersion, the diagram constitutes of straight lines in the first and third regions and a quadratic graph in the second region. The following equation shows the frequency-phase relationship for wave propagation in free space:

$$f(\beta d)=\left\{\begin{array}{ll}\dfrac{c}{2\pi d}(\beta_1 d) & \Gamma-\mathrm{X}:\left(0\le\beta_1 d\le\pi \quad \beta_2 d=0\right)\\ \dfrac{c}{2\pi d}\sqrt{\pi^2+(\beta_2 d)^2} & \mathrm{X}-\mathrm{M}:\left(0\le\beta_2 d\le\pi \quad \beta_1 d=\pi\right)\\ \dfrac{c\sqrt{2}}{2\pi d}(\beta_1 d) & \mathrm{M}-\Gamma:\left(0\le\beta_1 d\le\pi \quad \beta_2 d=\beta_1 d\right)\end{array}\right\}$$

Equation 2-1

where $d = a + g$ is the size of unit cell (periodicity length), c is the speed of light in free space, $\beta_1 = \beta_x$ and $\beta_2 = \beta_y$ are the wave numbers in the Γ-X and the X-M directions.

With the presence of EBG structures, the surface becomes dispersive; therefore the frequency-phase relationship of propagating modes will not be the same as in free space. A gap between the upper limit of any propagating mode and the intersection of the free space propagation line with the next propagating mode represents a region in which the surfaces do not support any propagation.

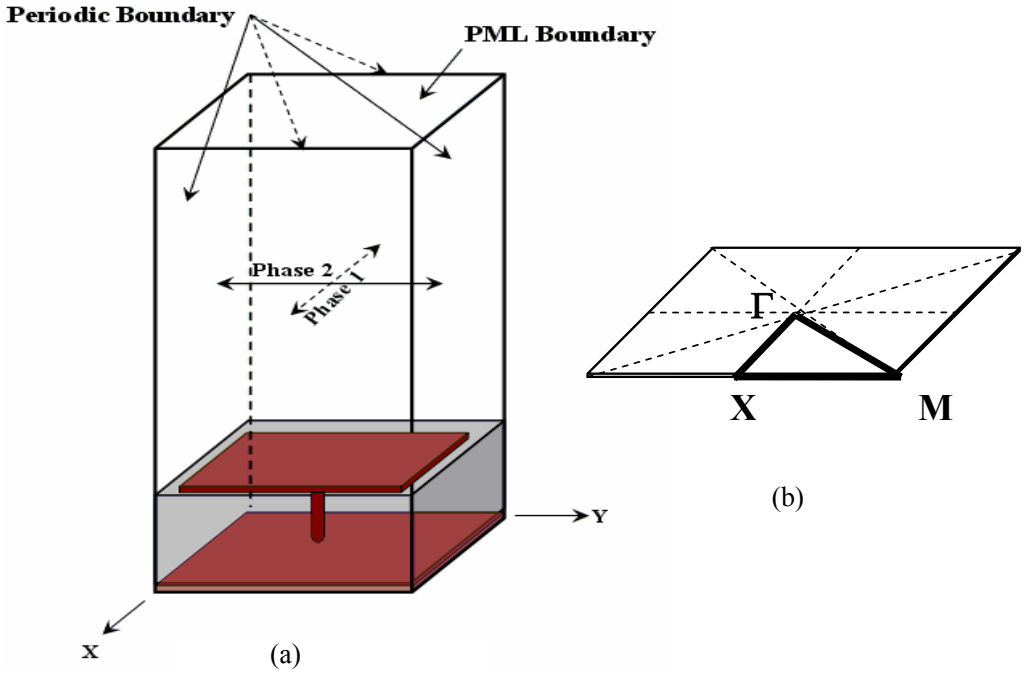

Figure 2.3. Schematic showing the simulation setup used to extract the bandgap of an EBG structure using dispersion diagrams. (a) Computational domain containing single cell. Periodic boundary conditions are placed at *x*-*z* and *y*-*z* planes and an absorbing condition (PML) is placed on the top face *x*-*y* plane. (b) The irreducible Brillouin zone triangle.

As an example to show how the Brillouin theory is used, we consider a 4 mm patch with a substrate of ε_r = 2.2, g = 0.4 mm, d = 0.8 mm, and h = 1.54 mm. The dispersion diagram for this structure obtained using HFSS is shown in Figure 2.4. From the dispersion diagram, the frequency band where no propagating modes exist is the corresponding bandgap of the structure. From Figure 2.4, the bandgap is observed to be between 8.4 GHz and 9.6 GHz. Also, the dispersion diagrams of two

other cases are shown in Figure 2.5 and Figure 2.6. The bandgap of EBG with a = 4 mm, ε_r = 4.8, g = 0.4 mm, d = 0.8 mm, and h = 1.54 mm is from 7 GHz to 8 GHz as shown in Figure 2.5. The bandgap of EBG with a = 2.6 mm, ε_r = 3, g = 0.4 mm, d = 0.8 mm, and h = 1.54 mm is between 11.9 GHz and 16 GHz as shown in Figure 2.6.

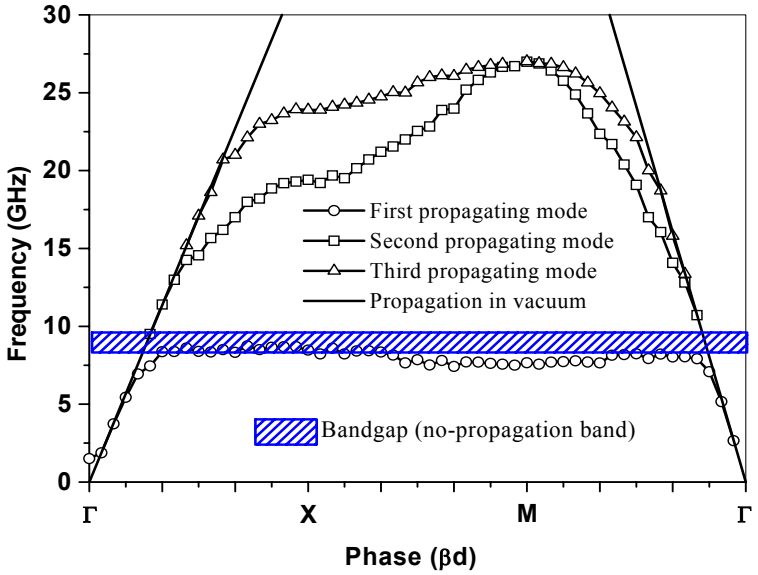

Figure 2.4. Dispersion diagram for the EBG structure having 4 mm square patches on a substrate with ε_r = 2.2.

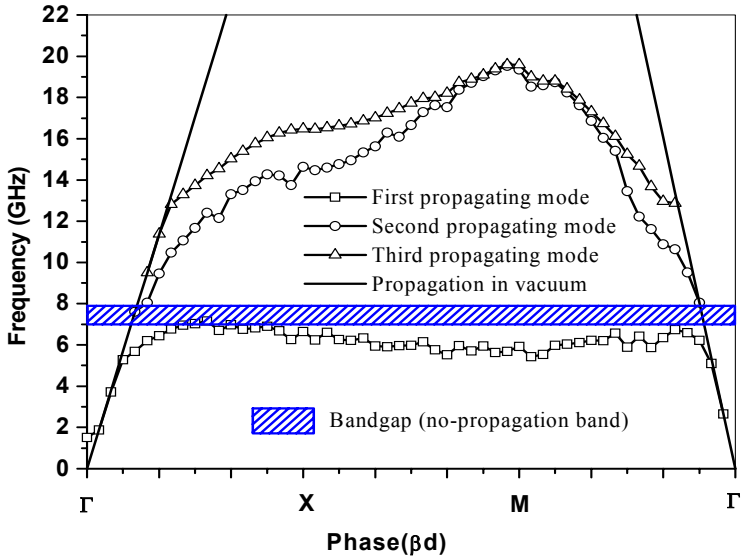

Figure 2.5. Dispersion diagram for the EBG structure having 4 mm square patches on a substrate with $\varepsilon_r = 4.8$.

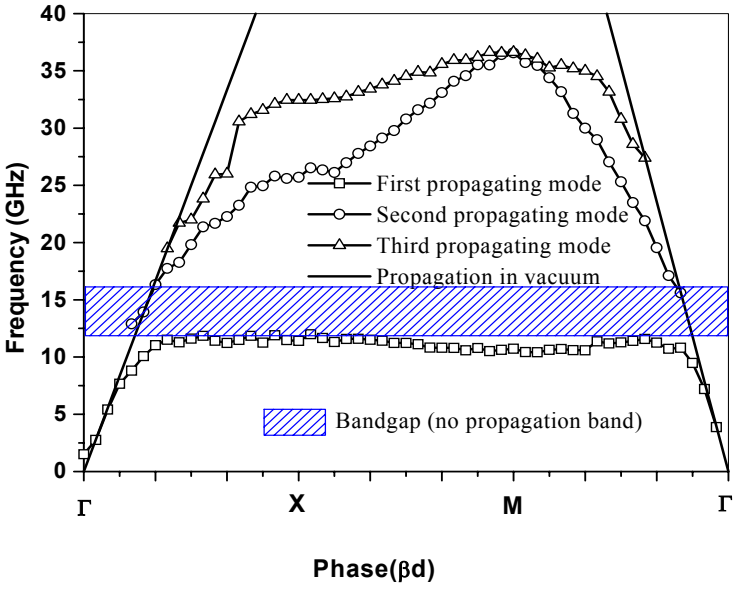

Figure 2.6 Dispersion diagram for the EBG structure having 2.6 mm square patches on a substrate with $\varepsilon_r = 3$.

2.3. Numerical Study of EBG Structures

As we mentioned in Section 2.1, there are no exact analytical formulas that relate the structural parameters of the EBG structures to the frequency stop band. Therefore, our goal here is to determine the effect of varying the EBG parameters on the width of the bandgap and its lower and upper frequency limits based on direct numerical simulation using HFSS.

The numerical setup consists of two parallel plate waveguides and the EBG structure to be tested is placed between them as shown in Figure 2.7. The EBG surface in Figure 2.7 is considered to be semi-infinite (infinite in the *x*-direction and finite in the *y*-direction) which is modeled in HFSS using symmetric boundary conditions. As a measure of the performance of the EBG structure, we consider the transmission loss (S_{21}) between the two ports shown in Figure 2.7 with and without the EBG surface. For example, in Figure 2.8 we show the magnitude of S_{21} for an EBG structure with the parameters a = 2.6mm, h = 1.54 mm, d = 0.8 mm, g = 0.4 mm, and $\varepsilon_r = 2$ (parameters are shown in Figure 2.1). The bandgap used throughout this study is defined as the difference between the two frequency points where the S_{21} suppression exceeds 3dB. The two frequency points defining the edge of the bandgap will be referred to as the lower and the upper frequency points. Figure 2.9-Figure 2.17 summarize the results of numerous simulations showing the relationship between the bandgap and the different parameters of the structure. Since the EBG patches are positioned in the direction of propagation of the waves, it is expected that the more EBG patches are used the suppression goes higher as shown in Figure 2.9 (a) and Figure 2.9 (b) where 4 rows and 8 rows of patches were used, respectively. Also,

from these figures we realize that increasing the patch size shifts the bandgap downward. In the following simulations, the distance between patches is 0.4 mm and via diameter is 0.8 mm.

Figure 2.10 and Figure 2.11 show the bandgap in relation to the separation between patches. We observe that increasing the gap between the patches causes the 3 dB bandgap to shift upward. Figure 2.12 and Figure 2.13 show the relationship between the bandgap and the height of via. Increasing the height of via shifts the bandgap downward. Figure 2.14 and Figure 2.15 show the relationship between the bandgap and the diameter of via. The trend of change of bandgap with diameter of via is not very clear. Figure 2.16 and Figure 2.17 show the relationship between the bandgap and the relative permittivity of the substrate. Increasing the permittivity shifts the bandgap downward. Generally, the relationship between the bandgap and the design parameters are not linear.

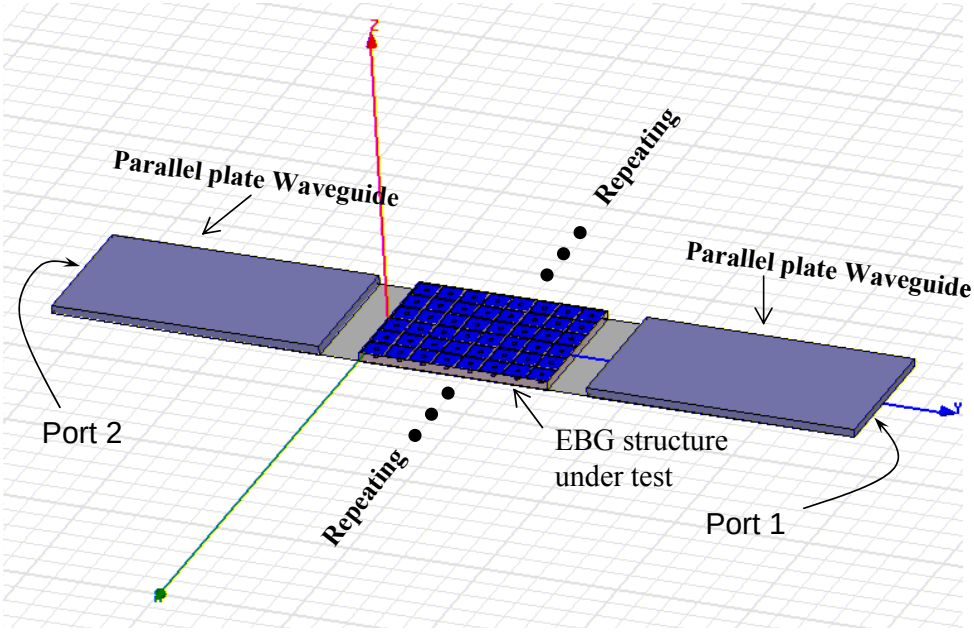

Figure 2.7. Numerical setup used to extract the bandgap of EBG structures.

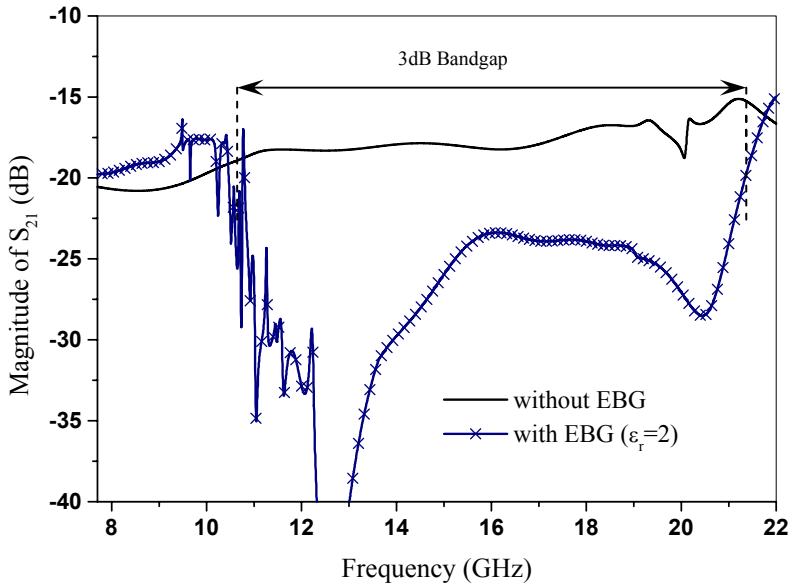

Figure 2.8. Magnitude of S_{21} for the setup shown in Figure 2.7 with and without and EBG surface with the following parameters a = 2.6 mm, h = 1.54 mm, d = 0.8 mm, g = 0.4 mm, and ε_r = 2. The design parameters are shown in Figure 2.1.

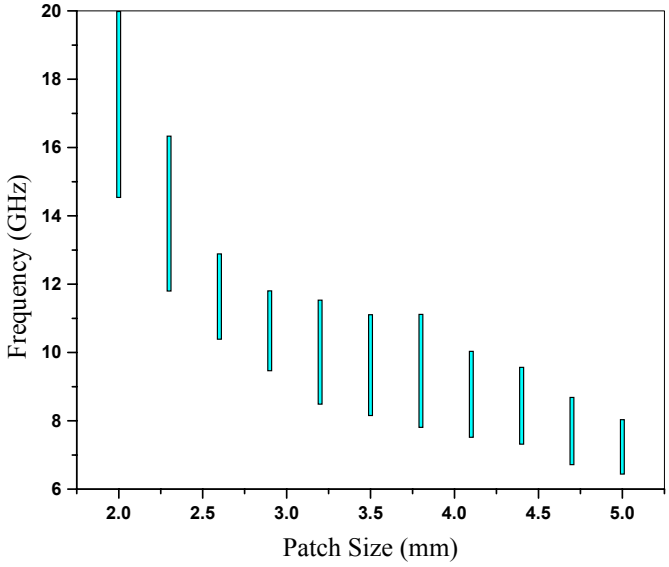

(a)

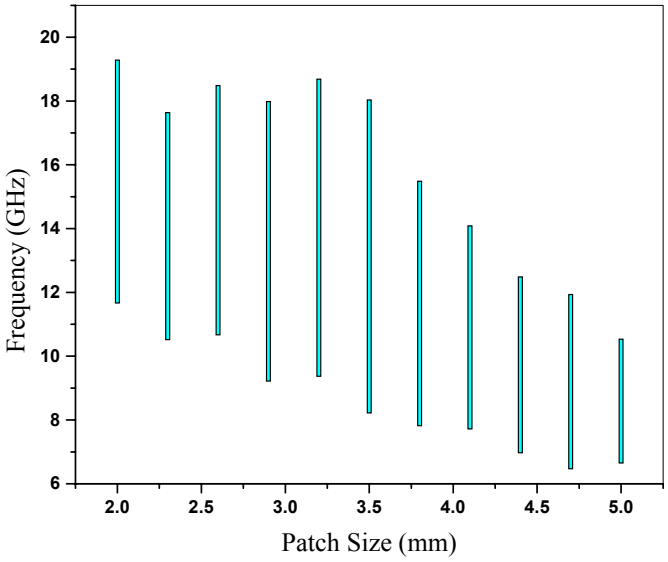

(b)

Figure 2.9. Frequency bandgap versus the patch size. (a) 4 rows of EBG patches, (b) 8 rows of EBG patches. EBG parameters: $\varepsilon_r = 3$, $h = 1.54$ mm, $d = 0.8$ mm, and $g = 0.4$ mm.

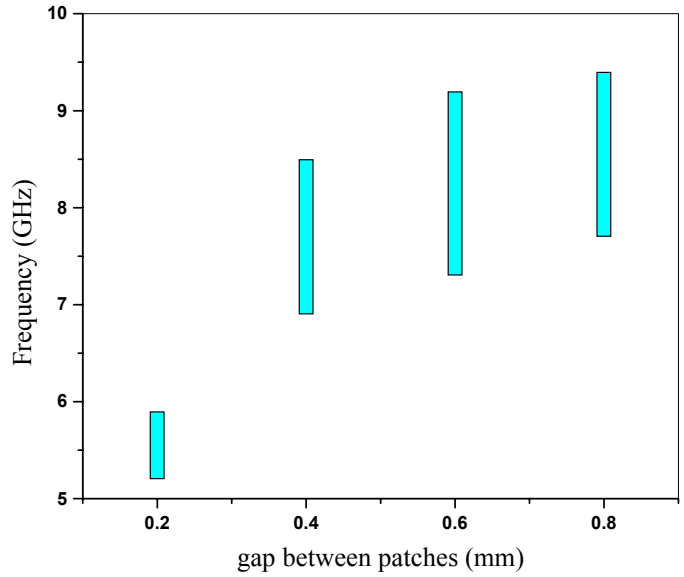

(a)

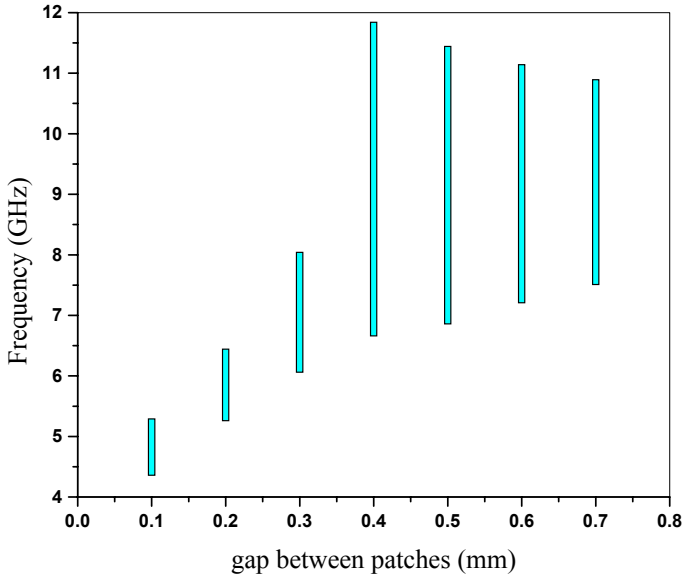

(b)

Figure 2.10. Frequency bandgap versus the gap between patches. (a) 4 rows of EBG patches, (b) 8 rows of EBG patches. EBG parameters: a = 4 mm, ε_r = 4.4, h = 1.54 mm, and d = 0.8 mm.

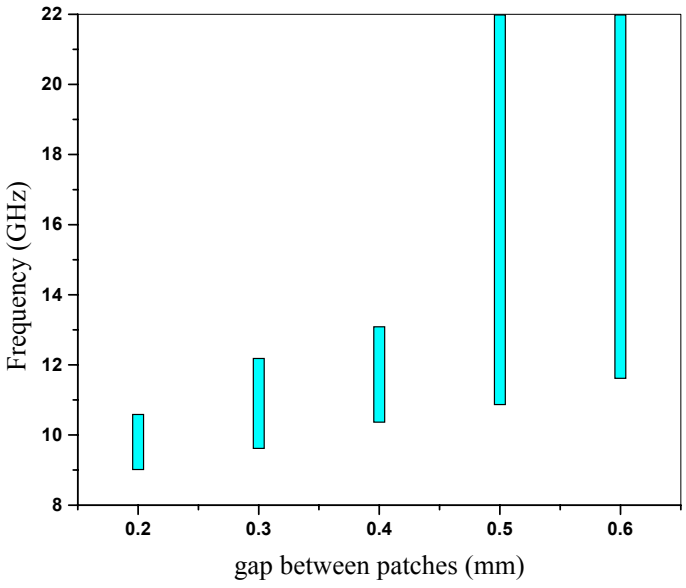

(a)

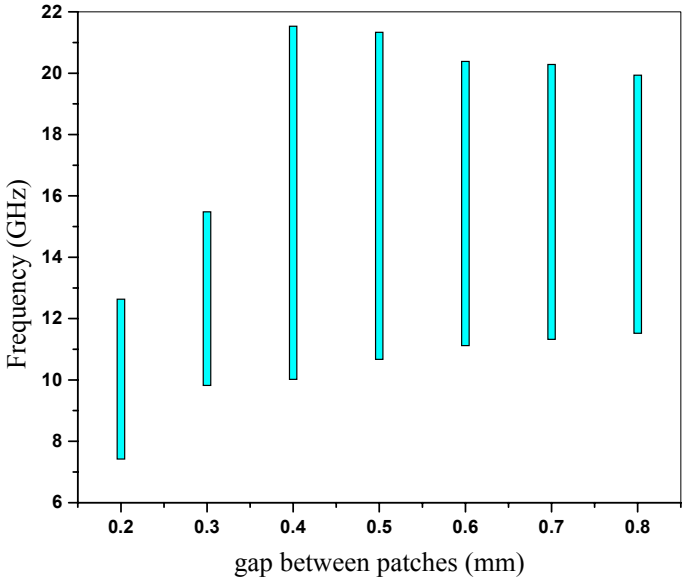

(b)

Figure 2.11. Frequency bandgap versus the gap between patches. (a) 4 rows of EBG patches, (b) 8 rows of EBG patches. EBG parameters: a = 2.6 mm, ε_r = 3, h = 1.54 mm, and d = 0.8 mm.

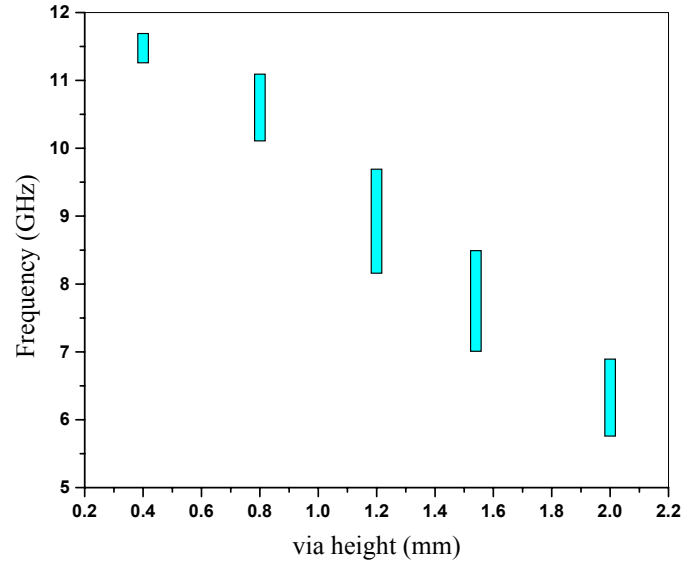

(a)

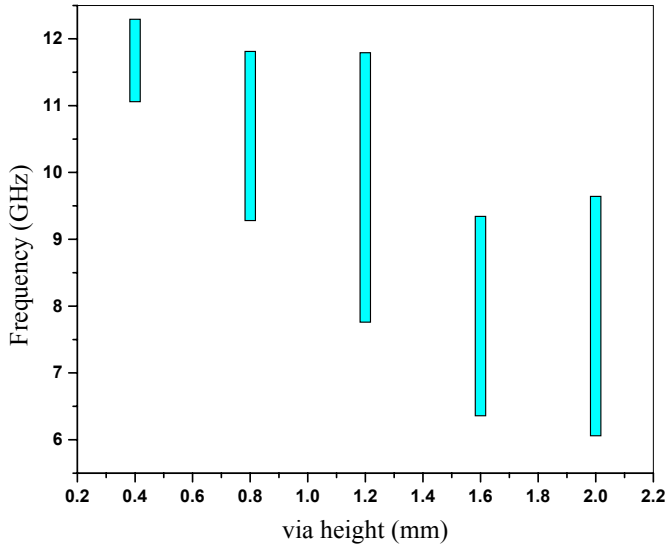

(b)

Figure 2.12. Frequency bandgap versus the height of via. (a) 4 rows of EBG patches, (b) 8 rows of EBG patches. EBG parameters: a = 4 mm, g = 0.4 mm, ε_r = 4.4, and d = 0.8 mm.

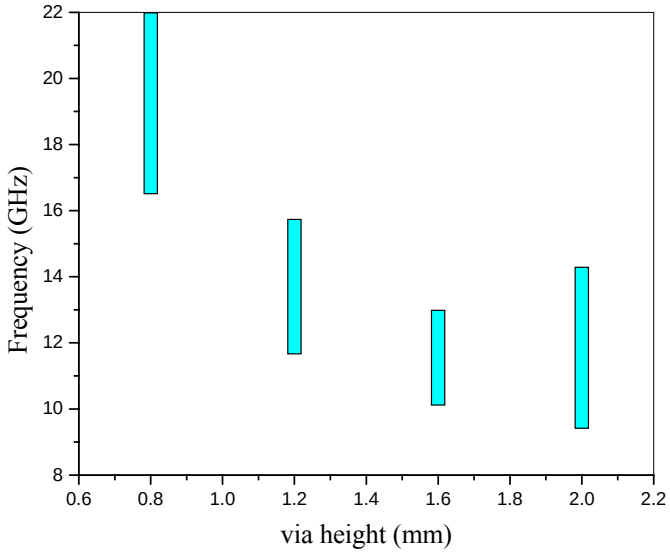

(a)

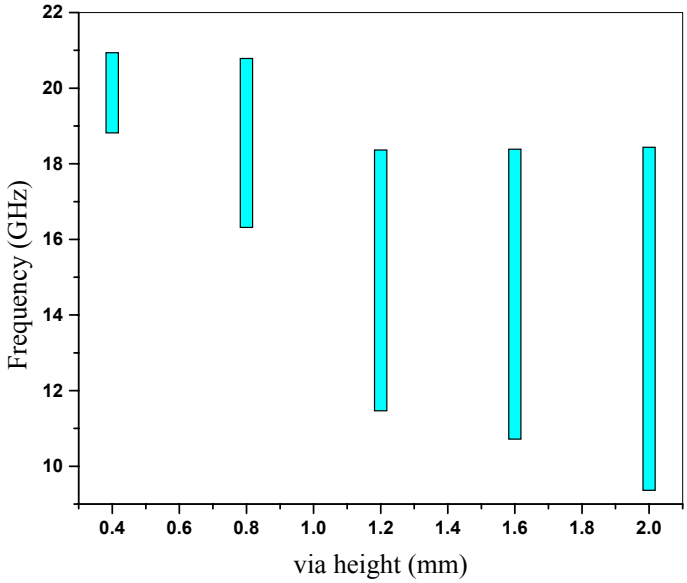

(b)

Figure 2.13. Frequency bandgap versus the height of via. (a) 4 rows of EBG patches, (b) 8 rows of EBG patches. EBG parameters: a = 2.6 mm, g = 0.4 mm, ε_r = 3, and d = 0.8 mm.

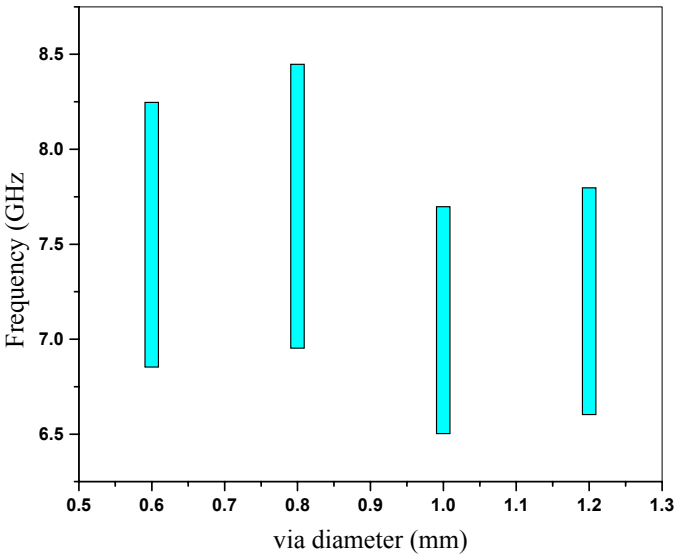

(a)

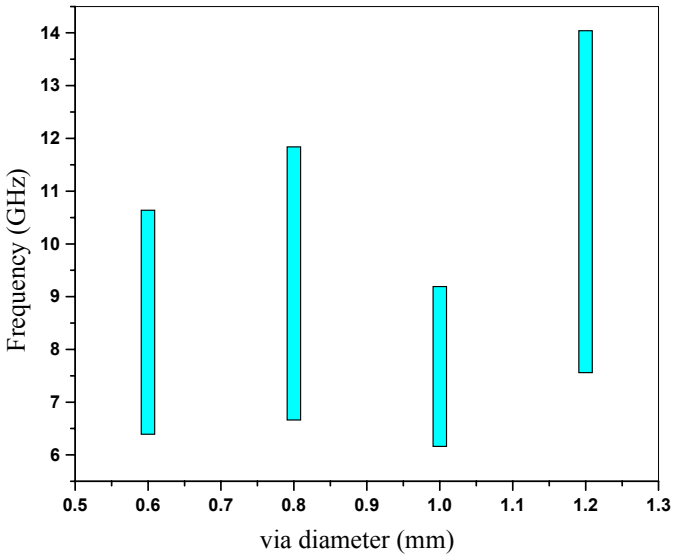

(b)

Figure 2.14. Frequency bandgap versus the diameter of via. (a) 4 rows of EBG patches, (b) 8 rows of EBG patches. EBG parameters: a = 4 mm, g = 0.4 mm, ε_r = 4.4, and h = 1.54 mm.

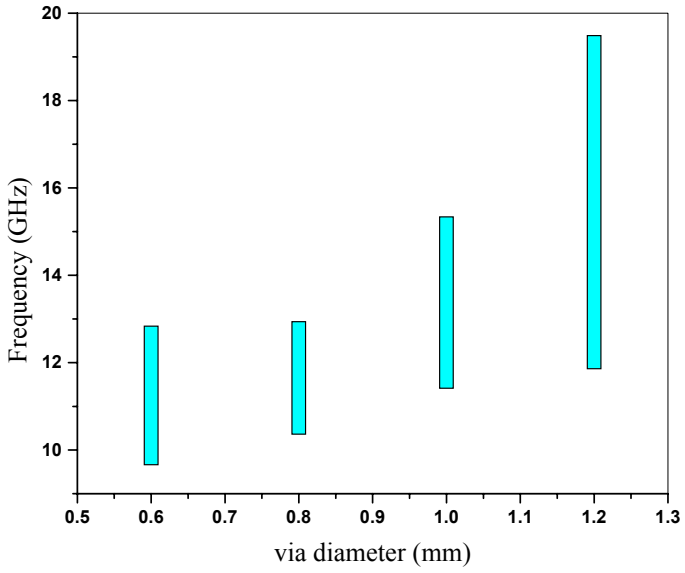

(a)

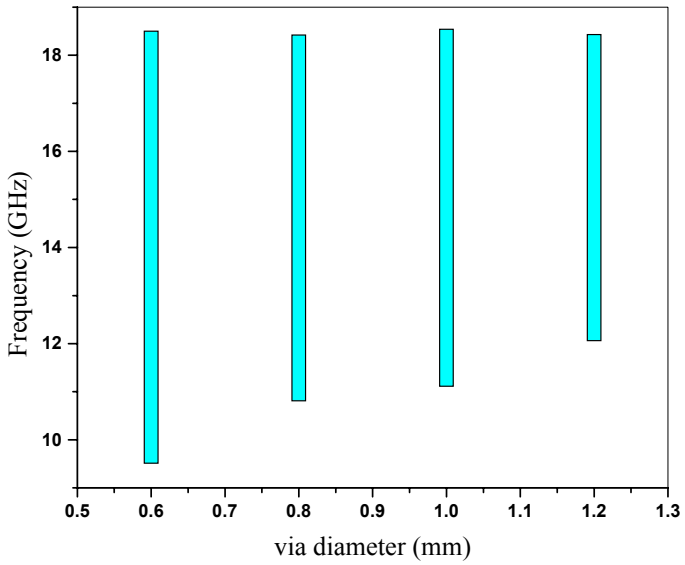

(b)

Figure 2.15. Frequency bandgap versus the diameter of via. (a) 4 rows of EBG patches, (b) 8 rows of EBG patches. EBG parameters: a = 2.6 mm, g = 0.4 mm, ε_r = 3, and h = 1.54 mm.

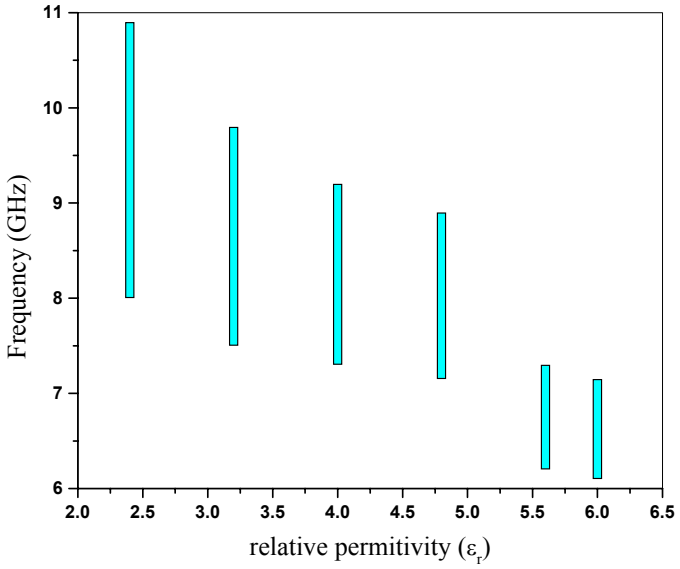

(a)

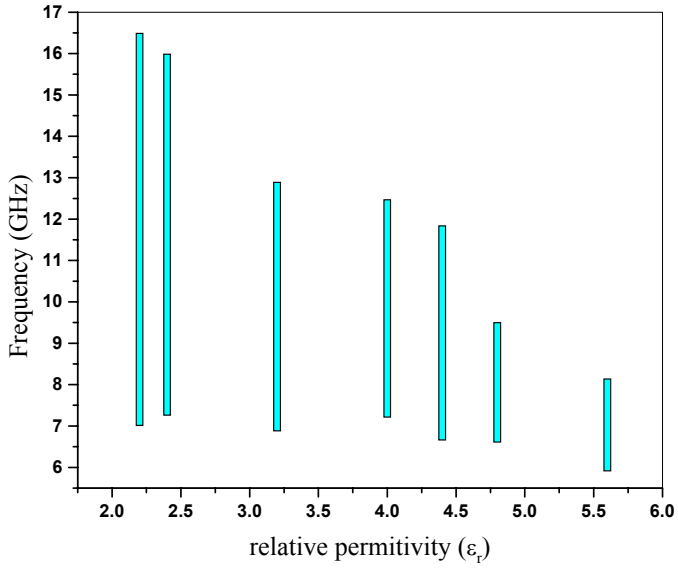

(b)

Figure 2.16. Frequency bandgap versus the relative permittivity of substrate. (a) 4 rows of EBG patches, (b) 8 rows of EBG patches. EBG parameters: a = 4 mm, g = 0.4 mm, d = 0.8 mm, and h = 1.54 mm.

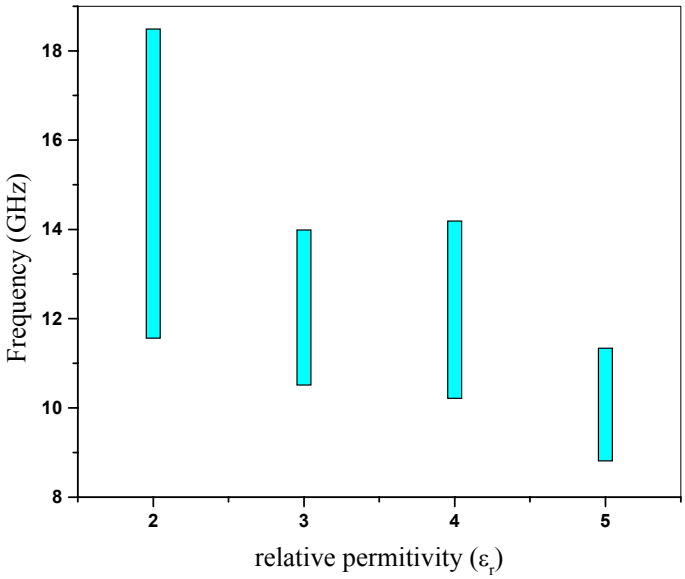

(a)

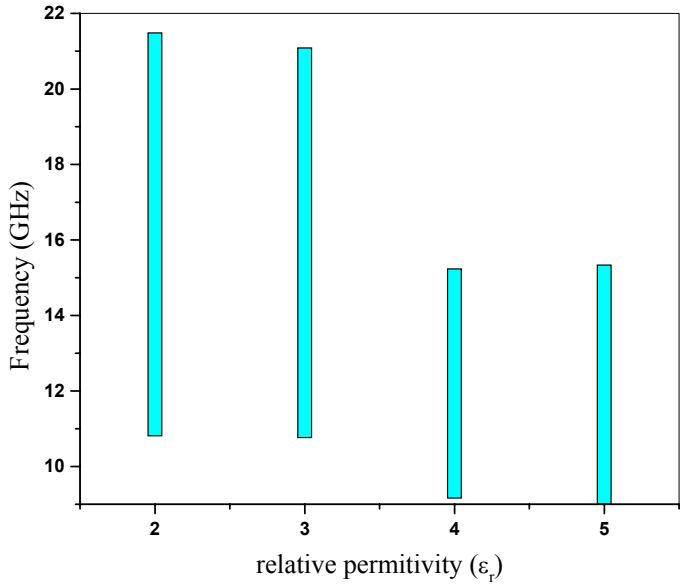

(b)

Figure 2.17. Frequency bandgap versus the relative permittivity of substrate (a) 4 rows of EBG patches, (b) 8 rows of EBG patches. EBG parameters: are a = 2.6 mm, g = 0.4 mm, d = 0.8 mm, and h = 1.54 mm.

Chapter 3 : Miniaturized EBG Structures

In this chapter, we investigate the use of very high-k dielectrics ($\varepsilon_r \geq 100$) in the design of EBG structures as strong contenders of surface wave suppressor for EMI/EMC applications. The basic idea behind the designs presented here is the use of high-k dielectrics to increase the effective capacitive load. The increased effective capacitance shifts the bandgap to lower frequencies, or alternatively, allows for maintaining the same frequency performance but with smaller size patches.

3.1. Miniaturization of Embedded EBG Structures between a Single Pair of Planes using High-K Dielectrics

The concept of embedding mushroom-type EBG structures for suppressing SSN and EMI has been studied in [4], [19]-[25]. Already there are several models based on the physics of structures and the lumped elements and transmission lines which characterize embedded EBGs and predicts the bandgaps [35], [40] with good approximation. Therefore, we do not intend to speak about the modeling of mushroom-type EBGs embedded in a plane pairs. However, briefly and using numerical tools we show the possibility of shrinking the dimensions of EBGs using very high-k dielectrics. This type of EBGs due to addition of layers and having vias are costly to manufacture. Recently, planar EBGs as a solution to these drawbacks were introduced [29]-[31]. We continue our studies on planar EBGs in Section 3.2.

3.1.1. Numerical Characterization of Embedded Mushroom-Type EBGs made of High-k Dielectrics

The square patch mushroom-type EBG studied in 0 is embedded between two metallic layers as shown in Figure 3.1. The design parameters including size of the square patch, diameter of the via, gap between the patches, thickness of the filling dielectric materials; the one surrounding the EBG structures and the one located between the patch and the top metallic plane; and a relative permittivity of these dielectrics are shown on the same figure. The physical-based model for a unit cell of EBG embedded between pairs of plane is shown in Figure 3.2 [41]. The resonant frequency (center frequency) of the unit cell is given by $f_c = 1/2\pi\sqrt{L(C_1 + C_2)}$. Therefore, by increasing the capacitive load or the inductive load the bandgap can be moved to lower frequencies or the same frequency performance can be maintained by reducing the size of inclusions. The effect of design parameters on the first suppression band is demonstrated numerically as follows.

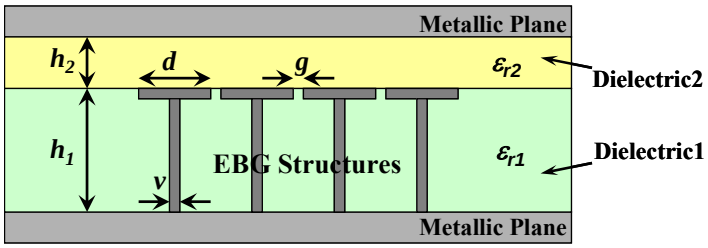

Figure 3.1. Side view of embedded mushroom-type EBG between parallel planes. The design parameters are included in the figure.

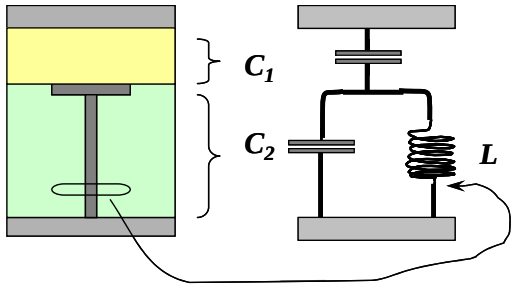

Figure 3.2. Physical-based model for a solid patch mushroom-type EBG embedded in between parallel planes. C_1 models the capacitance between the patch and the top plane, C_2 is the capacitance between the patch and the bottom plane, and L represents the inductance of via.

The suppression bandgap of EBGs is extracted from the computed S-parameters. For this purpose, we used the setup which is parallel plate waveguide loaded with 4 cells of EBG structures as shown in Figure 3.3. The EBGs are analyzed up to 20 GHz. The effective suppression band is defined to be the frequency band where suppression exceeds 20 dB. The relationship of the suppression band and the patch size for EBG structures, with the following parameters: $\varepsilon_{r1} = 4.4$, $h_1 = 100$ μm, $\varepsilon_{r2} = 50$, $h_2 = 16$ μm, $g = 200$ μm, and $v = 200$ μm, is shown in Figure 3.4. Increasing capacitive loads (C_1, C_2) through increasing patch dimension shifts the bandgap downward. The suppression band in relation to gap separation is plotted in Figure 3.5. The EBG parameters are as follows: $\varepsilon_{r1} = 4.4$, $h_1 = 100$ μm, $\varepsilon_{r2} = 50$, $h_2 = 16$ μm, $d =$ 1 mm, and $v = 200$ μm. As it is clear from graphs, in this scale the effect of gap on the lower edge of suppression band is not noticeable. The relationship between the suppression band and diameter of via is plotted in Figure 3.6. The EBG parameters are as follows: $\varepsilon_{r1} = 4.4$, $h_1 = 100$ μm, $\varepsilon_{r2} = 50$, $h_2 = 16$ μm, $d = 1$ mm, and $g = 40$ μm.

Decreasing the via diameter shifts the lower edge of the suppression band downward. This decrement equates the increment of the capacitive loads (C_1, C_2) due to increment of the effective patch area and the increment of inductance L [40]. The relationship between the suppression band and dielectric relative permittivity of media 1 is shown in Figure 3.7. The parameters of the EBG structure are as follows: h_1 = 100 μm, ε_{r2} = 50, h_2 = 16 μm, d = 0.4 mm, g = 40 μm, and v = 40 μm. Using high-k materials in media 1 increases the capacitance C_1. As a result, the suppression band shifts to lower frequencies. Decreasing h_1 and h_2 has similar effects, as it causes the capacitive loads (C_1, C_2) to increase correspondingly.

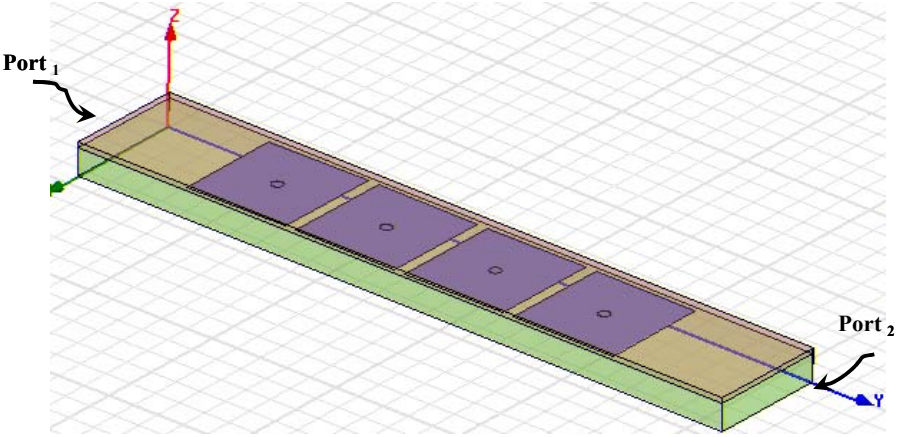

Figure 3.3. Simulation setup used to extract the suppression band of the EBG structure from computed S_{21}. The computational domain is ideal parallel plate waveguide with PMC boundary on the sides.

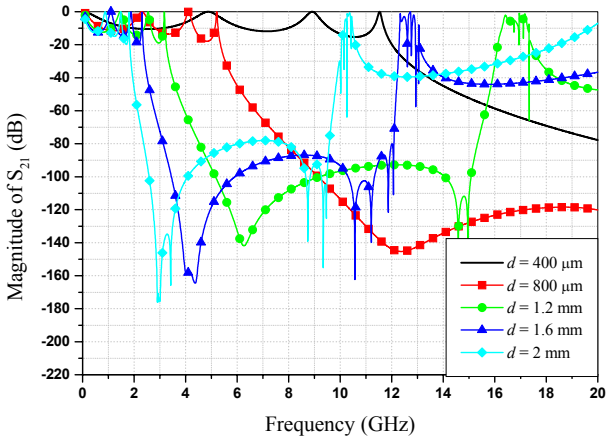

Figure 3.4. Magnitude of S_{21} for the embedded EBG structures in parallel planes with the different patch sizes. The EBG structures have the following parameters: $\varepsilon_{r1} = 4.4$, $h_1 = 100$ μm, $\varepsilon_{r2} = 50$, $h_2 = 16$ μm, $g = 200$ μm, and $v = 200$ μm (design parameters are shown in Figure 3.1).

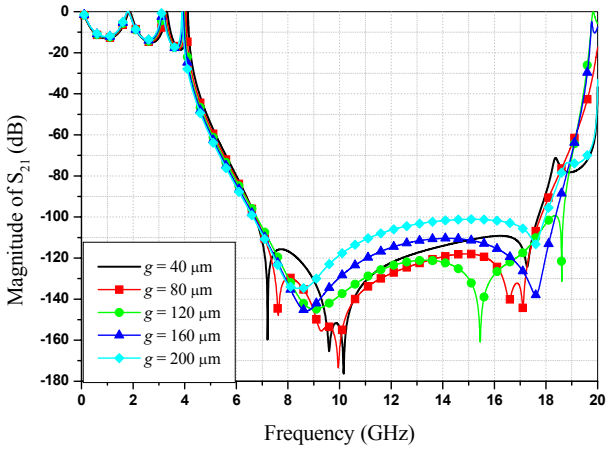

Figure 3.5. Magnitude of S_{21} for the embedded EBG structures in parallel planes with the different gap sizes. The EBG structures have the following parameters: $\varepsilon_{r1} = 4.4$, $h_1 = 100$ μm, $\varepsilon_{r2} = 50$, $h_2 = 16$ μm, $d = 1$ mm, and $v = 200$ μm (design parameters are shown in Figure 3.1).

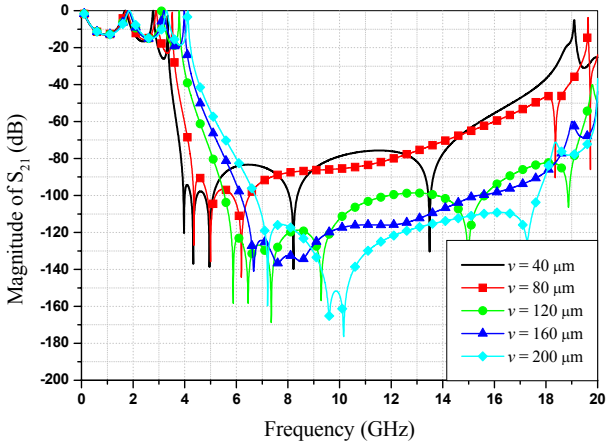

Figure 3.6. Magnitude of S_{21} for the embedded EBG structures in parallel planes with the different via diameters. The EBG structures have the following parameters: ε_{r1} = 4.4, h_1 = 100 μm, ε_{r2} = 50, h_2 = 16 μm, d = 1 mm, and g = 40 μm (design parameters are shown in Figure 3.1).

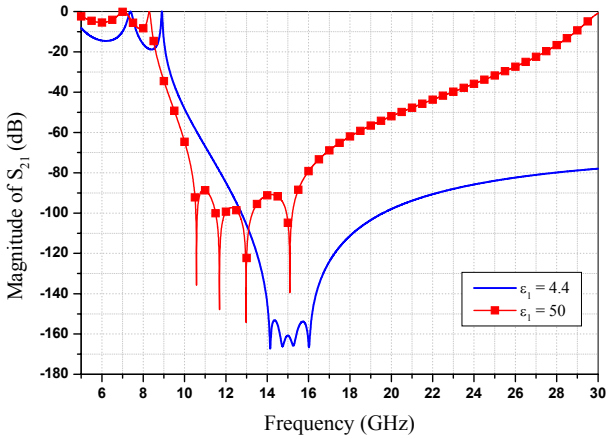

Figure 3.7. Magnitude of S_{21} for the embedded EBG structures in parallel planes with different values of dielectric relative permittivity for media 1. The EBG structures have the following parameters: h_1 = 100 μm, ε_{r2} = 50, h_2 = 16 μm, d = 0.4 mm, g = 40 μm, and v = 40 μm (design parameters are shown in Figure 3.1).

In Figure 3.8, the magnitude of S_{21} versus frequency is plotted for three different EBG structures embedded between plane pairs. The design parameters of the first sample referred to by the symbol (*a*) on the figure are: $\varepsilon_{r1} = 4.4$, $h_1 = 100$ μm, $\varepsilon_{r2} = 50$, $h_2 = 16$ μm, $d = 0.4$ mm, $g = 40$ μm, and $v = 40$ μm. The parameters of sample (*b*) are: $\varepsilon_{r1} = 4.4$, $h_1 = 100$ μm, $\varepsilon_{r2} = 70$, $h_2 = 16$ μm, $d = 0.4$ mm, $g = 40$ μm, and $v = 40$ μm. Sample (*c*) has the following parameters: $\varepsilon_{r1} = 4.4$, $h_1 = 108$ μm, $\varepsilon_{r2} = 70$, $h_2 = 8$ μm, $d = 0.4$ mm, $g = 40$ μm, and $v = 40$ μm. We can identify that increasing the capacitive loads (C_1, C_2) shifts the suppression band to lower frequencies. Additional type of samples are summarized in Table 3.I. Theses samples are sorted in such a way to show the effect of increment of the effective capacitive load on the suppression bandgap. The distance between two planes (the total thickness) is fixed at 116 μm and the permittivity of media 1 is equal to 4.4. It is obviously clear in Table 3.I the advantage of applying thin layer of very high-k material ($\varepsilon_r \geq 100$) between patch and upper metallic plane to provide suppression band at lower frequencies.

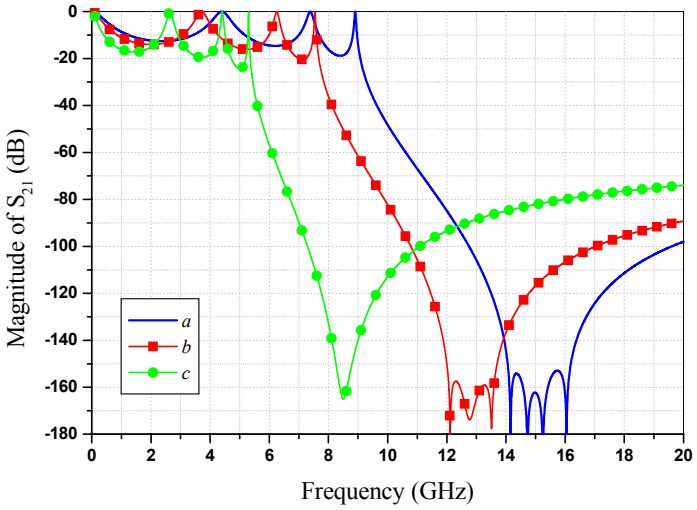

Figure 3.8. Magnitude of S_{21} for different embedded EBG structures in parallel planes. The samples have the following parameters: (*a*) ε_{r1} = 4.4, h_1 = 100 μm, ε_{r2} = 50, h_2 = 16 μm, d = 0.4 mm, g = 40 μm, and v = 40 μm. (*b*) ε_{r1} = 4.4, h_1 = 100 μm, ε_{r2} = 70, h_2 = 16 μm, d = 0.4 mm, g = 40 μm, and v = 40 μm. (*c*) ε_{r1} = 4.4, h_1 = 108 μm, ε_{r2} = 70, h_2 = 8 μm, d = 0.4 mm, g = 40 μm, and v = 40 μm (design parameters are shown in Figure 3.1).

Table 3.I. Specifications of the different square patch mushroom-type EBG structures embedded in parallel planes and related suppression bands (design parameters are shown in Figure 3.1). The thickness of parallel plane is equal to 116 μm and $\varepsilon_{r1} = 4.4$ for all samples.

ε_{r2}	d (mm)	g (μm)	v (μm)	h_1 (μm)	h_2 (μm)	Suppression Band (GHz)
50	0.4	40	40	100	16	9.1-20$^+$
70	0.4	40	40	100	16	7.7-20$^+$
70	0.4	40	40	108	8	5.4-20$^+$
70	0.4	40	40	112	4	3.8-20$^+$
100	0.4	40	40	112	4	3.2-20$^+$
100	0.43	10	40	113	3	2.5-20$^+$
100	0.43	10	40	114	2	2.1-20$^+$
120	0.43	10	40	114	2	1.9-20$^+$
120	0.43	10	20	114	2	1.6-20$^+$
120	0.44	10	20	114	2	1.5-20$^+$
150	0.44	10	20	114	2	1.4-20$^+$
120	0.44	10	20	115	1	1.2-20$^+$
150	0.44	10	20	115	1	1.1-20$^+$
200	0.44	10	20	115	1	0.8-20$^+$

$^+$ Shows suppression band extends beyond 20 GHz

3.2. Miniaturization of Planar EBG Structures using High-K Dielectrics

A planar EBG structure consists of two metallic layers isolated by a substrate. It is constructed by periodically patterning one of those metallic layers. Using spiral-inductors is the best choice to increase the net inductance of EBG structures leading

to a widening of the bandgap and decreasing the lower edge of bandgap. The innermost turn of spiral inductors are connected to other circuitries using wire-bonds, air-bridges or bridges through additional layers (In that case, the inductor isn't planar). The value of inductance may increase because of having positive mutual inductance between turns. However, fabrication of this type of inductor is costly. To reduce manufacturing cost, planar inductors such as Archimedean spiral inductor or meander line inductor shown in Figure 3.9 can be used. The inductance per unit area provided with these types of inductors is not as high as the one obtained from spiral-inductor with bridge. Reduction in the value of inductance is due to the negative mutual couplings between adjacent turns. Later, in the modeling section, we will discuss more about this effect. Choosing the planar inductor is a trade off between cost and performance. The efficacy of implementing meander lines was shown in [42]. In this work, meander lines are used as inductive bridges connecting the patches. The top views of a unit cell of a few planar EBG structures consisting of different meander lines with dissimilar number of turns and unequal lengths are shown in Figure 3.10. The meander lines are connected to the patches at the edge without any margin. Figure 3.11 shows the top view of a unit cell of EBG pattern with two-turn meander lines connected with a margin to the patch. In this study, unless it is clearly stated, we are dealing with structures with no margins. A planar EBG structure consisting of two-turn meander lines and its critical design parameters are shown in Figure 3.12. The design parameters include: size of the patch, dimensions of the meander line, thickness and dielectric constant of the substrate. The number of line

turns in meander is represented by N. In this work, it is assumed that the meander line parameters (M_G, M_W, M_L, M_B) are constant along the line to simplify the study.

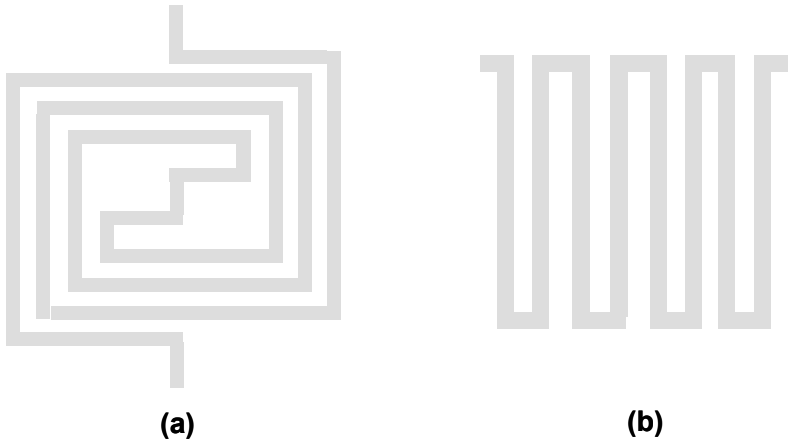

Figure 3.9. Planar inductors. (a) Archimedean spiral inductor. (b) Meander line inductor.

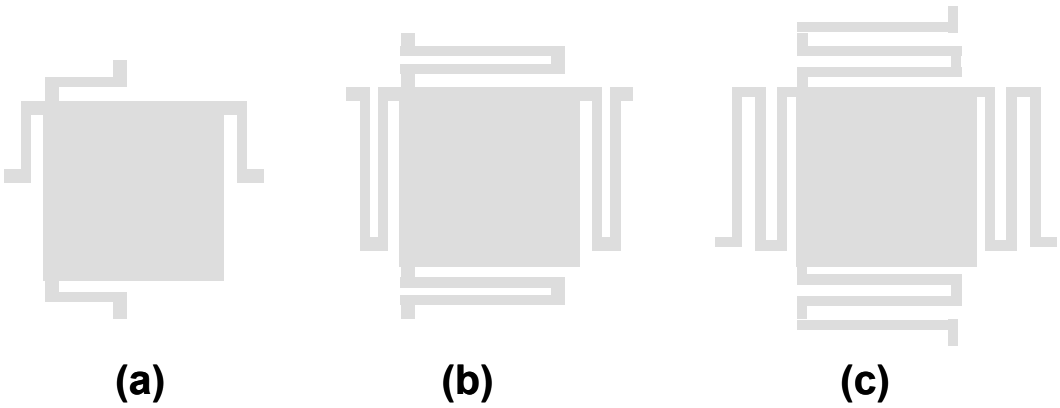

Figure 3.10. Top views of a unit cell of different planar EBG structures. The meander line as an inductive bridge connecting the patches in EBG structures consists of (a) one turn, (b) two turns, and (c) three turns.

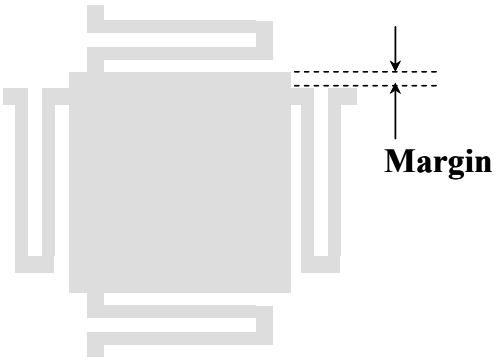

Figure 3.11. Top view of a unit cell of a planar EBG structure. The meander line as an inductive bridge providing current continuity between the patches in the EBG pattern is connected to two adjacent patches with a margin.

The physical-based model of a unit cell of planar EBG structure existing in a 1-D array of EBG structures is shown in Figure 3.13. In this model, the capacitance between patterned layer and ground is given by:

$$C = \varepsilon A / h$$

Equation 3-1

where ε and h are the permittivity and the thickness of the substrate, respectively. A is the area of the patterned planar conductive part. According to [26], [43], coupling capacitance between two adjacent arms of the meander line can be approximated as:

$$C_{cmm} = \frac{M_L(\varepsilon + \varepsilon_0)}{\pi} \cosh^{-1}(M_W / M_G)$$

Equation 3-2

Similarly, the coupling capacitance between each patch and its adjacent meander arm can be approximated as the geometrical mean of two capacitances as:

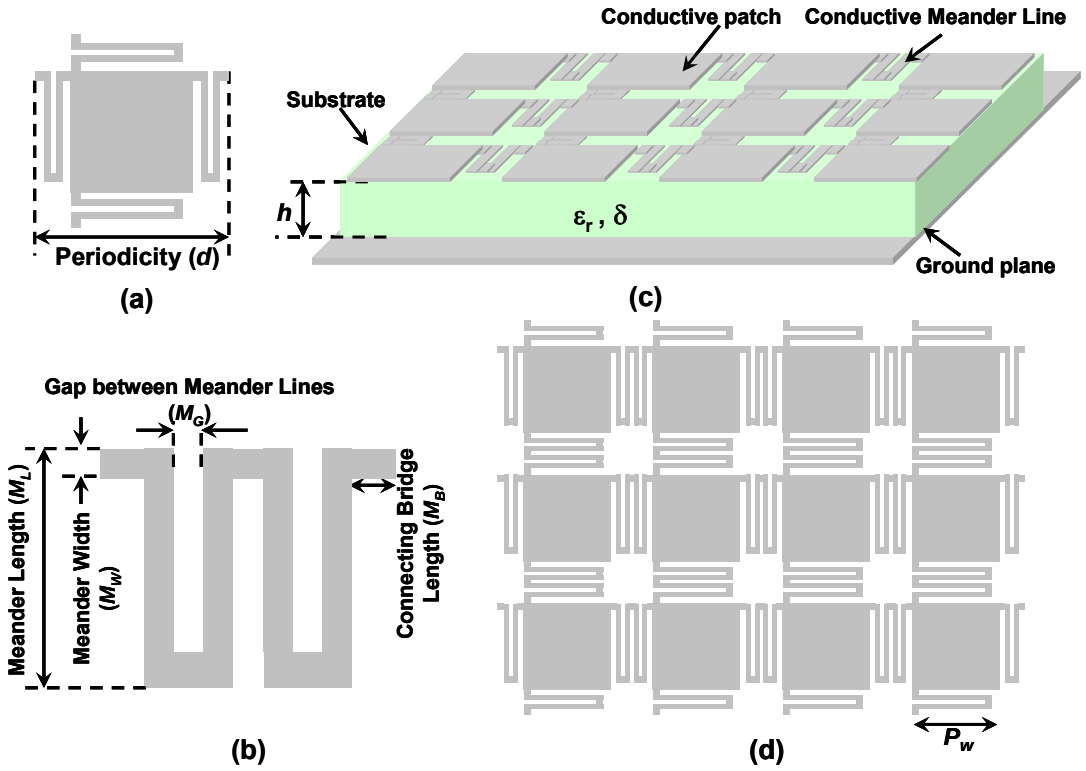

Figure 3.12. Planar EBG structure with two-turn meander lines as inductive bridges. (a) top view of the unit cell, (b) top view of the meander line bridge, (c) perspective view of the total structure, (d) top view of the total structure. The design parameters are shown in the diagram.

$$C_{cpm} = \sqrt{C'_{cmm} C'_{cpp}}$$

Equation 3-3

where C'_{cmm} represents the coupling between two adjacent arms which are spaced from each other by a gap equal to M_B. It is given similar to Equation 3-2 by:

$$C'_{cmm} = \frac{M_L(\varepsilon + \varepsilon_0)}{\pi} \cosh^{-1}(M_W / M_B)$$

Equation 3-4

Similarly, C'_{cpp} is the coupling between two adjacent patches which are spaced from each other by a gap equal to M_B and given by:

$$C'_{cpp} = \frac{M_L(\varepsilon + \varepsilon_0)}{\pi} \cosh^{-1}(P_W / M_B)$$

Equation 3-5

The total mutual coupling between adjacent arms of meander line can be approximated by: $C_1 = C_{cmm}/(2N-1)$. Similarly, C_2 showing the total mutual coupling between meander line and two adjacent patches is defined by: $C_2 = C_{cpm}/2$. The total inductance of meander line is represented by L. The center frequency (resonant frequency) of the unit cell of EBG is moved to lower values by increasing the effective capacitance (C_{eff}) or the effective inductance (L_{eff}) according to the relationship $f_c = 1/\left(2\pi\sqrt{L_{eff}C_{eff}}\right)$. L_{eff} is equal to L and $C_{eff} = \left(C/2 \parallel C/2\right) + (C_1 \parallel C_2)$. Therefore, to have a bandgap at lower frequencies, one needs to increase C_{eff} or L_{eff}. By inspection of formulas for C, C_{cmm}, and C_{cpm}, the capacitance is increased by increasing the metallic pattern dimensions or the dielectric constant. However, using high dielectric constant have the distinct advantage of allowing miniaturization of EBG patterns in addition to shifting the bandgap to lower frequencies. In following sections, we will discuss about the subject of accurate modeling. It will be shown that the effective inductance can be increased by increasing the length of meander line and the gap between adjacent arms of meander line. Increasing the gap will reduce the magnetic coupling.

The progress in material science has provided composite dielectric materials with very high dielectric constants ($\varepsilon_r \geq 100$) known as high-k dielectrics. Currently,

several companies are producing these types of materials with low losses. Following, we will show that the miniaturization of EBG structures is possible due to availability of these commercial high-k materials. Also, we will show advantages of combining these high-k materials with high effective inductive loads to have wide suppression bands at low frequencies.

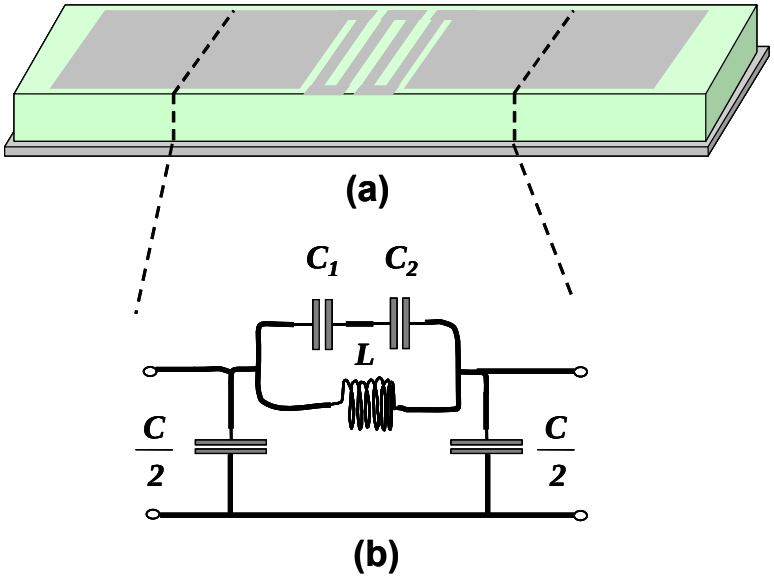

Figure 3.13. Physical-based model of the planar EBG structure. C_1 represents the mutual coupling capacitance between arms of the meander line. C_2 is the mutual coupling capacitance between meander line and two adjacent patches. C is the capacitance between the patch and the bottom plane, and L represents the inductance of meander line.

3.2.1. Numerical Characterization of Miniaturized-Wideband Planar EBG Structures

We used commercial software, Ansoft's HFSS, to validate the improvement obtained from the combination of high-k dielectric substrate and meander line bridge

in the proposed planar EBG structure. The EBGs are analyzed up to 14 GHz. If the suppression band goes beyond 14 GHz, we have indicated the upper bound of band by 14^{+} GHz. The setup used to extract the effective suppression band is illustrated in Figure 3.14. The ports defined for this structure are separated by N cells (in our case $N = 4$). Each port is located between the patterned layer and ground. The magnitude of the S_{21} parameter (defined between two ports) is indicative of the suppression band. Figure 3.15 shows the magnitude of S_{21} for the EBG pattern consisting of two-turn meanders as shown in Figure 3.12 with the following parameters: $P_W = 1.4$ mm, $h = 114.3$ μm (4.5 mil), $M_W = 0.02$ mm, $M_B = 0.02$ mm, $M_L = 1.34$ mm, $M_G = 0.02$ mm, $\varepsilon_r = 140$, and $tan\ \delta = 0.0015$. The reference case which is a similar setup without EBG pattern is included in the same figure. The effective suppression band considered throughout this study is defined to be the frequency band where the suppression exceeds 20 dB. For the proposed structures, a very wide suppression band (3.5 – 13.9 GHz) is achieved.

Few samples are summarized in the Table 3.II to show the effect of design parameters on the suppression bandgap. Samples No. 1 to 6 are tabulated in such a way that only one design parameter in each sample is different from the previous one. From these results, we conclude the following: 1) increasing the dimensions of patch shifts the bandgap to lower frequencies. This increment is equivalent to increasing the effective capacitive load. 2) The longer meander line which provides larger inductor not only shifts the bandgap to lower frequency but also widens the effective suppression band. In sample No. 6 compared to sample No. 5, a longer meander line with three turns is used. However, the patch size is decreased to keep approximately

the same unit cell size. As can be concluded from results of the suppression band, a comparable or even better performance is obtained. Generally, results in Table 3.II show the efficiency of using larger inductive load. Comparing samples No. 5 and No. 7 in this table emphasizes that not only the length of meander line is an important factor to clarify the suppression band but also the connection point between the patch and the meander line is important too. Sample No. 6 with a margin equal to 0 mm is providing larger bandgap than sample No. 7 with a margin equal to 0.1 mm (refer to Figure 3.11). All other design parameters are the same for both samples. However, the length of meander line in sample No. 5 is slightly longer than the length of meander line in sample No. 7. The step discontinuity in microstrip line can be modeled by a *T*-equivalent circuit. The values of lumped elements modeling the discontinuities with different margins are different. Later, in modeling section, we will include the discontinuity effect in our modeling.

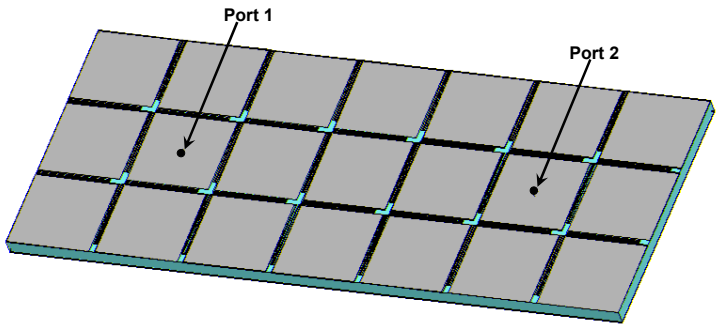

Figure 3.14. Schematic showing the simulation setup and location of the ports to extract the suppression band of the EBG structure from computed S_{21}.

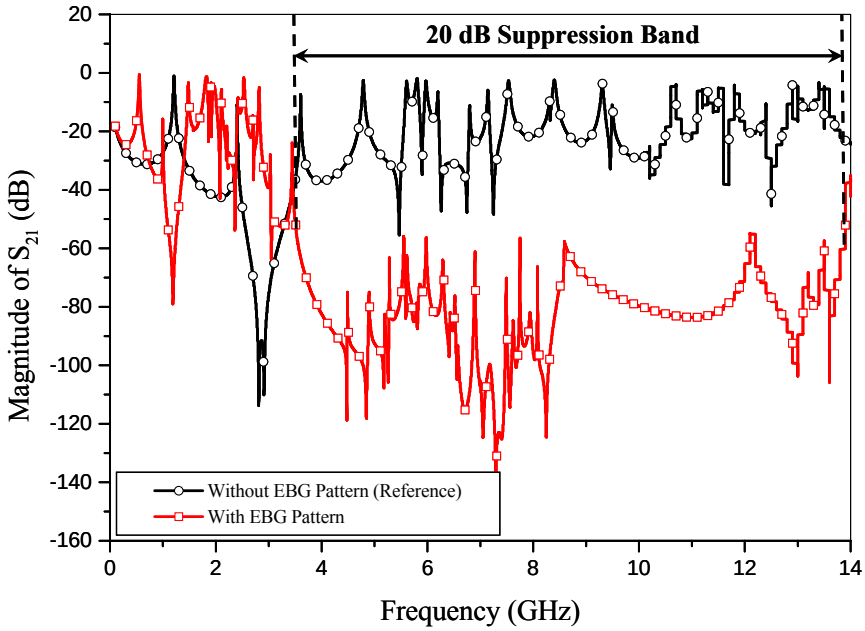

Figure 3.15. Magnitude of S_{21} versus frequency for the EBG structure shown in Figure 3.12 using the setup shown in Figure 3.14. The parameters of the EBG structure are: P_W = 1.4 mm, h = 114.3 µm, M_W = 0.02 mm, M_B = 0.02 mm, M_L = 1.34 mm, M_G = 0.02 mm, ε_r = 140, and $tan\ \delta$ = 0.0015 (design parameters are shown in Figure 3.12). The reference case which is parallel plane is included for the purpose of comparison.

Another set of samples consisting of two-turn meanders are listed in Table 3.III. These samples have been chosen in such a way that their suppression band covers the operating frequency of current microprocessors and resonant frequencies of the package. The data in this table clearly shows the advantage of using high permittivity dielectrics compared to conventional low ones (here FR-4) in reducing size of unit cell of EBGs. By comparing these cases, it is concluded that a size

reduction of more than 10 times is achieved. Also, we could approximately keep a similar wide suppression band. The effective wide suppression band in proposed planar EBGs can be easily tuned to filter EMI and electromagnetic noises in EMC applications. The sample designs provided here shows efficacy of combining very high-permittivity materials with inductive bridges in design of miniaturized wideband planar EBG structures.

Generally, the design of samples provided in this section has not been optimized. Optimizing inductive part of the design to provide more inductive load in small area can lead to a wider band in addition to smaller unit cell size. In the following section, we will continue our study on the modeling and the characterization of the proposed EBG structure proposed in this section.

Table 3.II Specifications of the different planar EBG patterns and related suppression band (design parameters are shown in Figure 3.12). For all samples h = 114.3 μm, ε_r = 140, and $tan\ \delta$ = 0.0015.

Sample N0.	**# Turns N**	**P_W (mm)**	**M_B (mm)**	**M_W (mm)**	**M_L (mm)**	**M_G (mm)**	**d (mm)**	**Suppression Band (GHz)**
1	1	1	0.02	0.02	0.44	0.02	1.1	7.9-14$^+$
2	1	1.4	0.02	0.02	0.44	0.02	1.5	4.9-9.7
3	1	1.4	0.02	0.02	1.34	0.02	1.5	3.7-11.3
4	2	1.4	0.02	0.02	1.34	0.02	1.58	3.5-13.9
5	2	1.4	0.02	0.02	1.24	0.02	1.58	3.45-14
6	3	1.3	0.02	0.02	1.24	0.02	1.56	3.5-14$^+$
7	2 (margin = 0.1 mm)	1.4	0.02	0.02	1.24	0.02	1.58	3.85-14.1

$^+$ shows suppression band extends beyond 14 GHz.

Table 3.III. Specifications of the different planar EBG patterns and related suppression band (design parameters are shown in Figure 3.12). For all samples h = 114.3 μm and N = 2.

Sample N0.	ε_r	tan δ	P_W (mm)	M_B (mm)	M_W (mm)	M_L (mm)	M_G (mm)	T (mm)	Suppression Band (GHz)
1	4.3	0.02	20	0.2	0.2	20	0.2	21.8	1.3-13.8
2	140	0.0015	1.4	0.02	0.02	1.34	0.02	1.58	3.5-13.9
3	140	0.0015	1.6	0.02	0.02	1.6	0.02	1.78	2.9-12.5
4	200	0.0015	1.2	0.02	0.02	1.2	0.02	1.38	3.4-11.5
5	200	0.0015	1.4	0.02	0.02	1.4	0.02	1.58	3-11.3
6	300	0.0015	1.2	0.02	0.02	1.2	0.02	1.38	3-11.3
7	200	0.0015	1.6	0.02	0.02	1.6	0.02	1.78	1.9-10.8

3.3. Modeling of the Proposed Planar EBG Structures

In the last few years, different methods have been used to characterize the EBG structures. The characterization is satisfied by relating the bandgap and center frequency to constituent materials and dimensions of inclusions. These methods include:

- Numerical analysis using various methods such as the Finite Elements Method (FEM), The Finite-Difference Time-domain (FDTD) method, …etc.
- Measurements
- Equivalent circuit modeling [20], [26], [33], [34], [41]
- Equivalent circuit-transmission line models [35], [40], [44]

Among the characterization methods, experimental methods consisting of fabrication of structures followed by measurements is favored due to its accuracy, but it is costly and time consuming. The full-wave numerical analysis such as commercial software

Ansoft's HFSS based on FEM, provides accurate results, however, at the cost of expensive computations in terms of time and memory. More often one encounters convergence or memory problem due to large number of meshes in the computational domain. The analysis using methods which are not full-wave based may compromise between accuracy, time, and cost. To use time and resources efficiently, several methods based on analyzing infinite periodic structures have been developed. These methods approximately characterize the required structures in a defined application based on analyzing a unit cell of the structure and implementing proper periodic boundary condition based on Floquet theorem [45]. Simplified setups decrease simulation time significantly. However, they are not still efficient to characterize a large number of structures to prepare data tables which may be used as guide for designing new EBG structures for the required operating regimes. Model-based methods were developed as a solution to these drawbacks. Generally, model-based methods give a qualitative perspective about the relationship between the bandgap and the topology and the composition of EBG structures. However, deriving a model which may predict accurately the dispersive effects through the entire range of frequencies is not viable, because of several EM effects that become strong at the higher frequencies and are typically not included in the models. Therefore, for accurate designs, further tunings and adjustments of the specifications of EBG structures are necessary using full-wave numerical analysis methods. As a result, the combination of two or more of the above mentioned methods are used to design new EBGs using trial and error procedure. A good initial guess using models, may decrease the load of work needed.

In [26], a simple lumped element model for the mushroom EBG structures was proposed. This model approximately works for normal wave incidence at low frequencies where the dimensions of the EBG are much smaller than the wavelength in media. Later, a model based on both transmission line theory and circuit elements was developed [44]. This model partially overcoming previous limitation can predict the bandgap with higher accuracy. Authors in [20], [34] developed a method for extracting the parameters of the model for a mushroom-type EBG embedded in parallel plate waveguide. This method uses simple formulas to derive initially the value of the lumped elements in the model and later uses a numerical algorithm for curve fitting on the S-parameters graph. This method usually is not efficient for characterization and designing of new EBG structures. Mostly, this method could be used for post analyzing, such as computing the delay time for the logic change in digital circuits connected to power planes or computing reservoir capacitors needed in different locations in power planes to improve the functioning of electronic circuits. In [41], a physical-based equivalent circuit model for mushroom EBGs embedded in parallel plate waveguide was derived. This model predicts only the center frequency of bandgap. Recently, authors in [35], [40] used the transmission line method to improve the modeling of embedded EBGs between parallel plate waveguide. Those models can predict the bandgap as well as the center frequency. Following, we are going to derive a model for planar EBG proposed in this study to get idea about the relation of bandgap to the constitutive materials and their dimensions. In Section 3.2, a physical-based equivalent circuit model was introduced to justify the advantage of using high-k materials in design of miniaturized planar EBG structure operating at

low frequencies. In this section, we derive an equivalent circuit-transmission line model which is more accurate in providing information about bandgaps.

3.3.1. Setup and Model Formulation

Detailed analysis of periodic structures based on transmission line theory and Floquet theorem is given in [45], [46]. A unit cell of planar EBG structure is shown in Figure 3.12. The computational domain and the boundary setup for extracting dispersion diagram for 2-D propagation is shown in Figure 3.16. A pairs of PBC setup for any two side walls in front of each other resembles the periodicity in that direction. To extract a 1-D equivalent circuit-transmission line model for a wave propagating through EBG patterns in *x*-direction with $\vec{k} = k_x \hat{x}$, the infinite 2-D array of EBG structures shown in Figure 3.12 may be reduced to a 1-D infinite array by applying perfect magnetic conducting (PMC) boundaries on both sides of the array as shown in Figure 3.17. Therefore, H-field is equal to zero on the sides of array. With this assumption, we have ignored the side coupling effects. A unit cell of the proposed planar EBG structure is shown in Figure 3.18. The setup shows the computational domain and the boundary setup which can be used to extract the bandgap using the dispersion diagram. This is the basic setup which will be used in later subsections for both the numerical full-wave analysis and the modeling for 1-D propagation (Γ-X region in the Brillouin zone). To prevent confusion, it should be mentioned that if we consider periodic boundary instead of PMC boundary in Figure 3.18 then dispersion in X-M and M-Γ regions in the Brillouin zone can be extrated. Results characterize new 2-D structure where in one direction its patches are

connected to each other through a meander line and in the other direction there is a gap between the two adjacent patches.

The frequency independent lumped elements used in the model represent the meander line, the patch, the mutual coupling between the meander line and the patch, and the step discontinuity between the patch and the meander line. The transmission lines connecting lumped elements are known to transfer impedance and to model the phase shift increasing with frequency. The transfer ABCD matrix presenting a unit cell of the EBG modeled with lumped elements and transmission lines is:

$$\begin{bmatrix} A & B \\ C & D \end{bmatrix} = \begin{bmatrix} A^m & B^m \\ C^m & D^m \end{bmatrix}$$

Equation 3-6

Considering the infinite array of EBG structure as a transmission line made of engineered materials with the effective propagation constant k_x and the effective characteristic impedance $Z_{0,eff}$, the ABCD parameters for this transmission line corresponding to a unit cell of EBG are presented by:

$$\begin{bmatrix} A & B \\ C & D \end{bmatrix} = \begin{bmatrix} \cos(k_x d) & jZ_{0,eff}\sin(k_x d) \\ jY_{0,eff}\sin(k_x d) & \cos(k_x d) \end{bmatrix}.$$

Equation 3-7

where d is the size of a unit cell (periodicity length). By equating Equation 3-6 and Equation 3-7 the dispersive behavior of structure is predicted. In the following subsections, we introduce the relationship between physical parameters of the structure and the lumped elements, and compute the elements of the transfer matrix A^m, B^m, C^m, and D^m. Without loss of generalization, the metallization thickness t and the metallic and dielectric losses are neglected.

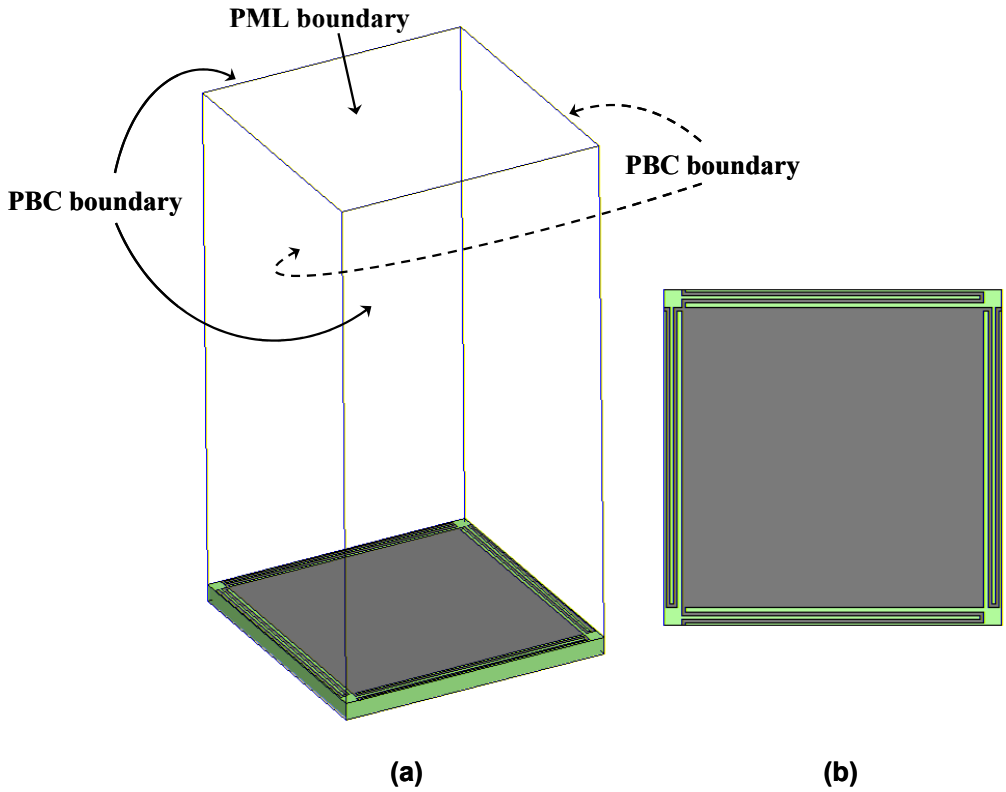

Figure 3.16. A unit cell of the planar EBG structure with two-turn meander bridges. (a) Setup used for extracting the bandgap of EBG structure in 2-D propagation using dispersion diagram. The boundary setup is shown in the figure. (b) Top view of EBG structure.

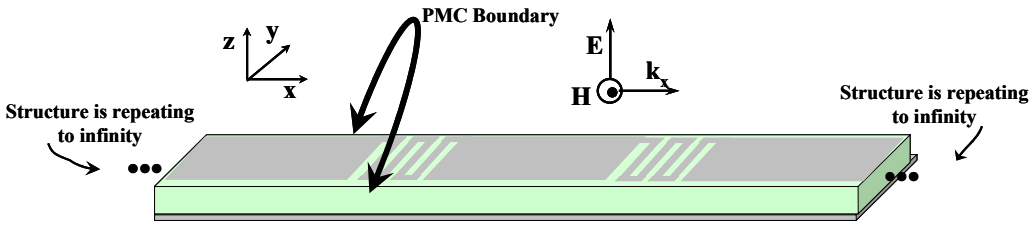

Figure 3.17. Infinite 1-D array of the proposed planar EBG.

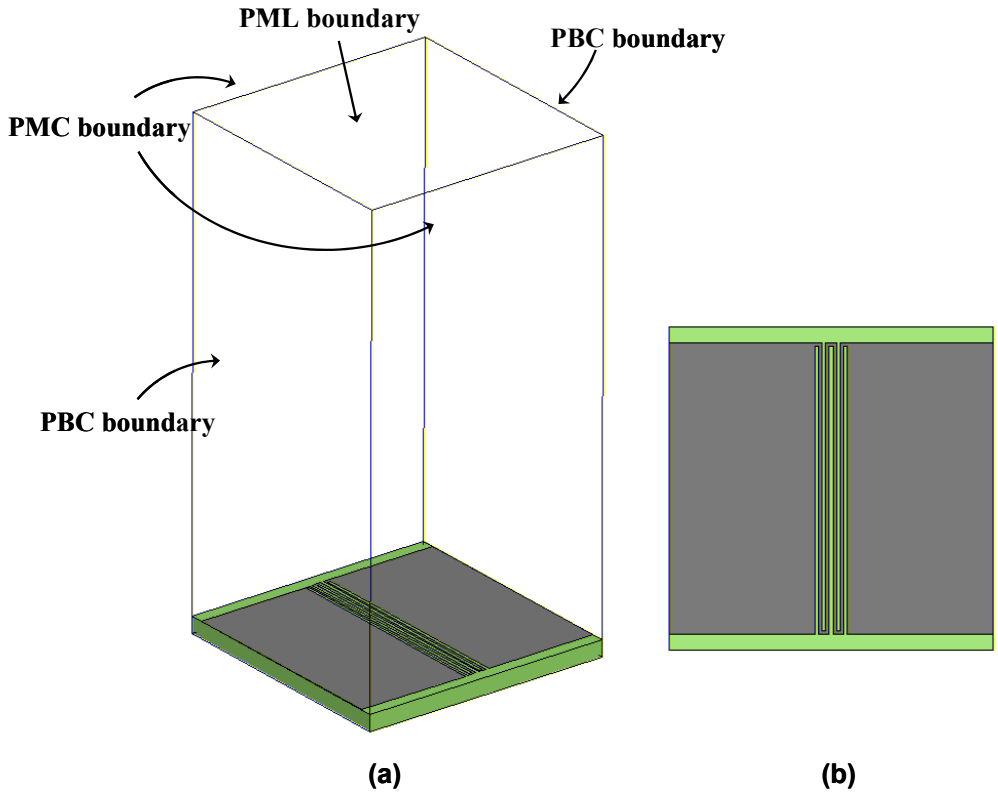

Figure 3.18. A unit cell of the planar EBG structure with two-turn meander bridge. (a) Setup used for extracting the bandgap of EBG structure in 1-D propagation using dispersion diagram. The boundary setup is shown in figure. (b) Top view of EBG structure. If PMC boundaries are replaced by a pair of PBC boundaries it resembles 2-D propagation which is different from Figure 3.16.

3.3.2. Characterization of EBG using Full-Wave Simulator

In this subsection to assess the performance of the model that will be developed in the following subsections, we are extracting the dispersion diagram of a few selective planar EBG structures using the setup shown in Figure 3.18. We use

full-wave numerical simulator Ansoft's HFSS and the irreducible Brillouin zone for this purpose. The selected samples are covering the combination of different specifications for the dielectric substrate such as high or low relative permittivity and thin or thick dielectric thickness. The first sample which is made of thin slab of high-k material has the following parameters: P_W = 1.6 mm, h = 114.3 μm, M_W = 0.02 mm, M_B = 0.02 mm, M_L = 1.6 mm, M_G = 0.02 mm, ε_r = 140, and $tan\ \delta$ = 0.0015. The dispersion diagram for this sample is shown in Figure 3.19. The first three modes and the bandgaps in between are clarified in the figure. Also, the dispersion diagram of this sample for the unit cell shown in Figure 3.16 is plotted in Figure 3.20. Comparison of results in Figure 3.19 and Figure 3.20 shows that the first and second modes are similar in both structures. However, there is a degenerate or very close mode to the second propagating mode in the structure of Figure 3.16. Again the third mode in Figure 3.18 is compatible with the fourth mode of Figure 3.16. (This way of mapping between modes of two unit cells is seen in the other chosen samples. The samples will be introduced in the following paragraphs).

The second sample which is made of thicker slab with the same permittivity is specified with the following design parameters: P_W = 1.6 mm, h = 500 μm, M_W = 0.02 mm, M_B = 0.02 mm, M_L = 1.6 mm, M_G = 0.02 mm, ε_r = 140, and $tan\ \delta$ = 0.0015. Figure 3.21 shows the dispersion diagram for the second sample. The first three modes and the bandgaps in between are clarified in the figure. The third case study is made of a thin slab with higher permittivity. This sample is specified by: P_W = 1.6 mm, h = 114.3 μm, M_W = 0.02 mm, M_B = 0.02 mm, M_L = 1.6 mm, M_G = 0.02 mm, ε_r = 200, and $tan\ \delta$ = 0.0015. The dispersion diagram including the first three propagating

modes is shown in Figure 3.22. The bandgaps in between of those modes are marked in the figure. The fourth sample is made of thin slab of low permittivity material. The design parameters for this sample are as: P_W = 20 mm, h = 114.3 μm, M_W = 0.2 mm, M_B = 0.2 mm, M_L = 20 mm, M_G = 0.2 mm, ε_r = 4.3, and $tan\ \delta$ = 0.02. The dispersion diagram for this case study is shown in Figure 3.23. The first three propagating modes and the bandgaps in between of these modes are clarified in Figure 3.23.

The small sudden variations seen in the graphs of propagating modes such as zigzag changes are numerical errors. Later, we will return back to these graphs and continue our studies with curve fitting on the *f-Bd* points in the dispersion diagrams to characterize performance of EBG structures in detail. In the following subsections, we continue the modeling discussion.

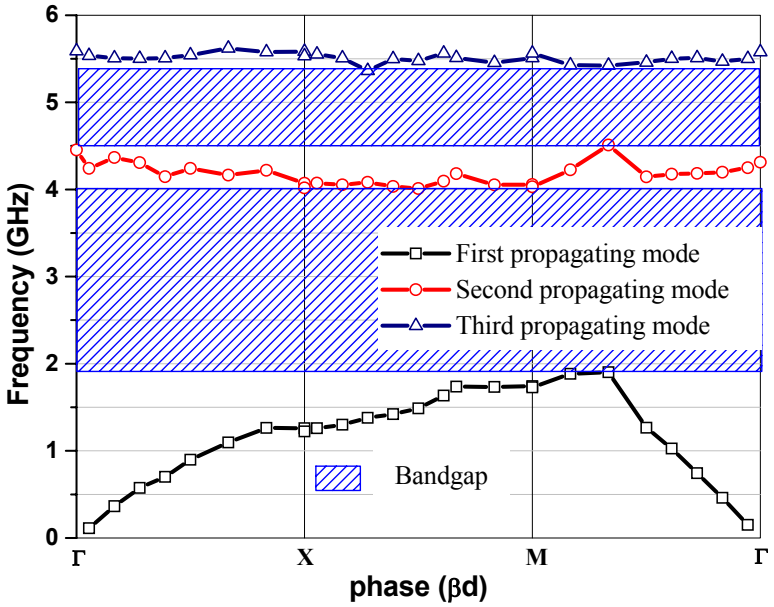

Figure 3.19. Dispersion diagram of the planar EBG structure shown in Figure 3.18 extracted using HFSS. The design parameters of the EBG are: P_W = 1.6 mm, h = 114.3 μm, M_W = 0.02 mm, M_B = 0.02 mm, M_L = 1.6 mm, M_G = 0.02 mm, ε_r = 140, and $tan\ \delta$ = 0.0015.

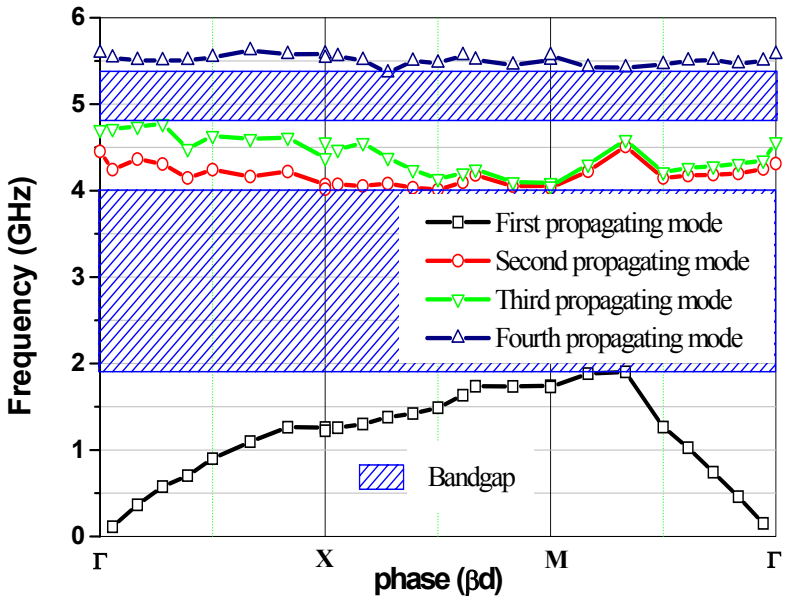

Figure 3.20. Dispersion diagram of the planar EBG structure shown in Figure 3.16 extracted using HFSS. The design parameters of the EBG are: P_W = 1.6 mm, h = 114.3 μm, M_W = 0.02 mm, M_B = 0.02 mm, M_L = 1.6 mm, M_G = 0.02 mm, ε_r = 140, and $tan\ \delta$ = 0.0015.

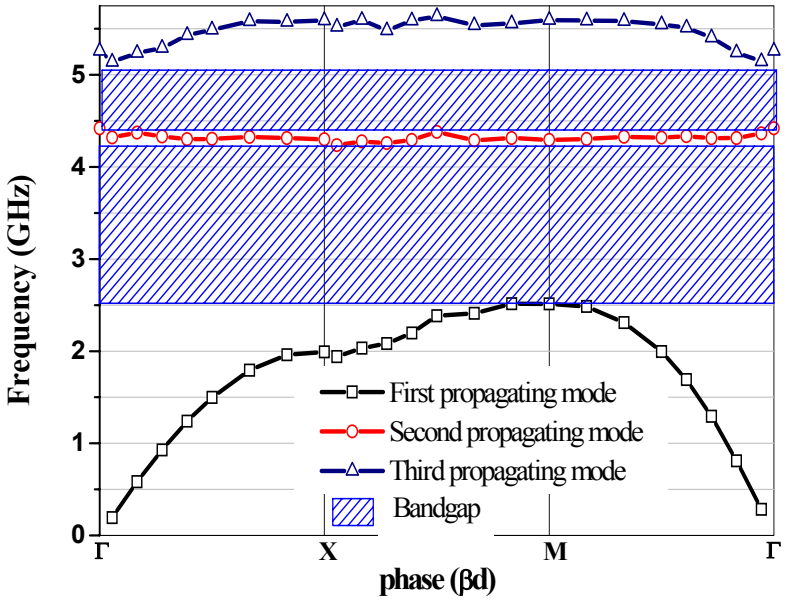

Figure 3.21. Dispersion diagram of the planar EBG structure shown in Figure 3.18 extracted using HFSS. The design parameters of the EBG are: P_W = 1.6 mm, h = 500 μm, M_W = 0.02 mm, M_B = 0.02 mm, M_L = 1.6 mm, M_G = 0.02 mm, ε_r = 140, and $tan\ \delta$ = 0.0015.

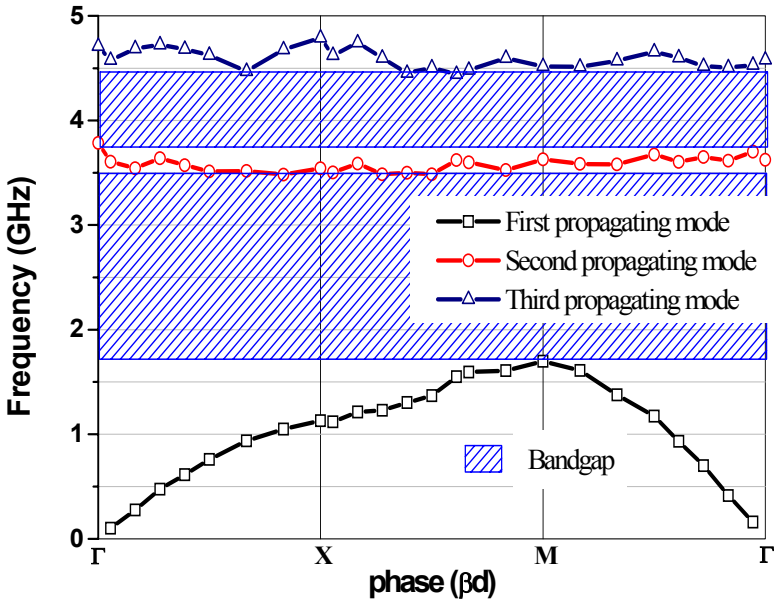

Figure 3.22. Dispersion diagram of the planar EBG structure shown in Figure 3.18 extracted using HFSS. The design parameters of the EBG are: P_W = 1.6 mm, h = 114.3 μm, M_W = 0.02 mm, M_B = 0.02 mm, M_L = 1.6 mm, M_G = 0.02 mm, ε_r = 200, and $tan\ \delta$ = 0.0015.

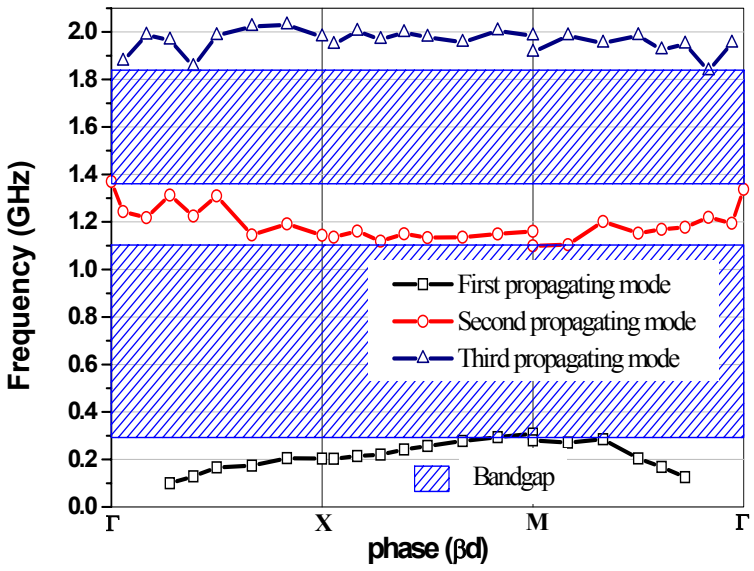

Figure 3.23. Dispersion diagram of the planar EBG structure shown in Figure 3.18 extracted using HFSS. The design parameters of the EBG are: P_W = 20 mm, h = 114.3 μm, M_W = 0.2 mm, M_B = 0.2 mm, M_L = 20 mm, M_G = 0.2 mm, ε_r = 4.3, and $tan\ \delta$ = 0.02.

3.3.3. Model of Patch

The characteristic impedances of the patch and the meander line are denoted by Z_P and Z_M, respectively (Formulas of the characteristic impedance and the effective relative dielectric permittivity for microstrip line are provided in Appendix). Z_P is much smaller than Z_M as the width of patch microstrip is much wider than the width of the meander line microstrip. At low frequencies, patch microstrip line behaves as an electrically short length line which has low impedance compare to adjacent meanders. For that scenario, the patch is modeled by a *T*-equivalent circuit

as shown in Figure 3.24 [47]. The series reactance and shunt susceptance are given by:

$$B \approx \frac{1}{Z_P}\left(\frac{2\pi P_W}{\lambda_g}\right) \Rightarrow C_{PH} \approx \frac{P_W\sqrt{\varepsilon_{reP}}}{Z_P c}$$

Equation 3-8

$$\frac{X}{2} \approx Z_P\left(\frac{\pi P_W}{\lambda_g}\right) \Rightarrow L_{PH} \approx \frac{P_W\sqrt{\varepsilon_{reP}}Z_P}{2c}$$

Equation 3-9

where P_W is the length of square patch, λ_g is the guided wavelength in dielectric substrate, c is the speed of light in free space and ε_{reP} is the effective relative permittivity of dielectric substrate. If $Z_P << Z_M$ then the patch may be approximated only by capacitance C_{PH} at low frequencies and the series inductance L_{PH} could be neglected.

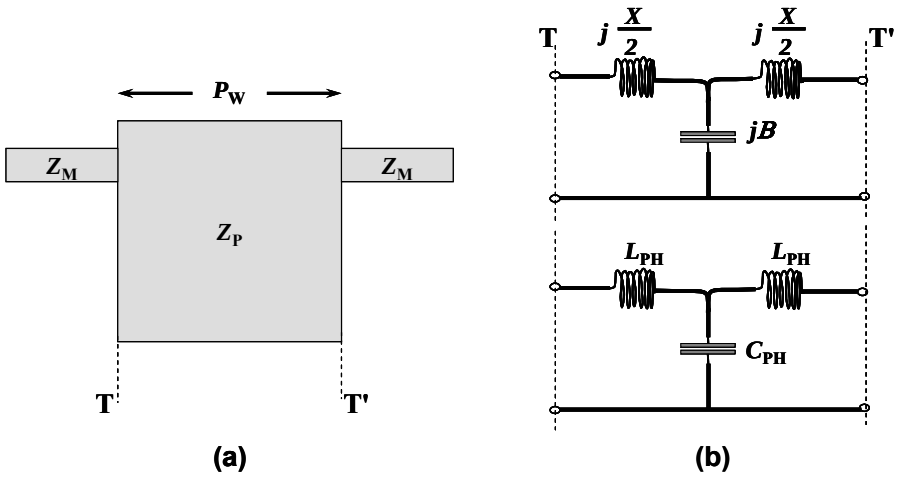

Figure 3.24. a) Patch of the planar EBG pattern which has short electrical length and low impedance. b) Equivalent lumped-element circuit.

3.3.4. Model of Patch-Meander Line Step Discontinuity

The discontinuity between the patch and the meander line in our planar EBG design is asymmetrical as shown in Figure 3.25 (a). Here, the meander line is connected to the patch at the edge (margin = 0). P_W is the width of patch and M_W is the width of the meander line. The *T*-equivalent circuit modeling the discontinuity is shown in Figure 3.25 (b). This type of discontinuity can be modeled approximately as follows. If we ignore the fringing field-effect along the side where the patch is uniformly connected to the meander then we can place PMC boundary (or H-symmetry boundary) along that side. With this assumption, we can replace the asymmetrical discontinuity with a symmetrical one as shown in Figure 3.26. The width of microstrip lines in the new step discontinuity is double the widths in original structure: $W_1 = 2P_W$ and $W_2 = 2M_W$. The elements modeling the symmetrical discontinuity are given by [47], [48]:

$$L_1 = \frac{L_{W1}}{L_{W1} + L_{W2}} L$$

Equation 3-10

$$L_2 = \frac{L_{W2}}{L_{W1} + L_{W2}} L$$

Equation 3-11

where the inductance per unit length in the microstrip line L_{wi} (i = 1, 2) is given by:

$$L_{Wi} = Z_{Ci} \sqrt{\varepsilon_{rei}} \Big/ c$$

Equation 3-12

$$L = 0.000987h\left(1 - \frac{Z_{C1}}{Z_{C2}}\sqrt{\frac{\varepsilon_{re1}}{\varepsilon_{re2}}}\right)^2$$

Equation 3-13

Z_{Ci} and ε_{rei} are the characteristic impedance and the effective relative permittivity of microstrip line with strip-width W_i, respectively. h is the dielectric thickness in micro meter. The capacitance is given by:

$$C = 0.00137h\frac{\sqrt{\varepsilon_{re1}}}{Z_{C1}}\left(1 - \frac{W_2}{W_1}\right)\left(\frac{\varepsilon_{re1} + 0.3}{\varepsilon_{re1} - 0.258}\right)\left(\frac{W_1/h + 0.264}{W_1/h + 0.8}\right)$$

Equation 3-14

C is in pF, L and L_i are in nH. The lumped elements of the model in Figure 3.25 and Figure 3.26 are mapped as follows: $C_D = C$, $L_{DP} = L_1$, and $L_{DM} = L_2$. In this approximation, the value of capacitance C_D is almost twice the value of capacitance for symmetrical step discontinuity with the same dimensions as the original asymmetrical one [49], [50].

It is to be noted that in this study we have not considered any case study with the general form of asymmetric step discontinuity where microstrips are connected with some margin from the sides. However, we propose to approximate the value of the capacitance and the inductance as the geometric mean of related values for two symmetric cases as shown in Figure 3.27. The accuracy of this proposal has not been verified and it remains as a point of investigation in future work.

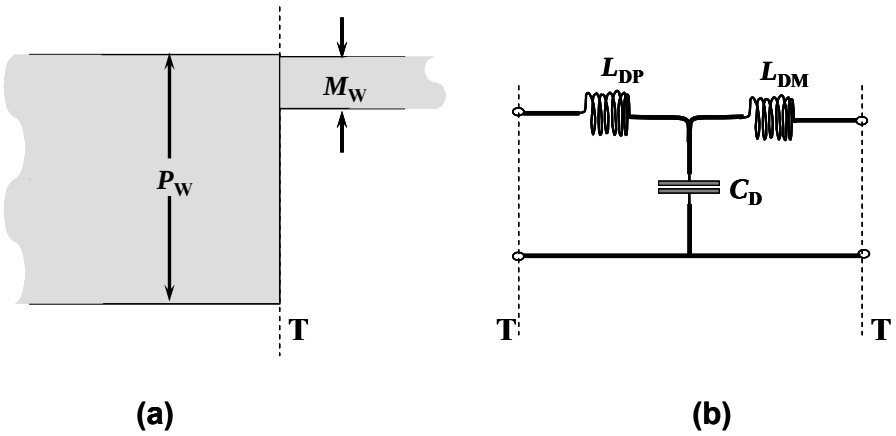

Figure 3.25. (a) Asymmetrical discontinuity between patch and meander line with margin = 0 (refer to Figure 3.11). (b) Equivalent lumped- element circuit.

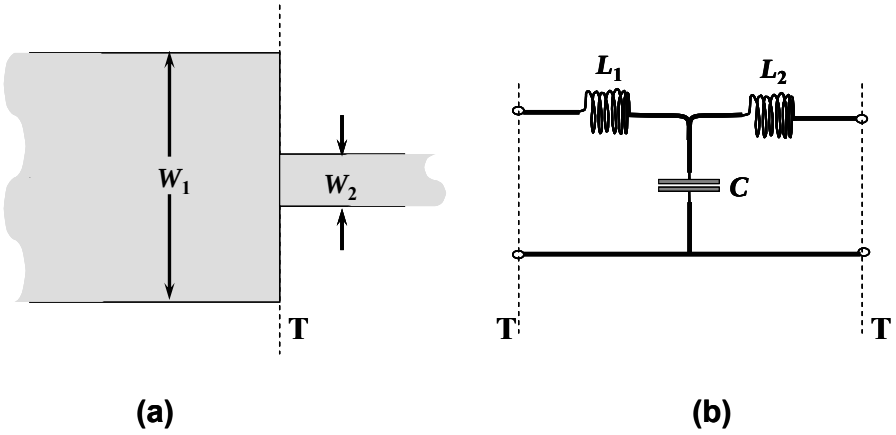

Figure 3.26. (a) Symmetrical discontinuity between microstrip lines. (b) Equivalent lumped- element circuit.

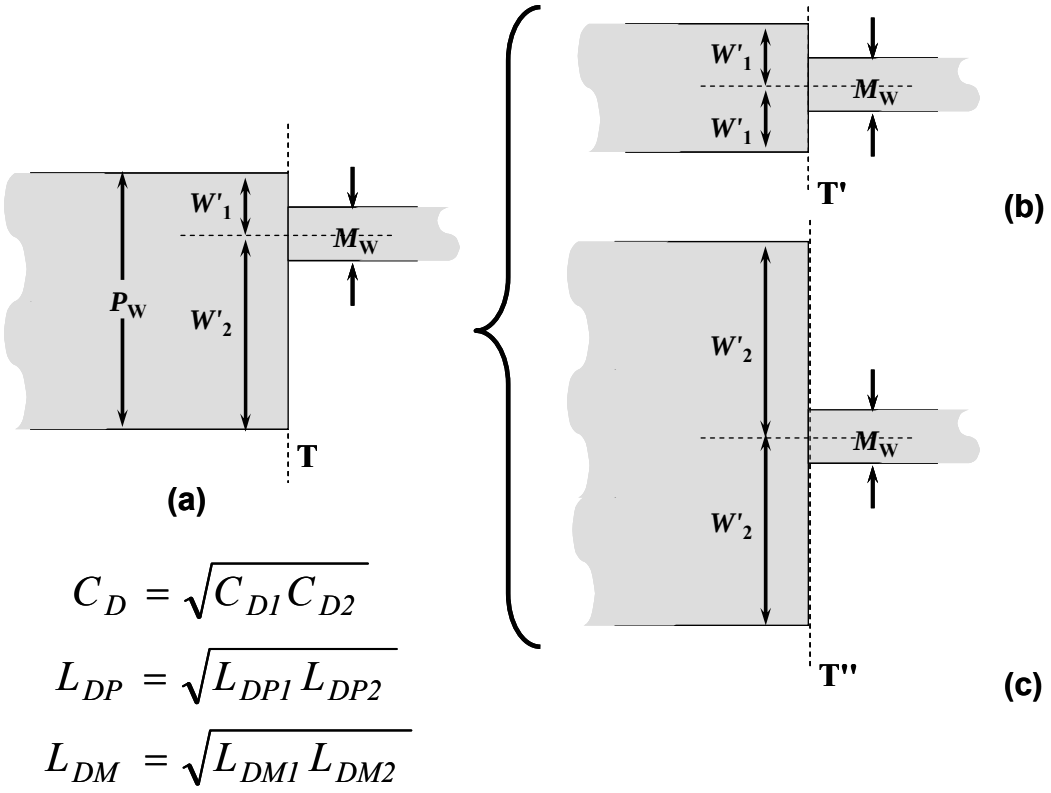

$$C_D = \sqrt{C_{D1} C_{D2}}$$

$$L_{DP} = \sqrt{L_{DP1} L_{DP2}}$$

$$L_{DM} = \sqrt{L_{DM1} L_{DM2}}$$

Figure 3.27. (a) Asymmetrical discontinuity between microstrip lines with margin ≠ 0 (refer to Figure 3.11). (b) and (c) Symmetrical discontinuity between microstrip lines. Design parameters are shown in the figure. (C_D, L_{DP}, L_{DM}), (C_{D1}, L_{DP1}, L_{DM1}), and (C_{D2}, L_{DP2}, L_{DM2}) show the elements modeling the step discontinuity at the connections (a), (b), and (c), respectively. The equivalent circuit model is shown in Figure 3.25 (b).

3.3.5. Model of Meander Line

A 3-D view of a planar meander line and its design parameters is shown in Figure 3.28. The meander line which is placed on the top of metal backed dielectric substrate consists of N metallic arms and ($N + 1$) metallic bridges connecting arms. The meander line in Figure 3.28 has 6 arms and 7 bridges. For simplicity of study, it

is assumed that all traces in the meander have same width, M_W; separation gap between two adjacent arms, M_G; arm length, M_L; input and output connecting bridges' length, $M_{Bi} = M_{Bo} = M_B$; and input and output arms' length, $M_{Li} = M_{Lo} = M_L$. However, the introduced models are general and easily can be applied to any configuration. The thickness and relative permittivity of dielectric substrate are h and ε_r, respectively. The π-equivalent circuit model of meander line is shown in Figure 3.29. The inductor is the dominant element in this model up to the first self resonant frequency. The capacitors model the parasitic effects. It should be noted, in this approximate modeling, we have not taken into account the effect of right angle bends in meander line which becomes important when a rigorous model is required at higher frequencies.

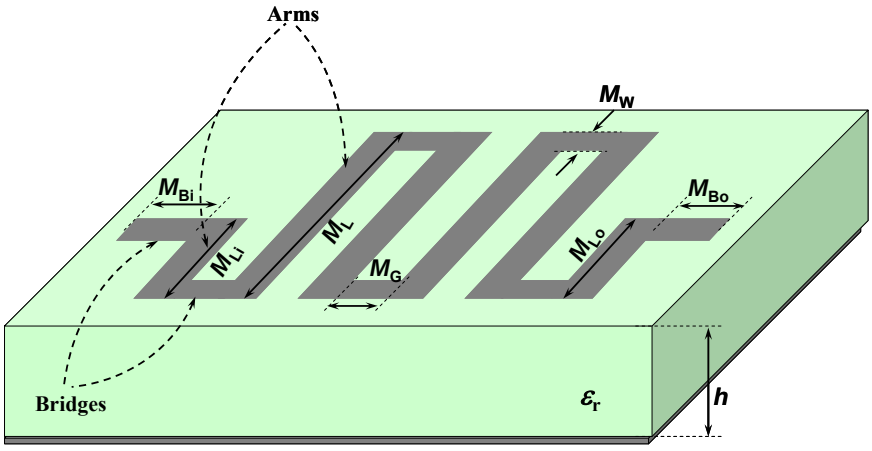

Figure 3.28. Three-dimensional view of meander line inductor. Design parameters are included in the figure.

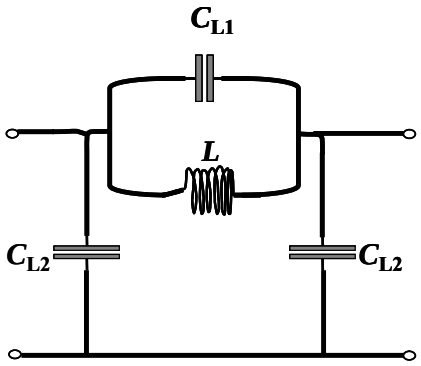

Figure 3.29. Equivalent circuit model of meander line.

3.3.5.A. *Computation of Inductance*

In this subsection, we provide a formula for meander line inductance based on the Greenhouse formulas [51]. The expression for inductance includes the self inductance of all sections in the inductor pattern (total of N arms and ($N+1$) bridges), the mutual inductance between all magnetically coupled arms and bridges, and the effect of ground. It is assumed that the meander line is electrically short (the total length of meander line is much less than the wavelength at the maximum operating frequency in the system). The root of this assumption is in the original formulation which was done assuming the magnitude and phase of current are constant across the line. Later, we will discuss about the effects related to phase changes along the electrically long lines. In the meander line, the mutual inductance between adjacent arms is negative due to opposite directions of current. The mutual inductance between arms separated by another arm is positive as the direction of current-flow is similar in both. Figure 3.30 (a) shows magnetic flux lines for two lines carrying current in the same direction providing positive mutual inductance. Figure 3.30 (b) shows magnetic flux lines for two lines carrying current in opposite directions providing negative

mutual inductance. Therefore, in the meander line the mutual inductance between one arm and all the magnetically coupled arms are sequentially alternating between negative and positive. The coupled arms are marked by solid line in Figure 3.31. The mutual inductance between one bridge and all the magnetically coupled bridges are positive. In this study, as a first-order approximation, we have considered only the coupling between adjacent bridges indicated by dashed marker in Figure 3.31. Coupling between other pairs of bridges are negligible as there is not any overlap along the traces as well as the increased gap between them. The total inductance of meander line pattern on top of thick dielectric or suspended in air (we have not discussed the effect of presence of ground yet) is given by:

$$L_P = \sum_{i=1}^{2N+1} L_i + 2\sum_{j=1}^{N-1}(-1)^j \sum_{i=1}^{N-j} M_{2i,2(i+j)} + 2\sum_{i=1}^{N} M_{2i-1,2i+1}$$

Equation 3-15

where the first sum represents the total self inductance, the second sum gives the total mutual inductance between coupled arms, and the third sum gives the total mutual inductance between adjacent bridges. We intend to use the developed model in the design of EBG structures with miniaturized dimensions, where the small separations between the arms and the long overlap length between arms can produce considerable increase in the total mutual coupling. Therefore, to develop a highly accurate model, it is better not to approximate the term of mutual coupling between arms by a first-order representation.

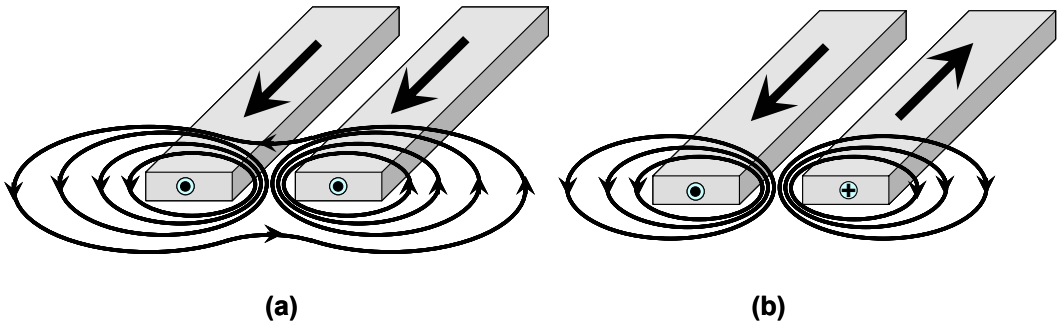

Figure 3.30. Magnetic flux lines showing the magnetic coupling between two adjacent lines for two cases: (a) positive mutual inductance and (b) negative mutual inductance.

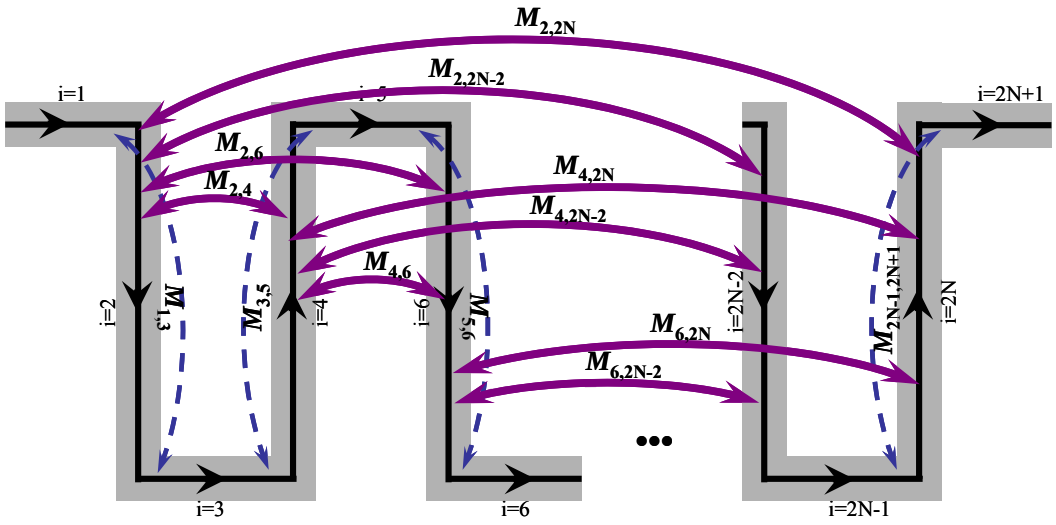

Figure 3.31. Magnetically coupled traces in a meander line inductor. The mutual coupling between pairs of arms and bridges is marked with solid lines and dashed lines, respectively.

From topology and composition of the structure, the inductances can be defined. The self inductance of *i*th section is given by [52], [53]:

$$L_i = 2\times10^{-4} l_i \left[\ln\left(\frac{l_i}{M_W + t}\right) + 1.193 + 0.2235\frac{M_W + t}{l_i} \right]$$

Equation 3-16

where it is assumed $t = 0$ and l_i is the length of line. All dimensions are in μm and L_i is in nH. The mutual inductance between two parallel filaments which are completely overlapping, as shown in Figure 3.32 (a), with length m and geometric mean distance d_{GMD} between them is computed by [51], [53], [54]:

$$M^{m,d_{GMD}} = 2\times10^{-4} m \left[\ln\left\{ \frac{m}{d_{GMD}} + \left(1 + \frac{m^2}{{d_{GMD}}^2}\right)^{1/2} \right\} - \left(1 + \frac{{d_{GMD}}^2}{m^2}\right)^{1/2} + \frac{d_{GMD}}{m} \right]$$

Equation 3-17

where all dimensions are in μm and M is in nH. The geometric mean distance between parallel strips in the meander which are distant from center to center by d_{ave} is calculated as [51], [54]:

$$\ln(d_{GMD}) = \ln(d_{ave}) - \left[\frac{1}{12(d_{ave}/M_W)^2} + \frac{1}{60(d_{ave}/M_W)^4} + \frac{1}{168(d_{ave}/M_W)^6} + \frac{1}{360(d_{ave}/M_W)^8} + \frac{1}{660(d_{ave}/M_W)^{10}} + \cdots \right]$$

Equation 3-18

To compute the mutual coupling between parallel strips, we need to consider different configurations [54] including: 1) the case without any overlap shown in Figure 3.32 (b). For that case, the mutual inductance, M, is given by:

$$2M = \left(M^{m+n+p,d_{GMD}} + M^{p,d_{GMD}}\right) - \left(M^{m+p,d_{GMD}} + M^{n+p,d_{GMD}}\right)$$

Equation 3-19

If the length p is equal to zero as shown in Figure 3.32 (c) then M is obtained from the relation:

$$2M = M^{m+n,d_{GMD}} - \left(M^{m,d_{GMD}} + M^{n,d_{GMD}}\right)$$

Equation 3-20

2) The case with partial overlap shown in Figure 3.32 (d) where M is given by:

$$2M = \left(M^{m+n-p,d_{GMD}} + M^{p,d_{GMD}}\right) - \left(M^{m-p,d_{GMD}} + M^{n-p,d_{GMD}}\right)$$

Equation 3-21

3) The case with overlap but unequal strip-lengths as shown in Figure 3.32 (e). M is computed as:

$$2M = \left(M^{m+p,d_{GMD}} + M^{m+q,d_{GMD}}\right) - \left(M^{p,d_{GMD}} + M^{q,d_{GMD}}\right)$$

Equation 3-22

If the length p is equal to zero as shown in Figure 3.32 (f) then M is given by:

$$2M = \left(M^{m,d_{GMD}} + M^{n,d_{GMD}}\right) - M^{q,d_{GMD}}$$

Equation 3-23

In those examples we will study later to asses our modeling due to choice of equal arms along the meander, only cases (a) and (c) in Figure 3.32 will be used. However, for general modeling of a meander line with arbitrary shape all the cases mentioned above are needed.

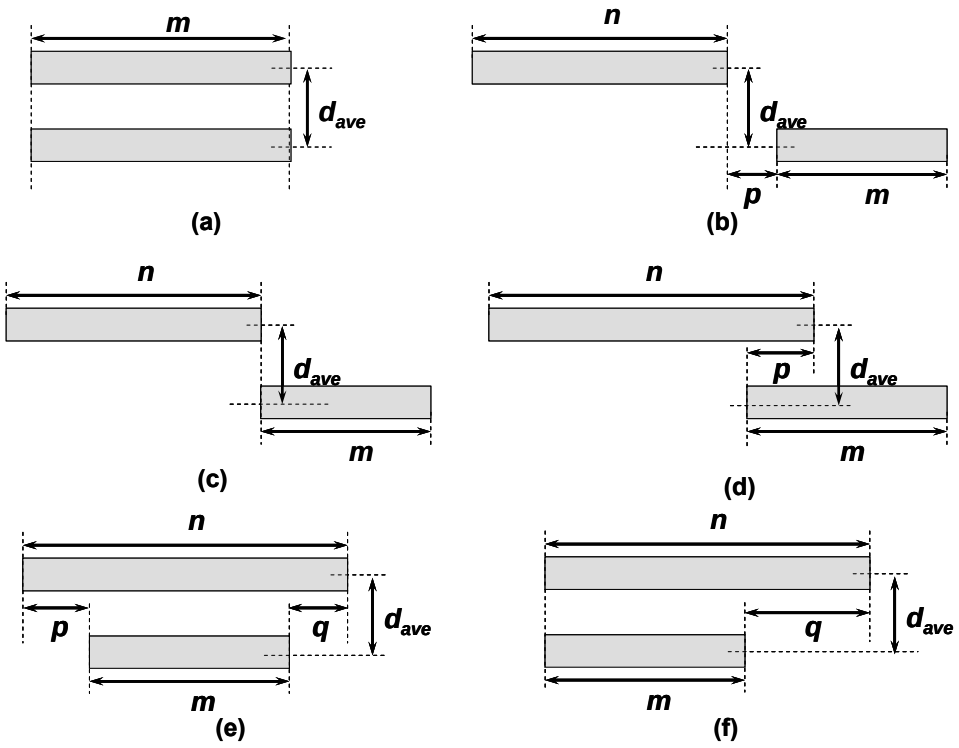

Figure 3.32. Magnetically coupled strips. Design parameters for computing mutual coupling are shown in the figure.

In the following, we apply the image theory to include the effect of ground plane on the total inductance of the meander line [55]. It is very important to consider this effect because of the trends of size shrinking as followed in the design of electronics which are affecting design architectures. Figure 3.33 shows a meander line and its image modeling the effect of ground plane. The image is located at a distance equal to twice the substrate-thickness from the actual meander location. The current in the image meander is in the reverse direction leading to a total negative mutual inductance represented by L_{MIP}. The mutual inductance between the magnetically coupled sections in the actual and the image meanders are computed through the formulas stated earlier. In those formulas, the geometric mean distance is

approximated by the distance between centers of strips. The decrement of the dielectric thickness leading to closer location of the ground plane to the meander pattern causes the total value of inductance to decrease. Therefore, the total net inductance of meander line is given by:

$$L = L_P + L_{MIP}$$

Equation 3-24

where the mutual inductance of image pattern is computed by:

$$L_{MIP} = \sum_{j=1}^{2N+1} \begin{cases} (-1)^j \sum_{i=0}^{N} M_{j,2i+1} & \text{if } j \text{ is odd} \\ \sum_{i=1}^{N} (-1)^{0.5(j+2i+2)} M_{j,2i} & \text{if } j \text{ is even} \end{cases}$$

Equation 3-25

It is noted that the mutual inductance between image and actual meanders does not need to be considered twice as the image pattern is not part of the actual one.

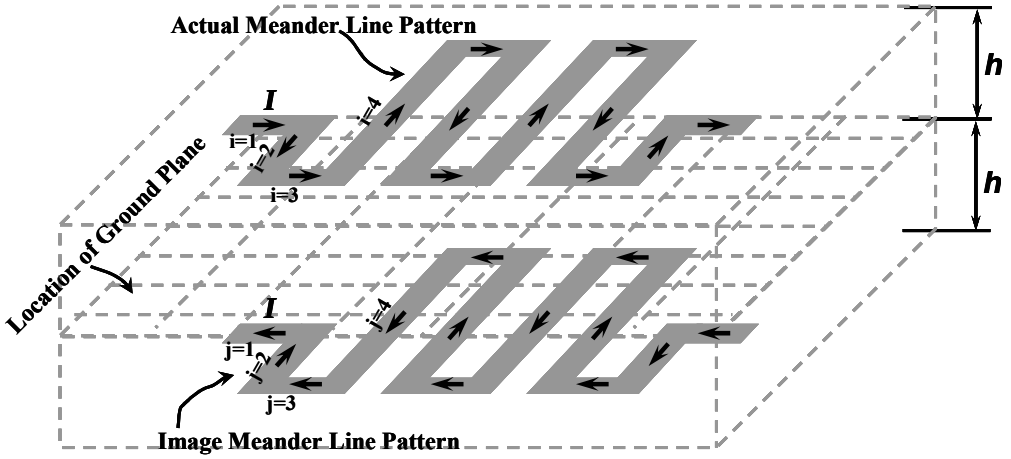

Figure 3.33. Image of meander line by ground plane.

3.3.5.B. *Computation of Parasitic Capacitances*

There are two types of parasitic capacitances in meander line model, C_{L1} and C_{L2} as shown in Figure 3.29. C_{L1} representing the parasitic capacitance in the meander pattern consists of different interline capacitances such as C_{in}, C_{top}, and C_{bottom} between adjacent arms and C_{top}, C_{bottom}, and C_{side} between adjacent bridges as shown in Figure 3.34. In this modeling, due to our assumption of zero metallization thickness, $t = 0$, C_{in} and C_{side} are negligible. Also, C_{top} and C_{bottom} between arms are much greater than C_{top} and C_{bottom} between bridges in our meander designs where we intentionally want large value of inductance per area. Therefore, the parasitic interline capacitance between two coupled adjacent arms j and $j+1$ is given by: $C_{g\_j} = C_{top\_arm\_j} + C_{bottom\_arm\_j}$ or $C_{g\_j} = 0.5 l_{g\_j}\left(C_{ga\_j} + C_{gd\_j}\right)$. l_{g_j} representing the effective coupled length between two arms is approximated by: $l_{g\_j} = \text{Minimum}(l_j, l_{j+1})$. $0.5 \times C_{ga\_j}$ and $0.5 \times C_{gd\_j}$ are the total fringing capacitance per unit length in gap between two arms through air and dielectric, respectively. Regarding our assumption that the strip width is constant along the meander line, two adjacent arms in meander pattern are symmetric coupled lines. Also, in this modeling we are approximating the parasitic capacitance by considering only the coupling effect between adjacent arms. In another word, the coupling between the non-adjacent arms as well as the coupling between the patch and the non-adjacent arms is neglected. Therefore, due to the assumption of equal gap between arms M_G, $C_{ga} = C_{ga\_j}$ and $C_{gd} = C_{gd\_j}$ for $1 \le j \le N-1$. Later in this subsubsection, we will provide formulas to compute C_{ga} and C_{gd}. Now, C_{L1} which is the equivalent capacitance resulting from series of gap capacitances C_{g_j}'s in $(N-1)$ consecutive inter-arm gaps is computed by:

$$C_{L1} = \frac{1}{\sum_{j=1}^{N-1} \frac{1}{C_{g\_j}}}$$

Equation 3-26

As it is assumed that all arms are equal in length, C_{L1} is given by:

$$C_{L1} = \frac{C_{g\_j}}{N-1}$$

Equation 3-27

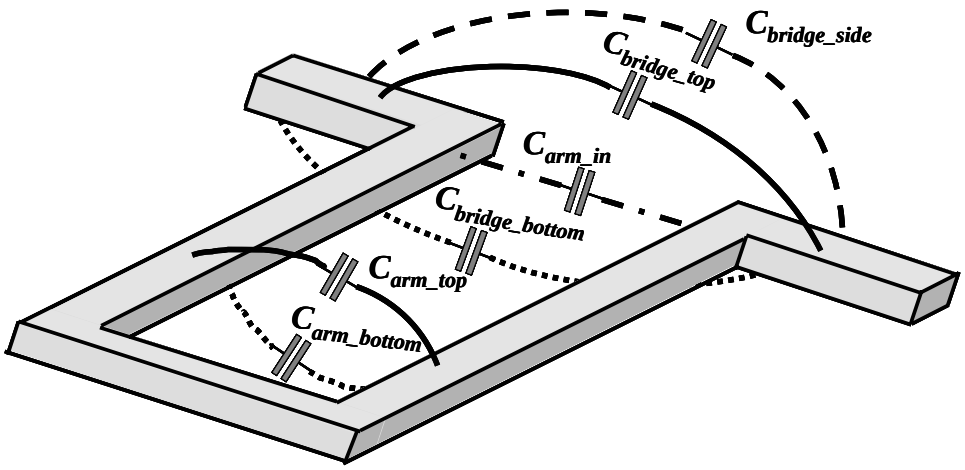

Figure 3.34. Parasitic capacitances in the meander pattern.

C_{L2} represents half of the parasitic capacitance between the meander line strip and the ground plane. To compute C_{L2}, we have to consider bridge-sections and arm-sections separately due to the different coupling effects. The capacitance per unit length between the strip and the ground in bridge-sections which are uncoupled microstrip lines is given by [53]:

$$C_{GD} = \frac{\sqrt{\varepsilon_{reM}}}{cZ_M}$$

Equation 3-28

where ε_{reM} is the effective relative permittivity of the meander microstrip. C_{GD} is the result of parallel combination of three capacitances: $C_{GD} = C_P + 2C_F$ as shown in Figure 3.35. C_p, the per unit length parallel plate capacitance between the strip and the ground plane is given by:

$$C_P = \varepsilon_0 \varepsilon_{rM} M_W / h$$

Equation 3-29

Where ε_{rM} is the relative permittivity of the meander microstrip. The fringing capacitance per unit length between the uncoupled strip and the ground is given by:

$$C_F = 0.5\left(\frac{\sqrt{\varepsilon_{reM}}}{cZ_M} - C_P\right)$$

Equation 3-30

For two symmetrically coupled microstrip lines, the capacitance per unit length between the strip and the ground is defined by [47], [48]:

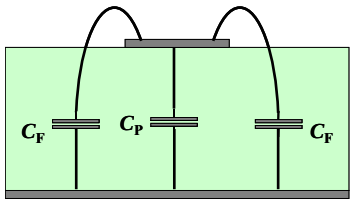

Figure 3.35. Parasitic capacitances between the strip and the ground plane in a microstrip line.

$$C_{GD} = C_e$$

Equation 3-31

The even mode capacitance per unit length, C_e, is given by $C_e = C_P + C_F + C'_F$ as shown in Figure 3.36 (a). It is worth to mention that the interline mutual capacitance between symmetric lines discussed earlier in this subsubsection can also be defined in terms of the odd and the even mode capacitances by $C_{g\_j} = 0.5 l_{g\_j}(C_o - C_e)$. C_o, the odd mode capacitance per unit length is given by $C_o = C_P + C_F + C'_F + C_{ga} + C_{gd}$ [47], [48], as shown in Figure 3.36 (b). C'_F, the fringing capacitance between the meander-strip and the ground in presence of another similar strip is given by [48]:

$$C'_F = \frac{C_F}{1 + A\left(\frac{h}{M_G}\right)\tanh\left(\frac{10M_G}{h}\right)}\left(\frac{\varepsilon_{rM}}{\varepsilon_{reM}}\right)^{\frac{1}{4}}$$

Equation 3-32

where $A = \exp\left[-0.1\exp\left(2.33 - 1.5\frac{M_W}{h}\right)\right]$. C_{gd}, the fringing capacitance per unit length between two symmetrical coupled microstrip lines through the dielectric gap is given by [48]:

$$C_{gd} = 0.5(C_{os} - C_{es})$$

Equation 3-33

where C_{es} and C_{os} are representing the even and the odd mode capacitances per unit length in the symmetrically coupled strip lines, respectively. A pair of symmetrically coupled strip lines and the representing parasitic capacitances in the configuration are shown in Figure 3.37. The even and the odd capacitances for the configuration of two symmetrically coupled arm-strips are given by [48]:

$$C_{xs} = 4\varepsilon_0 \varepsilon_{rM} \frac{K(k_x)}{K(k'_x)} \qquad x = e, o$$

Equation 3-34

$K(k_x)$ and $K(k'_x)$ are the elliptic function and its complement, respectively. The functional ratio $K(k_x)/K(k'_x)$ is approximated by [48], [56]:

$$\frac{K(k_x)}{K(k'_x)} = \begin{cases} \dfrac{1}{\pi} \ln\left(2\dfrac{1+\sqrt{k_x}}{1-\sqrt{k_x}}\right) & \text{if } \ 0.5 \le k_x^2 \le 1 \\ \dfrac{\pi}{\ln\left(2\dfrac{1+\sqrt{k'_x}}{1-\sqrt{k'_x}}\right)} & \text{if } \ 0 \le k_x^2 \le 0.5 \end{cases}$$

Equation 3-35

The argument k_x is given by [48]:

$$k_x = \begin{cases} \tanh\left(\dfrac{\pi}{4}\dfrac{M_W}{h}\right)\coth\left(\dfrac{\pi}{4}\dfrac{M_G + M_W}{h}\right) & \text{if } x = o \\ \tanh\left(\dfrac{\pi}{4}\dfrac{M_W}{h}\right)\tanh\left(\dfrac{\pi}{4}\dfrac{M_G + M_W}{h}\right) & \text{if } x = e \end{cases}$$

Equation 3-36

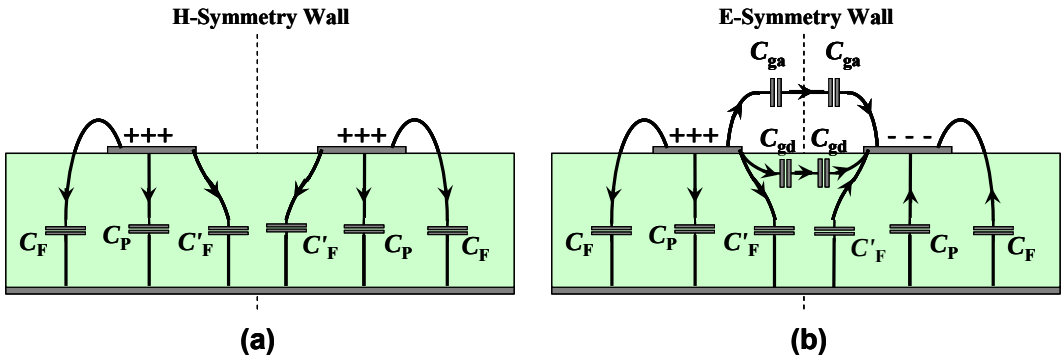

Figure 3.36. Constituents of (a) the even mode capacitance and (b) the odd mode capacitance in a pair of symmetric coupled microstrip lines.

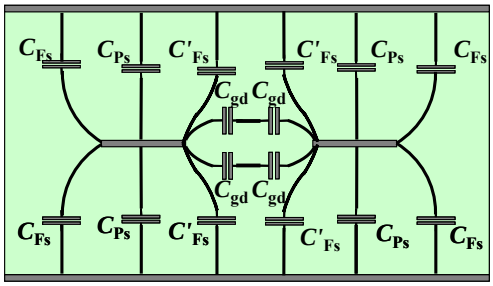

Figure 3.37. Parasitic capacitances for a pair of symmetric coupled strip lines.

where $k'_x = \sqrt{1-k_x^2}$. C_{ga}, the fringing capacitance per unit length between two symmetrical coupled microstrip lines through the air gap is given by [48], [57]:

$$C_{ga} = 0.5C^a_{cps} - \Delta C_F$$

Equation 3-37

where C^a_{cps} represents the fringing capacitance per unit length between the symmetric coupled coplanar lines when the dielectric material is air. The width of strips and the separation between them are similar to the arm-strips in the original meander structure and they are equal to M_W and M_G, respectively. C^a_{cps} is given by [48]:

$$C^a_{cps} = 2\varepsilon_0 \frac{K(k')}{K(k)}$$

Equation 3-38

where $k = \dfrac{M_G}{M_G + 2M_W}$ and $k' = \sqrt{1-k^2}$. ΔC_F is the fringing capacitance per unit length in the air not in the air gap between the two symmetric coupled arm-strips. It is approximated by [57]:

$$\Delta C_F = \left(C^a_F - C^a_{Fs}\right) + \left(C'^a_F - C'^a_{Fs}\right)$$

Equation 3-39

C_F^a, $C_F'^a$, C_{Fs}^a, and $C_{Fs}'^a$ are the fringing capacitances per unit length in the symmetric coupled microstrip and strip lines with air as a dielectric material. The value of those capacitances are obtained using the formulas discussed earlier in this subsubsection when substituting ε_r = 1. It should be considered that in the symmetric coupled strip lines the fringing capacitances are defined as $C_{Fs}^a + C_{Fs}'^a = 0.5C_{os}^a - C_{Ps}^a - C_{gd}^a = 0.5C_{es}^a - C_{Ps}^a$, where $C_{Ps}^a = C_P^a$.

To model the parasitic capacitance of a meander line, we deal with other configurations such as having three or more symmetric coupled microstrip lines. However, as mentioned earlier, we are approximating our modeling by neglecting the coupling between non-adjacent lines. Figure 3.38 shows the approximated parasitic capacitances of three symmetric coupled lines. For the middle strip, the parasitic apacitance per length between the strip and the ground is given by $C_{GD} = C_P + 2C_F'$.

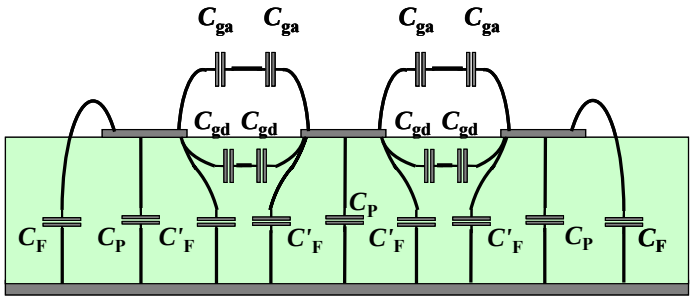

Figure 3.38. Parasitic capacitances for the three symmetric coupled microstrip lines, where the coupling effect between the non-adjacent arms is neglected.

In our EBG structure, to compute both the parasitic capacitances between the strip and the ground for the first and the last arms, and the coupling effect between meander line and the adjacent patches, we need to model the asymmetric coupled microstrip lines. In the next subsection, the available model and expressions are discussed.

3.3.6. Model of Coupling Effect between Patch and Meander line

In the proposed planar EBG structures, the configuration of a patch and an adjacent arm is asymmetric coupled microstrip lines as shown in Figure 3.39 (a). All capacitances per unit length characterizing that configuration including the parallel plate capacitances and the fringing capacitances are shown in that figure [58]. The unit cell of EBG structure under study may include several coupled microstrip lines parallel to each other such as a patch sandwiched between two arms from each side as shown in Figure 3.39 (b). The capacitances per unit length modeling those microstrips are shown in that figure. The capacitive equivalent circuit model of asymmetric coupled patch-arm configuration is shown in Figure 3.39 (c), where C_{GD_M} is representing the capacitance between the first arm and the ground plane. C_{GD_P} is the capacitance between the patch and the ground and C_{M_PM} is the mutual coupling between the patch and the arm. To complete the total value of the parasitic capacitance between the meander line and the ground discussed in Subsubsection 3.3.5.B, the capacitance C_{GD_M} is included in the value of C_{L2}. We can replace C_{PH} in Subsection 3.3.3 with C_{GD_P} which is approximating the capacitive load with higher accuracy due to the consideration of the fringing capacitances in presence of coupled

lines. The lumped elements in Figure 3.39 (c) for the configuration shown in Figure 3.39 (a) are approximated by:

$$C_{GD\_P} = \left(C_{P\_PH} + C_{F\_PH} + C''_{F\_PH}\right)\Delta l$$

Equation 3-40

$$C_{GD\_M} = \left(C_{P\_MR} + C_{F\_MR} + C''_{F\_MR}\right)\Delta l$$

Equation 3-41

$$C_{M\_PM} = \left(C_{ga\_PM} + C_{gd\_PM}\right)\Delta l$$

Equation 3-42

where Δl is the effective overlapping length between the patch and the meander arm. For the EBG structures under study Δl is equal to M_L - M_W. C_{P_PH} and C_{P_MR} represent the parallel plate capacitance per unit length for the patch and the meander-strip, respectively. C_{F_PH} and C''_{F_PH} demonstrate the fringing capacitances per unit length for the two coupled symmetric patch-microstrip lines. Similarly, C_{F_MR} and C''_{F_MR} represent the fringing capacitances per unit length for the two coupled symmetric meander-microstrip lines. The separation between the two symmetric strips is the same as the one in the original setup, M_B. Referring to the expressions provided for the meander line model in Subsubsection 3.3.5.B, $C_{P\_MR} = C_P$ and $C_{F\_MR} = C_F$. C''_{F_MR} is obtained from the formula C'_F by replacing a proper separation between coupled lines which corresponds to: ($M_B \rightarrow M_G$). If in the provided expressions, we replace the specifications of meander with the specifications of patch including: the width ($P_W \rightarrow M_W$), the characteristic impedance ($Z_P \rightarrow Z_M$), and the relative effective permittivity ($\varepsilon_{reP} \rightarrow \varepsilon_{reM}$) then the values of C_{P_PH}, C_{F_PH}, and C''_{F_PH} are easily

obtained. C_{gd_PM}, the capacitance per unit length through the dielectric gap is given by [58]:

$$C_{gd\_PM} = 0.5\sqrt{C_{gd\_PH} C_{gd\_MR}}$$

Equation 3-43

where $0.5 \times C_{gd\_MR}$ represents the total fringing capacitance per unit length between the two symmetric coupled meander-strips through the dielectric gap. That capacitance is computed through the formula provided for C_{gd} in Subsubsection 3.3.5.B by replacing the proper separation gap ($M_B \rightarrow M_G$). Similarly, $0.5 \times C_{gd\_PH}$, the total fringing capacitance per unit length between the two symmetric coupled patch-strips through the dielectric gap is computed. The fringing capacitance per unit length through air gap is given by [58]:

$$C_{ga\_PM} = 0.5C^{a}_{cps\_PM} - \Delta C_{F\_PM}$$

Equation 3-44

where $C^{a}_{cps\_PM}$ is the total fringing capacitance per unit length between the asymmetric coplanar strips that have same dimensional configuration as the patch-arm microstrips under study. It means that width of strips is the same as width of the patch and the meander-arm (P_W, M_W) and the separation gap is also the same (M_B). The dielectric material is air. That capacitance is given by [58], [59]:

$$C^{a}_{cps\_PM} = 2\varepsilon_0 \frac{K(k')}{K(k)}$$

Equation 3-45

where $k = \sqrt{\dfrac{1+{P_W}/{M_B}+{M_W}/{M_B}}{\left(1+{P_W}/{M_B}\right)\left(1+{M_W}/{M_B}\right)}}$ and $k' = \sqrt{1-k^2}$. ΔC_{F_PM} shows the fringing capacitance per unit length in the air not in the air gap between the asymmetric coupled patch-arm microstrips. It can be given by[1]:

$$\Delta C_{F\_PM} = \frac{\left(C^a_{F\_PH} - C^a_{Fs\_PH} + C''^a_{F\_PH} - C''^a_{Fs\_PH}\right)\left(C^a_{F\_MR} - C^a_{Fs\_MR} + C''^a_{F\_MR} - C''^a_{Fs\_MR}\right)}{\left(C^a_{F\_PH} - C^a_{Fs\_PH} + C''^a_{F\_PH} - C''^a_{Fs\_PH}\right) + \left(C^a_{F\_MR} - C^a_{Fs\_MR} + C''^a_{F\_MR} - C''^a_{Fs\_MR}\right)}$$

Equation 3-46

where $C^a_{F\_PH}$, $C''^a_{F\_PH}$, $C^a_{F\_MR}$, $C''^a_{F\_MR}$, $C^a_{Fs\_PH}$, $C''^a_{Fs\_PH}$, $C^a_{Fs\_MR}$, and $C''^a_{Fs\_MR}$ represent the fringing capacitances per unit length in the symmetric coupled microstrip and strip lines between the strips and the ground where the dielectric material is air. The configurations of the two coupled lines are meander-meander and patch-patch which are labeled by the subscripts *MR* and *PH*. The expressions for these capacitances are identical to those provided earlier in Subsubsection 3.3.5.B, except the relative permittivity which should be considered as $\varepsilon_r = 1$. When the structure under study is consisting of several coupled lines similar to Figure 3.39 (b), the expressions defining the lumped elements in the equivalent circuit model should be modified to include the

[1] Here, we are suggesting a more inclusive formula for the fringing field effects in air than the formula provided in [58]. Therefore, our suggested formula may provide better approximation.

coupling effects (the same issue was discussed previously while modeling the meander line in Subsubsection 3.3.5.B).

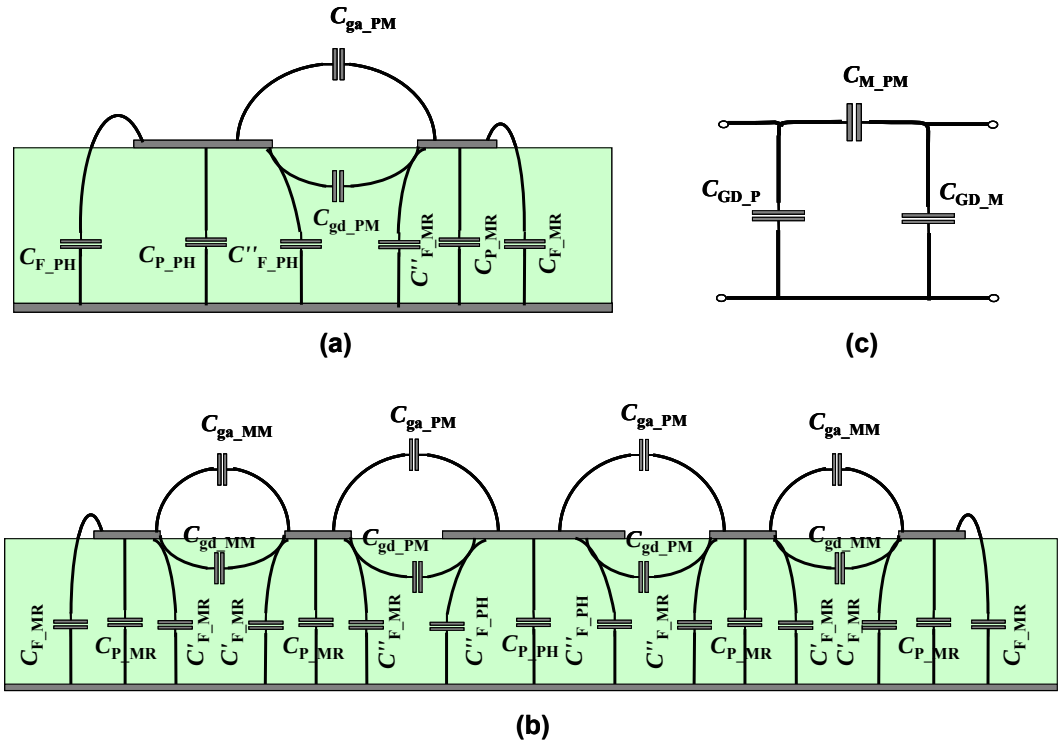

Figure 3.39. (a) Side view of patch and meander-arm microstrips as a pair of asymmetric coupled microstrip lines. (b) Side view of a patch microstrip between four meander-arm mirostrips. The capacitances modeling the coupled lines are shown in the figure. (c) Capacitive equivalent circuit model of the asymmetric coupled patch-arm microstrips.

To complete the modeling in this part, we should consider the bridge connecting the patch to adjacent arm as shown in Figure 3.40 (a). If the bridge-length, M_B, is a considerable portion of the total distance separating the two consecutive patches, then we can complete the modeling by considering the bridge-trace

inductance, L_B, the trace to ground capacitance, C_B, and the mutual coupling capacitance between the patch and meander-arm, C_{M_PM}, as one circuit block The complete π-equivalent circuit model of this case is shown in Figure 3.40 (b). However, if the bridge-length, M_B, is very small then L_B and C_B may be included in the total inductance and capacitance modeling the meander line (L and C_{L2}) discussed in Subsection 3.3.5. In this case, C_{M_PM} is modeled in series with C_{L1} and the total combination is parallel to L as shown in Figure 3.40 (c). In another word, we can model the coupling capacitor between the patch and the meander as part of the interline parasitic capacitances in the meander pattern. That is acceptable because we are developing an approximate model for initial guess in EBG design procedure.

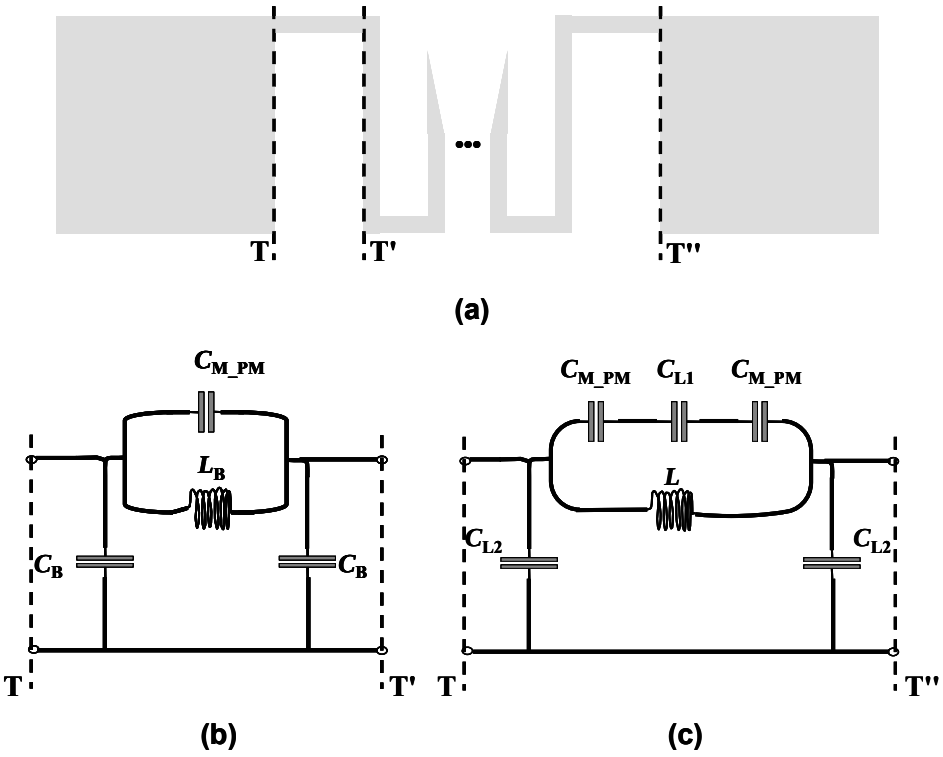

Figure 3.40. (a) A meander line between two patches. The bridge connecting the first arm to patch is marked in the figure. (b) Equivalent circuit modeling: 1) the mutual coupling effect between the patch and the adjacent meander-arm and 2) the connecting bridge-trace. (c) Equivalent circuit modeling the total meander line (refer to Figure 3.29). In this model, the effect of mutual coupling between the patch and the meander is considered as interline parasitic capacitance.

Example—We are computing the parasitic capacitance between pattern and ground for a meander line with six arms, N = 6, as shown in Figure 3.41. The meander line is connected to adjacent patches at the edge (margin = 0). Specifications of the meander are as follows: 1) identical line-width along the pattern M_W; 2) equal separating gap between the arms M_G; and 3) equal arm-length M_L. All the coupled/uncoupled traces are partially modeled with the different fringing

capacitances per unit length which are marked with different symbols and colors in that figure. The meander line consists of 7 (N + 1) bridge-sections which are uncoupled lines. The fringing capacitances per unit length in both sides of those traces are identical and they are equal to C_F. The total length of those bridges in the pattern is equal to $2(M_B + 0.5M_W) + (N-1)(M_G + M_W)$ and the parasitic capacitance to ground per unit length is given by $C_{GD} = C_P + 2C_F$. In the meander pattern, four (N – 2) arms are the symmetric coupled lines from both sides (one arm is sandwiched between two similar arms). Therefore, the fringing capacitances per unit length for both sides are identical and they are equal to C'_F. The total length of that type of arm is equal to $(N-2)(M_L - M_W)$ and the parasitic capacitance to ground per unit length is given by $C_{GD} = C_P + 2C'_F$.The last two remaining arms in the meander pattern (the first and the last ones) are the coupled lines sandwiched between a similar arm and a patch. Therefore, the fringing capacitance in the side corresponding to arm is C'_F and in the side corresponding to patch is C''_F. The total length of these two arms is equal to $2(M_L - M_W)$ and the parasitic capacitance to ground per unit length is equal to $C_{GD} = C_P + C''_F + C'_F$. Therefore, for that 3-turn meander line the total parasitic capacitance to ground is given by:

$$\begin{aligned} 2C_{L2} &= [2(M_B + 0.5M_W) + (N-1)(M_G + M_W)](C_P + 2C_F) + (N-2)(M_L - M_W)(C_P + 2C'_F) \\ &\quad + 2(M_L - M_W)[C_P + C''_F + C'_F] \\ &= [2(M_B + 0.5M_W) + 5(M_G + M_W)](C_P + 2C_F) + 4(M_L - M_W)(C_P + 2C'_F) \\ &\quad + 2(M_L - M_W)[C_P + C''_F + C'_F] \end{aligned}$$

Equation 3-47

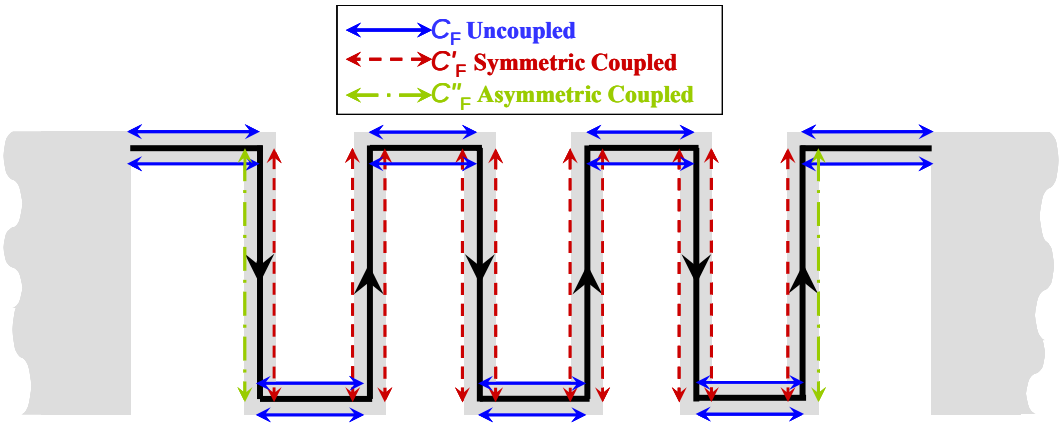

Figure 3.41. Different types of fringing capacitances per unit length for the coupled and uncoupled traces in the meander line are marked with different colors and symbols. The 3-turn meander has the following parameters: $M_{Li} = M_{Lo} = M_L$, ($M_{Bi} = M_{Bo} = M_B$) $\neq M_G$, and $P_W \neq M_W$ (The design parameters are shown in Figure 3.25 and Figure 3.28).

3.3.7. Model of Electrical Length in Planar EBG Structure

As reported by other researchers and mentioned earlier, the equivalent circuit-transmission line model can capture higher frequency effects more properly than the equivalent circuit model. The main reason for this superiority is that the transmission lines models the phase shift which is a function of frequency. The phase shift is the delay in the propagating field across the structure and it is increasing with frequency. To consider the phase delay across the unit cell of EBG structure, we are including two different types of microstrip transmission lines in our model consisting of patch-microstrip and meander-microstrip with total length of d_1 and d_2, respectively. Where $d = d_1 + d_2$ represents the periodicity-length (or the length of a unit cell of EBG structure), d_1 represents the length of a patch, and d_2 represents the length of

separation between the two consecutive patches. Therefore, the patch-microstrip models the phase difference across the patch and the meander-microstrip models the phase difference across the meander line (not along the meander line). The basic idea of modeling the phase delay in a meander line by the proposed method which is working properly as will be shown in later subsections is coming from the concept of modeling of meander-antennas used by Endo et al. [60]. In [60], the meander-antenna was modeled as a linear dipole antenna with inductive loading. It is possible to include the effect of phase difference between adjacent arms in meander line with higher accuracy by considering the coupling effects vectorially as [55]. However, in our applications the proposed level of accuracy is working well enough. The ABCD parameters for the microstrip line specified by the characteristic impedance, the relative effective permittivity, and the length (Z_0, ε_{re}, d_0) are available in microwave fundamental books such as [46].

3.3.8. The Model of a Unit Cell of the Proposed Planar EBG Structure

In this subsection, different models with different levels of accuracy in predicting bandgaps of an EBG structure are studied. These models are showing the effect of added elements in the configuration. We realize that modeling is not easy when the frequency is increasing. However, we could predict lower edge of bandgap with good accuracy which may decrease the load of full-wave simulations during the design procedure of EBG structure.

In Figure 3.42 a very simple circuit model for a unit cell of the proposed planar EBG structure including two capacitances each modeling half of the patch and

an inductance modeling the meander line is shown in Figure 3.18. The dispersion diagram of a unit cell of the first case study (defined previously in Subsection 3.3.2) extracted using this simple circuit model is shown in Figure 3.43. The design parameters of the EBG structure are repeated here for convenience: P_W = 1.6 mm, h = 114.3 μm, M_W = 0.02 mm, M_B = 0.02 mm, M_L = 1.6 mm, M_G = 0.02 mm, ε_r = 140, and $tan\ \delta$ = 0.0015. The ABCD transfer matrix defined in Equation 3-6 is given by:

$$\begin{bmatrix} A^m & B^m \\ C^m & D^m \end{bmatrix} = \begin{bmatrix} 1+\dfrac{y_1}{y_2} & \dfrac{1}{y_2} \\ 2y_1+\dfrac{{y_1}^2}{y_2} & 1+\dfrac{y_1}{y_2} \end{bmatrix}$$

Equation 3-48

where $y_1 = (j\omega C_{PH})/2$ and $y_2 = 1/(j\omega L)$. The dispersion extracted from numerical analysis was demonstrated in Figure 3.19. Comparison in the Γ-X zone shows that this model which is describing the EBG structure as a low pass filter could not predict accurately the lower edge of the bandgap.

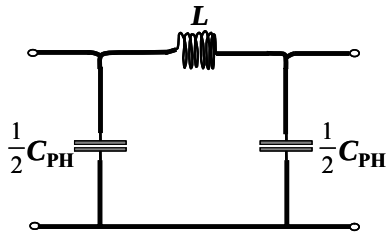

Figure 3.42. Simple physical-based circuit model for the proposed planar EBG structure.

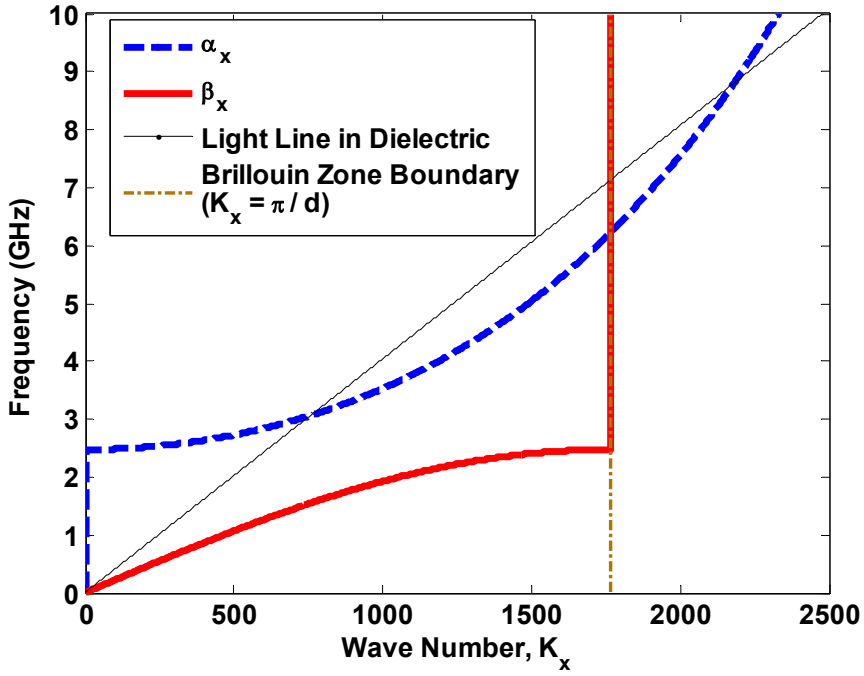

Figure 3.43. Dispersion diagram of the planar EBG structure shown in Figure 3.18 is modeled by the simple physical-based circuit model shown in Figure 3.42. The specifications of EBG are as follows: P_W = 1.6 mm, h = 114.3 μm, M_W = 0.02 mm, M_B = 0.02 mm, M_L = 1.6 mm, M_G = 0.02 mm, ε_r = 140, and $tan\ \delta$ = 0.0015.

An advanced physical-based model which includes physical specifications at low frequencies is shown in Figure 3.44. The model includes: 1) the inductances and the capacitances modeling the patch. 2) The inductances and the capacitances modeling the step discontinuities between the patch and the meander line. 3) The inductances and the parasitic capacitances modeling the meander line. 4) The capacitances modeling the coupling effect between the meander and the two adjacent patches. The dispersion diagram for the same EBG structure mentioned above is

extracted using this advanced circuit model shown in Figure 3.45. The ABCD matrix for this model is given by:

$$\begin{bmatrix} A^m & B^m \\ C^m & D^m \end{bmatrix} = \begin{bmatrix} 1 & z_2 \\ \frac{1}{z_1} & 1+\frac{z_2}{z_1} \end{bmatrix} \begin{bmatrix} 1+\frac{z_3}{z_5} & z_3+z_4+\frac{z_3 z_4}{z_5} \\ \frac{1}{z_5} & 1+\frac{z_4}{z_5} \end{bmatrix} \begin{bmatrix} 1+\frac{y_6}{y_7} & \frac{1}{y_7} \\ 2y_6+\frac{y_6^2}{y_7} & 1+\frac{y_6}{y_7} \end{bmatrix} \times$$
$$\begin{bmatrix} 1+\frac{z_4}{z_5} & z_3+z_4+\frac{z_3 z_4}{z_5} \\ \frac{1}{z_5} & 1+\frac{z_3}{z_5} \end{bmatrix} \begin{bmatrix} 1+\frac{z_2}{z_1} & z_2 \\ \frac{1}{z_1} & 1 \end{bmatrix}$$

Equation 3-49

where $z_1 = 2/(j\omega C_{PH})$, $z_2 = j\omega L_{PH}$, $z_3 = j\omega L_{DP}$, $z_4 = j\omega L_{DM}$, $z_5 = 1/(j\omega C_D)$, $y_6 = j\omega C_{L2}$, and $y_7 = j\omega(C_{M\_PM} \| C_{L1} \| C_{M\_PM}) + 1/(j\omega L)$. Comparing this result with those in Figure 3.19 and Figure 3.43 shows the improvement in the prediction of the lower edge of bandgap. Also, the next propagating mode has appeared. However, the model is not still acceptable and the error is high.

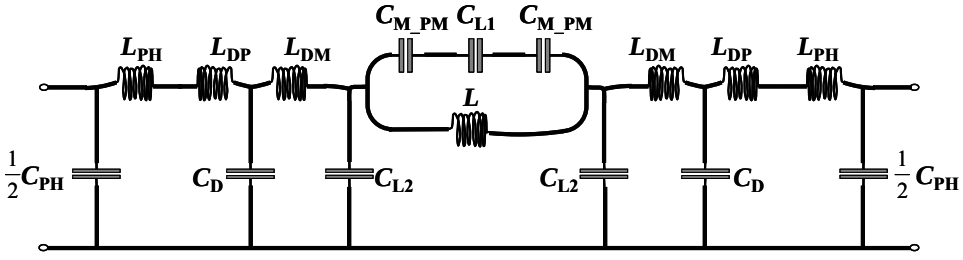

Figure 3.44. Advanced physical-based circuit model for the proposed planar EBG structure.

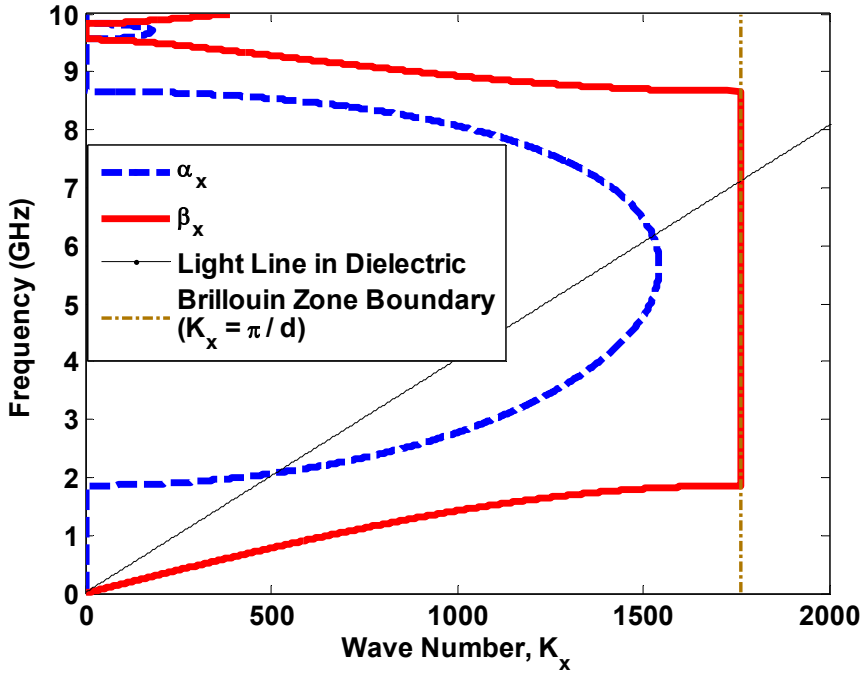

Figure 3.45. Dispersion diagram of the planar EBG structure shown in Figure 3.18 is modeled by the advanced physical-based circuit model shown in Figure 3.44. The specifications of EBG are as follows: P_W = 1.6 mm, h = 114.3 μm, M_W = 0.02 mm, M_B = 0.02 mm, M_L = 1.6 mm, M_G = 0.02 mm, ε_r = 140, and $tan\ \delta$ = 0.0015.

To improve our model, we consider the phase delay by including the transmission lines in the advanced circuit model. The simple equivalent circuit-transmission line model under study is shown in Figure 3.46. The different transmission lines included in the model consider the phase shift across the patch and the meander line separately. The dispersion diagram for this configuration is shown in Figure 3.47. The ABCD matrix for this model is given by:

$$\begin{bmatrix} A^m & B^m \\ C^m & D^m \end{bmatrix} = \begin{bmatrix} 1 & z_2 \\ \frac{1}{z_1} & 1+\frac{z_2}{z_1} \end{bmatrix} \begin{bmatrix} \cos(\beta_P d_1/2) & jZ_P \sin(\beta_P d_1/2) \\ jY_P \sin(\beta_P d_1/2) & \cos(\beta_P d_1/2) \end{bmatrix} \begin{bmatrix} 1+\frac{z_3}{z_5} & z_3+z_4+\frac{z_3 z_4}{z_5} \\ \frac{1}{z_5} & 1+\frac{z_4}{z_5} \end{bmatrix} \times$$

$$\begin{bmatrix} \cos(\beta_M d_2/2) & jZ_M \sin(\beta_M d_2/2) \\ jY_M \sin(\beta_M d_2/2) & \cos(\beta_M d_2/2) \end{bmatrix} \begin{bmatrix} 1+\frac{y_6}{y_7} & \frac{1}{y_7} \\ 2y_6+\frac{{y_6}^2}{y_7} & 1+\frac{y_6}{y_7} \end{bmatrix} \begin{bmatrix} \cos(\beta_M d_2/2) & jZ_M \sin(\beta_M d_2/2) \\ jY_M \sin(\beta_M d_2/2) & \cos(\beta_M d_2/2) \end{bmatrix}$$

$$\times \begin{bmatrix} 1+\frac{z_4}{z_5} & z_3+z_4+\frac{z_3 z_4}{z_5} \\ \frac{1}{z_5} & 1+\frac{z_3}{z_5} \end{bmatrix} \begin{bmatrix} \cos(\beta_P d_1/2) & jZ_P \sin(\beta_P d_1/2) \\ jY_P \sin(\beta_P d_1/2) & \cos(\beta_P d_1/2) \end{bmatrix} \begin{bmatrix} 1+\frac{z_2}{z_1} & z_2 \\ \frac{1}{z_1} & 1 \end{bmatrix}$$

Equation 3-50

where $z_1 = {}^{2}\!\!\diagup\!\!_{(j\omega C_{PH})}$, $z_2 = j\omega L_{PH}$, $z_3 = j\omega L_{DP}$, $z_4 = j\omega L_{DM}$, $z_5 = {}^{1}\!\!\diagup\!\!_{(j\omega C_D)}$, $y_6 = j\omega C_{L2}$, and $y_7 = j\omega\left(C_{M\_PM} \parallel C_{L1} \parallel C_{M\_PM}\right) + {}^{1}\!\!\diagup\!\!_{(j\omega L)}$. The characteristic impedance and the propagation constant of patch-microstrip are shown by pairs of (Z_P, B_P), respectively. d_1 is the length of a patch. The characteristic impedance and propagation constant of meander-microstrip are shown by pairs of (Z_M, B_M), respectively. d_2 is the distance between two consecutive patches. Comparison between the dispersion diagram in this figure and the previous one shown in Figure 3.19 shows that although the second propagating mode is well predicted and the third propagating mode has inaccurately located, the model could not correctly predict the lower edge of the first bandgap which is our main target in this modeling.

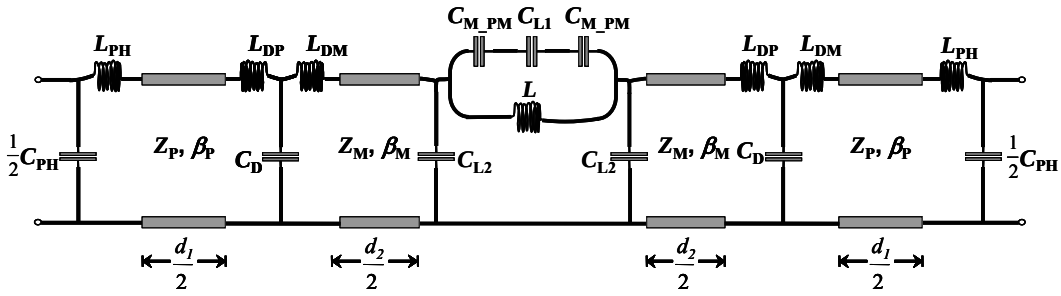

Figure 3.46. Simple equivalent circuit-transmission line model for the proposed planar EBG structure.

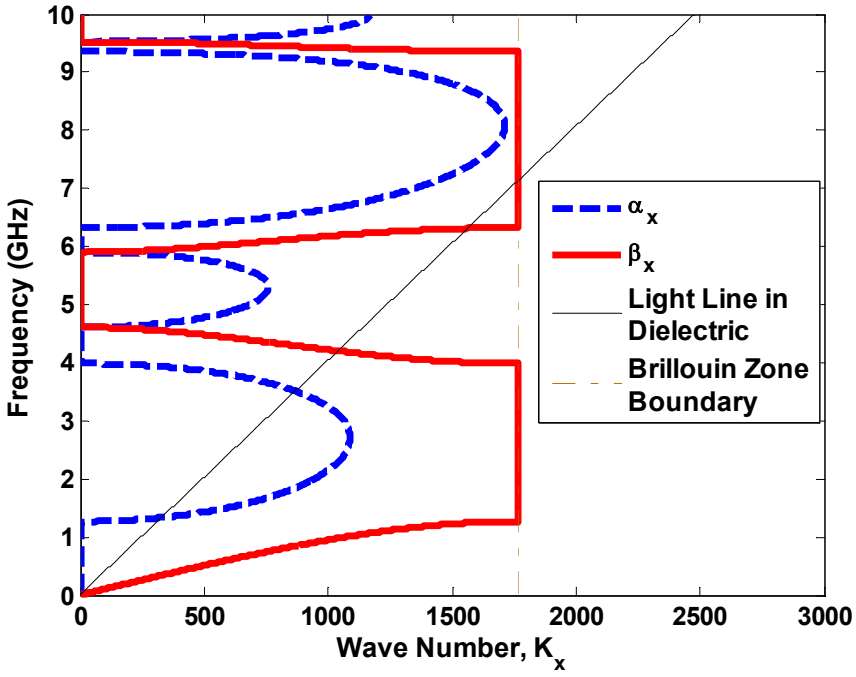

Figure 3.47. Dispersion diagram of the planar EBG structure shown in Figure 3.18 is modeled by the simple equivalent circuit-transmission line model shown in Figure 3.46. The specifications of EBG are as follows: P_W = 1.6 mm, h = 114.3 μm, M_W = 0.02 mm, M_B = 0.02 mm, M_L = 1.6 mm, M_G = 0.02 mm, ε_r = 140, and $tan\ \delta$ = 0.0015.

To improve our modeling we need to consider an important fact. We are modeling the wave propagation in the *x*-direction in a 1-D infinite array of EBG structures (refer to Figure 3.17) but when the frequency increases the propagation in the *y*-direction starts to be effective. In the Γ-X zone, the propagation constant in the *y*-direction is equal to zero ($k_y = 0$). Therefore, to include the propagation in *y*-direction in our model, it is enough to consider the following elements: 1) the open end (or the capacitance modeling the open end microstrip), 2) the patch-microstrips modeling the phase delay for wave propagating in *y*-direction across the patch, and 3) the inductances and capacitances modeling the patch in *y*-direction. The advanced equivalent circuit-transmission line model for the proposed planar EBG structure is shown in Figure 3.48. The dispersion diagram for this model is shown in Figure 3.49. The ABCD matrix for this model is given by:

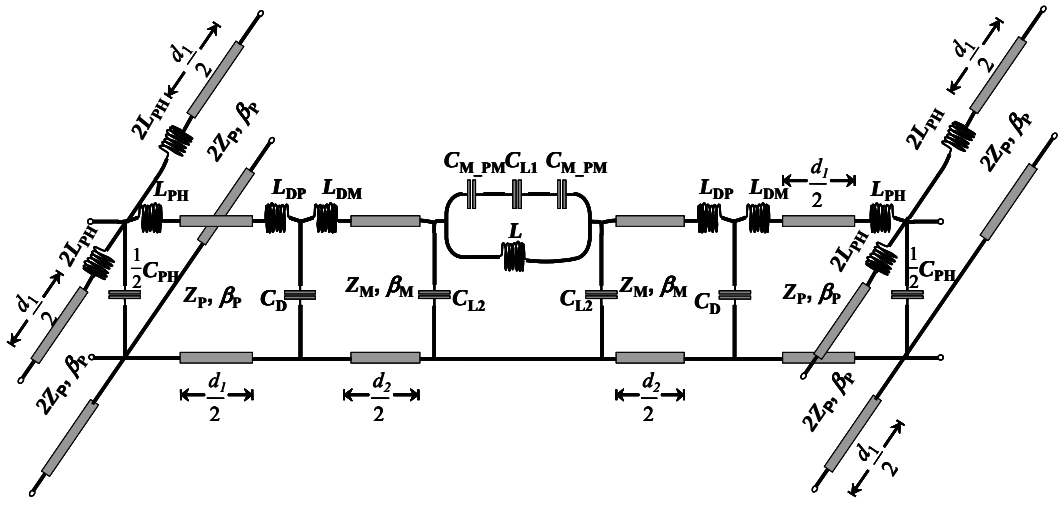

Figure 3.48. Advanced equivalent circuit-transmission line model for the planar proposed EBG structure.

$$\begin{bmatrix} A^m & B^m \\ C^m & D^m \end{bmatrix} = \begin{bmatrix} 1 & z_2 \\ \frac{1}{z_1} & 1+\frac{z_2}{z_1} \end{bmatrix} \begin{bmatrix} \cos(\beta_P d_1/2) & jZ_P \sin(\beta_P d_1/2) \\ jY_P \sin(\beta_P d_1/2) & \cos(\beta_P d_1/2) \end{bmatrix} \begin{bmatrix} 1+\frac{z_3}{z_5} & z_3+z_4+\frac{z_3 z_4}{z_5} \\ \frac{1}{z_5} & 1+\frac{z_4}{z_5} \end{bmatrix} \times$$

$$\begin{bmatrix} \cos(\beta_M d_2/2) & jZ_M \sin(\beta_M d_2/2) \\ jY_M \sin(\beta_M d_2/2) & \cos(\beta_M d_2/2) \end{bmatrix} \begin{bmatrix} 1+\frac{y_6}{y_7} & \frac{1}{y_7} \\ 2y_6+\frac{y_6^2}{y_7} & 1+\frac{y_6}{y_7} \end{bmatrix} \begin{bmatrix} \cos(\beta_M d_2/2) & jZ_M \sin(\beta_M d_2/2) \\ jY_M \sin(\beta_M d_2/2) & \cos(\beta_M d_2/2) \end{bmatrix}$$

$$\times \begin{bmatrix} 1+\frac{z_4}{z_5} & z_3+z_4+\frac{z_3 z_4}{z_5} \\ \frac{1}{z_5} & 1+\frac{z_3}{z_5} \end{bmatrix} \begin{bmatrix} \cos(\beta_P d_1/2) & jZ_P \sin(\beta_P d_1/2) \\ jY_P \sin(\beta_P d_1/2) & \cos(\beta_P d_1/2) \end{bmatrix} \begin{bmatrix} 1+\frac{z_2}{z_1} & z_2 \\ \frac{1}{z_1} & 1 \end{bmatrix}$$

Equation 3-51

where $z_1 = {}^{2}\!\!\diagup\!\!_{(j\omega C_{PH})} + z$, $z = {}^{Z_P}\!\!\diagup\!\!_{j\tan(\beta_P d_1/2)} + j\omega L_{PH}$, $z_2 = j\omega L_{PH}$, $z_3 = j\omega L_{DP}$, $z_4 = j\omega L_{DM}$, $z_5 = {}^{1}\!\!\diagup\!\!_{(j\omega C_D)}$, $y_6 = j\omega C_{L2}$, and $y_7 = j\omega\left(C_{M\_PM} \parallel C_{L1} \parallel C_{M\_PM}\right) + {}^{1}\!\!\diagup\!\!_{(j\omega L)}$.

The characteristic impedance and the propagation constant of patch-microstrip are shown by pairs of (Z_P, B_P), respectively. d_1 is the length of a patch. The characteristic impedance and the propagation constant of meander-microstrip are shown by pairs of (Z_M, B_M), respectively. d_2 is the distance between two consecutive patches. The comparison of results in this diagram and the numerical ones in Figure 3.19 shows a prediction with high accuracy for the first three propagating modes indicated in the figures. The developed advanced equivalent circuit-transmission line model will be used in the rest of this study.

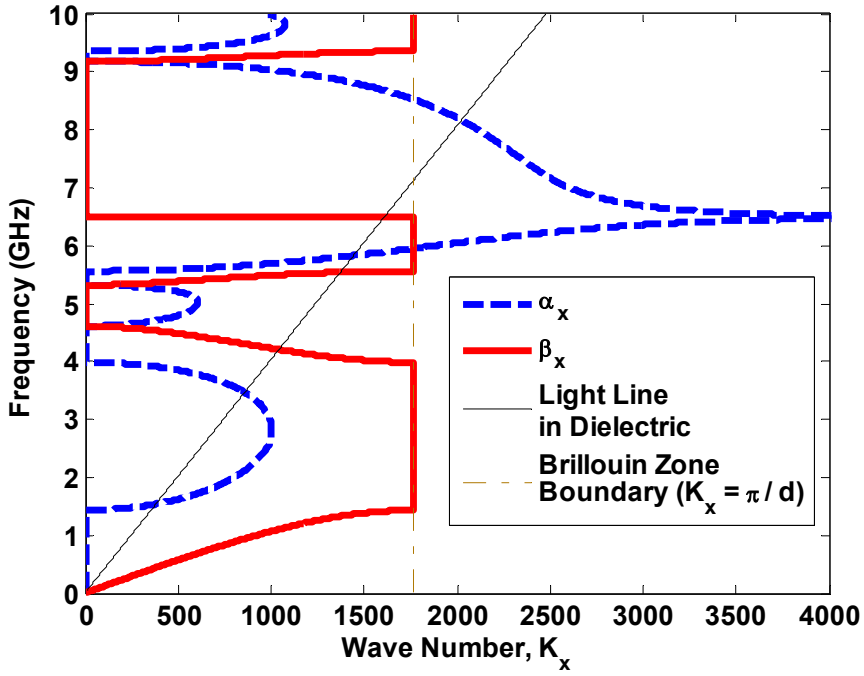

Figure 3.49. Dispersion diagram of the planar EBG structure shown in Figure 3.18 is modeled by the advanced equivalent circuit-transmission line model shown in Figure 3.48. The specifications of EBG are as follows: P_W = 1.6 mm, h = 114.3 μm, M_W = 0.02 mm, M_B = 0.02 mm, M_L = 1.6 mm, M_G = 0.02 mm, ε_r = 140, and $tan\ \delta$ = 0.0015.

3.3.9. Case Studies and Performance of the Developed Model

In this subsection, we are going to asses the performance of the developed circuit-transmission line model in the Γ-X region of the Brillouin zone for the samples defined in Subsection 3.3.2. In the Figure 3.50 for the first case study where ε_r = 140 and h = 114.3 μm the comparison between the dispersion diagrams extracted by (a) the developed model and (b) the full-wave numerical simulator is shown. Clearly, the agreement between graphs for the first three propagating modes is

excellent. The attenuation diagram extracted from the equivalent circuit-transmission line model for a unit cell of the first sample is shown in Figure 3.51 (a). The attenuation diagram for the four samples is plotted in Figure 3.51 (b) which shows the suppression level that could be reached in the bandgaps if the source and the destination ports are distant from each other by four EBG unit cells. By increasing the number of EBG unit cells between the two ports, we can increase the attenuation level. The 20 dB suppression level is marked in Figure 3.51 (b).

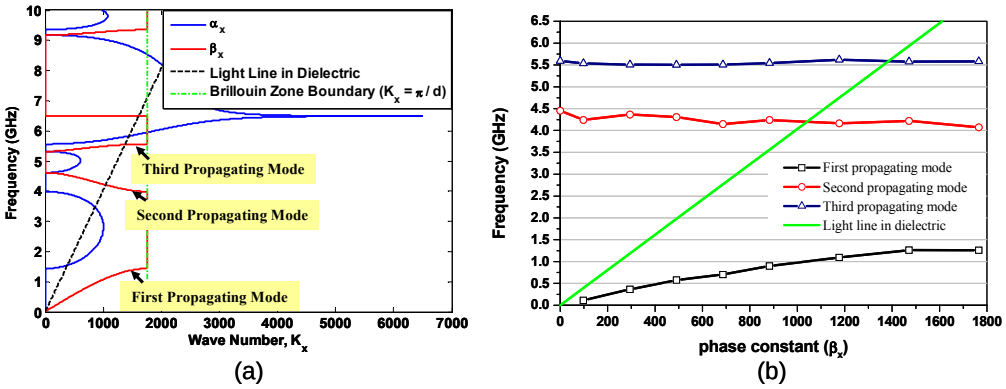

Figure 3.50. Dispersion diagram in Γ-X zone for the planar EBG structure shown in Figure 3.18 is extracted using (a) advanced equivalent circuit-transmission line model and (b) numerical full-wave analysis by Ansoft HFSS. The specifications of EBG are as follows: P_W = 1.6 mm, h = 114.3 μm, M_W = 0.02 mm, M_B = 0.02 mm, M_L = 1.6 mm, M_G = 0.02 mm, ε_r = 140, and $tan\ \delta$ = 0.0015.

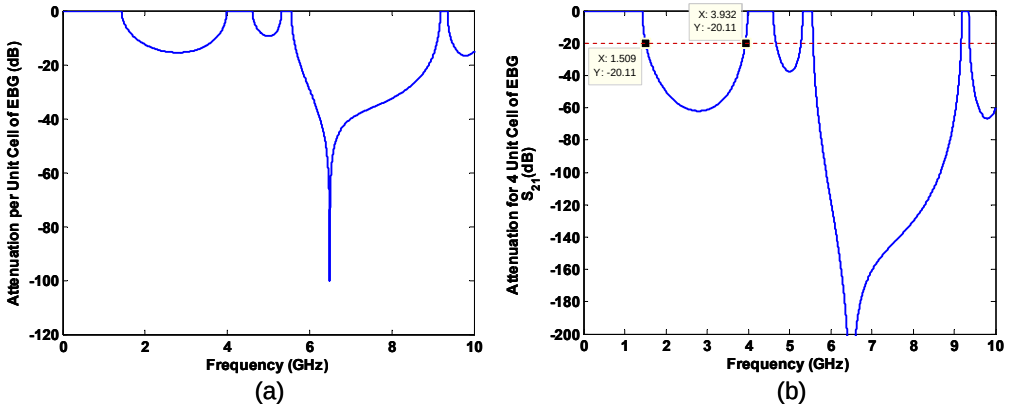

Figure 3.51. The attenuation diagram in Γ-X zone for the planar EBG structure shown in Figure 3.18 is extracted using advanced equivalent circuit-transmission line model for (a) a unit cell of EBG and (b) 4 unit cells of EBG. The 20 dB attenuation level is marked in the graph. The specifications of EBG are as follows: P_W = 1.6 mm, h = 114.3 μm, M_W = 0.02 mm, M_B = 0.02 mm, M_L = 1.6 mm, M_G = 0.02 mm, ε_r = 140, and $tan\ \delta$ = 0.0015.

For the second case study where ε_r = 200 and h = 114.3 μm, the comparison between the dispersion diagrams extracted by (a) the developed model and (b) the full-wave numerical simulator is shown in Figure 3.52. Here, also the agreement is very good between the first three propagating modes. The comparison for the third case study where ε_r = 140 and h = 500 μm between the dispersion diagrams extracted by (a) the developed model and (b) the full-wave numerical analysis is shown in the Figure 3.53. The first and the third propagating modes are in excellent agreement. However, the second propagating mode extracted by the developed model covers larger frequency band around the frequency region predicted by the full-wave

analysis. This difference comes from approximate models implemented in our developed model for the different configurations of microstrips such as the step discontinuity discussed earlier in the modeling subsections. In Figure 3.54, for the fourth case study where ε_r = 4.3 and h = 114.3 μm the comparison between the dispersion diagrams extracted by (a) the developed model and (b) the full-wave numerical simulator is shown. Diagrams show that the first propagating mode and as a result the lower edge of the bandgap are predicted accurately. However, the higher order propagating modes are not accurately predicted.

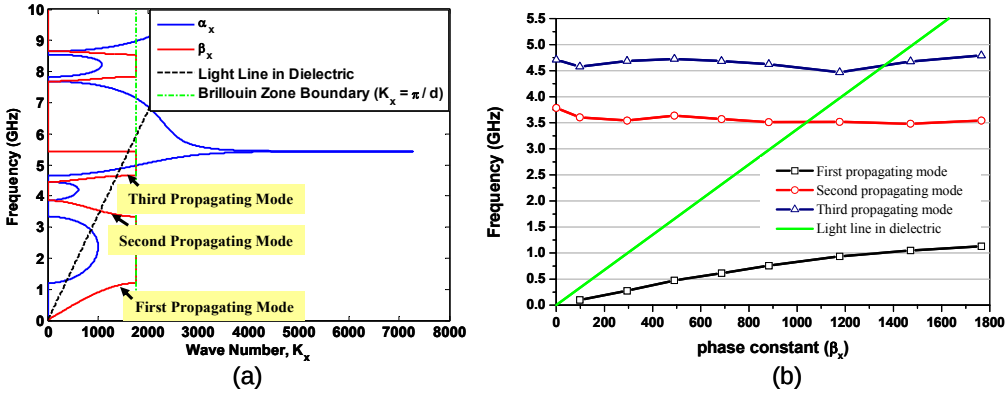

Figure 3.52. Dispersion diagram in Γ-X zone for the planar EBG structure shown in Figure 3.18 is extracted using (a) advanced equivalent circuit-transmission line model and (b) numerical full-wave analysis by Ansoft HFSS. The specifications of EBG are as follows: P_W = 1.6 mm, h = 114.3 μm, M_W = 0.02 mm, M_B = 0.02 mm, M_L = 1.6 mm, M_G = 0.02 mm, ε_r = 200, and $tan\ \delta$ = 0.0015.

It can be concluded that 1) the developed model based on the available low frequency approximated circuit models for the different microstrip configurations is working excellent for the thin slab of high-k dielectric materials in the range of couples of GHz. 2) The model is well behaving for the increasing thickness of slab of high-k materials in the range of couples of GHz. But, 3) the developed model is inaccurate for thin low permittivity dielectrics in the range of couples of GHz. However, 4) for all the combination of specifications in the dielectric the performance of model is excellent for extracting the first propagating mode. It means the developed model can predict the lower edge of the bandgap with high accuracy. Therefore, the model is excellent for low GHz frequency range. The main reason for the mentioned level of performance for the developed model is that: we have approximated a considerable portion of transmission lines in the structure as uncoupled microstrips. Also, we have neglected non-adjacent couplings. In the uncoupled microstrips the fields produced around the structures do not affect each other. This assumption in the structures under study is much more valid in the microstrips made of high-k materials than the ones made of conventional dielectrics such as FR-4. In the structures made of high-k, the fringing fields outside the strip are bounded to strip and concentrated at the edge of strip. Therefore, the approximation used in the developed model about the couplings between the constituting parts is working with higher accuracy in high-k materials. In another word, to improve the performance in the model we may need to consider non-adjacent coupling.

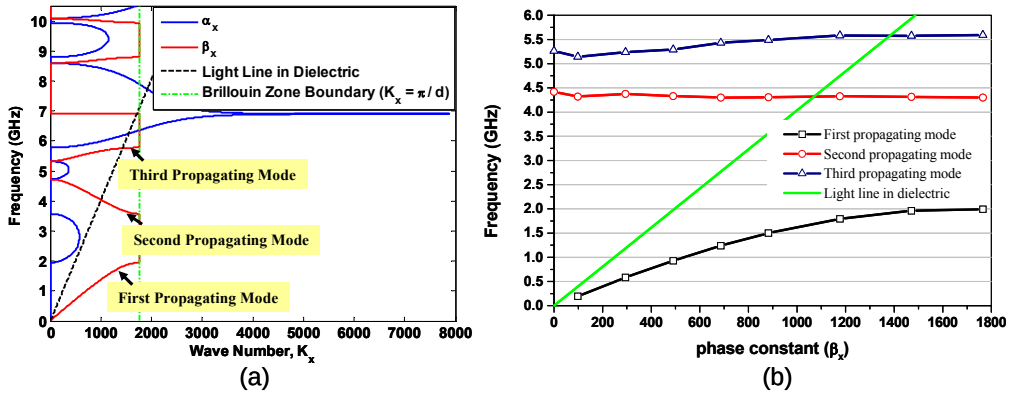

Figure 3.53. Dispersion diagram in Γ-X zone for the planar EBG structure shown in Figure 3.18 is extracted using (a) advanced equivalent circuit-transmission line model and (b) numerical full-wave analysis by Ansoft HFSS. The specifications of EBG are as follows: P_W = 1.6 mm, h = 500 μm, M_W = 0.02 mm, M_B = 0.02 mm, M_L = 1.6 mm, M_G = 0.02 mm, ε_r = 140, and $tan\ \delta$ = 0.0015.

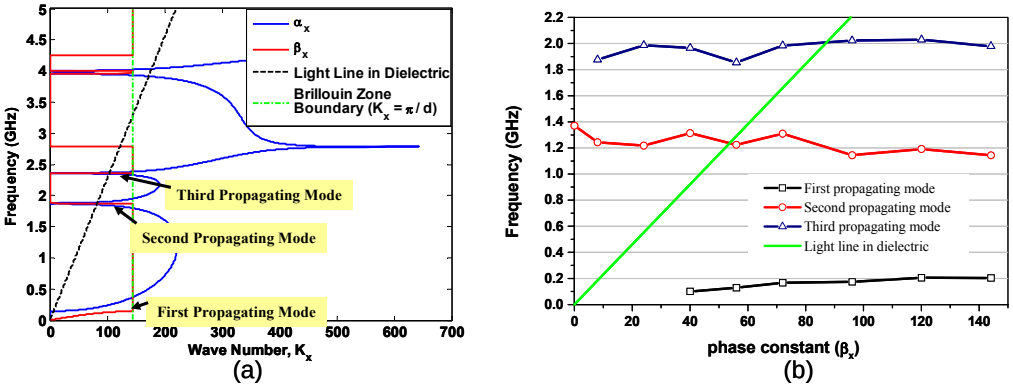

Figure 3.54. Dispersion diagram in Γ-X zone for the planar EBG structure shown in Figure 3.18 is extracted using (a) advanced equivalent circuit-transmission line model and (b) numerical full-wave analysis by Ansoft HFSS. The specifications of EBG are as follows: P_W = 20 mm, h = 114.3 μm, M_W = 0.2 mm, M_B = 0.2 mm, M_L = 20 mm, M_G = 0.2 mm, ε_r = 4.3, and $tan\ \delta$ = 0.02.

We continue our studies in later subsections to investigate about the relationship between the bandgap and the elements included in the model. We will present how the values of elements are affecting the bandgap and controlling the location of the bandgap in different frequency regimes.

3.3.10. Characterization of the Proposed Planar EBG Structure

In this subsection, we investigate about characteristics of the planar EBG structures in more details. For this purpose, we continue our study on the first sample discussed in Subsection 3.3.2. We fit the best and the lowest order polynomials on the data points of propagating modes in dispersion diagrams extracted by the full-wave numerical analysis using Ansoft HFSS. We do not intend to fit a high order polynomial which exactly follows the variations of data points in dispersion diagram. We want a simple approximate graph to study and extract information about our suggested EBGs. The fitted polynomials are plotted for each region of irreducible Brillouin zone: Γ-X, X-M, and M-Γ in Figure 3.55 to Figure 3.57, respectively. The light lines in dielectric plotted in those regions are defined by:

$$\beta d = \begin{cases} k_x d & \Gamma - \text{X Zone} \begin{cases} k_x d = [0, \pi] \\ k_y d = 0 \end{cases} \\ \sqrt{\pi^2 + (k_y d)^2} & \text{X} - \text{M Zone} \begin{cases} k_x d = \pi \\ k_y d = [0, \pi] \end{cases} \\ k_x d\sqrt{2} & \text{M} - \Gamma \text{ Zone} \begin{cases} k_x d = k_y d = [0, \pi] \end{cases} \end{cases}$$

Equation 3-52

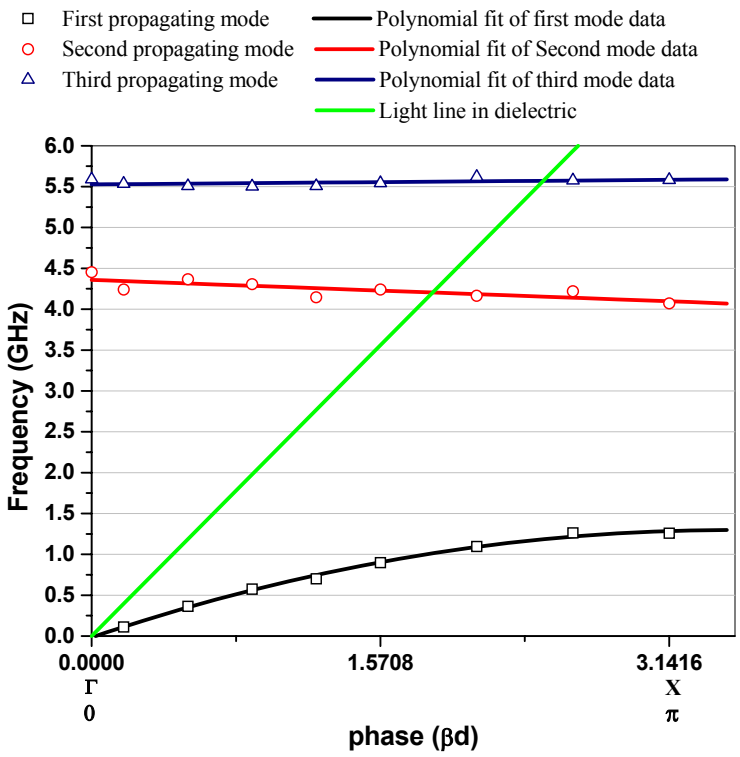

Figure 3.55. Dispersion diagram of the planar EBG structure shown in Figure 3.18 in the Γ-X region. The data points of the propagating modes representing the dispersion relation are extracted numerically by Ansoft HFSS. The polynomial fit of these data points of the propagating modes show dispersion graphs. The specifications of the EBG are as follows: P_W = 1.6 mm, h = 114.3 μm, M_W = 0.02 mm, M_B = 0.02 mm, M_L = 1.6 mm, M_G = 0.02 mm, ε_r = 140, and $tan\ \delta$ = 0.0015.

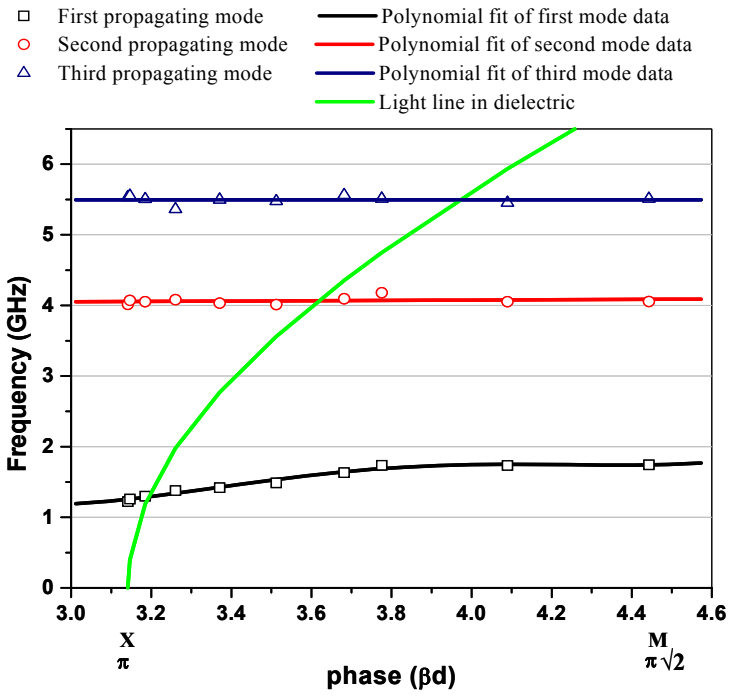

Figure 3.56. Dispersion diagram of the planar EBG structure shown in Figure 3.18 in the X-M region. The data points of the propagating modes representing the dispersion relation are extracted numerically by Ansoft HFSS. The polynomial fit of these data points of the propagating modes show dispersion graphs. The specifications of the EBG are defined in Figure 3.55.

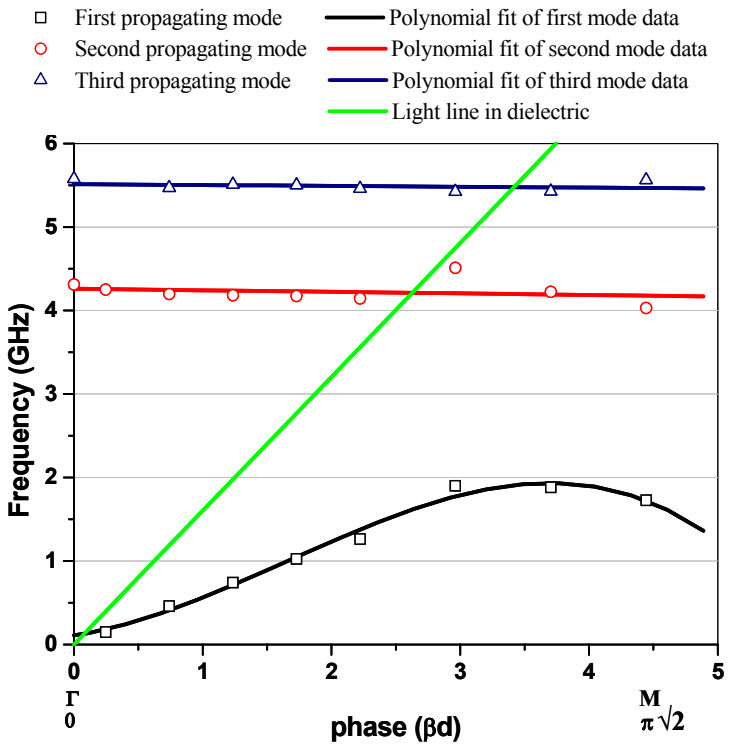

Figure 3.57. Dispersion diagram of the planar EBG structure shown in Figure 3.18 in the M-Γ region. The data points of the propagating modes representing the dispersion relation are extracted numerically by Ansoft HFSS. The polynomial fit of these data points of the propagating modes show dispersion graphs. The specifications of the EBG are defined in Figure 3.55.

At the edge of the bandgap, the lower and the upper propagating modes are slow modes. For slow modes compared to light line, the group velocity defined by $Vg^{-1} = \partial\beta / \partial\omega$ is much lower. Therefore, the slow modes are very dispersive. As it is clear from the dispersion diagrams of the sample under study in three regions, the variation of the frequency versus the phase for the second and the third propagating modes is very small. The dispersion graphs are approximately straight lines with zero degree tilt which show that the group velocities of these modes are very low. For the miniaturized planar EBG sample, the group velocity of the first three propagating modes and the light line in dielectric for the Γ-X, X-M, and M-Γ regions are plotted in Figure 3.58 to Figure 3.60, respectively. The group velocity of light line is defined by:

$$Vg^{-1} = \begin{cases} \sqrt{\varepsilon_r}/c & \Gamma - \text{X Zone} \begin{cases} k_x d = [0, \pi] \\ k_y d = 0 \end{cases} \\ \dfrac{\sqrt{\varepsilon_r}}{c} \dfrac{\left(2\pi f \sqrt{\varepsilon_r} d\right)/c}{\sqrt{\pi^2 + \left(\left(2\pi f \sqrt{\varepsilon_r} d\right)/c\right)^2}} & \text{X} - \text{M Zone} \begin{cases} k_x d = \pi \\ k_y d = [0, \pi] \end{cases} \\ \sqrt{2\varepsilon_r}/c & \text{M} - \Gamma \text{ Zone} \begin{cases} k_x d = k_y d = [0, \pi] \end{cases} \end{cases}$$

Equation 3-53

It is clear in the diagrams that the group velocity of the first propagating mode at the lower edge of the first bandgap abruptly and very sharply changes to zero. In the three regions of the Brillouin zone, the group velocity of the second and the third propagating modes are more than 10 times slower than the group velocity of the light in the dielectric. This means that for the existing modes, the media is completely dispersive.

From the dispersion diagrams and the group velocity diagrams in Brillouin zone we conclude that the lower edge of the first bandgap is located at 1.9 GHz. However, if we consider the 20 dB suppression band for this sample which is labeled in Table 3.III as sample No. 3, we notice that this band extends from 2.9 GHz to 12.5 GHz. Therefore, the lower edge of the suppression band is not the same as the lower edge of the bandgap for this sample. In addition, it is expected although there is not such a rule that the suppression band is wider than the bandgap and it encompass the bandgap. The difference at the lower edge of the two extracted bands is attributed to the following reasons: 1) the dispersion diagram is extracted for an idealistic case where the periodic array of EBG structures is infinite. However, the suppression band is extracted for a finite number of EBG structures where in our case; we set up 4 units of EBG structure between the two measuring ports. 2) In a bandgap which is defined with upper cut off frequency (f_{CU}) of lower propagating mode and lower cut off frequency (f_{CH}) of upper propagating mode, evanescent modes are propagating. The power of these evanescent modes is decreasing at f_{CU} and increasing at f_{CH}. In another word, the attenuation diagram of bandgap is increasing at f_{CU} and decreasing at f_{CH}. Therefore, if there is not infinite number of EBG structures between the source and the receiver ports then the 20 dB suppression band limits might not locate precisely at the edge of the bandgap. This fact is shown in Figure 3.51.

The 20 dB suppression band of this sample is very wide. It is consisting of upper part of the first bandgap, several higher order propagating modes, and several higher order bandgaps as partially shown in dispersion diagrams. A bandgap is a gap of propagating modes, however, a suppression band is not. A suppression band is a

gap of power. In another words: in the suppression band, the level of transferred power between two ports (S_{21}), where EBG structures are located between them, either through evanescent modes or propagating modes is reduced by more than 20 dB. It is noted that the bandgap is the inherent feature of periodic bandgap structure which directly relates to topology and composition of structure and not to losses of constructive materials. However, in measuring the suppression band we consider losses including metallic loss and dielectric loss. Lossess in the structure contribute to the attenuation level, however, considering the range of frequencies where we are studying these structures and the presence of limited numbers of structures in our setup reveals that the value of loss is not in the order of 20 dB. So we need to find out what is happening to the energy of these slow propagating modes. Our guess is: these modes instead of propagating through structures may radiate out. Therefore, the EBG sample, similar to a bandstop filter, blocks through-propagation in the suppression band.

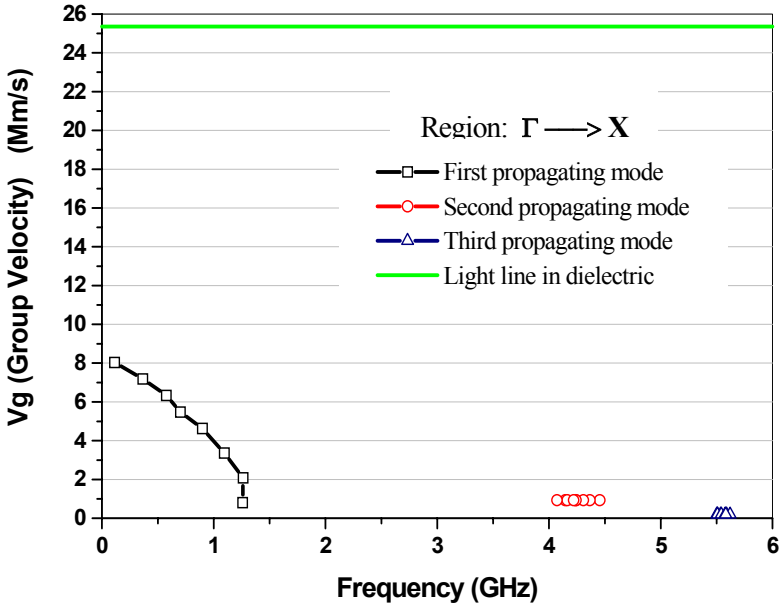

Figure 3.58. Group velocity of the propagating modes of the planar EBG structure and the light line in the dielectric in the Γ-X region as defined in Figure 3.55. The Vg graphs are obtained from the polynomials fit of the propagating modes.

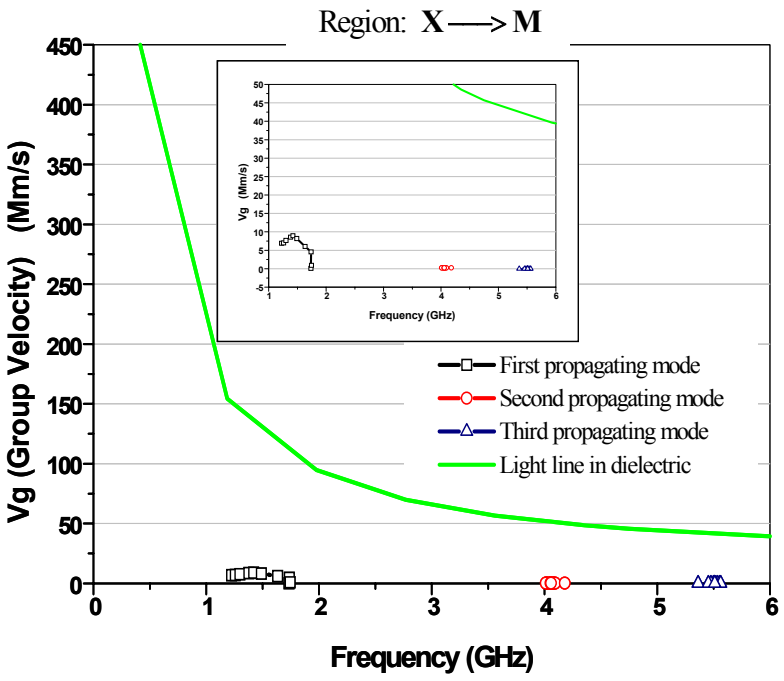

Figure 3.59. Group velocity of the propagating modes of the planar EBG structure and the light line in the dielectric in the X-M region as defined in Figure 3.56. The Vg graphs are obtained from the polynomials fit of the propagating modes.

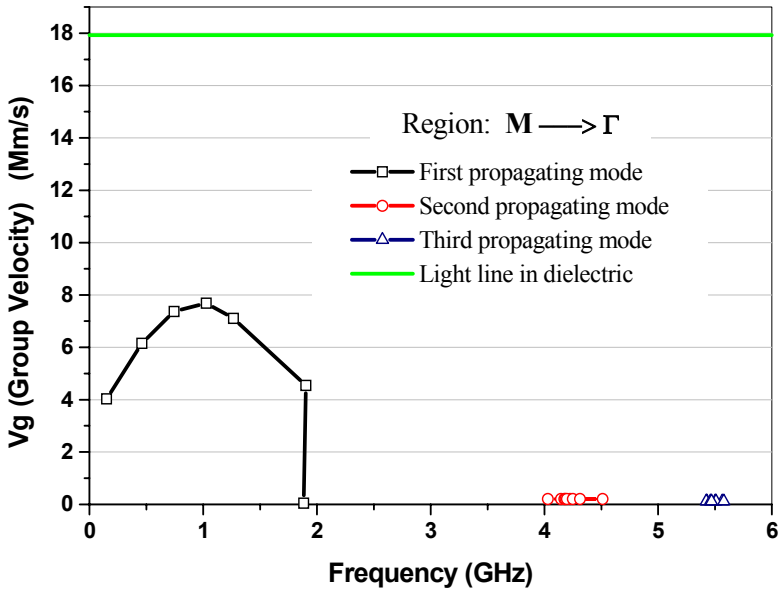

Figure 3.60. Group velocity of the propagating modes of the planar EBG structure and the light line in the dielectric in the M-Γ region as defined in Figure 3.57. The Vg graphs are obtained from the polynomials fit of the propagating modes.

Following, we investigate the hypothesis of energy radiation from opening of the patterned structure to surrounding media nearby the slow mode frequency regimes. The solid parallel plate radiates out energy at the edges to surrounding environment. The radiated power at the excited resonant frequency of the parallel plate is stronger. For example, if we consider a setup consisting of a finite parallel plate with two ports inside, the total sum of the normalized transferred energy between two ports and the normalized reflected energy to source at the considered frequency is not equal to unity. In a lossy-opened system, the radiation loss can be characterized by the quantity of radiation loss parameter which is defined as: $1- |S_{11}|^2 - |S_{21}|^2$. In our study, we calculate the radiation loss parameter for the EBG structures by using the S-parameters extracted from the setup shown in Figure 3.14. For comparison purpose, the radiation loss parameter for the solid parallel planes setup with the same dimensions and port locations as the EBG patterned structure is extracted.

The radiation loss for the first sample is shown in Figure 3.61. The 20 dB suppression band of this sample which is extended from 2.9 GHz to 12.5 GHz is marked in the figure. The figure clearly shows that the local peaks of radiation loss from solid parallel planes are excessively reduced by the EBG patterning of one of the planes. Therefore, patterning not only does not increase the radiation to surrounding environment but also it decreases EMI in the band where EBG is effective. In the suppression band, there are few local peaks in the radiation loss diagram of the EBG patterned planes. Comparing the frequency band of these peaks with the frequency band of the slow propagating modes in the dispersion diagram of

Figure 3.20 shows that the frequency regions could be mapped with acceptable accuracy. The second and third local peaks which are compatible with the third and the fourth propagating modes are marked in Figure 3.61. Therefore, the results for the first sample verify our proposal about the radiating emissions from openings of EBG patterns to surrounding environment at the frequency bands where dispersive modes exist. We could say that these slow modes radiate out instead of propagating through structures.

To investigate more about the slow modes which exists in the suppression band of planar EBG structures, we look to the second EBG sample. The radiation loss diagram for this sample and the reference case are plotted in Figure 3.62. The 20 dB suppression band which extends from 1.9 GHz to 10.8 GHz is marked in the figure. The reduction of radiation loss in the frequency band where the EBG pattern is effective is obvious in the figure. Also, comparing the propagating modes from dispersion diagram with the local peaks of radiation loss diagram for the EBG patterned planes proves the validity of our idea. Therefore, the dispersive slow modes radiate out instead of propagating through structure. These radiating emissions may interfere with the performance of other parts of a system which should be considered in design of a system with high functionality.

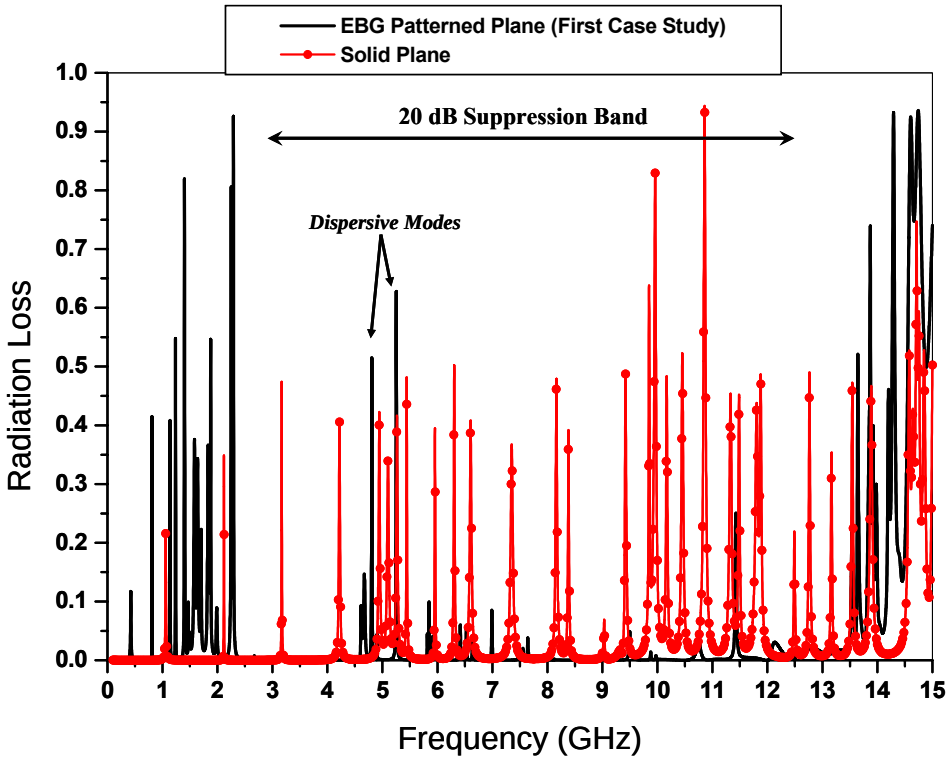

Figure 3.61. Radiation loss (1- $|S_{11}|^2$ - $|S_{21}|^2$) versus frequency for two cases: 1) the EBG patterned parallel planes and 2) solid parallel planes as reference. The S-parameters are extracted using the setup shown in Figure 3.14. The planar EBG structure and the design parameters are shown in Figure 3.12. The parameters of the EBG structure are: P_W = 1.6 mm, h = 114.3 μm, M_W = 0.02 mm, M_B = 0.02 mm, M_L = 1.6 mm, M_G = 0.02 mm, ε_r = 140, and $tan\ \delta$ = 0.0015.

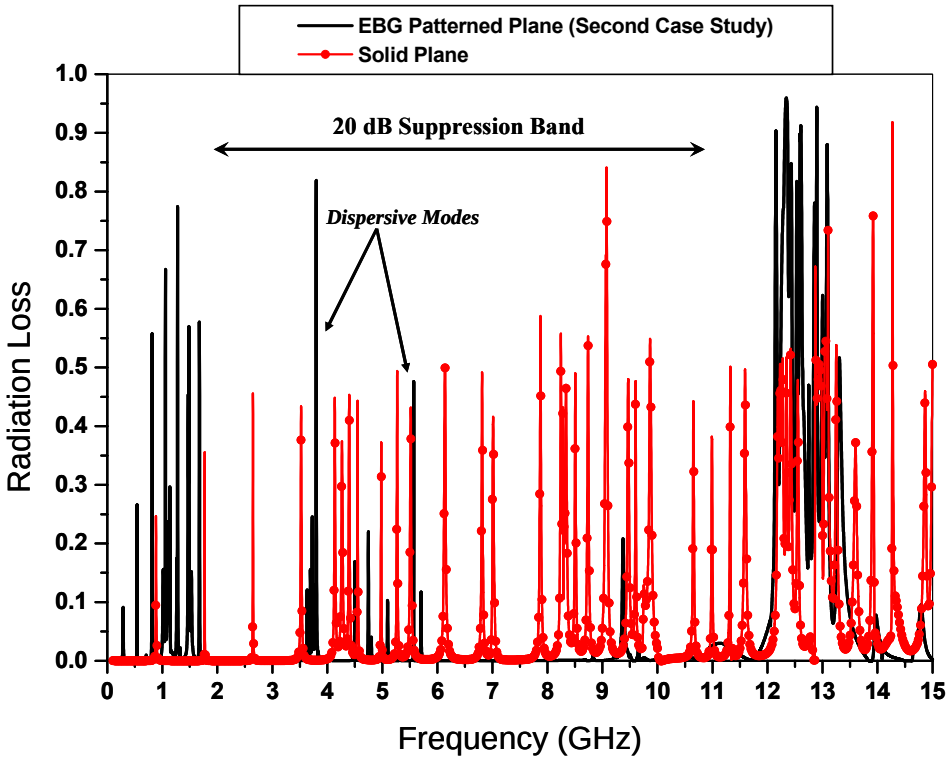

Figure 3.62. Radiation loss (1- $|S_{11}|^2$ - $|S_{21}|^2$) versus frequency for two cases: 1) the EBG patterned parallel planes and 2) solid parallel planes as reference. The S-parameters are extracted using the setup shown in Figure 3.14. The planar EBG structure and the design parameters are shown in Figure 3.12. The parameters of the EBG structure are: P_W = 1.6 mm, h = 114.3 μm, M_W = 0.02 mm, M_B = 0.02 mm, M_L = 1.6 mm, M_G = 0.02 mm, ε_r = 200, and $tan\ \delta$ = 0.0015.

3.3.11. Effects of Variation of Elements in Circuit-Transmission Line Model on Bandgaps

In this subsection, we study the effects of variation of the value of elements in the equivalent circuit–transmission line model of the planar EBG structure on its bandgaps. This study will help us to control the location of bandgaps by changing the physical parameters in the structure. Primarily, our focus is on the miniaturized EBG structures made of thin slab of high-k materials. At the end of this subsection, we will briefly speak about the possible existing differences in EBG structures made of dielectrics with low permittivity or higher thickness. Figure 3.63 to Figure 3.72 present the relationships of the location of bandgaps and the attenuation levels versus the different values of elements modeling a unit cell of the first sample of planar EBG structure discussed in Subsection 3.3.2. We varied the value of elements once at a time in these figures where the values of other elements are equal to their nominal values. The nominal values are extracted using our developed model. For the first study case, the nominal values of elements in Figure 3.48 are as follows: C_{PH} = 27.9 pF, L_{PH} = 0.0587 nH, L = 0.5921 nH, C_{L1} = 0.3039 pF, C_{L2} = 1.7926 pF, C_{M_PM} = 1.0633 pF, L_{DP} = 5.9511 pH, L_{DM} = 0.0936 nH, C_D = 1.6468 pF, d = 1.78 mm, d_1 = P_W = 1.6 mm, and $d_2 = d - d_1$ = 0.18 mm. Figure 3.63 shows the variations of the dispersion/attenuation diagram for the different values of L = {0.2921, 0.5921, 0.8921} nH. This change affects the lower edge of the first bandgap. Increasing L pushes the bandgap to lower frequencies. Also, this increment increases widths of the first three bandgaps which is clear in the plot. Also the attenuation level in the bandgaps increases. Generally, it is concluded that increasing L can provide a wider suppression bandgap with higher attenuation level.

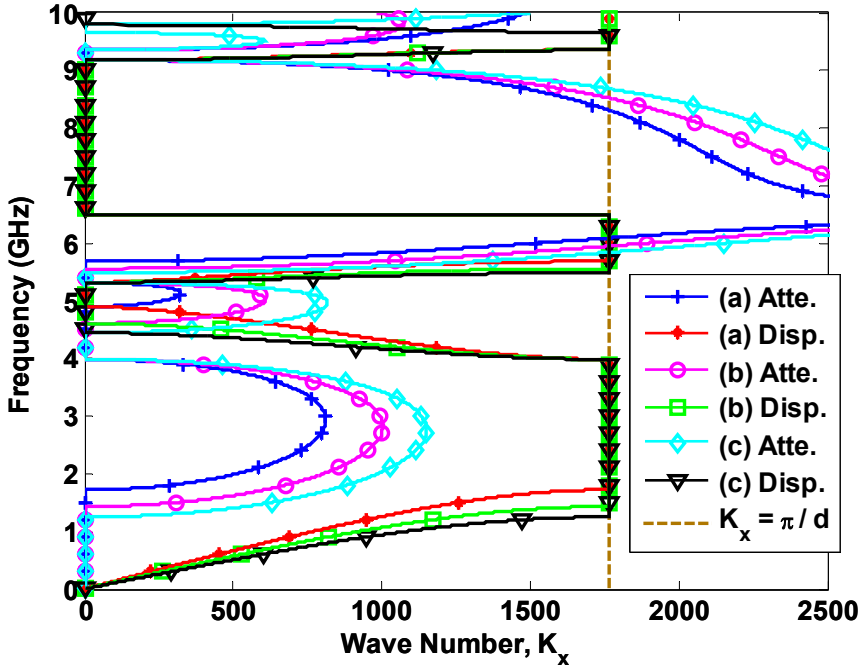

Figure 3.63. Relationship between the dispersion/attenuation diagram and the inductance L modeling the meander line in the planar EBG structure shown in Figure 3.18. The value of L is equal to (a) 0.2921 nH, (b) 0.5921 nH, and (c) 0.8921 nH. Figure 3.48 demonstrates the equivalent circuit-transmission line model of EBG. The nominal values of elements in the model are extracted for the EBG with the following specifications: P_W = 1.6 mm, h = 114.3 μm, M_W = 0.02 mm, M_B = 0.02 mm, M_L = 1.6 mm, M_G = 0.02 mm, ε_r = 140, and $tan\ \delta$ = 0.0015.

The variations of the dispersion/attenuation diagram for the different values of C_{L2} = {1.2926, 1.7926, 2.2926} pF are presented in Figure 3.64. There is not any noticeable effect at the lower edge of the first bandgap by this change. However, increasing C_{L2} pushes the second and the third propagating modes to lower frequencies. Yet, these variations compared to the variations resulting from change of inductance are small. Increasing C_{L2} decreases the attenuation level in the first and the second bandgaps. Also, the second and the third propagating modes with the lower value of C_{L2} are more dispersive and slower modes which may widen the suppression band and increase the filtering effect. The change of C_{L2} obviously affects the higher order modes. The smaller C_{L2} provides the wider third bandgap. Therefore, we conclude that decreasing C_{L2} may provide a better effective suppression band.

The variations of the dispersion/attenuation diagram for the different values of the equivalent capacitance which is resulting from the following combination (C_{M_PM} || C_{L1} || C_{M_PM}) = {0.19337, 0.39337, 0.59337} pF are plotted in Figure 3.65. Change of the value of interline parasitic capacitances on the lower edge of the first bandgap is negligible. Increasing these capacitances slightly shifts the second and the third propagating modes to lower frequencies and at the same time the attenuation level in the second and the third bandgaps increases. It is concluded that increasing interline coupling capacitances provides a suppression band with higher efficiency.

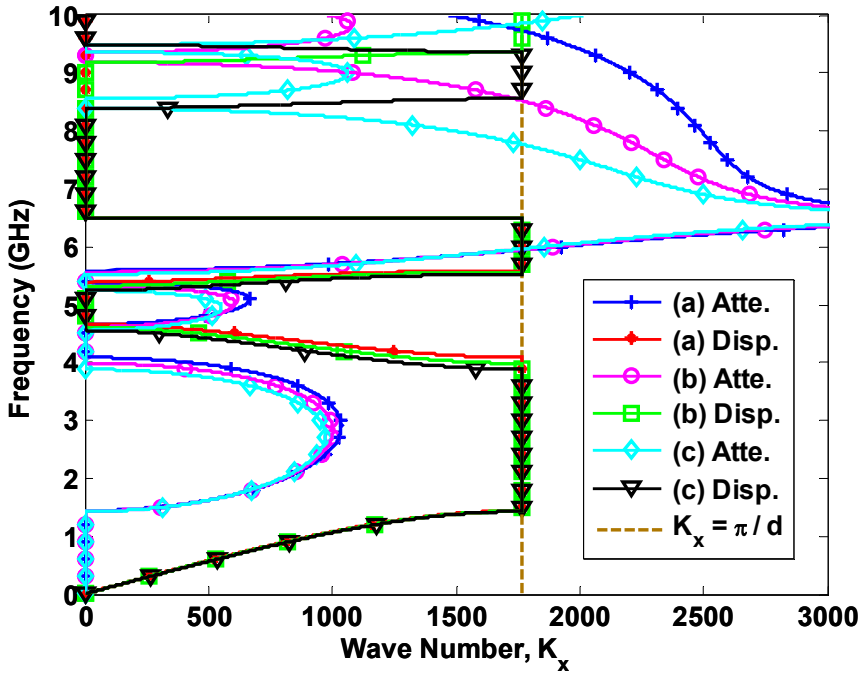

Figure 3.64. Relationship between the dispersion/attenuation diagram and the capacitance C_{L2} modeling the meander line in the planar EBG structure shown in Figure 3.18. The value of C_{L2} is equal to (a) 1.2926 pF, (b) 1.7926 pF, and (c) 2.2926 pF. Figure 3.48 demonstrates the equivalent circuit-transmission line model of EBG. The nominal values of elements in the model are extracted for the EBG with following the specifications: P_W = 1.6 mm, h = 114.3 μm, M_W = 0.02 mm, M_B = 0.02 mm, M_L = 1.6 mm, M_G = 0.02 mm, ε_r = 140, and $tan\ \delta$ = 0.0015.

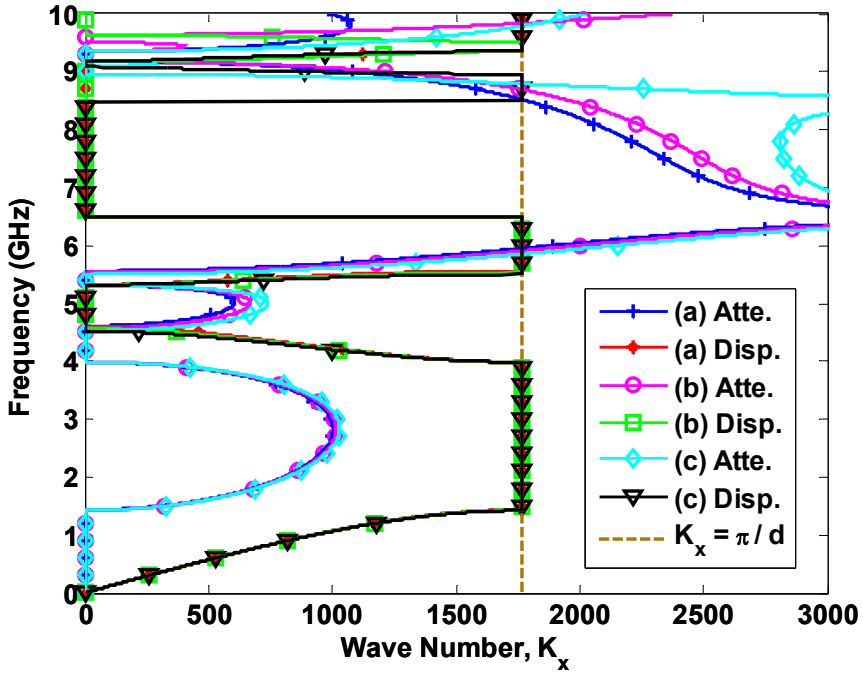

Figure 3.65. Relationship between the dispersion/attenuation diagram and the (C_{M_PM} || C_{L1} || C_{M_PM}) modeling the interline coupling between the meander line and two adjacent patches and between the arms of meander line in the planar EBG structure shown in Figure 3.18. The value of the equivalent capacitance is equal to (a) 0.19337 pF, (b) 0.39337 pF, and (c) 0.59337 pF. Figure 3.48 demonstrates the equivalent circuit-transmission line model of EBG. The nominal values of elements in the model are extracted for the EBG with following the specifications: P_W = 1.6 mm, h = 114.3 μm, M_W = 0.02 mm, M_B = 0.02 mm, M_L = 1.6 mm, M_G = 0.02 mm, ε_r = 140, and $tan\ \delta$ = 0.0015.

Figure 3.66 presents the variations of the dispersion/attenuation diagram for the different values of L_{PH} = {0.0287, 0.0587, 0.0887} nH. The effects of these variations are negligible on the lower edge of the first bandgap. However, increasing

L_{PH} pushes the second, the third, and the fourth propagating modes shown in the plot to lower frequencies. Also, this increment decreases the attenuation level in the first and second bandgap. Therefore, designing for low values of L_{PH} may be more efficient in providing a suppression band which will be starting at low frequencies.

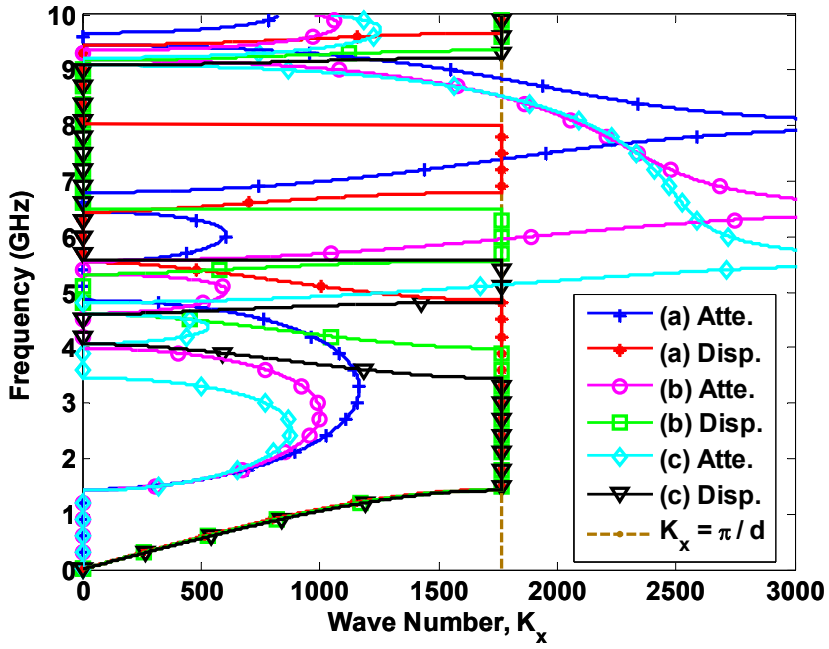

Figure 3.66. Relationship between the dispersion/attenuation diagram and the inductance L_{PH} modeling the patch in the planar EBG structure shown in Figure 3.18. The value of L_{PH} is equal to (a) 0.0287 nH, (b) 0.0587 nH, and (c) 0.0887 nH. Figure 3.48 demonstrates the equivalent circuit-transmission line model of EBG. The nominal values of elements in the model are extracted for the EBG with following the specifications: P_W = 1.6 mm, h = 114.3 μm, M_W = 0.02 mm, M_B = 0.02 mm, M_L = 1.6 mm, M_G = 0.02 mm, ε_r = 140, and $tan\ \delta$ = 0.0015.

The variations of the dispersion/attenuation diagram for the different values of C_{PH} = {17.903, 27.903, 37.903} pF are shown in Figure 3.67. Increasing C_{PH} pushes the lower edge of the first bandgap to lower frequencies. The changes of the second and the fourth propagating modes are negligible and the third propagating mode shifts to lower frequencies. Therefore, by increasing C_{PH}, widths of the first and the third bandgaps and their attenuation levels increase. However, the width of the second bandgap and its attenuation level decrease. The third propagating mode, by increasing C_{PH}, becomes more dispersive or slower mode which may result in widening of the suppression band and increasing of the filtering effect. As a result, increasing the value of C_{PH} increases the efficiency of suppression bandgap. Generally, in the designed EBG structures the value of inductance L is considerably high; therefore, variation in the value of L shows its effects more obviously than the variations in other elements. It should be considered that in the designs, the inductance is in the order of 10^{-9} but the capacitance is in the order of 10^{-12}.

Figure 3.68 shows the variations of the dispersion/attenuation diagram for the different values of d_1 = {0.75 × P_W, P_W, 1.25 × P_W}. Increasing the length of patch-microstrip pushes all the propagating modes to lower frequencies. However, the changes in location of the second propagating mode are more than the changes in the locations of other propagating modes in these diagrams. Therefore, the first bandgap narrows down and reversely, the second bandgap widens. The level of attenuation in the first bandgap decreases and in the second bandgap increases. The visible higher order propagating modes in the diagrams are slow modes. So it is possible by increasing d_1 we widen the suppression band and increase the filtering effect.

Therefore, we conclude that increasing d_1 may increase efficiency and width of the suppression bandgap.

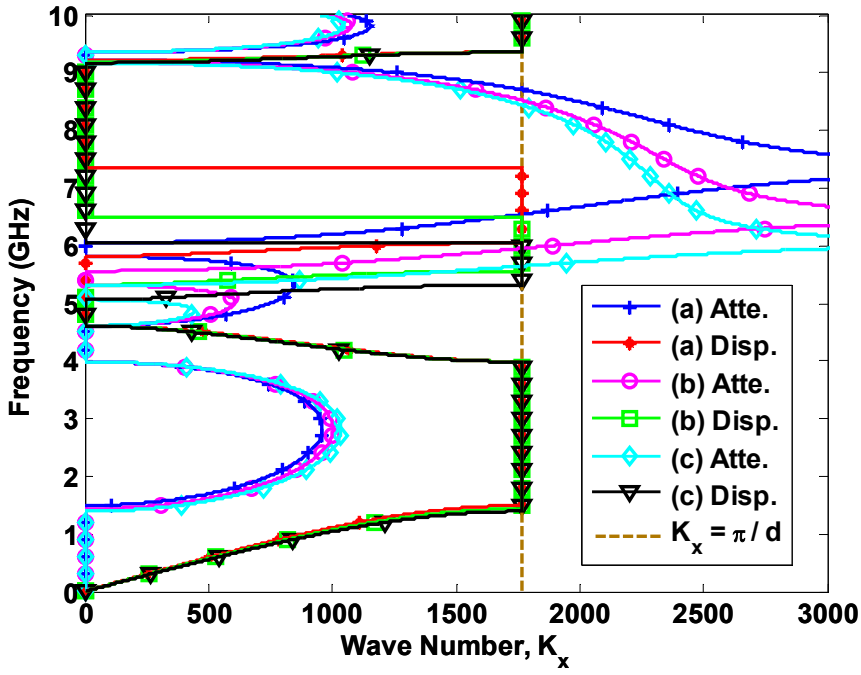

Figure 3.67. Relationship between the dispersion/attenuation diagram and the capacitance C_{PH} modeling the patch in the planar EBG structure shown in Figure 3.18. The value of C_{PH} is equal to (a) 17.903 pF, (b) 27.903 pF, and (c) 37.903 pF. Figure 3.48 demonstrates the equivalent circuit-transmission line model of EBG. The nominal values of elements in the model are extracted for the EBG with following the specifications: P_W = 1.6 mm, h = 114.3 μm, M_W = 0.02 mm, M_B = 0.02 mm, M_L = 1.6 mm, M_G = 0.02 mm, ε_r = 140, and $tan\ \delta$ = 0.0015.

The variations of the dispersion/attenuation diagram for the different values of $d_2 = \{0.75 \times D_2, D_2, 1.25 \times D_2\}$ where $D_2 = 2 \times M_B + N \times M_W + (N\text{-}1) \times M_G$ are shown in Figure 3.69. Increasing d_2 negligibly pushes the first, the second, and the third propagating modes down in frequencies. Therefore, the change of the first and the second bandgaps are negligent. Increasing d_2 shifts the fourth propagating mode to lower frequencies so the third bandgap narrows down. We conclude from these results that the decrease of d_2 in the planar EBG structures made of thin slab of high-k dielectrics may increase width of the suppression band.

The variations of the dispersion/attenuation diagram for the different values of $L_{DP} = \{0.9511, 5.9511, 10.9511\}$ pH are demonstrated in Figure 3.70. The change of value of this element affects the first, the second, and the third propagating modes and as a result the first and the second bandgaps are negligibly affected. Increasing L_{DP} pushes the fourth propagating mode down in frequencies. Therefore, the third bandgap narrows down. It can be concluded that we can get a more efficient suppression bandgap by decreasing L_{DP}.

The variations of the dispersion/attenuation diagram for the different values of $L_{DM} = \{43.576, 93.576, 143.576\}$ pH are shown in Figure 3.71. Increasing L_{DM} pushes the first propagating mode to lower frequencies. The effect of this change on the second and the third propagating modes is negligible. Therefore, the first and the second bandgaps slightly change. Increasing L_{DM} shifts the fourth propagating mode down in frequencies; this will narrow the third bandgap. As a conclusion, decreasing L_{DM} may widen the suppression bandgap but increasing L_{DM} may push the bandgap to lower frequencies. Designing L_{DM} with low value can be more efficient.

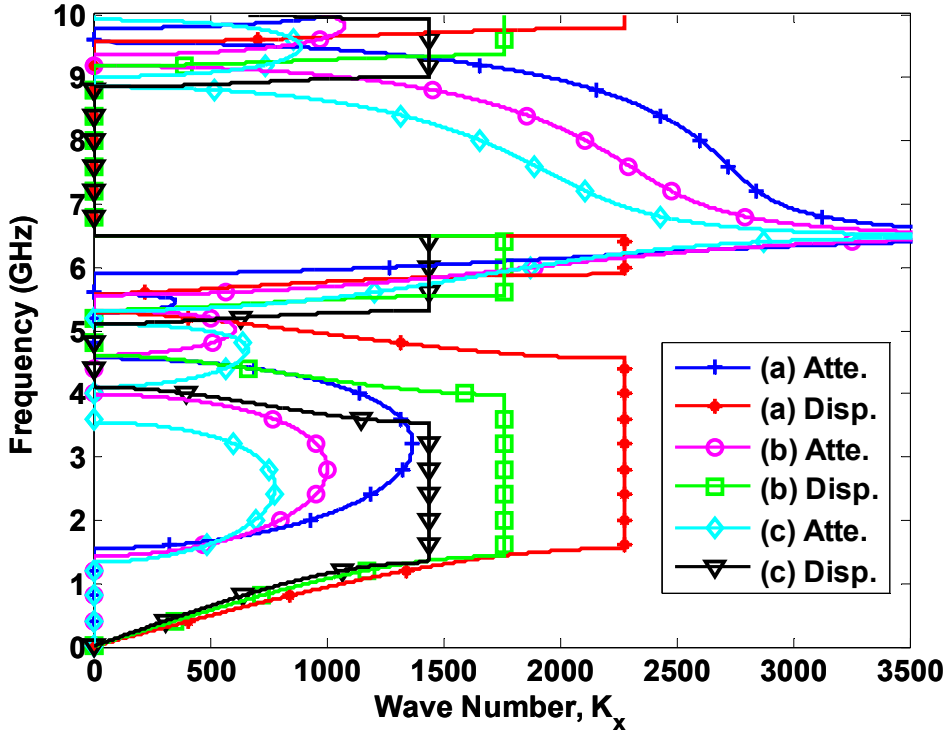

Figure 3.68. Relationship between the dispersion/attenuation diagram and the length of patch-microstrip d_1 modeling the phase difference along the patch in the planar EBG structure shown in Figure 3.18. The value of d_1 is equal to (a) 0.75 × P_W, (b) P_W, and (c) 1.25 × P_W. P_W is the width of patch-microstrip, the spacing between two consecutive patches $d_2 = 2 \times M_B + N \times M_W + (N\text{-}1) \times M_G$, and the length of a unit cell of EBG $d = d_1 + d_2$. Figure 3.48 demonstrates the equivalent circuit-transmission line model of EBG. The nominal values of elements in the model are extracted for the EBG with following the specifications: P_W = 1.6 mm, h = 114.3 μm, M_W = 0.02 mm, M_B = 0.02 mm, M_L = 1.6 mm, M_G = 0.02 mm, ε_r = 140, and $tan\ \delta$ = 0.0015.

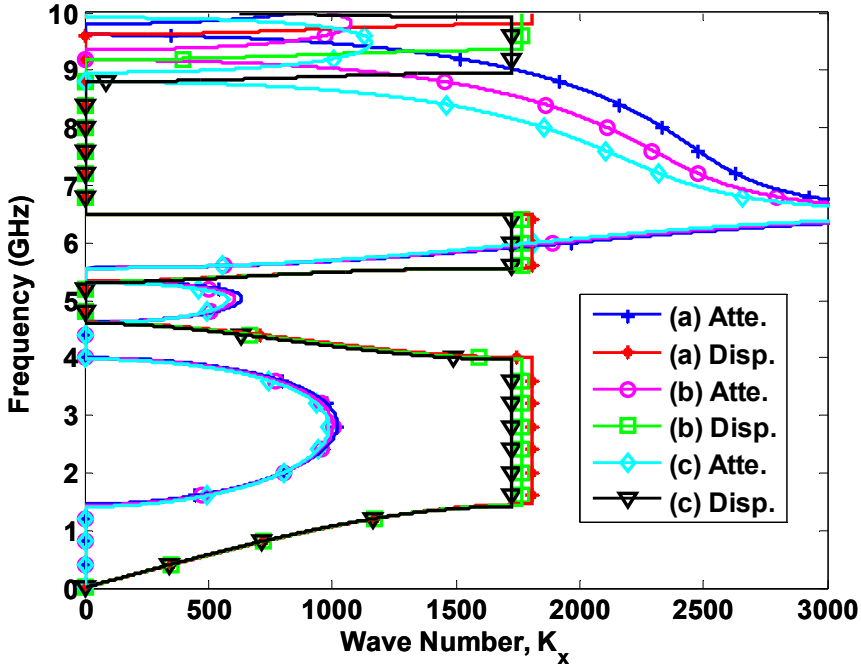

Figure 3.69. Relationship between the dispersion/attenuation diagram and the length of meander-microstrip d_2 modeling the phase difference across the meander line in the planar EBG structure shown in Figure 3.18. The value of d_2 showing the spacing between the two consecutive patches is equal to (a) 0.75 × D_2, (b) D_2, and (c) 1.25 × D_2 where $D_2 = 2 \times M_B + N \times M_W + (N\text{-}1) \times M_G$. M_W is the width of meander-microstrip, the length of patch $d_1 = P_W$, and the length of a unit cell of EBG $d = d_1 + d_2$. Figure 3.48 demonstrates the equivalent circuit-transmission line model of EBG. The nominal values of elements in the model are extracted for the EBG with following the specifications: $P_W = 1.6$ mm, $h = 114.3$ μm, $M_W = 0.02$ mm, $M_B = 0.02$ mm, $M_L = 1.6$ mm, $M_G = 0.02$ mm, $\varepsilon_r = 140$, and $tan\ \delta = 0.0015$.

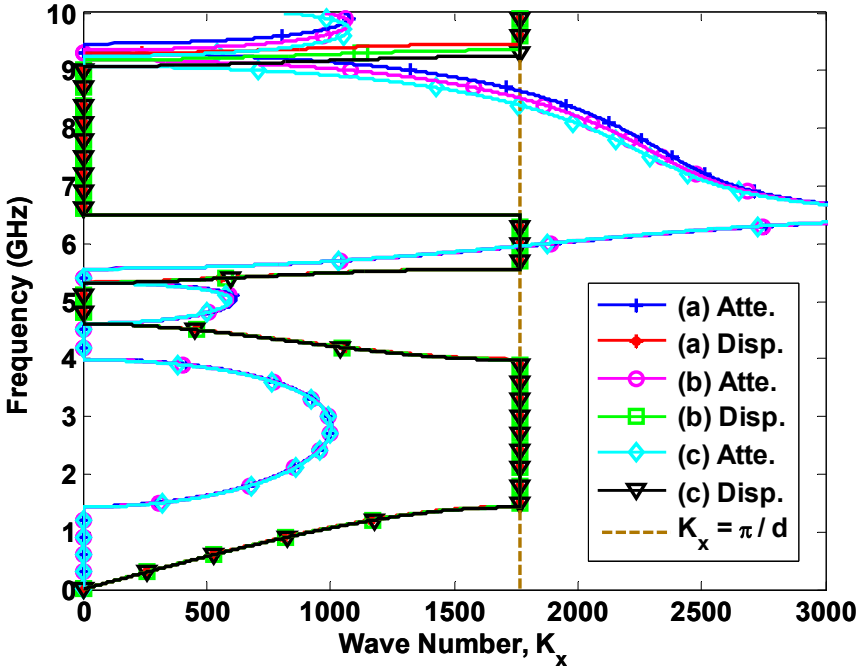

Figure 3.70 Relationship between the dispersion/attenuation diagram and the inductance L_{DP} modeling the step discontinuity between the patch and the meander line in the planar EBG structure shown in Figure 3.18. The value of L_{DP} is equal to (a) 0.9511 pH, (b) 5.9511 pH, and (c) 10.9511 pH. Figure 3.48 demonstrates the equivalent circuit-transmission line model of EBG. The nominal values of elements in the model are extracted for the EBG with following the specifications: P_W = 1.6 mm, h = 114.3 μm, M_W = 0.02 mm, M_B = 0.02 mm, M_L = 1.6 mm, M_G = 0.02 mm, ε_r = 140, and $tan\ \delta$ = 0.0015.

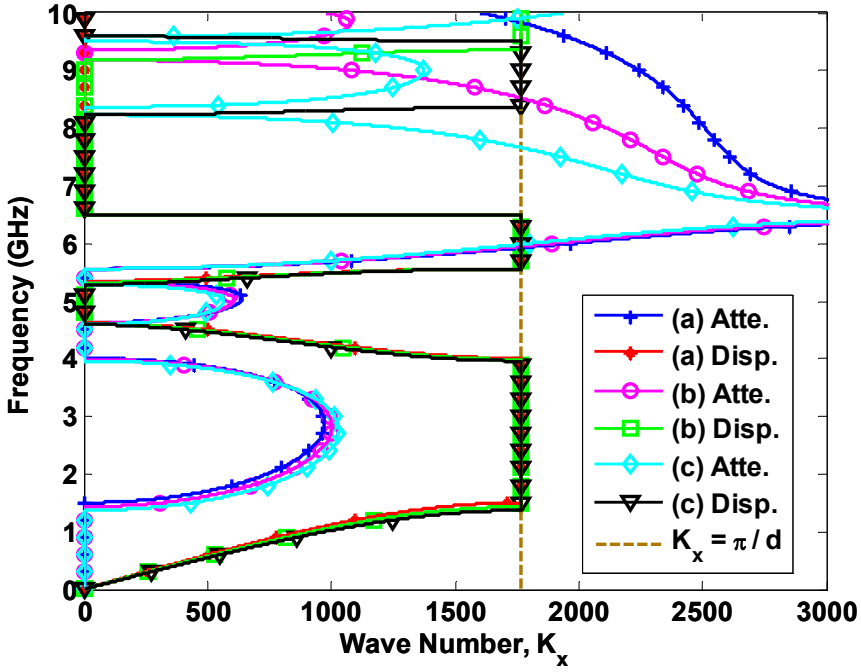

Figure 3.71. Relationship between the dispersion/attenuation diagram and the inductance L_{DM} modeling the step discontinuity between the patch and the meander line in the planar EBG structure shown in Figure 3.18. The value of L_{DM} is equal to (a) 43.576 pH, (b) 93.576 pH, and (c) 143.576 pH. Figure 3.48 demonstrates the equivalent circuit-transmission line model of EBG. The nominal values of elements in the model are extracted for the EBG with following the specifications: P_W = 1.6 mm, h = 114.3 μm, M_W = 0.02 mm, M_B = 0.02 mm, M_L = 1.6 mm, M_G = 0.02 mm, ε_r = 140, and $tan\ \delta$ = 0.0015.

Figure 3.72 shows the variations of the dispersion/attenuation diagram for the different values of C_D = {0.6468, 1.6468, 2.6468} pF. Increasing C_D negligibly pushes the first propagating mode down in frequencies. However, the second and the third propagating modes obviously shift to lower frequencies. As a result, the first bandgap narrows down but change the in width of the second bandgap is very small. The change of the fourth propagation mode is negligible. Therefore, width of the third bandgap increases. We conclude that decreasing C_D may widen the first bandgap but effectsw on the suppression bandgap may be negligible.

The conclusions up to this end are related to planar EBG structures made of thin slab of high-k materials. We can not generalize these results to materials with lower permittivity or higher thickness. For example, in the fourth sample discussed in Subsection 3.3.2 where ε_r = 4.3 and h = 114.3 μm the second and the third propagating modes are more sensitive to variation of L_{PH} and C_{PH}. The variation of elements of the step discontinuity does not affect these modes noticeably. However, in the third sample discussed in Subsection 3.3.2 where ε_r = 140 and h = 500 μm the variation of elements of the step discontinuity affects the second and the third propagating modes clearly.

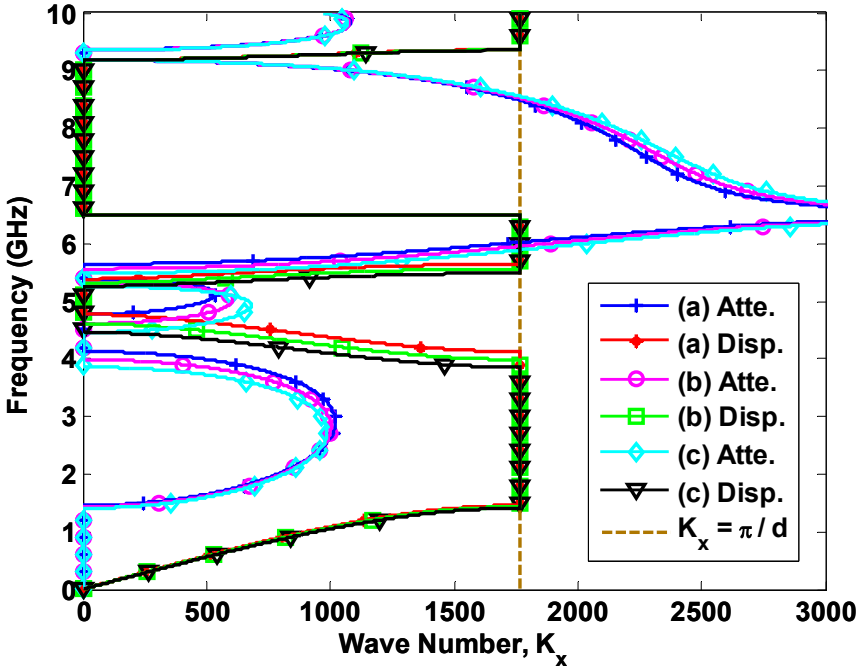

Figure 3.72. Relationship between the dispersion/attenuation diagram and the capacitance C_D modeling the step discontinuity between the patch and the meander line in the planar EBG structure shown in Figure 3.18. The value of C_D is equal to (a) 0.6468 pF, (b) 1.6468 pF, and (c) 2.6468 pF. Figure 3.48 demonstrates the equivalent circuit-transmission line model of EBG. The nominal values of elements in the model are extracted for the EBG with following the specifications: P_W = 1.6 mm, h = 114.3 μm, M_W = 0.02 mm, M_B = 0.02 mm, M_L = 1.6 mm, M_G = 0.02 mm, ε_r = 140, and $tan\ \delta$ = 0.0015.

In continue of our discussion, the relationship between the dispersion/attenuation diagram and the capacitance of step discontinuity for the third and the fourth case studies are plotted in Figure 3.73 and Figure 3.74, respectively. The nominal values of the elements of the model shown in Figure 3.48 for the third sample are as follows: C_{PH} = 6.5507 pF, L_{PH} = 0.17897 nH, L = 0.62373 nH, C_{L1} = 0.38232 pF, C_{L2} = 0.83432 pF, C_{M_PM} = 1.5698 pF, L_{DP} = 0.046319 nH, L_{DM} = 0.31122 nH, C_D = 1.7066 pF, d = 1.78 mm, $d_1 = P_W$ = 1.6 mm, and $d_2 = d - d_1$ = 0.18 mm. The variations of the dispersion/attenuation diagram for the different values of C_D = {0.7066, 1.7066, 2.7066} pF are shown in Figure 3.73. This figure shows that the increasing C_D pushes the propagating modes and the bandgaps to lower frequencies. This increment narrows the first bandgap and widens the second and the third bandgaps. The third propagating mode becomes a slower mode by this increment. Therefore, if this increment combines the second and the third bandgaps then the suppression band is wide. We may conclude that decreasing C_D widens the first bandgap and increasing C_D pushes the first narrow bandgap to lower frequencies. Totally, the effect of this change on the suppression bandgap is not very clear.

The nominal values of the elements of the model shown in Figure 3.48 for the fourth sample are as follows: C_{PH} = 136.73 pF, L_{PH} = 0.0703 nH, L = 22.847 nH, C_{L1} = 0.074304 pF, C_{L2} = 4.074 pF, C_{M_PM} = 0.69867 pF, L_{DP} = 0.018134 nH, L_{DM} = 0.10791 nH, C_D = 0.72452 pF, d = 21.8 mm, $d_1 = P_W$ = 20 mm, and $d_2 = d - d_1$ = 1.8 mm. Figure 3.74 shows the variations of the dispersion/attenuation diagram for the different values of C_D = {0.22452, 0.72452, 1.22452} pF. Figure 3.74 demonstrates that this change has negligible effect on the propagating modes and the bandgaps. So

we can not clearly change the efficiency of the suppression band by varying this element.

After studying the relationship between the dispersion diagram and the elements modeling the EBG, by considering 1) the frequency region or the suppression band where the EBG is effective and 2) the available spacing for a unit cell design we can change the proper elements in the model or basically the physical design parameters to get the required suppression band. Therefore, the procedures of design might be done by using recursive optimization code. We can manually define the priority to change the elements in model by defining weight coefficients for these elements. Similar studies to what we did in this subsection could introduce the weight coefficients.

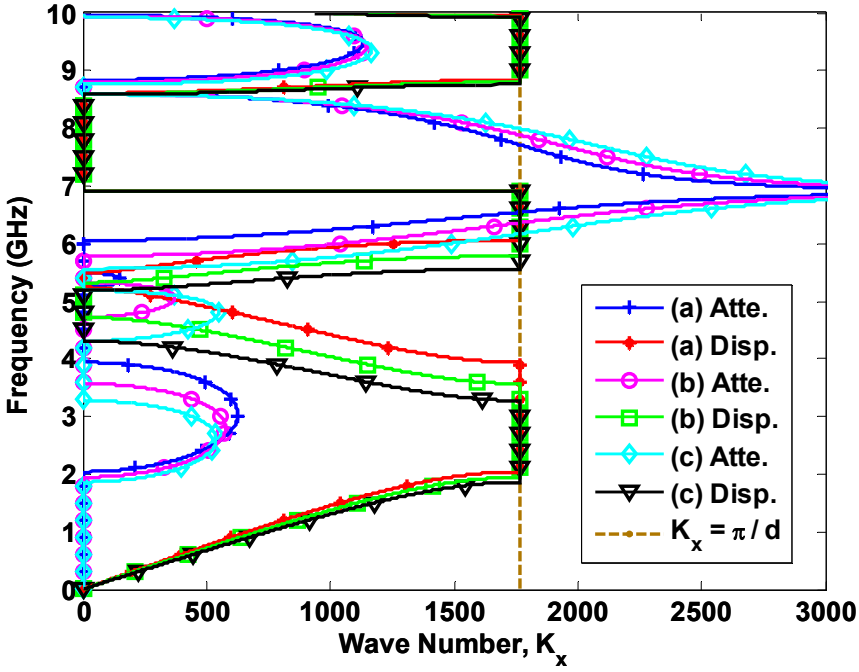

Figure 3.73. Relationship between the dispersion/attenuation diagram and the capacitance C_D modeling the step discontinuity between the patch and the meander line in the planar EBG structure shown in Figure 3.18. The value of C_D is equal to (a) 0.7066 pF, (b) 1.7066 pF, and (c) 2.7066 pF. Figure 3.48 demonstrates the equivalent circuit-transmission line model of EBG. The nominal values of elements in the model are extracted for the EBG with following the specifications: P_W = 1.6 mm, h = 500 μm, M_W = 0.02 mm, M_B = 0.02 mm, M_L = 1.6 mm, M_G = 0.02 mm, ε_r = 140, and $tan\ \delta$ = 0.0015.

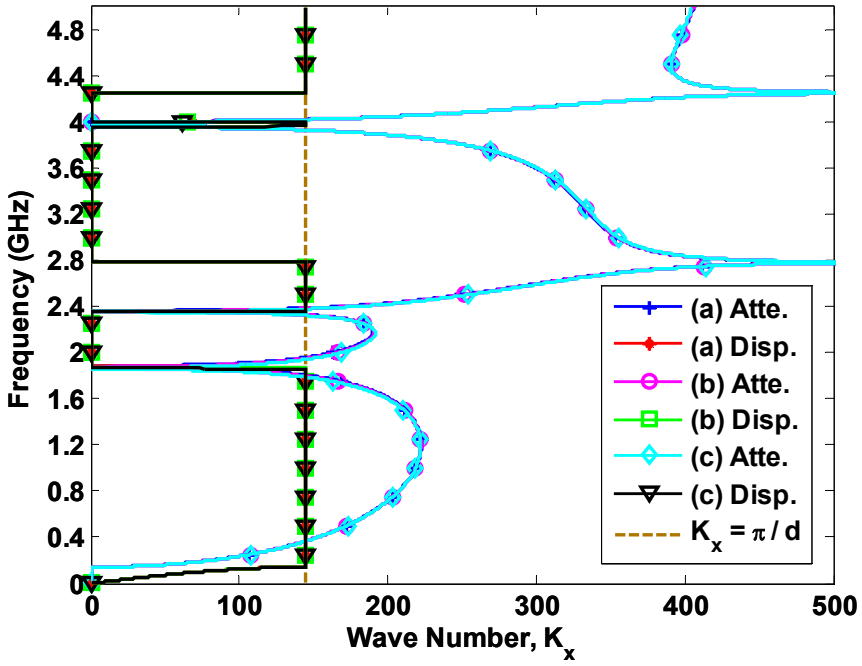

Figure 3.74. Relationship between the dispersion/attenuation diagram and the capacitance C_D modeling the step discontinuity between the patch and the meander line in the planar EBG structure shown in Figure 3.18. The value of C_D is equal to (a) 0.22452 pF, (b) 0.72452 pF, and (c) 1.22452 pF. Figure 3.48 demonstrates the equivalent circuit-transmission line model of EBG. The nominal values of elements in the model are extracted for the EBG with following the specifications: P_W = 20 mm, h = 114.3 μm, M_W = 0.2 mm, M_B = 0.2 mm, M_L = 20 mm, M_G = 0.2 mm, ε_r = 4.3, and $tan\ \delta$ = 0.02.

Chapter 4 : Switching Noise and Electromagnetic Noise in High Speed Packages

The most common type of noise in high speed packages is the simultaneous switching noise (SSN). SSN, also referred to as voltage bounce or delta-I noise, is caused by the switching of digital circuit between two different logic levels. When switching takes place, a surge of current travels between power and ground planes causing a voltage drop between them and a voltage drop across segments of the power plane itself. These voltage drops are directly proportional to the current switching rate and the effective inductance of current paths. SSN was studied extensively in the past decade [1]-[4]. There are waves propagating between metallic layers of laminated substrate acting as parallel plate waveguide. These waves supported by traveling current on planes can interfere with other vias passing through these planes or connected to these planes. When the traveling waves reach the edges, part of their power radiate out and the remainder reflect back inside the package. The waves radiated out of package may interfere with other surrounding electronics. Another design artifact that exacerbates the noise induced by switching is the natural resonance of the package itself. If the natural resonant frequencies of the package encompass the switching frequency or the clock frequency and its harmonics, then the potential for further disturbance to the reference voltage levels increase and equally important the potential for EMI increases.

In the following, we explain briefly the range of frequencies where we have to protect vias and interconnects from EM interference. There are vias in the package which are routing the signal lines through layers from one trace to another. The power

spectral density of the electrical signal on signal lines (also known as data bus and address bus) is concentrated around the operating frequencies and their harmonics. Therefore, to provide clean data we have to mitigate the electromagnetic noise around the operating frequency and its related harmonics. Suppressing noise from clock-transmission lines is equally important. The bus and clock operate at the same frequency; however, the rate of external clock in a system discussed extensively in the subject of noise suppressions in PCB boards is a fraction of the internal clock or core clock of the state-of-the-art processors which is the subject of our discussion in this chapter. The internal bus or the backside bus in processor package is operating at the same speed of the processor. The external bus or front side bus (FSB) connecting the processor to external memory and peripherals is operating at the rate of external clock on the PCB.

Other types of vias in the package connect the power planes to electronic circuits to provide power and ground. Switching or change of logic in those circuits leads to a surge of current from power planes to circuits through vias which induces EMI noise in whole band of frequencies. Therefore, for the suppression of switching noise, the interest is in broad band suppression.

4.1. Analytical Model of EM Noise in Packages

Coupling of EMI noise in a multilayer package occurs both transversally and vertically. The field propagating in transverse direction can couple to vias and interconnects passing through layers [2], [3] or can couple vertically, through cut-outs and apertures in the planes, to another layers [63], [64] and traps the vias in those

layers. Also, the field can penetrate through conductor plane; however this penetration is negligible beyond tens of MHz where the thickness of metallic planes is much larger than the skin depth. In this study, we mainly focus on the transverse coupling between vias and interconnects located in the same layer over the range of frequencies above hundreds of megahertz. Therefore, we analyze only a single plane pair.

Characterization of scattering parameters between interconnects in boards or packages is important for understanding the potential of the board or the package to transfer electromagnetic energy or noise between two specific points or ports. Impedance parameters which could be extracted from S-parameters are alternatively used for characterization of interconnects [43]. Analyzing S-parameters or Z-parameters help the package designers to estimate the frequency range where the EMI noise and switching noise are strong. In this section, and without loss of generality, we consider impedance parameters. Our analysis is based on the principle of resonators modeled with lumped elements [61], [62]. Following, we introduce this model and verify its performance.

A 3-D view of the single plane pair is shown in Figure 4.1 (a). The structure considered here is basically a parallel plate waveguide. The top and bottom metallic plates are rectangular with dimensions ($a \times b$) and conductivity σ. A dielectric with thickness h, permittivity ε, loss angle δ, and permeability μ is sandwiched between the metallic plates. The dimensions of the microprocessor package satisfy the following conditions: $a >> h$, $b >> h$, and $h << \lambda$, where λ is the wavelength in the dielectric material. With such conditions, the complex impedance between two

different ports, as shown in Figure 4.1 (b), using planar resonator model [61], [62] is given by :

$$Z_{ij}(\omega) = j\omega\mu\, h \sum_{n=0}^{N} \sum_{m=0}^{M} \frac{N_{mni}\, N_{mnj}}{ab\left(k_{mn}^{2} - k^{2}\right)}$$

Equation 4-1

Equation 4-1 may be approximated by an equivalent circuit model [62] as:

$$Z_{ij}(\omega) = \sum_{n=0}^{N} \sum_{m=0}^{M} \frac{N_{mni}\, N_{mnj}}{\frac{1}{j\omega L_{mn}} + j\omega C_{mn} + G_{mn}}$$

Equation 4-2

where $k = k' - jk''$ is the wave number with $k' = \omega\sqrt{\varepsilon\mu}$ and $k'' = \omega\sqrt{\varepsilon\mu}\left(\tan\delta + \delta_s/h\right)/2$.

$L_{mn} = h/(\omega_{mn}^{2}\, ab\, \varepsilon)$, $C_{mn} = ab\,\varepsilon/h$, $G_{mn} = \frac{ab\varepsilon}{h}\omega_{mn}\left(\tan\delta + \frac{\delta_{smn}}{h}\right)$, and

$N_{mni} = \varepsilon_n \varepsilon_m \cos(m\pi x_i/a)\cos(n\pi y_i/b)$.

Here, m and n are the indices of the (m,n) mode corresponding to the resonant frequency f_{mn}. $\omega_{mn} = 1/\sqrt{L_{mn}C_{mn}} = 2\pi f_{mn} = k_{mn}/\sqrt{\mu\varepsilon}$ *and* $k_{mn} = \sqrt{(m\pi/a)^2 + (n\pi/b)^2}$. $\delta_{smn} = \sqrt{2/(\omega_{mn}\mu\sigma)}$ is the skin depth for the (m,n) mode and the ratio δ_s/h represents the normalized skin depth with respect to the separation between the metallic layers. ε_m, $\varepsilon_n = 1$ for m, $n = 0$ and $\sqrt{2}$ otherwise. (x_i, y_i) and (x_j, y_j) are the coordinates of the via (port) at the ith and jth locations, respectively. The dimension of each port is neglected. Z_{ii} is the input impedance at the ith port. Z_{ij} is the mutual impedance (trans-impedance) between the ith and jth ports. Input and mutual impedances introduce noise voltage and/or bounce in the voltage level in power planes.

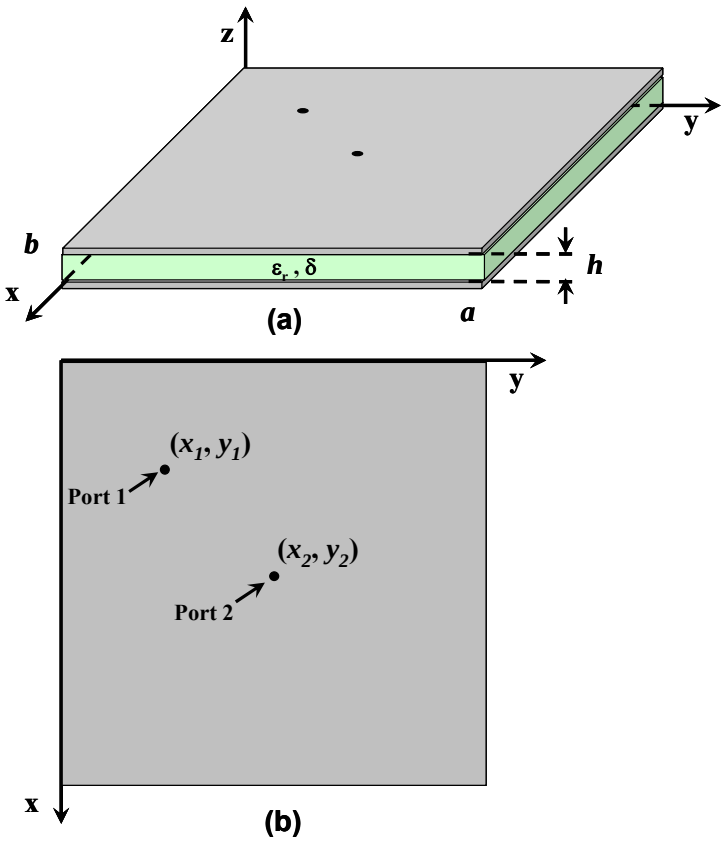

Figure 4.1. Single plane pair in the package consisting of metal-dielectric-metal layers is modeled as parallel plate waveguide. (a) 3-D view. (b) Top view. Typical dimensions of a microprocessor package are: $a = b = 4$ cm. Each via shown in the figure represents a port. Port 1 and Port 2 are located at ($x_1 = 1$ cm, $y_1 = 1$ cm), and ($x_2 = 2$ cm, $y_2 = 2$ cm), respectively.

In the following, we discuss a numerical experiment to validate the analytical expression for the impedance Z_{ij} extracted from the resonator model based on the planar structure. Ansoft's HFSS is used to perform full-wave simulation. The case study is a 4 cm × 4 cm package. Conductor is copper and dielectric is FR-4 with

thickness of 200 μm. The first port is located at (1 cm, 1 cm) and the second one at (2 cm, 2 cm). Figure 4.2 (a) and (b) show a comparison between the magnitudes of the impedances Z_{21} and Z_{22} calculated using full-wave simulation and the calculations obtained from two different analytical formulas including Equation 4-1 incorporating the resonator model and Equation 4-2 showing the resonator model approximated with the equivalent circuit lumped elements. These results confirm that Equation 4-2 is a good approximation for Equation 4-1.

Furthermore, the magnitude of Z_{21} from the planar analysis compares very favorably to that obtained using numerical full-wave analysis. However, the magnitude of the input impedance, Z_{22}, is in close agreement at low frequencies and the discrepancy increases at higher frequencies. This difference is expected as in full-wave simulation at the port discontinuity several modes including propagating and evanescent waves with fields in *x*, *y*, and *z* directions are excited. However, in planar analysis only E-fields in *z*-direction are considered. At the port junction, and at higher frequencies, the variation of the field in all directions becomes more complex causing more variation from planar analysis. Evanescent fields, on the other hand, diminish in strength as the distance from the excited port increases, therefore, we expect a good match between the different calculation methods for the trans-impedance Z_{21} as shown in Figure 4.2 (b).

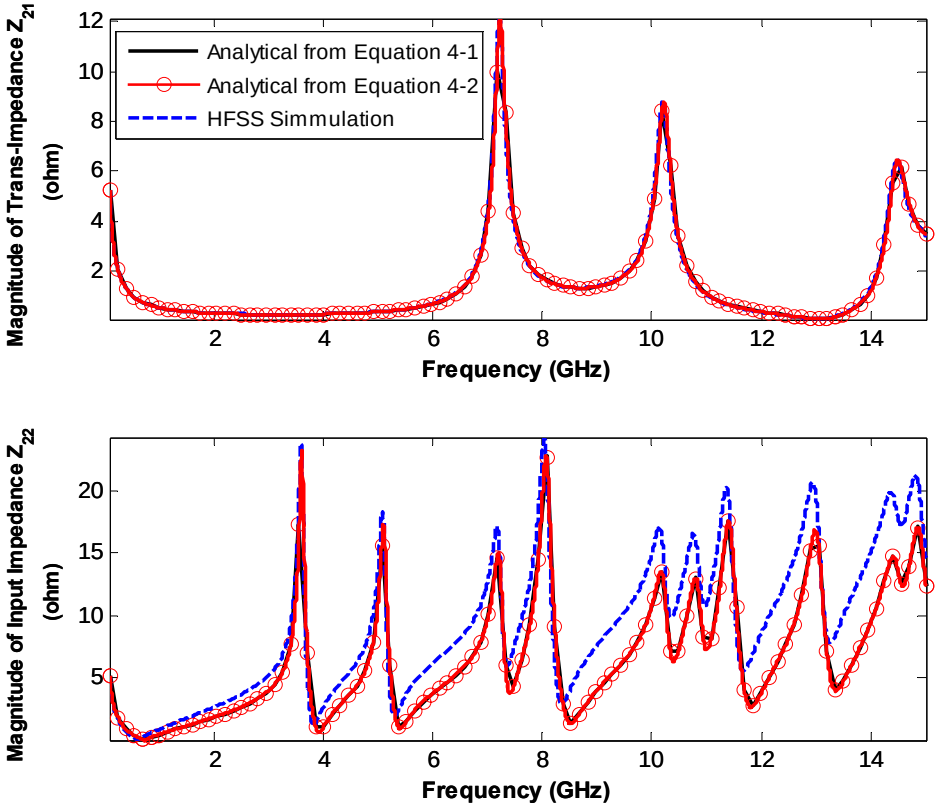

Figure 4.2. Magnitude of (a) trans-impedance between ports 1 and 2, and (b) input impedance at port 2 for the package shown in Figure 4.1. The plane separation is h = 200 μm. The Impedances are obtained through three different methods including: analytical method using Equation 4-1 plotted by the solid line, analytical method using Equation 4-2 plotted by the circle symbol line, and full-wave simulation using HFSS plotted by the dashed line.

4.2. SSN and EMI Noise Mitigation in Packages using High-K Embedded Capacitance

Following we will discuss about the concept of EM noise mitigation in IC packages using very high value embedded capacitance. The embedded capacitance technique as a strong EM noise suppressor has been used in the microwave regimes in the PCBs. We investigate about this technique in IC packages using very high-k materials which are newly commercially available. We need this study to assess the performance of one of our proposals related to the application of EBG structures in IC packages.

In the processor packaging compare to PCBs, we need to suppress EM noise at higher frequencies where the loss tangent becomes comparable or even higher than normalized skin depth. Therefore, in our analysis we include the dielectric losses as well as the skin depth effect for accurate modeling. Our Objective is to study analytically the effect of embedded capacitance and the limitations of using high-k materials.

4.2.1. Analytical Relationship between Package Topology and Noise Suppression

The complex resonant frequencies for each mode of the package layer are extracted from Equation 4-2. For typical dimensions of IC packages such as microprocessors, the ratio $G_{mn}^2 L_{mn} / 4C_{mn}$ is much smaller than 1. For such case, the complex resonant frequencies of the package layer in S-domain (Laplace domain) reduce to:

$$S_{mn} = \sigma_{smn} \pm j\omega_{smn} = -\frac{G_{mn}}{2C_{mn}} \pm j\omega_{mn}\left(1 - \frac{G_{mn}^{2} L_{mn}}{8C_{mn}}\right)$$

Equation 4-3

where σ_{smn} and ω_{smn} represent the wave attenuation and phase constant respectively. Substituting L_{mn}, C_{mn}, and G_{mn} in Equation 4-3, the second term of the imaginary part is given by:

$$I = \frac{G_{mn}^2}{8C_{mn}}\sqrt{\frac{L_{mn}}{C_{mn}}} = \frac{ab\varepsilon\omega_{mn}}{8h}\left(\tan\delta + \frac{\delta_{smn}}{h}\right)^2$$

Equation 4-4

Equation 4-4 shows that both the dielectric losses and the skin depth are affecting the imaginary part of the resonant frequency. The normalized skin depth versus frequency is plotted in Figure 4.3 for a plane pair with the following parameters: $a = b = 4$ cm, $h = 114.3$ μm, and copper conductors. This figure indicates the range of frequencies where each type of loss term is dominant and where both of them need to be considered. If one of the terms is dominant over the other then Equation 4-4 can be rewritten as:

$$I \cong \begin{Bmatrix} \dfrac{ab\,\varepsilon}{4h^3\mu\sigma} & \tan\delta << \delta_{smn}/h \\ \dfrac{ab\,\varepsilon\omega_{mn}}{8h}(\tan\delta)^2 & \tan\delta >> \delta_{smn}/h \end{Bmatrix}$$

Equation 4-5

For the typical dimensions and materials used in microprocessor packages, the computed value of I is always close to few Hertz ($I << \omega_{mn}$). Therefore, the complex resonant frequencies are approximated as:

$$S_{mn} = -\frac{G_{mn}}{2C_{mn}} \pm j\omega_{mn}$$

Equation 4-6

Substituting C_{mn} and G_{mn} in Equation 4-6, the wave attenuation constant σ_{smn} is then expressed as:

$$\sigma_{smn} = -\frac{\omega_{mn}}{2}\left(\tan\delta + \frac{\delta_{smn}}{h}\right)$$

Equation 4-7

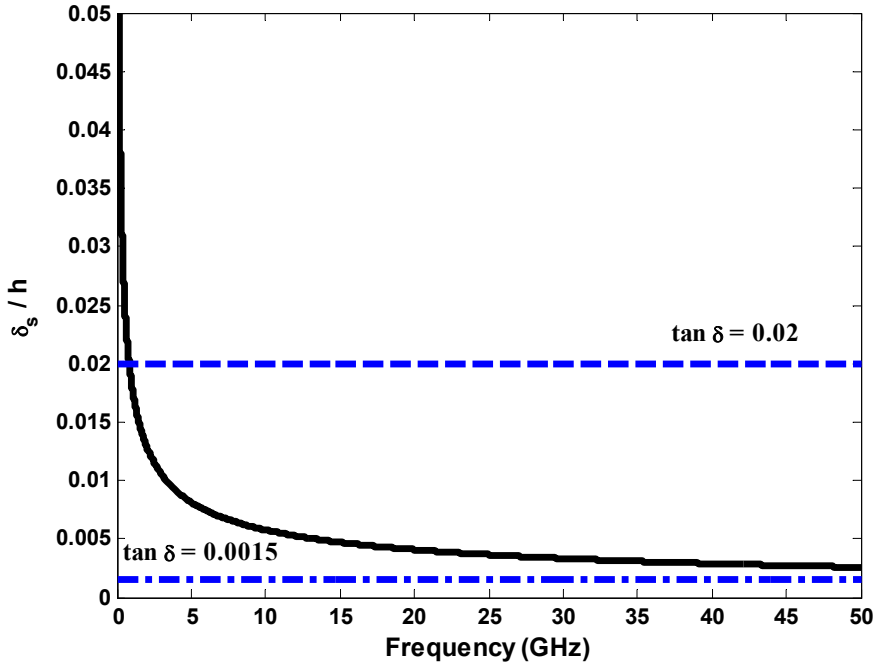

Figure 4.3. Normalized skin depth versus frequency for a single plane pair in the package shown in Figure 4.1. The dimensions of the layer are: a = b = 4 cm, h = 114.3 μm, and $\sigma = 5.8\times10^{7}$ S/m.

Equation 4-7 shows that increasing the dielectric losses or decreasing the dielectric thickness h, will lead to increase of the wave attenuation constant approximately at

the resonant frequency ω_{mn}. If any of the terms in Equation 4-7 is dominant over the other, we can rewrite Equation 4-7 as:

$$\sigma_{smn} = \begin{cases} -\dfrac{\omega_{mn}\,\delta_{smn}}{2h} & \tan\delta << \dfrac{\delta_{smn}}{h} \\ -0.5\,\omega_{mn}\tan\delta & \tan\delta >> \dfrac{\delta_{smn}}{h} \end{cases}$$

Equation 4-8

Thus, for dielectrics where the loss tangent is much smaller than the normalized skin depth, the wave attenuation constant becomes inversely proportional to the layer separation *h*. Conversely, if the loss tangent is much larger than the normalized skin depth, the wave attenuation constant becomes directly proportional to the loss tangent. Shrinking the thickness of dielectric between the metallic layers and/or increasing dielectric loss lead to suppress of the EMI noise at the resonant frequencies.

Including both, the dielectric losses and skin depth effect, and rearranging Equation 4-2, the mutual impedance can be expressed as:

$$Z_{ij}(\omega) = \sum_{n=0}^{N}\sum_{m=0}^{M}\Gamma_{ijmn}\frac{h}{\varepsilon}\left(\frac{\omega_{mn}\left(\tan\delta+\frac{\delta_{smn}}{h}\right)}{\omega_{mn}^2\left(\tan\delta+\frac{\delta_{smn}}{h}\right)^2+\omega^2F_{cmn}^2(\omega)}+j\frac{\omega F_{cmn}(\omega)}{\omega_{mn}^2\left(\tan\delta+\frac{\delta_{smn}}{h}\right)^2+\omega^2F_{cmn}^2(\omega)}\right)$$

Equation 4-9

where

$\Gamma_{ijmn} = \dfrac{\varepsilon_n^2\varepsilon_m^2}{ab}\cos(m\pi x_i/a)\cos(n\pi y_i/b)\cos(m\pi x_j/a)\cos(n\pi y_j/b)$ and

$F_{cmn}(\omega) = \omega_{mn}^2/\omega^2 - 1$.

The real part of mutual impedance at the resonant frequency of the (m_k, n_k) mode is:

$$Real\left\{Z_{ij}(\omega_{m_k n_k})\right\} = \left(\frac{\Gamma_{ijm_k n_k}}{\omega_{m_k n_k}\left(\tan\delta + \frac{\delta_{sm_k n_k}}{h}\right)} + \sum_{n=0}^{N}\sum_{m=0}^{M}{}_{(m,n)\neq(m_k,n_k)} \frac{\Gamma_{ijmn}\omega_{mn}\left(\tan\delta + \frac{\delta_{smn}}{h}\right)}{\omega_{mn}^2\left(\tan\delta + \frac{\delta_{smn}}{h}\right)^2 + \omega_{m_k n_k}{}^2 F_{cmn}^2\left(\omega_{m_k n_k}\right)} \right)\frac{h}{\varepsilon}$$

Equation 4-10

If we assume that the resonant frequencies of the different modes are distant enough, then we can neglect effects of mutual coupling between different modes. So, at each resonant frequency, the effect of the self resonant frequency on the real part of impedance is much larger than the effect of the resonant frequencies of other modes. The second term in Equation 4-10 which represents all the mutual coupling terms is neglected compared to the first term. The real part of the mutual impedance of the resonant frequency $\omega_{m_k n_k}$ is approximated as:

$$Real\left\{Z_{ij}(\omega_{m_k n_k})\right\} \cong \frac{h}{\varepsilon}\frac{\Gamma_{ijm_k n_k}}{\omega_{m_k n_k}\left(\tan\delta + \frac{\delta_{sm_k n_k}}{h}\right)}$$

Equation 4-11

Similarly, the imaginary part of the mutual impedance at the resonant frequency of the (m_k,n_k) mode can be written as:

$$Imag\left\{Z_{ij}(\omega_{m_k n_k})\right\} = \frac{h}{\varepsilon\omega_{m_k n_k}}\sum_{n=0}^{N}\sum_{m=0}^{M}{}_{(m,n)\neq(m_k,n_k)} \frac{F_{cmn}\left(\omega_{m_k n_k}\right)\Gamma_{ijmn}}{\frac{\omega_{mn}^2}{\omega_{m_k n_k}^2}\left(\tan\delta + \frac{\delta_{smn}}{h}\right)^2 + F_{cmn}^2\left(\omega_{m_k n_k}\right)}$$

Equation 4-12

At each resonant frequency of the (m_k,n_k) mode, the self resonant frequency does not contribute to the imaginary part of the mutual impedance in Equation 4-12. The contribution of the other resonant frequencies to the double summation can be

estimated as follows. Let us define the ratio $\omega_{mn}/\omega_{m_k n_k}$ to be equal *x*. Then the argument of the sum in Equation 4-12 is expressed as:

$$f(x) = \frac{\gamma\left(x^2 - 1\right)}{(\alpha_1 x + \alpha_2\sqrt{x})^2 + \beta\,(x^2-1)^2}.$$

Where $\alpha_1 = \tan\delta\sqrt{\frac{ab\varepsilon}{h\varepsilon_n{}^2\varepsilon_m{}^2}}$, $\alpha_2 = \sqrt{\frac{2ab\,\varepsilon}{h^3\mu\sigma\varepsilon_n{}^2\varepsilon_m{}^2\omega_{m_k n_k}}}$, and $\beta = \frac{ab\,\varepsilon}{h\,\varepsilon_n{}^2\varepsilon_m{}^2}$.

The practical dimensions and materials of the microprocessor packages imply the following conditions:

$$|\gamma| = \left|\frac{\Gamma_{ijmn}\,ab}{\omega_{m_k n_k}\varepsilon_n{}^2\varepsilon_m{}^2}\right| << 1,\ \alpha_1 << 1,\ \alpha_2 << 1, \text{ and } \beta << 1.$$

If the condition $\sqrt{\beta}\left(x^2-1\right) >> \alpha_1 x + \alpha_2\sqrt{x}$ is satisfied then we have two different approximations for the function *f*. The first approximation is: $|f(x)| \cong \left|\frac{\gamma}{\beta\,(x^2-1)}\right| << 1$ if $\beta\left(x^2-1\right) >> |\gamma|$. Therefore, the effect of high order resonant frequency modes on the (m_k,n_k) mode can be ignored. The second approximation is: $|f(x)| \cong |\gamma/\beta| \le \frac{h\,\varepsilon_n{}^2\varepsilon_m{}^2}{\omega_{m_k n_k} ab\ \varepsilon}$ for the lower-order resonant frequencies ($x << 1$). This value can be very small using high-k thin dielectric. Thus only around $x = 1$, $f(x) \neq 0$. Therefore, with the assumption: 1) the resonant modes are not coupled to each other, and 2) the filling between layers is high permittivity, thin dielectric, it can be concluded that:

$$Imag\left(Z_{ij}(\omega_{m_k n_k})\right) \cong 0$$

Equation 4-13

From Equation 4-11 and Equation 4-13, the mutual impedance at the frequency $\omega_{m_k n_k}$ is represented as:

$$Z_{ij}(\omega_{m_k n_k}) \cong \frac{h\,\Gamma_{ijm_k n_k}}{\varepsilon\omega_{m_k n_k}\left(\tan\delta + \frac{\delta_{sm_k n_k}}{h}\right)}$$

Equation 4-14

Validity of above mentioned assumptions through selection of dielectric material and its thickness in a package layer leading to approximate formula Equation 4-14 are studied through numerical examples. The magnitude, the real part, and the imaginary part of input and trans-impedances shown respectively by (a), (b), and (c) for a single plane pair defined in Figure 4.1 are illustrated in Figure 4.4 - Figure 4.9 for the three different configurations. The solid line shows the actual value of impedance obtained by Equation 4-2 in the total frequency range under consideration. The square symbol shows the actual value of impedance at the resonant modes of a plane pair. The star symbol shows the approximate value of impedance at resonant modes obtained from Equation 4-11, Equation 4-13, and Equation 4-14. In the first configuration, FR-4 with thickness equal to 200 μm is used. Figure 4.4 shows the input impedance at port 2, Z_{22}. Figure 4.5 shows the trans-impedance between port 1 and 2, Z_{21}. In the second configuration, a dielectric with permittivity equal to 140, loss tangent equal to 0.0015, and thickness equal to 200 μm is used. Figure 4.6 shows Z_{22} and Figure 4.7 shows Z_{21}. In the third configuration, a dielectric with permittivity equal to 140, loss tangent equal to 0.0015, and thickness equal to 100 μm is used. Figure 4.8 shows Z_{22} and Figure 4.9 shows the Z_{21}. These results show that the approximation for the real part of the impedance, (Equation 4-11), works well.

Neglecting the imaginary part at resonant modes (Equation 4-13) leads to an error in the actual value of the magnitude of the impedance. However, this error at excited resonant modes is negligibly small (the excited modes are defined by the location of the port in the package layer). In other words, at the excited resonant frequencies which are shown by local peaks at the magnitude of impedance graph (or more correctly the frequency at which the imaginary part of impedance is equal to zero), the approximate expression for the impedance (Equation 4-14) estimates the acceptable impedance. At other resonant modes (the ones that are not excited), the value of the impedance is expressed by the coupling effects. It means other adjacent modes which are not vanished at the frequency of interest contribute to the value of impedance.

Equation 4-14 indicates that the mutual impedance at each resonant frequency mode is decreased by reducing the separation between the planes, h, increasing the permittivity of the dielectric, ε, or increasing the loss tangent of the dielectric. Again two cases for approximating Equation 4-14 occur: If $\tan\delta << \delta_{sm_kn_k}/h$, then Equation 4-14 simplifies to: $Z_{ij}(\omega_{m_kn_k}) \cong \left(h^2\Gamma_{ijm_kn_k}\right)/\left(\varepsilon\omega_{m_kn_k}\delta_{sm_kn_k}\right)$. This means that $Z_{ij}(\omega_{m_kn_k}) \propto h^2$ and $Z_{ij}(\omega_{m_kn_k}) \propto \varepsilon^{-0.75}$. If $\tan\delta >> \delta_{sm_kn_k}/h$ then $Z_{ij}(\omega_{m_kn_k}) \cong \left(h\Gamma_{ijm_kn_k}\right)/\left(\varepsilon\omega_{m_kn_k}\right)$. Thus, $Z_{ij}(\omega_{m_kn_k}) \propto h$ and $Z_{ij}(\omega_{m_kn_k}) \propto \varepsilon^{-0.5}$.

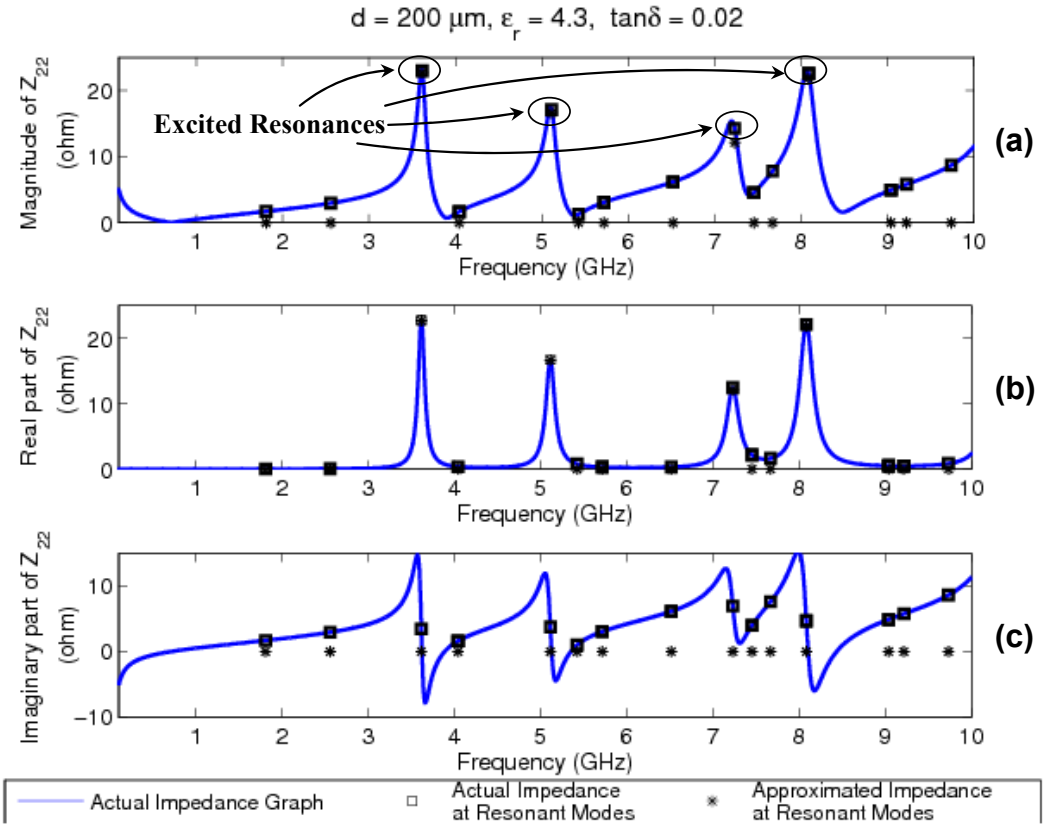

Figure 4.4. (a) Magnitude, (b) real part, and (c) imaginary part of input impedance at port 2 for the package shown in Figure 4.1. The plane separation is h = 200 μm and dielectric material is FR-4. The Impedance from Equation 4-2 is plotted by the solid line. The impedance value at the resonant modes of a plane pair is marked by square symbol. The approximate value of impedance from Equation 4-11, Equation 4-13, and Equation 4-14 is marked by star symbol.

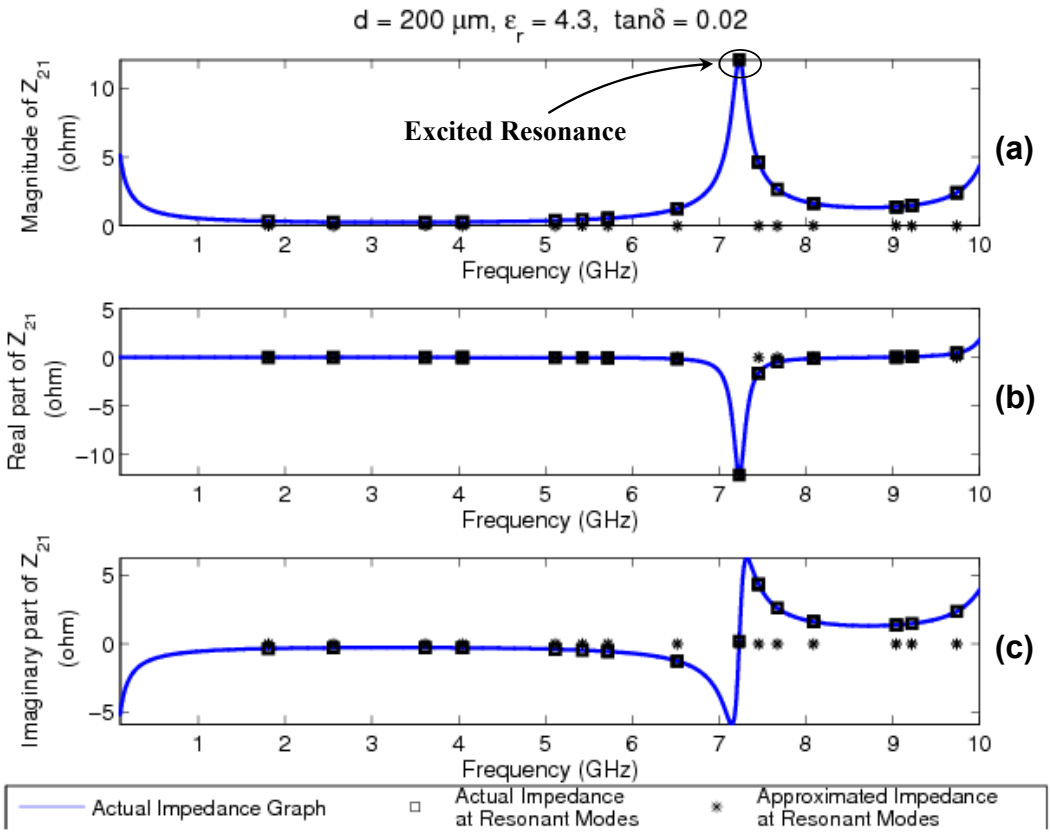

Figure 4.5. (a) Magnitude, (b) real part, and (c) imaginary part of trans-impedance between ports 1 and 2 for the package shown in Figure 4.1. The plane separation is *h* = 200 μm and dielectric material is FR-4. The Impedance from Equation 4-2 is plotted by the solid line. The impedance value at the resonant modes of a plane pair is marked by square symbol. The approximate value of impedance from Equation 4-11, Equation 4-13, and Equation 4-14 is marked by star symbol.

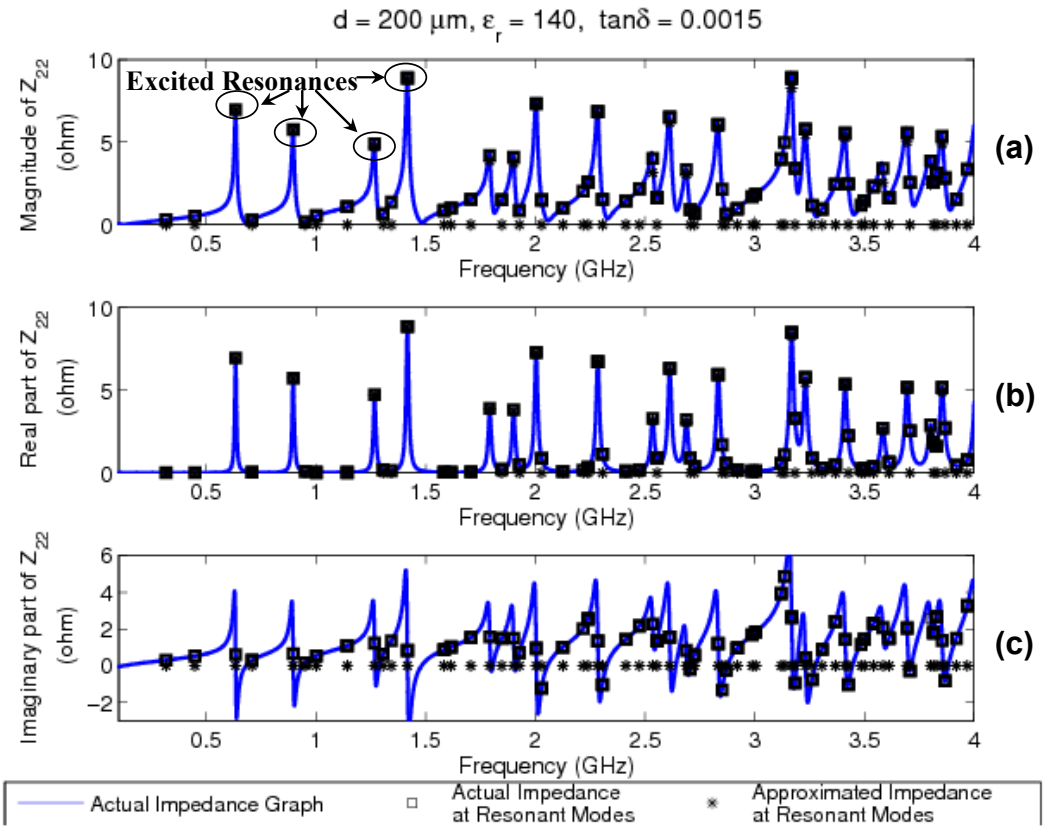

Figure 4.6. (a) Magnitude, (b) real part, and (c) imaginary part of input impedance at port 2 for the package shown in Figure 4.1. The plane separation is h = 200 μm and dielectric material has permittivity of 140 and loss tangent of 0.0015. The Impedance from Equation 4-2 is plotted by the solid line. The impedance value at the resonant modes of a plane pair is marked by square symbol. The approximate value of impedance from Equation 4-11, Equation 4-13, and Equation 4-14 is marked by star symbol.

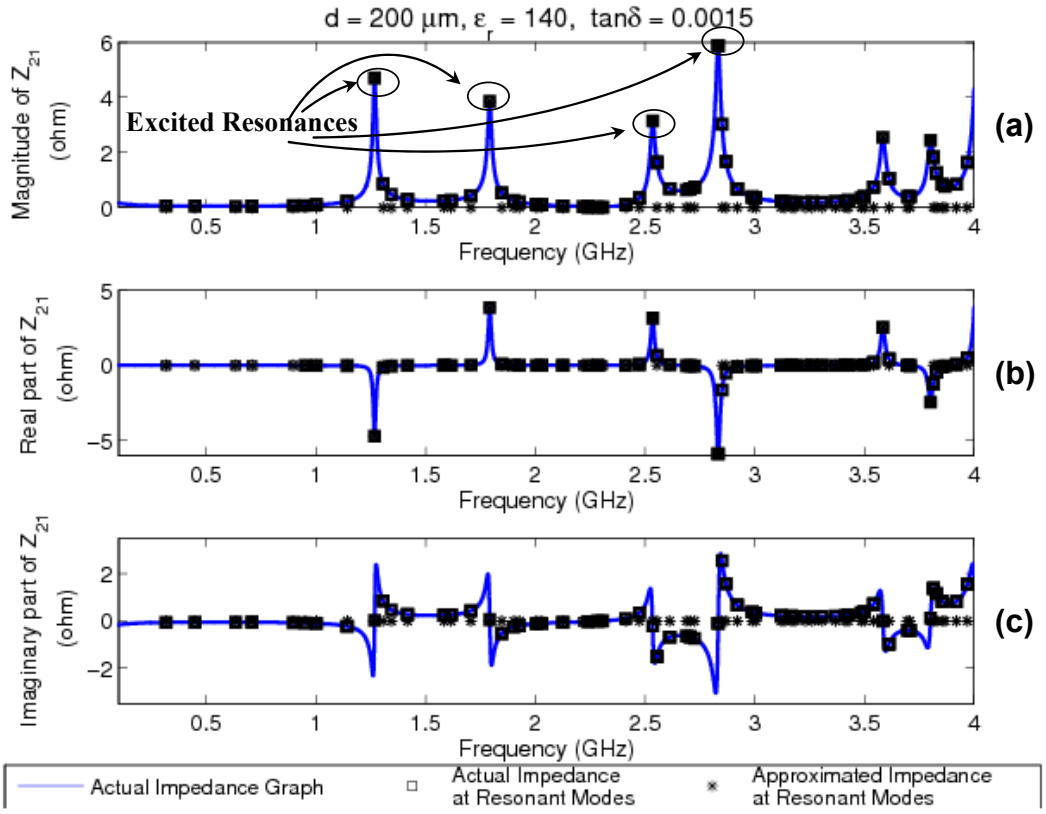

Figure 4.7. (a) Magnitude, (b) real part, and (c) imaginary part of trans-impedance between ports 1 and 2 for the package shown in Figure 4.1. The plane separation is *h* = 200 μm and dielectric material has permittivity of 140 and loss tangent of 0.0015. The Impedance from Equation 4-2 is plotted by the solid line. The impedance value at the resonant modes of a plane pair is marked by square symbol. The approximate value of impedance from Equation 4-11, Equation 4-13, and Equation 4-14 is marked by star symbol.

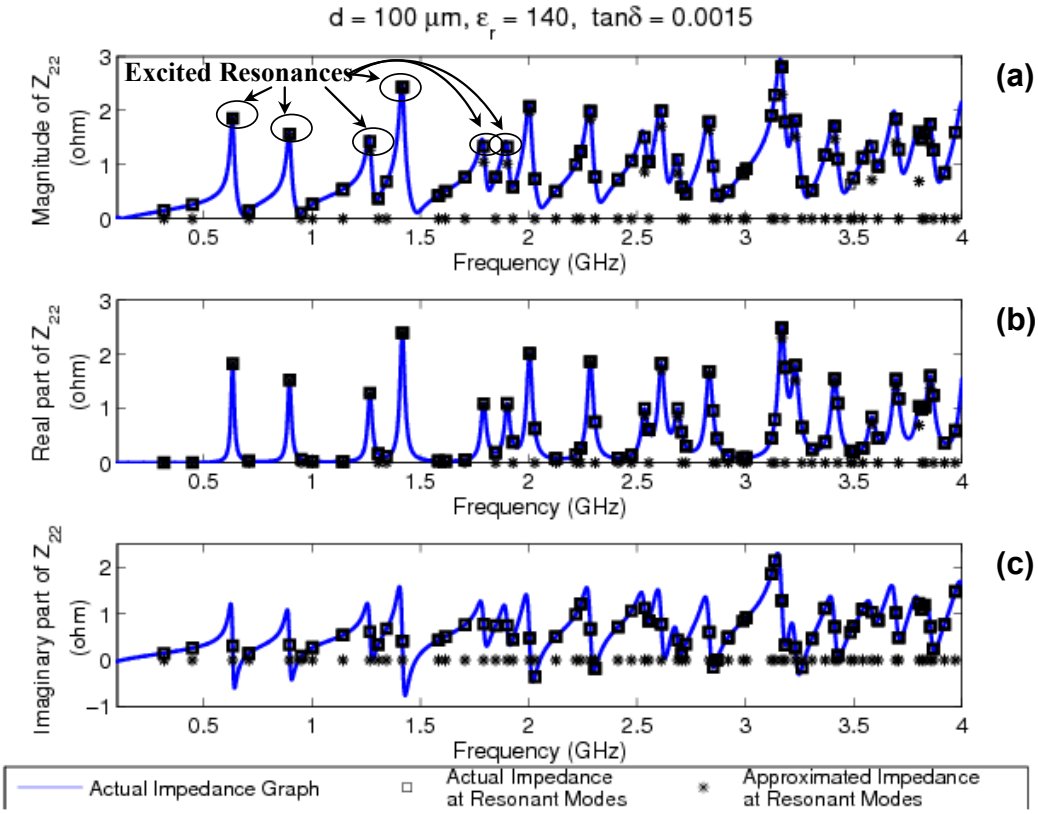

Figure 4.8. (a) Magnitude, (b) real part, and (c) imaginary part of input impedance at port 2 for the package shown in Figure 4.1. The plane separation is h = 100 μm and dielectric material has permittivity of 140 and loss tangent of 0.0015. The Impedance from Equation 4-2 is plotted by the solid line. The impedance value at the resonant modes of a plane pair is marked by square symbol. The approximate value of impedance from Equation 4-11, Equation 4-13, and Equation 4-14 is marked by star symbol.

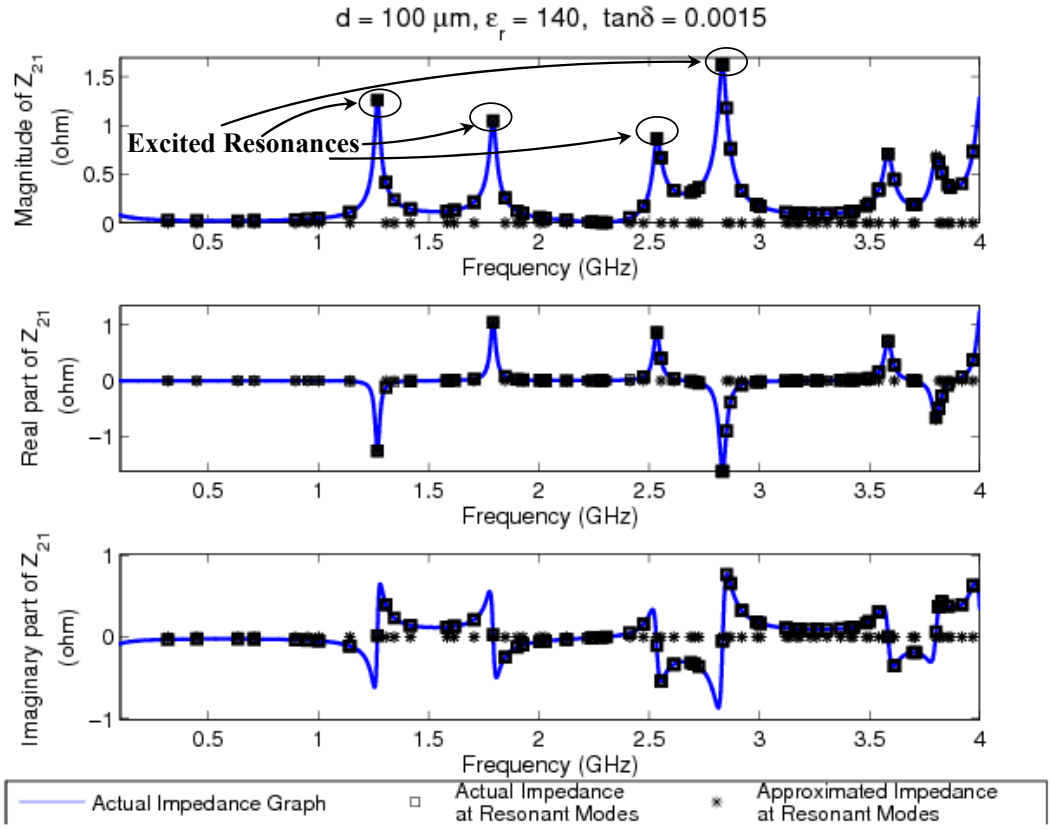

Figure 4.9. (a) Magnitude, (b) real part, and (c) imaginary part of trans-impedance between ports 1 and 2 for the package shown in Figure 4.1. The plane separation is *h* = 100 μm and dielectric material has permittivity of 140 and loss tangent of 0.0015. The Impedance from Equation 4-2 is plotted by the solid line. The impedance value at the resonant modes of a plane pair is marked by square symbol. The approximate value of impedance from Equation 4-11, Equation 4-13, and Equation 4-14 is marked by star symbol.

Therefore, in IC packages similar to PCB packages [14], [15], three factors contribute to noise suppression: Decreasing the thickness of the package, increasing the permittivity of the dielectric material of the package, or increasing the loss in the dielectrics. However, increasing loss is not an optimum solution for EMI and SSN noise suppression. The heat generated due to losses needs to be transferred out of the package, otherwise the performance of electronic circuit degrades and other types of noise related to heating of the circuit increases. Another drawback of using high-loss substrates is the decrease in the bandwidth of signal traces which is a concern for high data transfers rates in the future generation of microprocessors [65]. Overall, the embedded capacitance method does not eliminate EM wave in any frequency range. Decoupling level depends to the limitations in fabrication techniques, such as: limitation in using different dielectric materials and minimum isolation distance between two metallic layers (dielectric thickness).

4.2.2. Case Studies

We follow our study on microprocessor package. In present microprocessor packaging technology, the typical dimension of a package is approximately 4 cm × 4 cm. The height of layers is varying from tens of μm to hundreds of μm. Conductors are made of copper. The permittivity of the filling dielectric is 4.3. The speed of the processor is less than 4 GHz. Without any loss of generality, these practical dimensions are used in the numerical experiments provided here. The goal here is to provide a solution to minimize the EMI within a broad-band of frequencies including the operating frequency of the microprocessor and the package resonant frequencies.

To this end, we focus on the impedance parameters of two interconnects located within the package (see the ports in Figure 4.1). The first interconnect (port) is located at (x_1 = 1 cm, y_1 = 1 cm). The second one is located at (x_2 = 2 cm, y_2 = 2 cm).

The magnitude of the input impedance at port 2 and the trans-impedance between the two ports, for two different cases h =100, 200 μm are shown in Figure 4.10. The first three resonances are marked with different symbols in the plot and table. The similar symbols in each graph show corresponding resonances. As can be seen from the tables, the corresponding resonance frequencies have changed slightly which is expected from ω_{smn} in Equation 4-3. Here, ω_{mn} is not function of h, and I (defined in Equation 4-4) is function of h but it is negligibly small. Figure 4.10 shows for the second case (case with larger h), the magnitude of impedance has decreased at resonances. Figure 4.11 and Figure 4.12 show the magnitude of trans-impedance between the ports and input impedance at port 2, respectively, for three different cases: (ε_r = 4.3, tan δ = 0.02), ε_r = 30, tan δ = 0.02), and (ε_r = 30 and tan δ = 0.0015). For these three cases, the dielectric thickness h = 150 μm. In Figure 4.11 and Figure 4.12, a couple of lower frequencies are marked with different symbols in the plot and table. In each plot, similar symbols on the curves show the corresponding resonances. For the second and third cases the resonant frequencies are shifted to lower values by the approximate ratio $\sqrt{\{\varepsilon_{r1} / (\varepsilon_{r2} \text{ or } \varepsilon_{r3})\}}$ = 0.3786 using ω_{smn} in Equation 4-3 where ω_{smn} is inversely proportional to square root of permittivity. I is function of ε and loss tangent but it is negligibly small. Those slight differences in resonance frequencies between the second and third case are due to the differences in the loss tangent. At the corresponding resonant frequencies in the second case which has same loss

tangent as the first one, the decrease of the magnitude of the impedance by increasing ε_r is obvious in both figures. In the third case, we have increased the permittivity but decreased loss tangent in comparison to the first case which is inefficient in suppressing the magnitude of impedance at resonances.

The progress in material science provides composite dielectrics with very high permittivity ($\varepsilon_r \geq 100$) known as high-k dielectrics. In fact, several companies have started commercially producing such material with low loss. Those dielectrics are the one referred to during our analysis henceforth. They provide effective embedded capacitance for interference noise filtering in the packaging technologies. This fact is shown in Figure 4.13 (a) and (b) which respectively presents the input impedance at port 2 and the trans-impedance between ports in the package under study for three different cases of ($\varepsilon_r = 4.3$, $\tan \delta = 0.02$, $h = 200$ μm), ($\varepsilon_r = 100$, $\tan \delta = 0.0015$, $h = 100$ μm), and ($\varepsilon_r = 140$, $\tan \delta = 0.0015$, $h = 50$ μm). The specifications of the high-k dielectrics used here are obtained from [66]. As shown in Figure 4.13, the combination of parameters for the third case has provided the lowest maximum of magnitude of impedance in the entire band which leads to decrease in interference. Generally by using this method, the resonances with the decreased magnitude shift to lower frequencies.

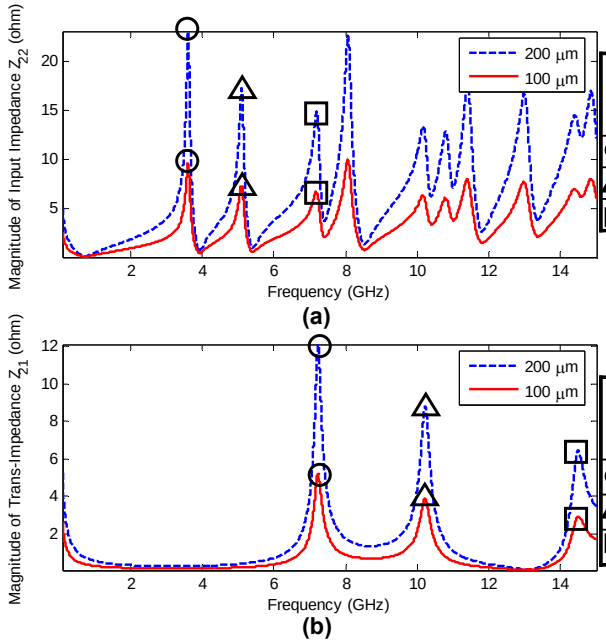

F (GHz)	Z_{22} (ohm) at $h = 200$ μm	F (GHz)	$\|Z_{22}\|$ (ohm) at $h = 100$ μm
3.609	23.14	3.607	9.603
5.101	17.3	5.097	7.392
7.201	14.9	7.191	6.733

F (GHz)	Z_{21} (ohm) at $h = 200$ μm	F (GHz)	$\|Z_{21}\|$ (ohm) at $h = 100$ μm
7.232	12.1	7.232	5.204
10.22	8.79	10.22	3.854
14.49	6.462	14.5	2.895

Figure 4.10. Magnitude of (a) input impedance at port 2, and (b) trans-impedance between ports 1 and 2 for the package shown in Figure 4.1. Impedances are provided for two different configurations. The impedance for plane separation h = 200 μm is plotted by the dashed line and the impedance for h = 100 μm is plotted by the solid line. The first three resonances are marked with different symbols in the plot and table. The similar symbols in each graph show the corresponding resonances.

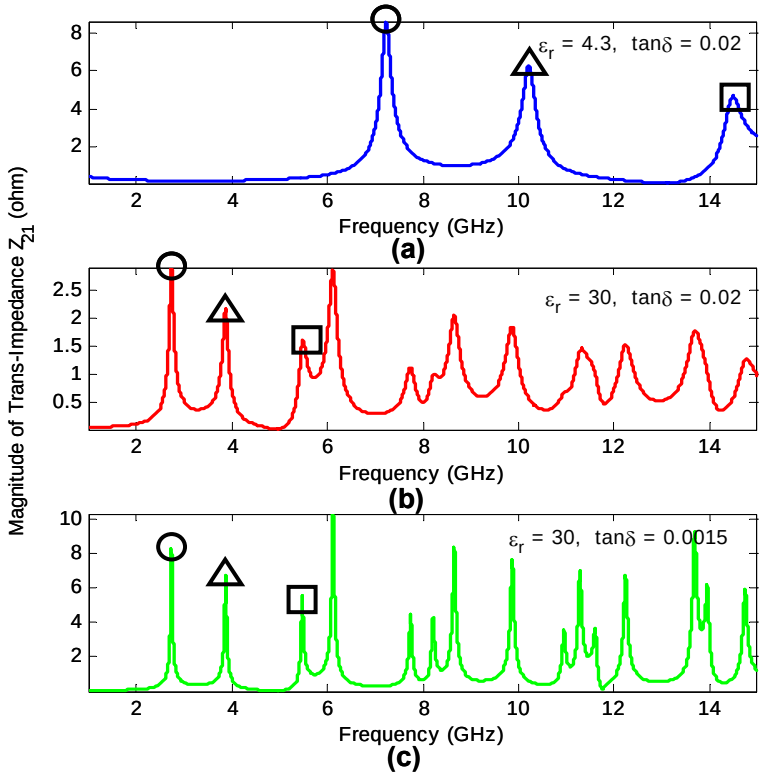

(a)		(b)		(c)	
F (GHz)	$\|Z_{21}\|$ (ohm)	F (GHz)	$\|Z_{21}\|$ (ohm)	F (GHz)	$\|Z_{21}\|$ (ohm)
○ 7.232	8.609	○ 2.738	2.887	○ 2.738	8.277
△ 10.22	6.295	△ 3.869	2.144	△ 3.871	6.767
□ 14.49	4.666	□ 5.492	1.616	□ 5.476	5.518

Figure 4.11. Magnitude of trans-impedance between ports 1 and 2 for the package under study shown in Figure 4.1. The impedance is illustrated for three different configurations: (a) ($\varepsilon_r = 4.3$, tan $\delta = 0.02$), (b) ($\varepsilon_r = 30$, tan $\delta = 0.02$), and (c) ($\varepsilon_r = 30$, tan $\delta = 0.0015$). In all configurations, the plane separation is h = 150 μm. The first three resonances are marked with different symbols in the plot and table. The similar symbols on the curves show the corresponding resonances.

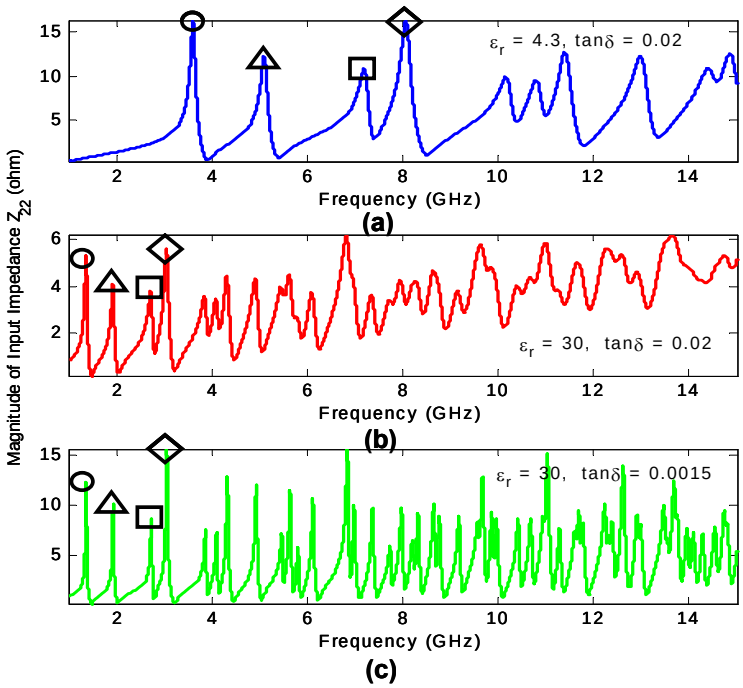

(a)		(b)		(c)	
F (GHz)	$\|Z_{22}\|$ (ohm)	F (GHz)	$\|Z_{22}\|$ (ohm)	F (GHz)	$\|Z_{22}\|$ (ohm)
○ 3.608	16.24	○ 1.365	5.309	○ 1.368	12.32
△ 5.099	12.28	△ 1.929	4.107	△ 1.935	10.18
□ 7.193	10.82	□ 2.721	3.782	□ 2.734	8.687
◇ 8.066	16.31	◇ 3.052	5.559	◇ 3.059	15.63

Figure 4.12. Magnitude of input impedance at port 2 for the package under study shown in Figure 4.1. The impedance is illustrated for three different configurations: (a) ($\varepsilon_r = 4.3$, tan $\delta = 0.02$), (b) ($\varepsilon_r = 30$, tan $\delta = 0.02$), and (c) ($\varepsilon_r = 30$, tan $\delta = 0.0015$). In all configurations, the plane separation is h = 150 μm. The first four resonances are marked with different symbols in the plot and table. The similar symbols on the curves show the corresponding resonances.

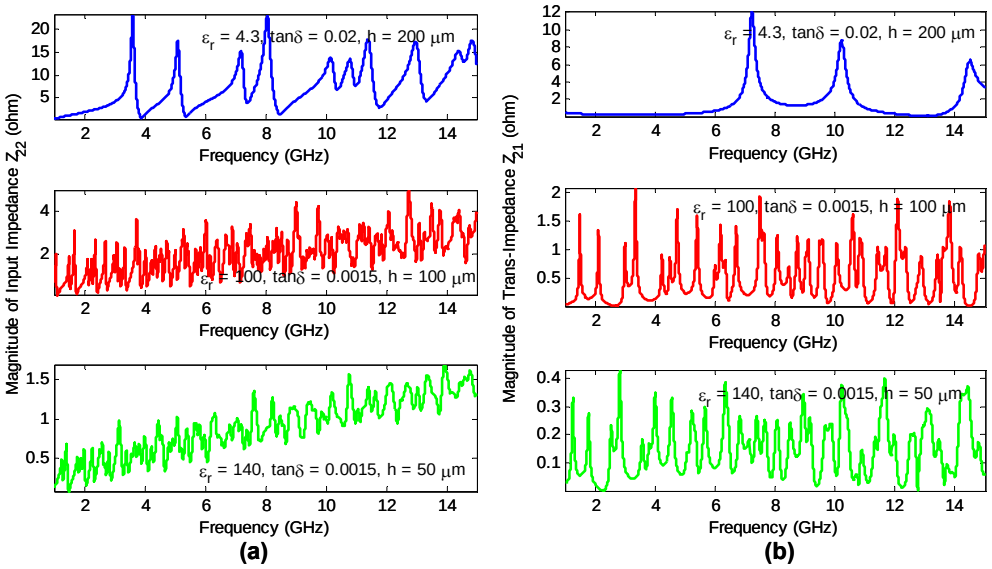

Figure 4.13. Magnitude of (a) input impedance at port 2, and (b) trans-impedance between ports 1 and 2 for the package under study shown in Figure 4.1. The impedance is illustrated for three different cases of (ε_r = 4.3, tan δ = 0.02, h = 200 μm), (ε_r = 100, tan δ = 0.0015, h = 100 μm), and (ε_r = 140, tan δ = 0.0015, h = 50 μm).

Chapter 5 : Application of EBG Structures

In the following sections we will demonstrate effectiveness of implementing EBG structures in few applications categorized under "*EMI Reduction*" and "*Design of Low Profile Antenna*".

5.1. EMI Reduction

Under this category, we will study the advantages of using EBG structures for the suppression of EM noise. Suggested applications are:

- Reduction of EMI in Enclosures and Chassis using the EBG Structures
- Reduction of EMI Coupling between Cavities and Antennas using EBG Structures
- EMI and SSN Noise Mitigation in IC Packages using Miniaturized Planar EBGs

5.1.1. Reduction of EMI in Enclosures and Chassis using the EBG Structures

In enclosures and chassis, the mechanism of coupling between an internal electromagnetic source and the external electromagnetic environment takes place either by direct penetration of electromagnetic fields through openings or through induced currents on conducting surfaces. Currents on the internal walls supporting the fields inside the enclosure can travel out through openings and apertures to outside walls. Once these currents reach external surfaces or the currents induced by external fields on outer walls, they travel and penetrate other cavities sharing the same surface and create fields in these so-called victim cavities. A highly effective way to prevent

the field coupling as described is proposed here. This consists of employing EBG patches, which play a critical role in an important class of EMI/EMC applications [4], [19]-[28], [67]-[70], [71], on the surface of the structure thus blocking the flow of surface currents. The proposed technique consists of surrounding the perimeter of critical openings and apertures of an enclosure or package with a ribbon of EBG surface designed around the frequency of interest as shown in Figure 5.1. The EBG structure acts as a band stop filter which eliminates the interfering surface currents arising from radiators.

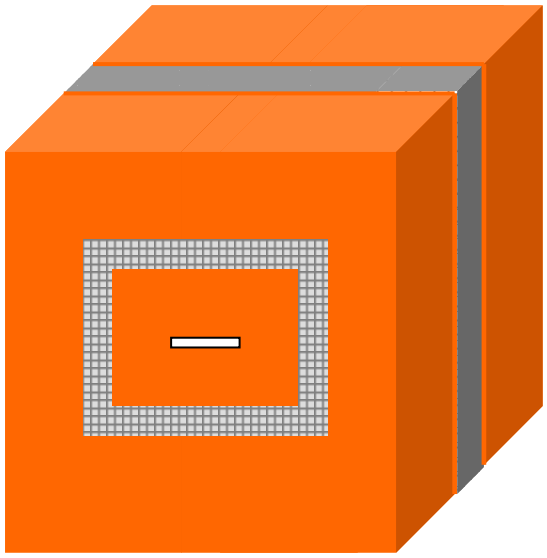

Figure 5.1. Enclosure cavity with two EBG ribbons.

5.1.1.A. *Modeling*

From a purely electromagnetic perspective, this set of problems can be described and modeled as coupling between antennas or radiators. Therefore, it is necessary primarily to determine the frequency ranges that are important for accurate

functioning of the system. Then, we need to design EBG structure that covers the frequency range of interest. This frequency band can be either narrowbnad, wideband or even consisting of multiple bands [20], [23], [24]. In our study, we use a simple form of EBG patterns known as mushroom structures which were discussed in 0.

5.1.1.B. *Numerical Case Study*

To demonstrate the effectiveness of this technique, two identical metallic boxes of sizes 80 mm × 160 mm × 60 mm are joined together as shown in Figure 5.2. Both boxes are completely closed except for one side of each box which has a 20 mm × 4 mm aperture in the middle as shown in Figure 5.2. A 10 mm probe is located inside of each box normal to the aperture. The probe is distant by 20 mm from corner in both *x* and *y* directions. The direction of the probe is parallel to the shorter side of the aperture (in order to maximize its coupling to the aperture). This setup ensures that any possible coupling between the two boxes is only through surface currents. (Perfectly conducting boxes are used in order to eliminate any field penetration through the skin. However, for the frequency range of interest, the skin depth is much smaller than the thickness of metals used in practical enclosures.)

This particular example represents a wide class of problems where coupling takes place between two separate compartments associated with a single chassis (common reference plane). In this chosen example, the emphasis is not on the type and geometry of excitation, but rather on the potential of EBG structures to reduce coupling through the suppression of surface waves. The frequency of significant coupling depends on several factors including the probe location and size, enclosure

and aperture dimensions. Here, we consider coupling in the 7-10 GHz frequency range. This range includes the frequency at which the apertures and probes are resonant (7.5 GHz).

The EBG structure chosen to suppress coupling in this example is picked up from those data obtained previously in Section 2.3, Figure 2.16, with ε_r of 2.2 and patch size of 4 mm. The effectiveness of the performance of the EBG ribbon can be gauged by considering the power coupling between the two different probes shown in Figure 5.2 (b). The power coupling between the two ports is proportional to the transmission coefficient S_{21}. Figure 5.3 shows simulation results for the entire structure in Figure 5.2 with and without the presence of the EBG ribbon. The width of the ribbon is 88 mm. The application of the EBG ribbon resulted in coupling reduction between the two probes within the operating frequency range of interest. Figure 5.4 shows the magnitude of S_{21} between two ports with and without the presence of EBG for a second studied case. The specifications of this structure are chosen from Section 2.3, Figure 2.16, with ε_r of 4.8 and patch size of 4 mm. This pattern is effective in reducing the EMI coupling in the frequency range 5.8 GHz to 9 GHz.

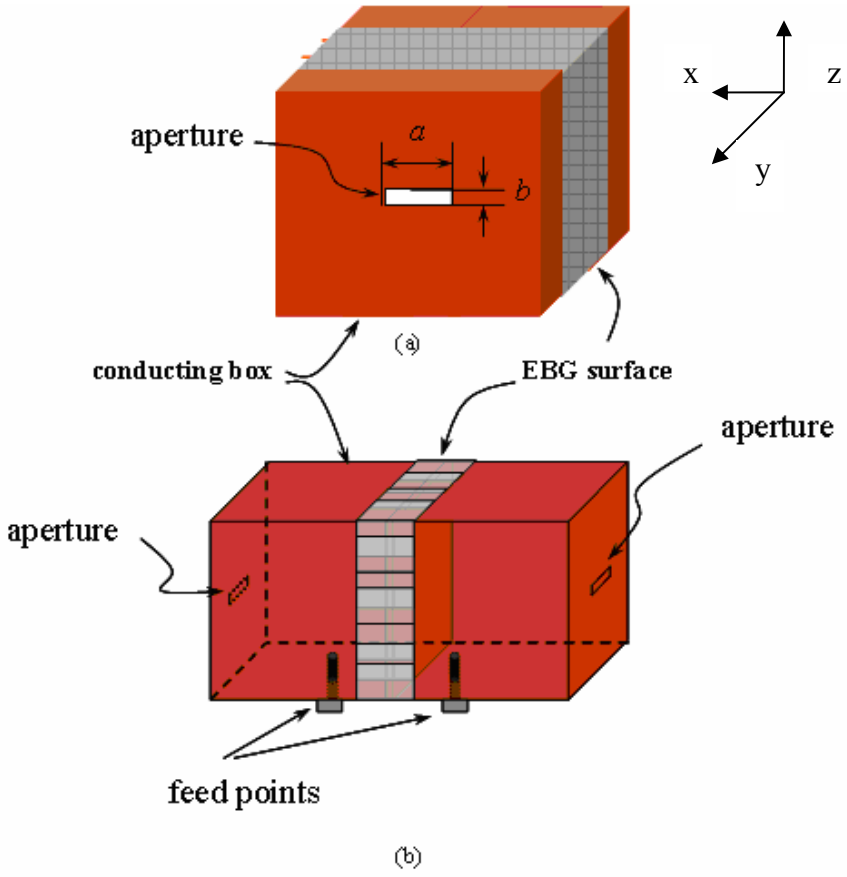

Figure 5.2. Schematic of two back-to-back perfectly conducting boxes. One of them contains the excitation probe and the second contains the receiver probe. Both of them have a small aperture in the middle of their external y-z plane with dimensions a= 20 mm, b= 4 mm. The EBG surface is placed as a ribbon completely surrounding the structure. (a) Front view. (b) Side view.

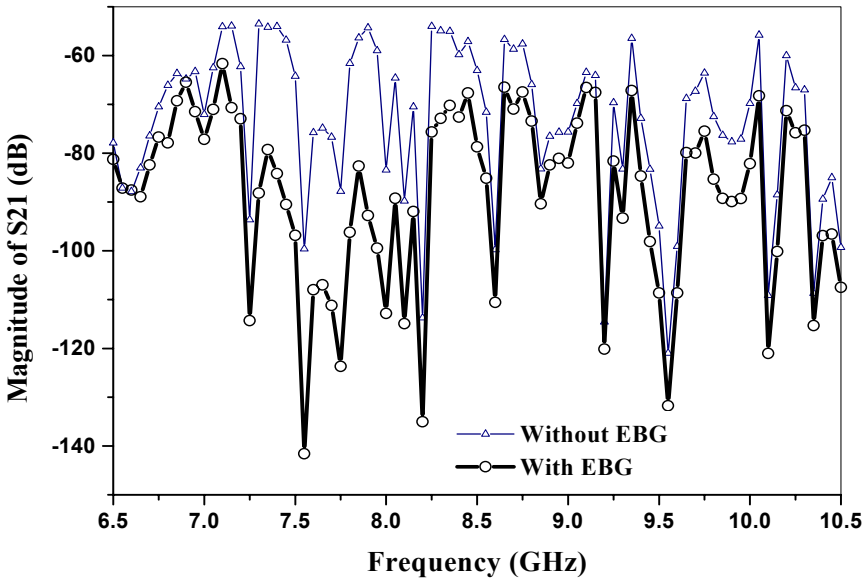

Figure 5.3. Magnitude of S_{21} between two probes positioned as shows in Figure 5.2 (b). The EBG structures consists of 4 × 4 mm patches with 0.4 mm gap and $\varepsilon_r = 2.2$.

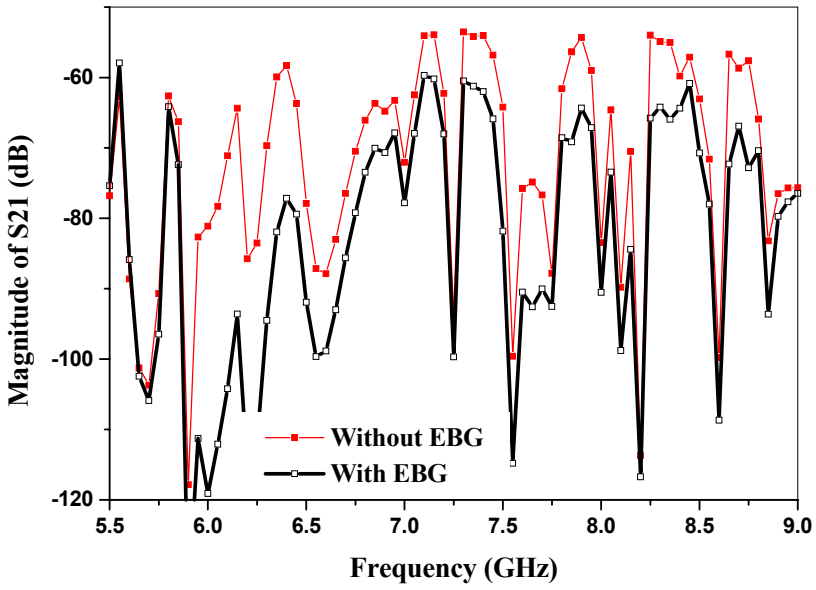

Figure 5.4. Magnitude of S_{21} between two probes positioned as shows in Figure 5.2 (b). The EBG structures consists of 4 × 4 mm patches with 0.4 mm gap and $\varepsilon_r = 4.8$.

5.1.2. Reduction of EMI Coupling between Cavities and Antennas using EBG Structures

Continuous advances in communication and electronic circuits increase the need for complicated systems with several electromagnetic sources that operate in the same environment such as array of antennas and different electronics in compartments of a chassis. The proximity of these radiation sources increases the probability of interference, or mutual coupling between them. To this end, we consider the case of two apertures or cavities sharing a common reference plane. More specifically, we consider the cavities as a constitutive part of Cavity-Backed Slot (CBS) antennas. CBS antennas have been used in space vehicles, satellites, radar and mobile telephony as they are easy to manufacture, small in size, and light weighted. In this study, we propose to implement EBG structures designed around the frequency of interest in the common surface between two cavities to reduce the coupling between them.

5.1.2.A. *Modeling*

In order to suppress surface current traveling between cavities, EBG structure is designed to cover the operating frequency of the cavity-backed antennas or the electronic systems located in cavities that are the compartments of chassis. EBG structure is designed using trial and error procedure educated by the data obtained from HFSS simulator mentioned in 0.

5.1.2.B. *Numerical Case Study*

The case study chosen here will be that of a two CBS antennas system discussed in detail in [7]. This two-antenna system is reproduced in Figure 5.5 and Figure 5.6. The common reference plane (Ground plane) is finite with dimension of 10 cm × 6 cm and antennas are separated from each other by 4 cm. The EBG surface is placed between the two antennas as shown in Figure 5.7.

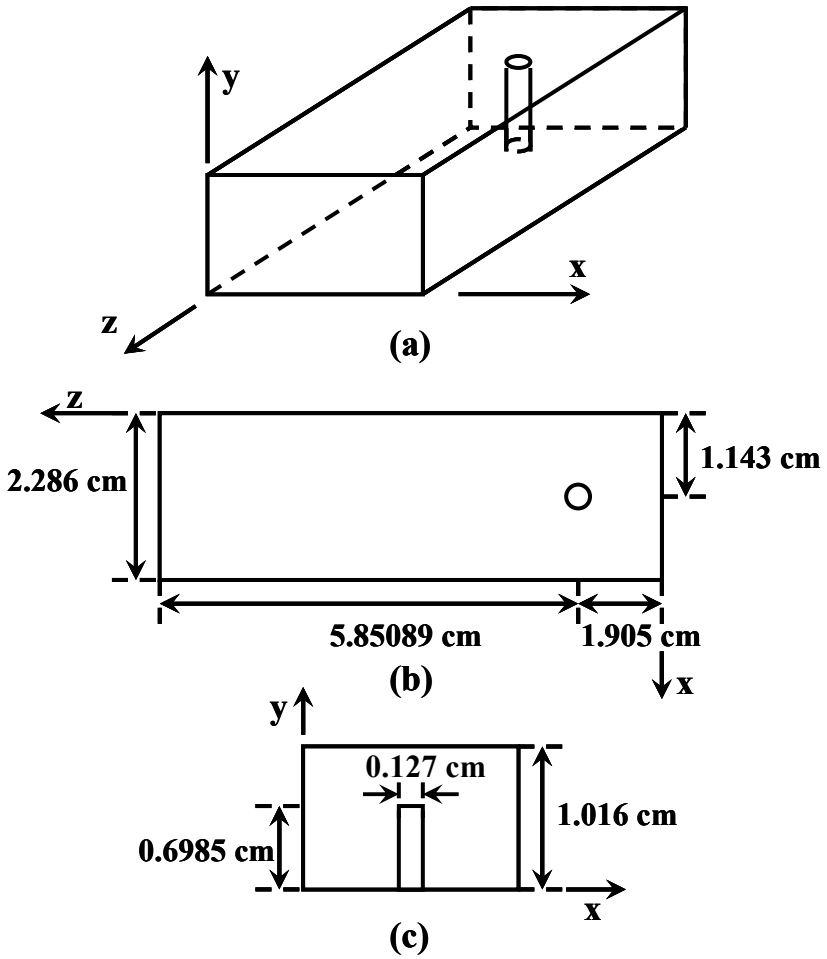

Figure 5.5. Air-filled rectangular cavity-backed antenna fed with a probe oriented in the *y*-direction. (a) 3-D view, (b) top view and (c) side view (*x*-*y* plane).

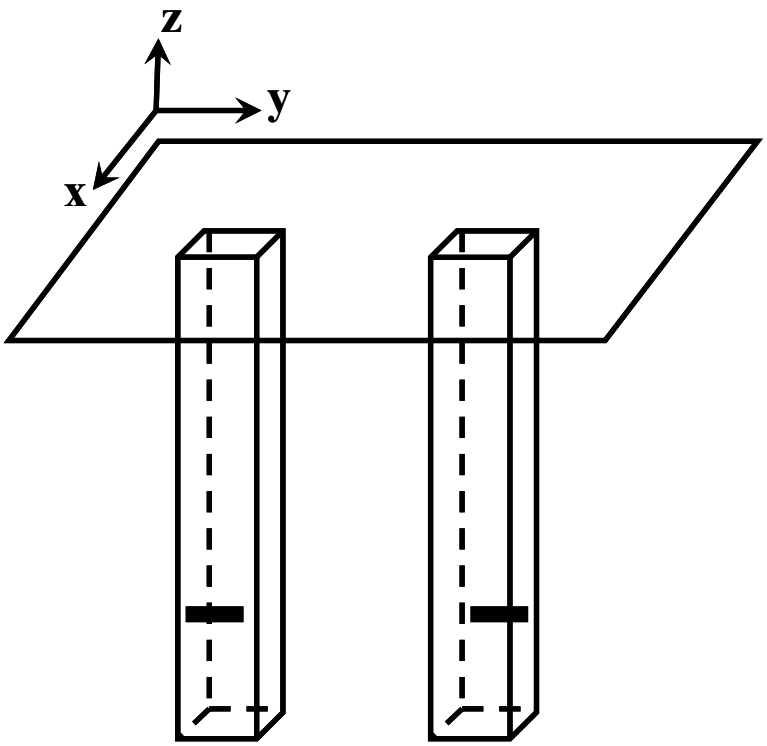

Figure 5.6. Three dimensional schematic diagram showing two identical cavity-backed antennas mounted on a rectangular ground plane. The structure of each antenna is as described in Figure 5.5.

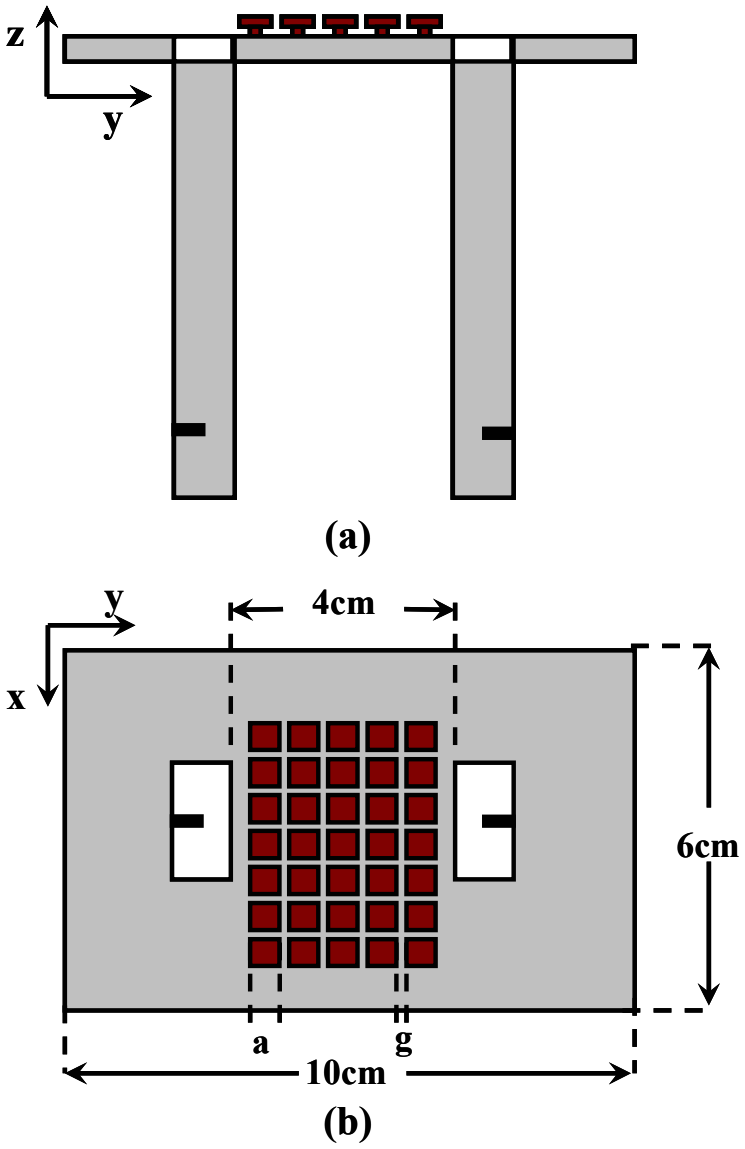

Figure 5.7. (a) Side view and (b) top view of a CBS antennas system showing the placement of the EBG patches.

In order to design an EBG structure having the desired characteristics, the CBS antenna system (the two antennas and ground plane) without the EBG structure is first simulated and its operational frequencies are derived. These frequencies correspond to the frequencies at which each antenna has its maximum power emission, in another words, they are the frequencies of minimum reflection, S_{11}. Figure 5.8 shows the result of this simulation and the resonant frequencies of antennas: 7.5 GHz, 10.7 GHz, and 12 GHz. It should be noted that since there is a strong reflection around 10.4 GHz (S_{11} is close to 0dB), the resonance at 10.7 GHz is not considered a working frequency both in [7] and in this work. For the other two operating frequencies, two designs are considered: an EBG structure with an effective operating frequency range from 7 GHz to 8 GHz, and another with an effective operating frequency range from 11.9 to 16 GHz. For the 7 GHz to 8 GHz range, we choose an EBG structure, henceforth referred to as Pattern 1, with 4 mm patch size and substrate permittivity $\varepsilon_r = 4.8$. For the 11.9 GHz to 16 GHz, we choose an EBG structure, henceforth referred to as Pattern 2, with 2.6 mm patch size and permittivity $\varepsilon_r = 3.0$. These designs were obtained using the method described in 0, where the data were shown in Figure 2.16 and Figure 2.17.

Figure 5.9 shows the transmission parameter, S_{21} (where one antenna is acting as a source and the other as a receiver) between the CBS antennas with and without EBG structures. These simulations show that significant coupling reduction is achieved, reaching up to 35 dB at certain frequencies. As a comparative reference, in [7] the largest achieved coupling reduction obtained using lossy material was 7 dB. We note that over very narrow bands, the coupling reduction due to the

implementation of the EBG surface was slight, and in fact, an enhancement in the coupling was observed between 6.5 GHz and 7 GHz. However, we need to remember that the frequency band over which the coupling enhancement takes place is outside the operating frequency band of each antenna.

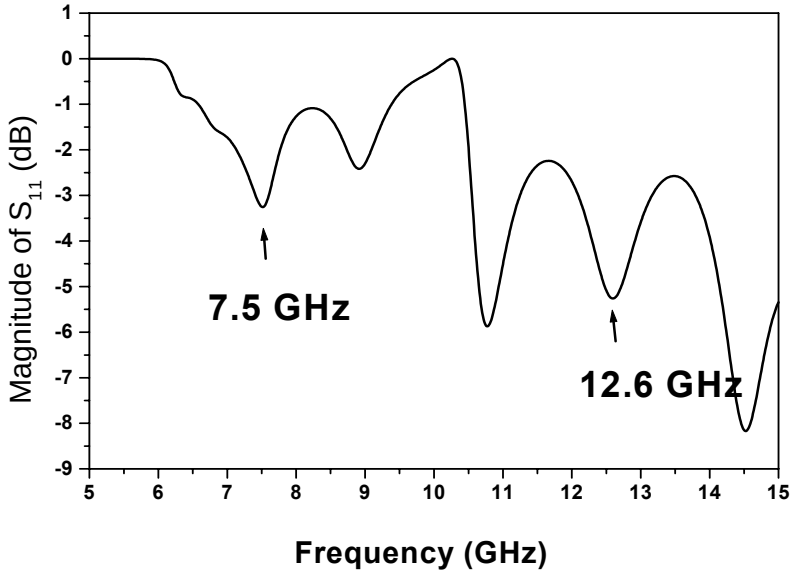

Figure 5.8. Magnitude of S_{11} of two identical CBS antennas mounted on a rectangular ground plane (without the EBG structures). This antenna resonates at both 7.5 and 12.6 GHz as marked on the plot.

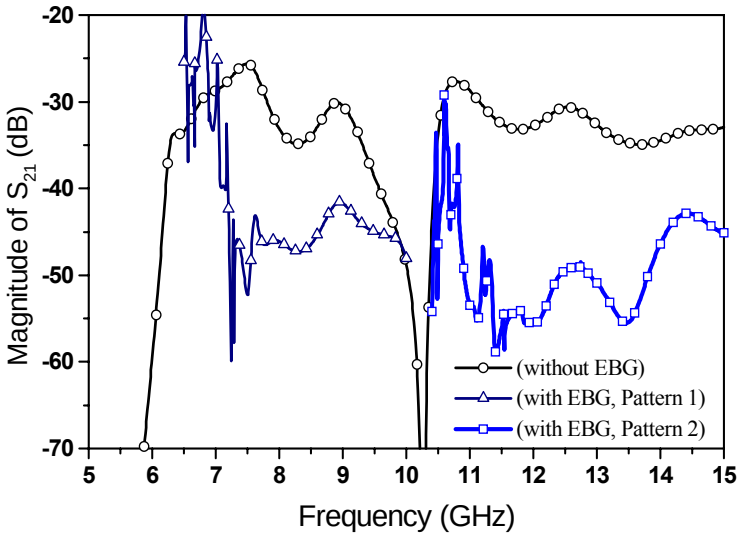

Figure 5.9. Coupling between the two antennas is represented by the magnitude of the S_{21} parameter. Two different EBG designs for two operating frequencies are implemented and simulated. Pattern 1 corresponds to a patch size of 4 mm and ε_r of 4.8. Pattern 2 corresponds to a patch size of 2.6 mm and ε_r of 3.

Figure 5.10 shows the reduction of surface waves and currents due to the presence of EBG structures. As it is evident from these simulations, when one of the antennas is excited, surface currents are generated and travel to the second antenna, therefore creating strong coupling. In Figure 5.10 (b), the EBG structure with an operating frequency band from 7 GHz to 8 GHz was applied while the first antenna is excited at 7.5 GHz. The decrease in coupling is obvious compared to Figure 5.10 (a) which shows the surface currents without the EBG surface. Figure 5.10 (d) shows coupling reduction compared to Figure 5.10 (c) where an EBG structure with an effective bandgap from 11.9 GHz to 16 GHz is applied while the antenna is excited at

12.6 GHz. Figure 5.11 and Figure 5.12 show the E-field distribution in the *y-z* plane cross section intersecting the two antennas.

A disadvantage of using EBG surface between the two CBS antennas is a change in the radiation pattern and directivity of each antenna. The amount of this change depends on the proximity of the EBG structures to the antennas. It is easy to infer such consequence from the surface current plots shows in Figure 5.10. The presence of EBG surface results an asymmetric distribution of the surface currents, consequently an asymmetric radiated field pattern. Since the EBG structure does not support any wave propagation at a frequency that falls within its bandgap, it is expected that the directive pattern of the antennas would rotate in the direction opposite to the side in which the EBG structures are located. In other words, since the flow of energy in directions close to the EBG structure is prohibited, the antenna gain in such directions is expected to drop. In order to investigate this prediction, we extracted the radiation patterns of one of the antennas for three different cases: First, without the EBG structure; second, with the EBG structure of Pattern 1 (4 mm square patches with $\varepsilon_r = 4.8$), and third, with the EBG structure of Pattern 2 (2.6 mm square patches with $\varepsilon_r = 3$). Figure 5.13 shows a comparison between the first and second case while Figure 5.14 shows a comparison between the first and third case. From these results, we conclude that the EBG structures lead to reduced coupling between the two antennas. However, this reduction takes place at the expense of symmetry in the antenna pattern, and more specifically, at the expense of radiated gain in the direction of the adjacent antenna. We note that the decrease of gain by implementing lossy material was previously reported in [7].

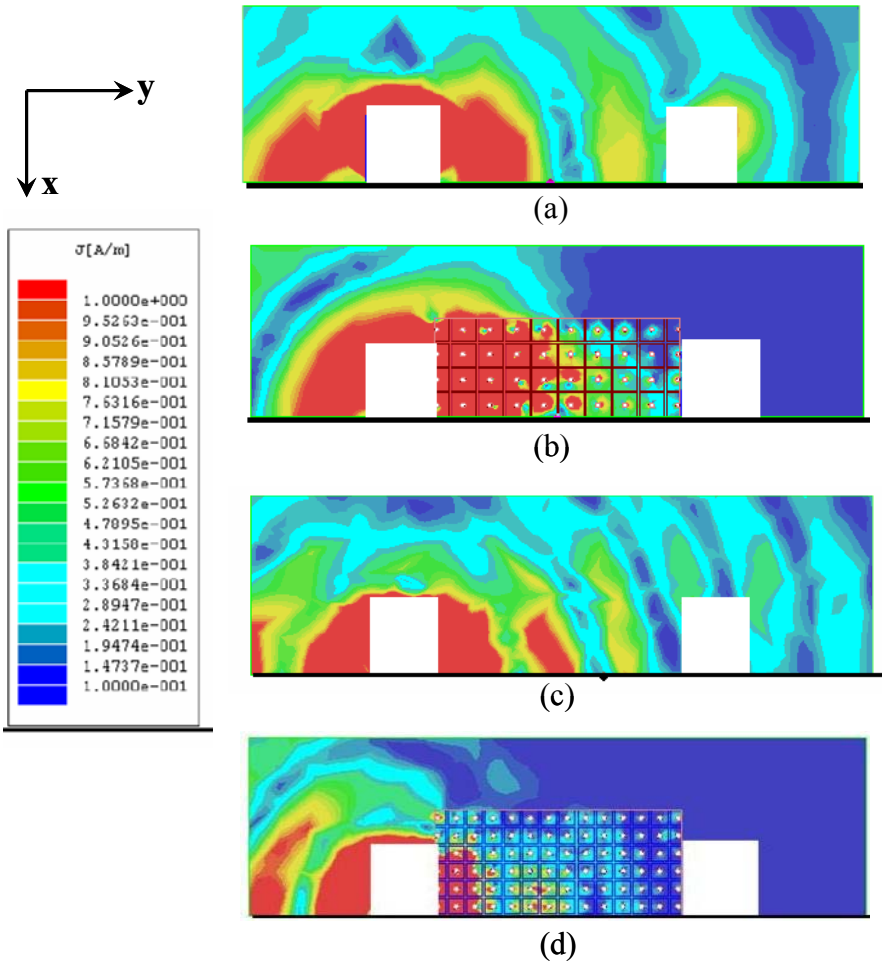

Figure 5.10. Top view of the magnitude of the total surface current density J_{tot} (a) without the EBG structure when the antenna is operating at 7.5 GHz, (b) with the EBG Pattern 1 when the antenna is operating at 7.5 GHz, (c) without the EBG structure when the CBS antenna is operating at 12.6 GHz, and (d) with the EBG Pattern 2 when the antenna is operating at 12.6 GHz. Due to symmetry, only half of the structure is shown.

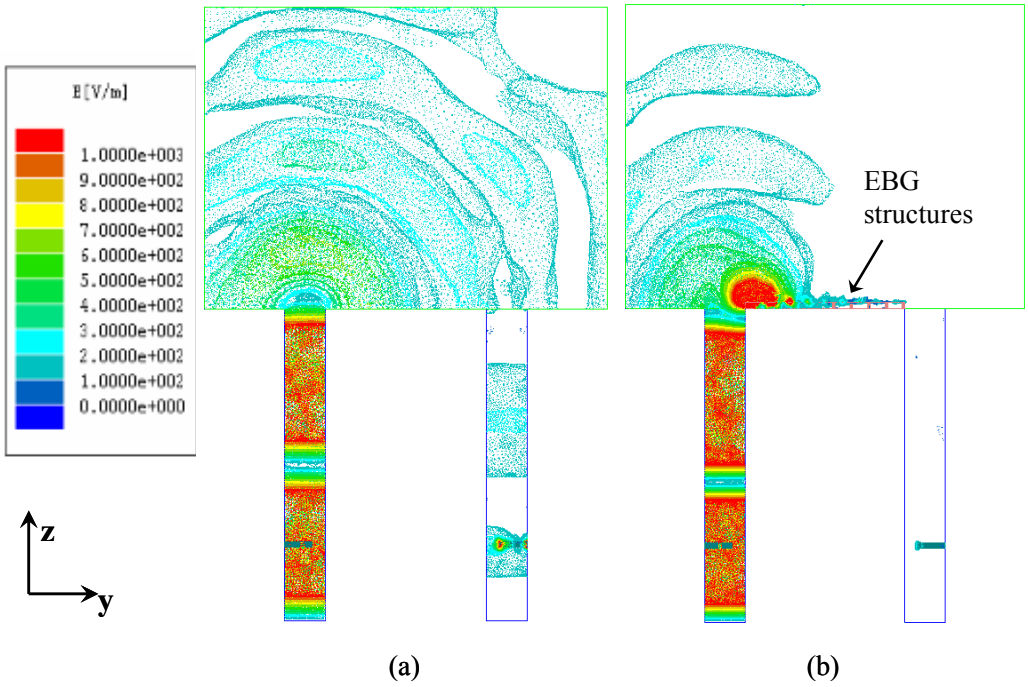

Figure 5.11. E-Field distribution in the *y*-*z* plane (intersecting the two antennas) when one of the antennas is excited at 7.5 GHz while the second one is receiving. (a) Without and (b) with the EBG Pattern 1.

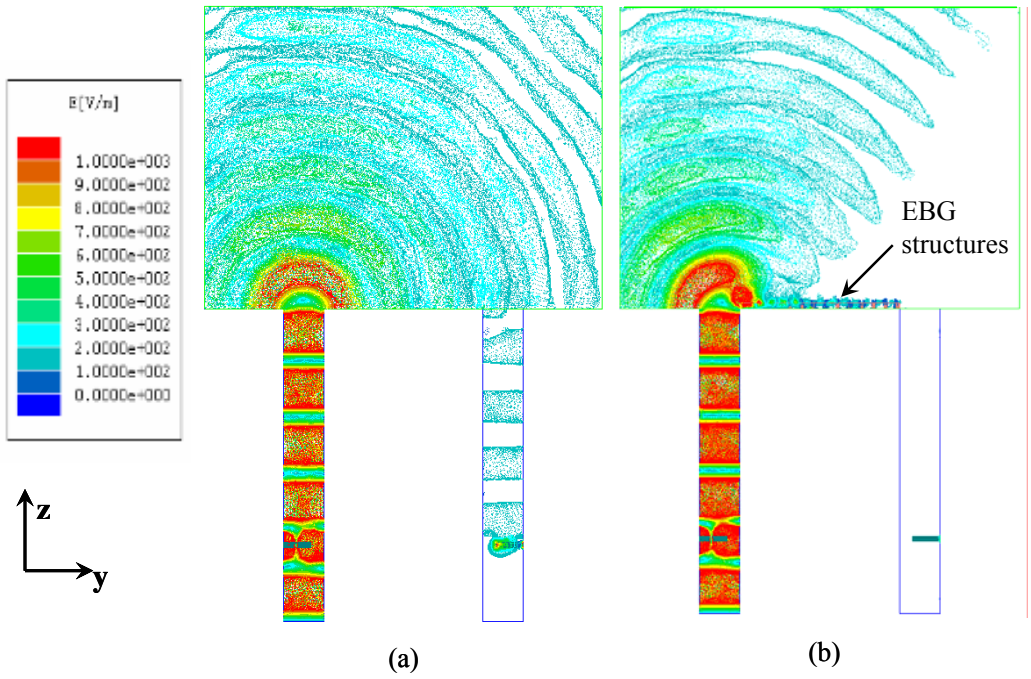

Figure 5.12. E-Field distribution in the *y*-*z* plane (intersecting the two antennas) when one of the antennas is excited at 12.6 GHz while the second one is receiving. (a) Without and (b) with the EBG Pattern 2.

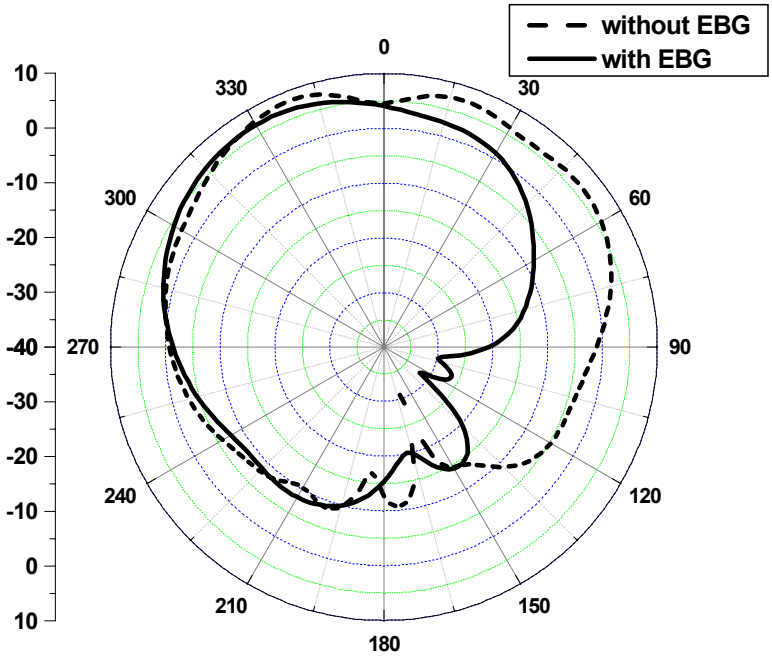

Figure 5.13. Radiated field patterns at 7.5 GHz with and without EBG Pattern 1. The rgain pattern is in the *y*-*z* plane (*E*-plane) where 0 corresponds to the azimuth.

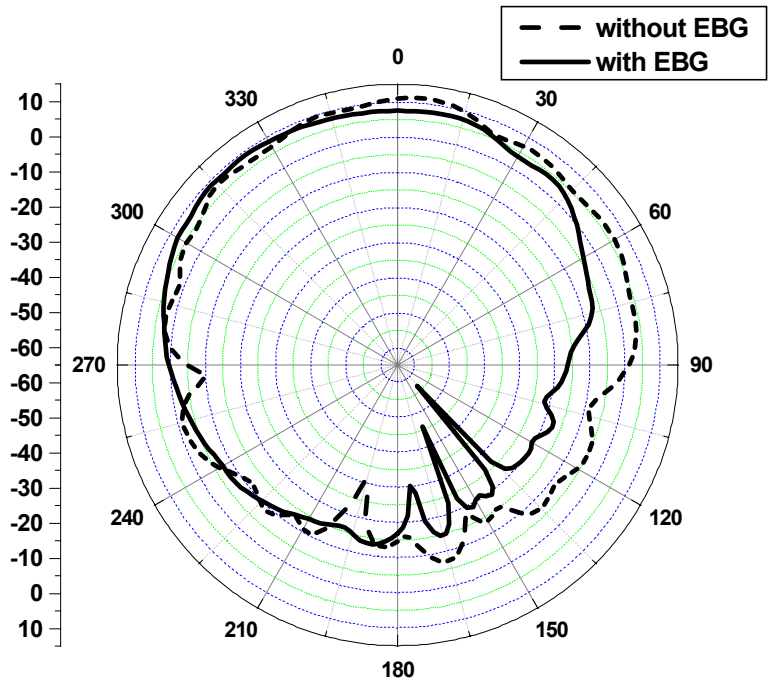

Figure 5.14. Radiated field patterns at 12.6 GHz with and without EBG Pattern 2. The gain pattern is in the *y*-*z* plane (*E*-plane) where 0 corresponds to the azimuth.

5.1.2.C. *CBS Antenna System with Presence of EBG Structures*

In this subsubsection, we continue our studies on the effects of presence of EBG structures in the CBS antennas system. We investigate about EMI coupling reduction between antennas as well as gain pattern. In the previous subsubsection, we concluded that the gain pattern is changing while reducing interference between two antennas. We investigate about EMI coupling reduction between antennas as well as gain pattern. For this purpose, we are covering not only the spacing between antennas but also all around the opening of CBS antennas by the EBG Pattern 2 which is 2.6 mm square patches with $\varepsilon_r = 3$ as shown in Figure 5.15. The size of this patch of EBG

structures implemented on common surface is 12 cells × 28 cells which are covering around the apertures and the separation between antennas (intersections of apertures and EBG structures are removed from the slab). The size of slab of EBG structures implemented only between antennas was 12 cells × 14 cells. Figure 5.16 shows the magnitude of S_{21} for the setup covering around and between apertures. For comparison purpose, the insertion loss curves for setups without EBG and with EBG located only in between antennas are included in the same figure. The system with EBG structures located in between antennas is performing more efficient than the system with EBG structures placed all around the antennas reducing coupling effect. However, both systems have similar coupling reduction performance of 18 dB at the operating frequency of antennas 12.6 GHz. The radiation patterns of these setups are illustrated in Figure 5.17. As it can be seen from the radiation pattern, the broadside gain of the antenna with added EBG structures decreases. This reduction for the case with EBG in between is 3 dB and for the case with EBG around and between antennas is 2 dB. The presence of EBG structures all around the apertures of antennas prevent the flowing of surface current on the common surface in all directions at the operating frequency of EBG pattern. Therefore, the directivity of antenna in those directions is decreasing and the radiation bandwidth becomes narrower. The radiation pattern obtained for the case where the EBGs are in all sides is almost symmetric similar to the case without EBGs.

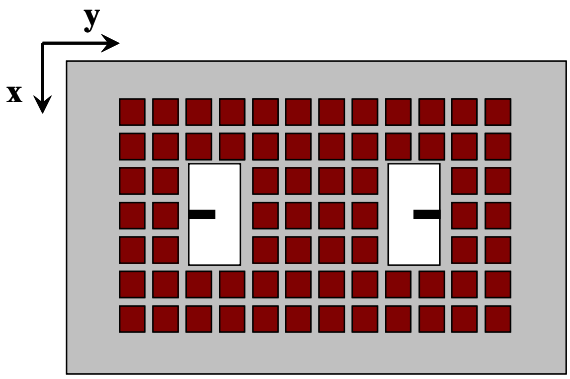

Figure 5.15. Top view of the CBS antennas system showing the placement of the EBG structures all around the apertures and between the antennas on a common plane.

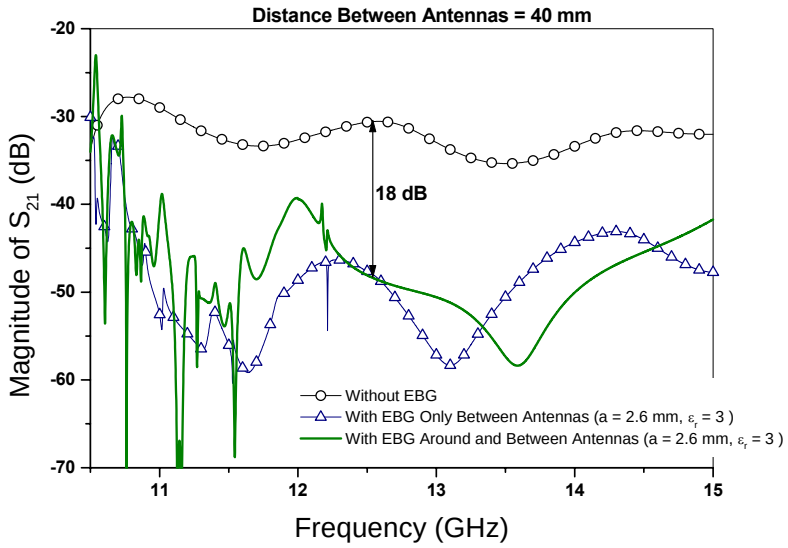

Figure 5.16. Coupling between the two antennas operating at 12.6 GHz for three different setups is represented by the magnitude of S_{21}. 1) Without EBG structures, 2) with EBG Pattern 2 only between antennas, and 3) with EBG Pattern 2 around and in between the apertures. Separation between antennas is 40 mm.

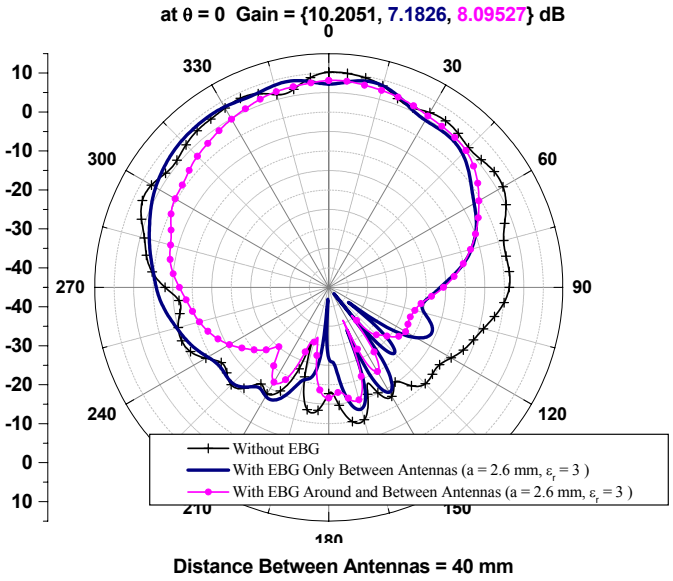

Figure 5.17. Radiated Gain patterns at 12.6 GHz for three different setups for the antenna system: 1) without EBG structures, 2) with EBG Pattern 2 only between antennas, and 3) with EBG Pattern 2 around and in between the apertures. The pattern is in the *y*-*z* plane (*E*-plane) where 0 corresponds to the azimuth. Separation between antennas is 40 mm.

We have studied previously in 0 that the periodicity of EBGs is an important factor which affects the effective suppression bandwidth. As the number of EBGs between the two sources increases, we get wider and better suppression. However, the need for integrity and presence of several electromagnetic sources close to each other is another concern. Therefore, we are going to study the effect of placement of CBS antennas in proximity to each other. The separation between two antennas is reduced to 13.84 mm. A patch of 16 cells × 20 cells of EBG Pattern 2 is implemented on common surface, around and between the apertures of antennas. Between the two

antennas, we have only 4 rows of EBGs. The magnitude of S_{21} for this setup with and without EBGs is shown in Figure 5.18. Comparing the data in Figure 5.18 to Figure 5.16 shows that the interference coupling increases as we decrease the distance between these cavities. Also, we realize that the level of coupling suppression as well as the effective bandwidth for EBGs decreases. At the operating frequency of antennas 12.6 GHz, the EMI suppression is equal to 12 dB. Totally, the EMI coupling increases by more than 10 dB if we decrease the distance between antennas in presence of EBGs.

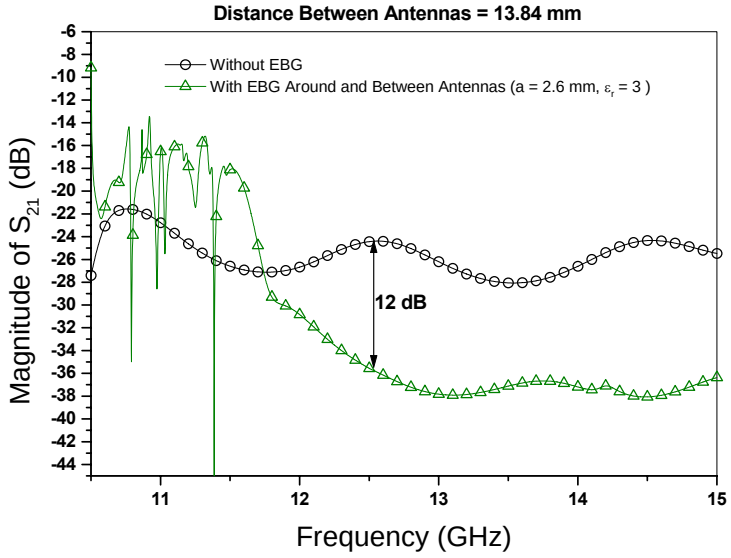

Figure 5.18. Coupling between the two antennas operating at 12.6 GHz for 2 different setups is represented by the magnitude of S_{21}. 1) Without EBG structures and 2) with EBG Pattern 2 around and in between the apertures of antennas. Separation between antennas is 13.84 mm.

The radiation patterns of these setups, which are distant by 13.84 mm, are illustrated in Figure 5.19. Comparison between this figure and Figure 5.17 shows that the broadside gain for the setups without EBG is decreased from 10.2 dB to 8.5 dB. This is expected as we have more interference coupling between two cavities. Implementing EBGs is improving the broadside gain by almost 0.7 dB. This effect is different from the results of earlier setups.

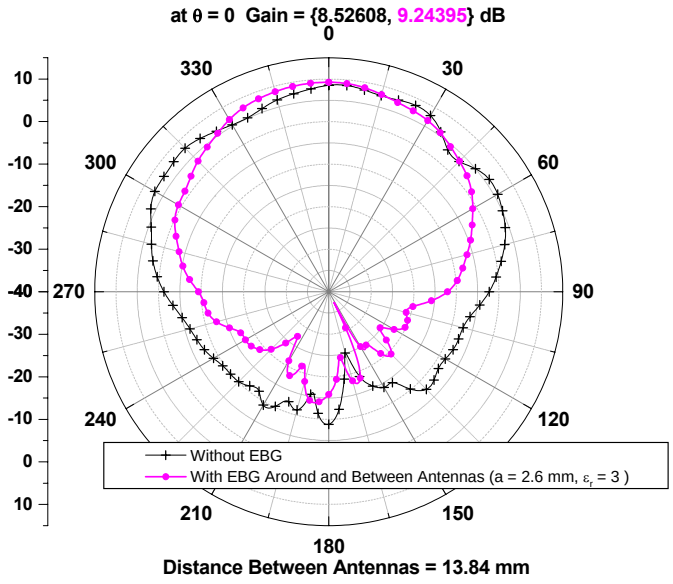

Figure 5.19. Radiated field patterns at 12.6 GHz for 2 different setups for the antenna system: 1) without EBG structures and 2) with EBG Pattern 2 around and in between the apertures of antennas. The pattern is in the *y*-*z* plane (*E*-plane) where 0 corresponds to the azimuth. Separation between antennas is 13.84 mm.

From the obtained results we conclude the following: when we are working with cavity-backed antennas we have trade off between different parameters such as: the separating space between radiators, the tolerating limit for EMI coupling, and the gain of antennas. For example, if we compare two antennas distant by 40 mm without presence of any EBGs with the case where two antennas distant by 13.84 mm and surrounded by EBG patterns then we see that in the second case we have almost 5 dB less EMI coupling but the first case has almost 1 dB better broadside gain. In the second case, the space between two antennas is decreased by more than 26 mm but at the same time we have added the engineered material to our common ground. Considering that the EBG structures used in this study are not optimized, we conclude that we could design cavity-backed antennas system where antennas are closer to each other and having acceptable radiation pattern and at the same time with less EMI coupling.

In 0, it is mentioned that the relationship between different design parameters of EBG structure and the suppression band is not linear. Also, the results of this subsubsection, up to here, confirm that to study an antenna system in presence of EBGs we have to consider the entire system. The effect of implementation of different EBG structures on the specifications and performance of the antenna system is not consistent. Therefore, these types of antenna systems for efficient performance should be optimized in the presence of EBGs. For further investigation, we study the same antenna system separated by 40 mm at the operating frequency of 12.6 GHz. New EBG structure named Pattern 3 specified by 1.2 mm square patches with $\varepsilon_r = 6$ and via diameter 0.5 mm is implemented between the two antennas. The size of this

slab of EBGs is 18 cells × 14 cells located in the middle of two antennas and its width is 22.4 mm as shown in Figure 5.20. The coupling between the two antennas is shown in Figure 5.21. The insertion loss curves for setups without and with EBG Pattern 2 placed only in the gap between antennas are included in the same figure. The results show that at the operating frequency of antenna, Pattern 2 suppresses interference coupling by 8 dB better than Pattern 3. The radiation patterns of these three cases included in Figure 5.22 show that at the broadside, the gain is degraded by almost 0.6 dB when using Pattern 3 while the degradation was 3 dB when using Pattern 2. Therefore, in this setup again we are experiencing a tradeoff between the EMI suppression and the gain pattern degradation.

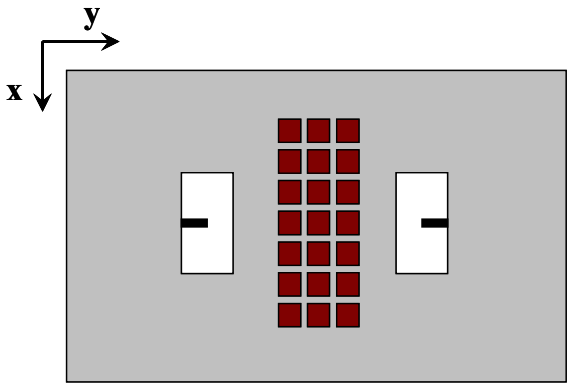

Figure 5.20. Top view of the CBS antennas system showing the placement of a slab of the EBG structures between the antennas on a common plane. The slab is partially covering the separation between antennas.

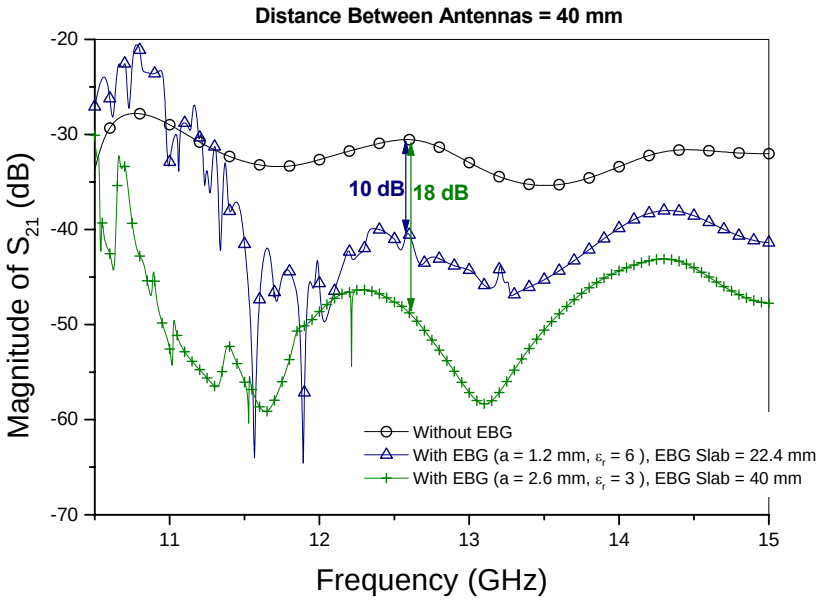

Figure 5.21. Coupling between the two antennas operating at 12.6 GHz for three different setups is represented by the magnitude of S_{21}. 1) Without EBG structures. 2) With slab of EBG Pattern 2 between antennas. The width of slab is 40 mm. 3) With slab of EBG Pattern 3 between antennas. The width of slab is 22.4 mm. Separation between antennas is 40 mm.

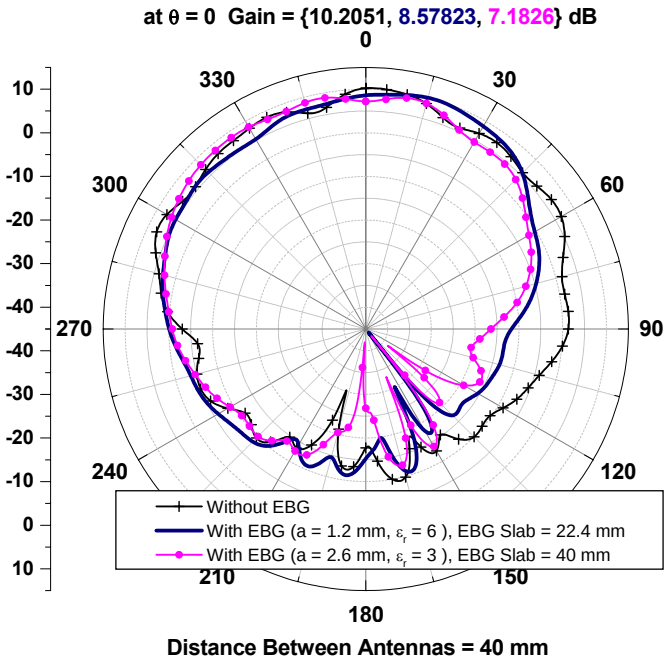

Figure 5.22. Radiated Gain patterns at 12.6 GHz for three different setups for the antenna system. 1) Without EBG structures. 2) With slab of EBG Pattern 2 between antennas. The width of slab is 40 mm. 3) With slab of EBG Pattern 3 between antennas. The width of slab is 22.4 mm. Separation between antennas is 40 mm. The pattern is in the *y*-*z* plane (*E*-plane) where 0 corresponds to the azimuth.

Now we look at new configurations for the CBS antenna system in which the antennas are separated by 22.4 mm. The antennas are operating at 12.6 GHz. Three different cases are considered: 1) without EBG structures, 2) with EBG structures between antennas, and 3) with EBG structures around and between apertures of antennas. The EBG Pattern 3 is used in the simulations. For the second setup, the size of the slab of EBGs is 18 cells × 14 cells which fully cover the separation between

antennas. For the third setup, the size of the slab of EBGs is 22 cells × 36 cells which cover the area around the apertures and the seperation between antennas (intersection of apertures and the EBG structures are removed from the slab). The level of EMI coupling for these configurations is shown in Figure 5.23. For the second case, at 12.6 GHz the EM suppression is equal to 13 dB. It means that in this configuration there is almost 8 dB less coupling between the two antennas compared to the case where antennas were separated by 40 mm without any EBG structures (refer to the original study case). The gain patterns of those three configurations are shown in Figure 5.24. The results indicate that by implanting EBG pattern between the antennas, the broadside gain is reduced by 2.4 dB. The setup with EBGs around the apertures and between antennas reduces the broadside gain by 1.2 dB. Applying EBGs all around the apertures did not improve the symmetry of radiation pattern.

We present in Figure 5.17, Figure 5.19, and Figure 5.24 the gain patterns of three different antenna systems without EBG structures. These configurations have different separation distances between antennas. The results show that the broadside gain is 10.2 dB, 7.2 dB, and 8.5 dB for the separations 40 mm, 22.4 mm, and 13.84 mm, respectively. Therefore, the change of gain versus the gap distance is not monotonic. However, the results obtaind from the figures presenting the magnitude of S_{21} for these configurations show that the coupling interference increases by decreasing the seperation between antennas. As a result, we do conclude that changes in the gain pattern are not certainly predictable.

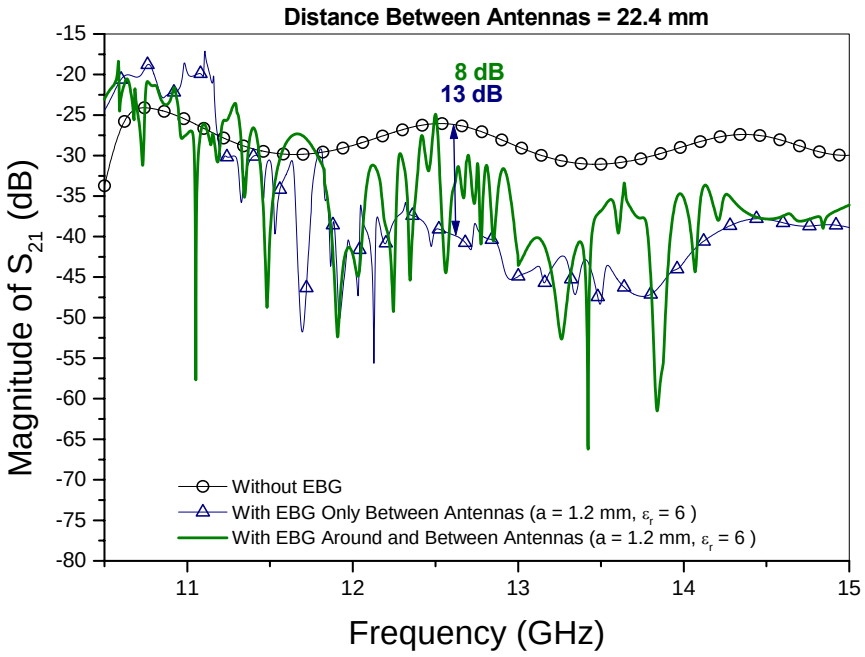

Figure 5.23. Coupling between two antennas operating at 12.6 GHz for three different setups is represented by the magnitude of the S_{21}. 1) Without EBG structures. 2) With EBG Pattern 3 only between antennas. 3) With EBG Pattern 3 around and between the apertures of antennas. Separation between antennas is 22.4 mm.

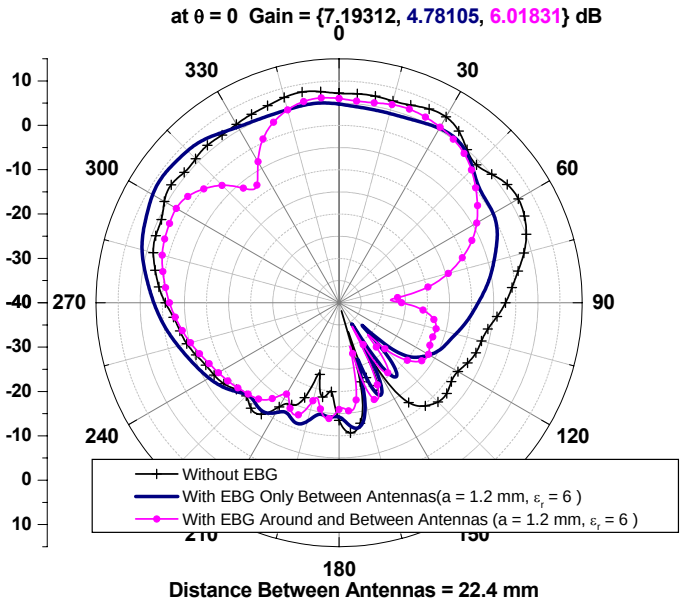

Figure 5.24. Radiated Gain patterns at 12.6 GHz for three different setups for the antenna system: 1) without EBG structures, 2) with EBG Pattern 3 only between antennas, and 3) with EBG Pattern 3 around and in between the apertures of antennas. The pattern is in the *y*-*z* plane (*E*-plane) where 0 corresponds to the azimuth. Separation between antennas is 22.4 mm.

To complete our study, in what follows, we continue our investigation on the effect of proximity of EBG structures to the aperture of the CBS antenna on the directivity pattern when the perimeter of the opening of antenna is covered with EBG structures. Figure 5.25 shows the top view of a single antenna system in which a ribbon of EBG structures is surrounding the aperture of CBS antenna. The antenna has the same specifications as in Figure 5.5. The width of the ribbon is 4 unit cells. The distance of ribbon of EBGs from aperture is determined by the two parameters:

d_1 and d_2. In our numerical studies, we assume that the ground plane is infinite. Therefore, the radiation pattern occupies the upper half space. The EBG pattern, with square patch size of 5 mm and ε_r = 4.4 (FR-4) which is effective at the operating frequency of antenna 7.5 GHz, is used in the following numerical simulations.

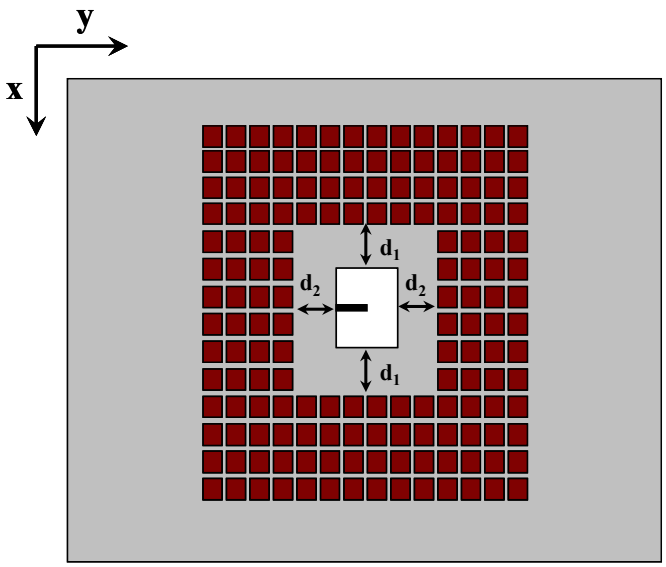

Figure 5.25. Top view of the CBS antenna system showing the placement of a ribbon of EBG structures around the aperture. The distance of this ribbon from antenna is determined by the two parameters: d_1 and d_2.

The case studies include the following antenna systems: 1) without EBG, 2) with EBG where d_1 = 4.77 mm and d_2 = 3.02 mm, 3) with EBG where d_1 = 10.17 mm and d_2 = 8.42 mm, and 4) with EBG where d_1 = 15.57 mm and d_2 = 13.82 mm. In the setups with presence of ribbon of EBGs we have changed the distance of ribbon from antenna aperture. Figure 5.26 shows the gain patterns of those four configurations. The results show that we can control the directivity pattern by changing the location

of EBG structures with respect to aperture of antenna. The setup without EBG has approximately a uniform gain pattern in the upper half space. By implementing EBG ribbon around the aperture in the second case study we have a broadside directive antenna with almost 3 dB increment in the gain. The third case study is a broadside directive antenna. It has almost 0.5 dB less gain at broadside compared to second case study. In addition, this configuration has side lobes. The fourth case study is a directive antenna with maximum gain at ± 30° and minimum gain at the broadside direction. These results confirm that we can use EBGs in designing directive antennas.

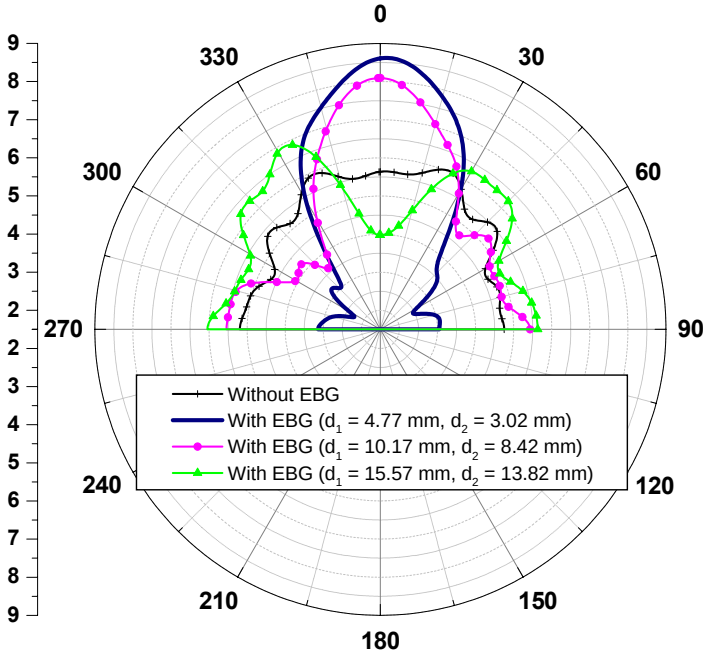

Figure 5.26. Radiated gain patterns at 7.5 GHz obtained for four different setups for a single antenna system. 1) Without EBG structures. 2) With ribbon of EBGs distant from antenna by d_1 = 4.77 mm and d_2 = 3.02 mm. 3) With ribbon of EBGs distant from antenna by d_1 = 10.17 mm and d_2 = 8.42 mm. 4) With ribbon of EBGs distant from antenna by d_1 = 15.57 mm and d_2 = 13.82 mm (refer to Figure 5.25). The pattern is in the *y*-*z* plane (*E*-plane) where 0 corresponds to the azimuth.

5.1.2.D. *Experimental Study*

In this subsubsection, we present the experimental results showing the performance of EBG surfaces of various patch sizes. The setup used in this experiment is shown in Figure 5.27 where two waveguides lead to two CBS antennas 16 cm apart and sharing a common ground plane in a manner similar to the numerical

case study discussed in Subsubsection 5.1.2.B. The two ports of the waveguides are fed through SMA connectors and then connected to an Agilent PNA series vector network analyzer (VNA). Figure 5.27 also shows the placement of the EBG surface under study between the two antennas. The EBG structures used in this experiment are made of FR-4 substrate with via diameter and height of 0.8 mm and 1.54 mm, respectively. The distance between the patches is 0.4 mm and the width of EBG structures used is 6cm. EBG of different patch sizes ranging from 2 mm to 5 mm are tested and comparison is made to the reference case where EBG surface is removed.

Figure 5.28-Figure 5.31 show the results of measurements. In each plot, the magnitude of S_{21} is presented for the cases with and without the EBG surface. The 3 dB bandgap is marked in each graph. In Figure 5.32, we present the numerical simulation results obtained by the numerical simulation procedure depicted in Figure 2.7 with 8 infinite rows of EBG patches. Table 5.I summarizes the bandgap obtained from measurements and numerical simulations.

While we have good agreement between the bandgaps calculated numerically and measured experimentally, we attribute the discrepancies observed between the bandgap edges primarily to: first, the non-ideal environment inherent in the experimental setup such as the finiteness of the EBG surface in contrast to the infinite rows which were numerically modeled using field symmetry boundary conditions, second, the assumption that the permittivity of the FR-4 is 4.4 whereas in reality the permittivity varies with frequency.

(a)

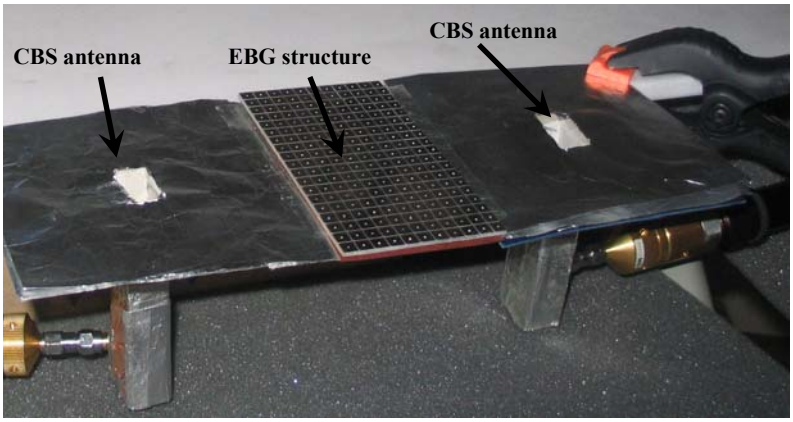

(b)

Figure 5.27. (a) Setup used to assess coupling mitigation using EBG structures. (b) Close up view of antenna system with presence of EBG structure. EBG structures with different configurations (patch sizes of 2 mm to 5 mm) in the area between two antennas separated by 16 cm are implemented. Width of EBG separator is 6 cm.

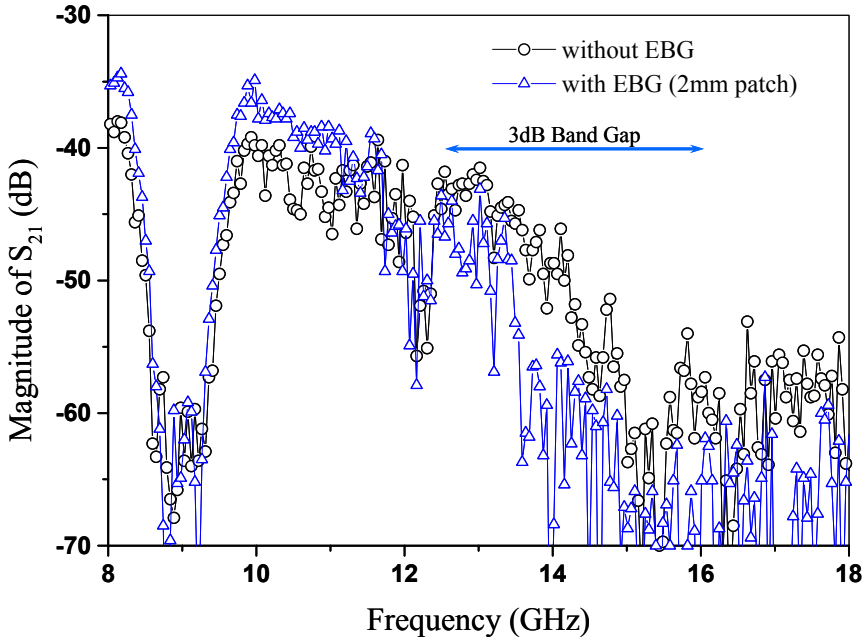

Figure 5.28. Experimental results show the coupling between the two antennas with and without the EBG surface as represented by the magnitude of S_{21}. EBG parameters: 2 mm patch, h = 1.54 mm, g = 0.4 mm, d = 0.8 mm, and FR-4 substrate.

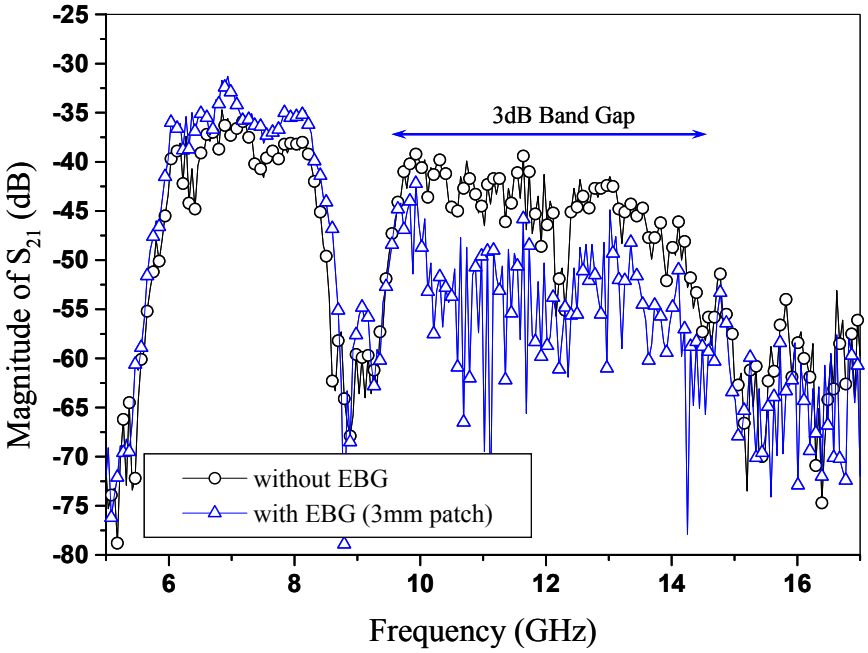

Figure 5.29. Experimental results show the coupling between the two antennas with and without the EBG surface as represented by the magnitude of S_{21}. EBG parameters: 3 mm patch, h = 1.54 mm, g = 0.4 mm, d = 0.8 mm, and FR-4 substrate

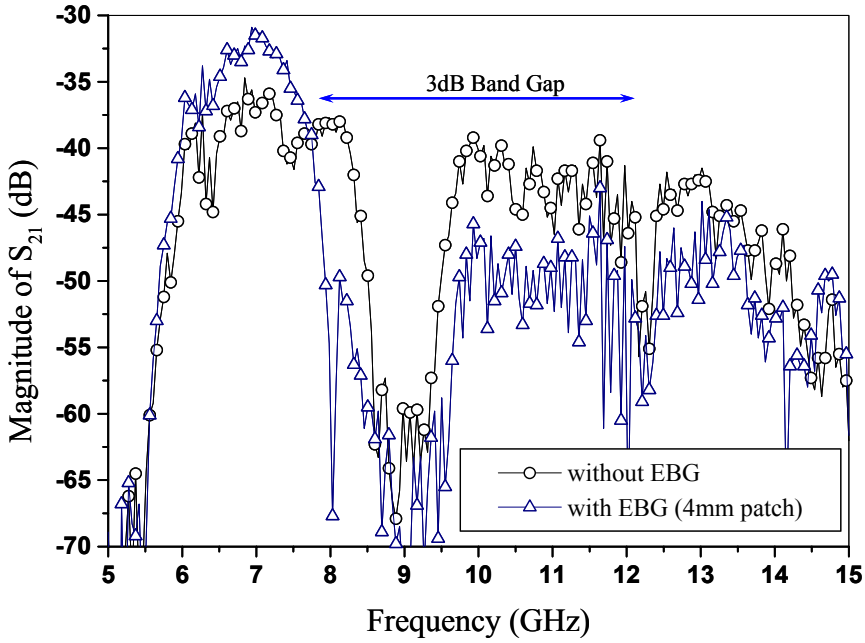

Figure 5.30. Experimental results show the coupling between the two antennas with and without the EBG surface as represented by the magnitude of S_{21}. EBG parameters: 4 mm patch, h = 1.54 mm, g = 0.4 mm, d = 0.8 mm, and FR-4 substrate

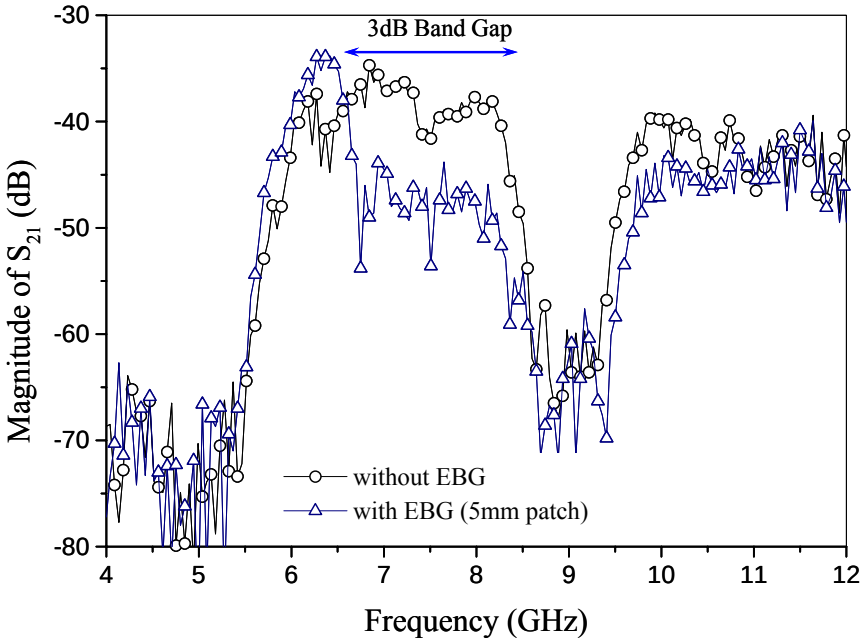

Figure 5.31. Experimental results show the coupling between the two antennas with and without the EBG surface as represented by the magnitude of S_{21}. EBG parameters: 5 mm patch, h = 1.54 mm, g = 0.4 mm, d = 0.8 mm, and FR-4 substrate.

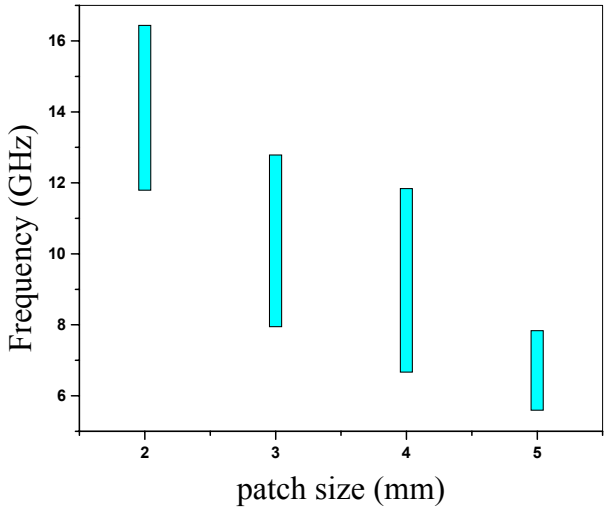

Figure 5.32. Bandgap obtained using numerical simulation. EBG parameters: $\varepsilon_r = 4.4$, $h = 1.54$ mm, $d = 0.8$ mm, and $g = 0.4$ mm.

Table 5.I. Bandgap Obtained From Numerical Simulation and Experimental Measurements

EBG Patch Size (in mm)	Numerically Derived Bandgap (in GHz)	Experimentally Derived Bandgap (in GHz)
2	11.8 - 16.4	12.7 - 16.3
3	8 - 12.8	9.7 - 14.6
4	6.65 -11.85	7.8 - 12.1
5	5.6 - 7.9	6.6 - 8.5

5.1.3. EMI and SSN Noise Mitigation in IC Packages using Miniaturized Planar EBGs

By analyzing the S-parameters between different interconnects in parallel metallic layers of package, it is possible to estimate the range of frequencies where the EMI noise and power/ground bounce are strong. The EM noise with internal and external sources can interfere with the operation of electronic circuits in chip. Therefore, this analysis is necessary for accurate operation of IC. In this subsection, we investigate about EM noise suppression in IC packages using EBG structures. This novel method of noise suppression in IC packages as strong contender of surface wave suppression has become possible due to design of the miniaturized EBGs proposed in our research and discussed earlier in Chapter 3.

5.1.3.A. *Modeling*

After analyzing the S-parameters to extract the range of frequency where the EM noise is strong enough to degrade the operation of electronics, we need to design EBG structure at the requested frequency band. This frequency band can be either narrowband, wideband or even consisting of multiple bands. In packages, the engineered structures are implemented surround the source or the receiver of noise to block the propagation of wave. This is an efficient method to suppress EM noise in the packages.

5.1.3.B. *Numerical Case Studies*

In this subsubsection, by mean of numerical studies we demonstrate the efficiency of this proposed method. We continue our studies on the typical

microprocessor package as our case of study as considered earlier in Chapter 4. For convenience, the structure of this single layer package and the setup of ports are redrawn in Figure 5.33. The dimensions of the package are 4 cm × 4 cm. The dielectric thickness h = 114.3 μm. Following, two different EBG setups are studied. We use EBG sample No. 7 from Table 3.III, which has a suppression band from 1.9 GHz to10.8 GHz, in both setups. The design parameters of this EBG structure shown in Figure 3.12 are: P_W = 1.6 mm, h = 114.3 μm (4.5 mil), M_W = 0.02 mm, M_B = 0.02 mm, M_L = 1.6 mm, M_G = 0.02 mm, and ε_r = 200.

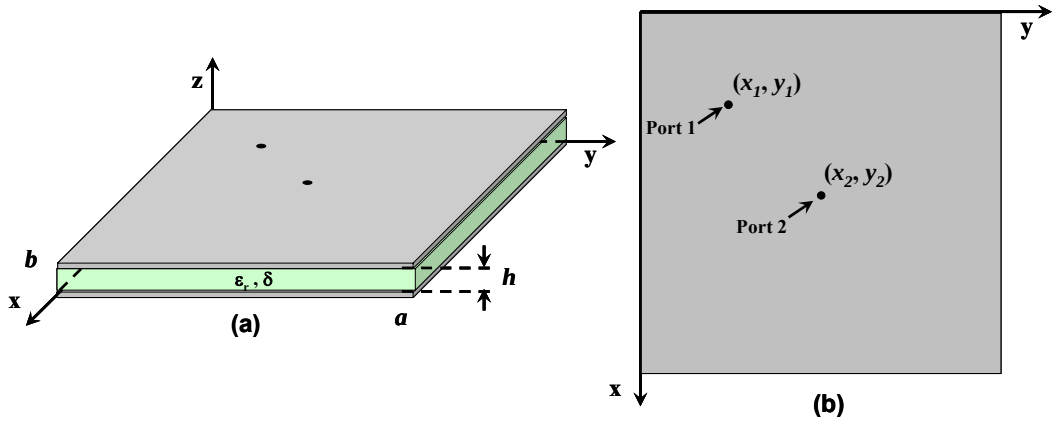

Figure 5.33. Single plane pair in the package consisting of metal-dielectric-metal layers is modeled as parallel plate waveguide. (a) 3-D view. (b) Top view. Typical dimensions of a microprocessor package are: a = b = 4 cm. Each via shown in the figure represents a port. Port 1 and Port 2 are located at (x_1 = 1 cm, y_1 = 1 cm), and (x_2 = 2 cm, y_2 = 2 cm), respectively.

In the first setup, the two ports are isolated with the EBG patterns as shown in Figure 5.34. Each port is centered in a patch of EBG cells. Each patch is made of 5

cells × 5 cells in both *x*- and *y*-direction. The magnitude of S_{21} for this configuration is illustrated in Figure 5.35. In the second setup, only the second port is isolated with the EBG patterns as shown in Figure 5.36. The second port is centered in the patch of EBG cells. The size of patch in this experiment is 5 cells × 5 cells. The magnitude of S_{21} for this configuration is also shown in Figure 5.35. Comparison is made with two different embedded capacitance cases studied in Chapter 4. Embedded capacitance method is implemented to packages as an effective method of EMI suppression in the entire frequency band. These cases are applied to a single plane pair with two different materials of $\varepsilon_r = 4.3$ and $\tan \delta = 0.02$ (low value embedded capacitance), and $\varepsilon_r = 200$ and $\tan \delta = 0.0015$ (high value embedded capacitance). The magnitude of S_{21} for both cases is included in Figure 5.35. The results show that to protect the ports from EMI noise in the package, it is enough to isolate either the source or the receiver. The level of EMI noise mitigation we can get from EBG patterned power planes compared to high embedded capacitance case is very high.

In another study, we use the second test setup in two different cases. In the first case, the EBG patch is 5 cells × 5 cells. In the second case, it is 9 cells × 9 cells. The magnitude of S_{21} for each case is shown in Figure 5.37. The simulation results show that the level of electromagnetic noise suppression depends on the number of EBG unit cells. Therefore, if we increase the EBG cell population between source and receiver, more suppression is achieved. However, simulating a fully EBG-populated board is prohibitive due to the large number of meshes required to model meander bridges between patches.

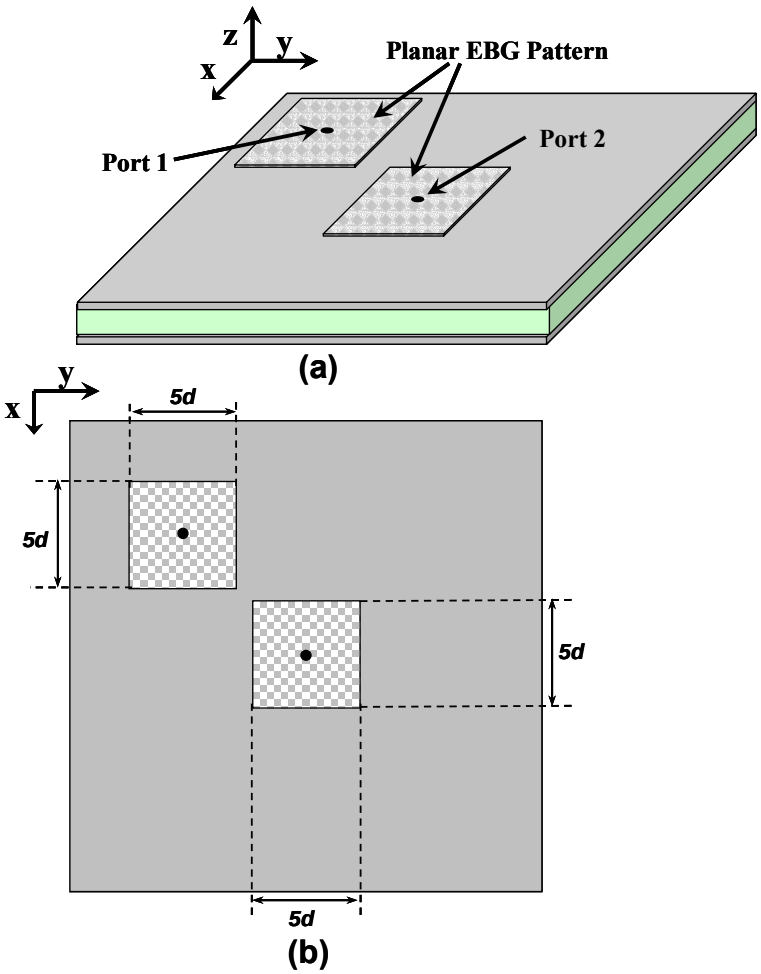

Figure 5.34. Test Setup 1. The ports in the package under study are isolated with EBG pattern, (a) 3-D view and (b) top view. The specifications of package and ports are shown in Figure 5.33. In this experiment the EBG sample No. 7, specified in Table 3.III, is used. Each port is centered in the middle of the EBGs patch. The size of patch is 5 cells × 5 cells.

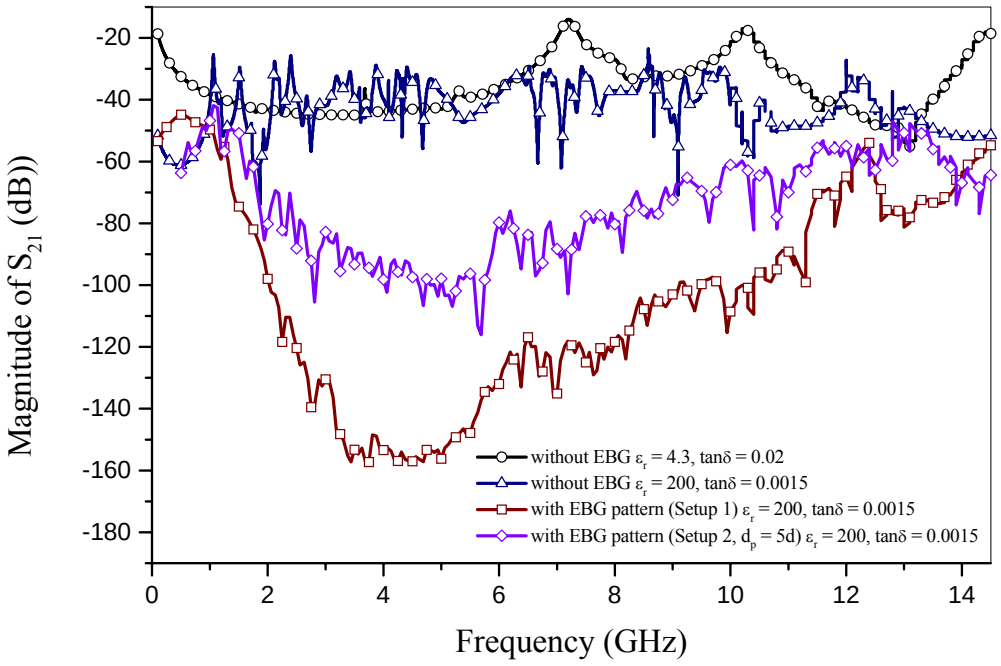

Figure 5.35. Magnitude of S_{21} between ports 1 and 2 in the single plane pair under study for four different scenarios (design parameters and port setup are shown in Figure 5.33). The first and second cases show embedded capacitance. The third case shows test setup 1 (refer to Figure 5.34). The fourth case corresponds to test setup 2 (refer to Figure 5.36). In all configurations h = 114.3 μm.

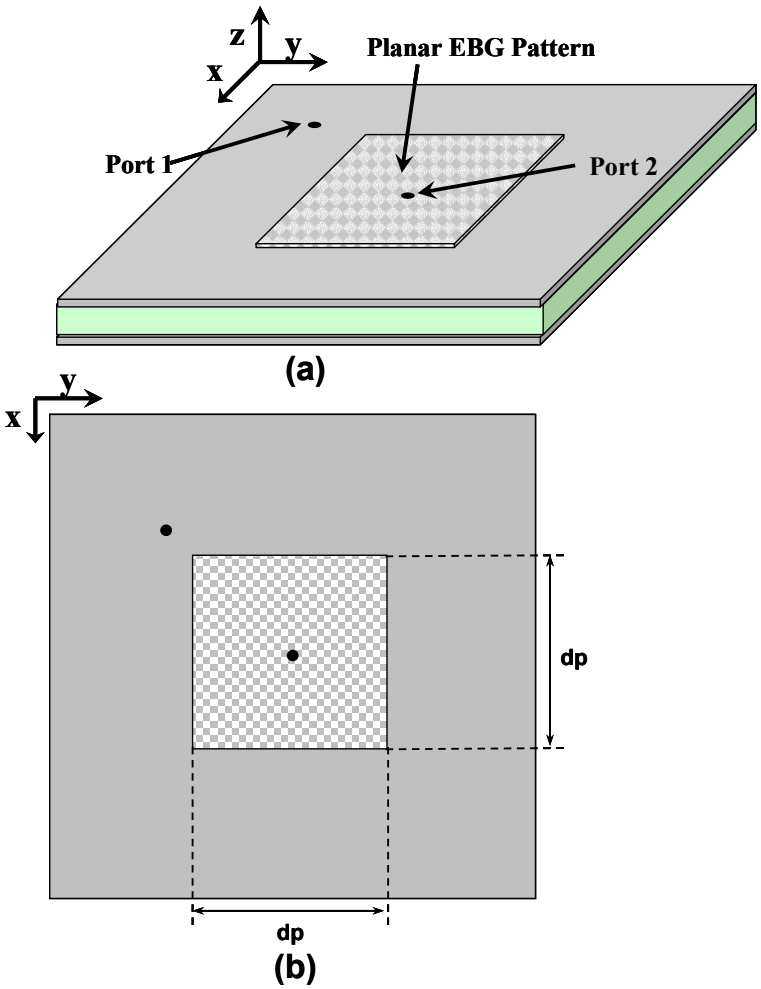

Figure 5.36. Test Setup 2. The second port in the package under study is isolated with EBG pattern, (a) perspective view and (b) top view. Specifications of package and ports are shown in Figure 5.33. In this experiment the EBG sample No. 7, specified in Table 3.III, is used. The second port is centered in a patch of EBGs. The size of patch is $d_P \times d_P$, where in two different experiments d_P = {5 cells, 9 cells}.

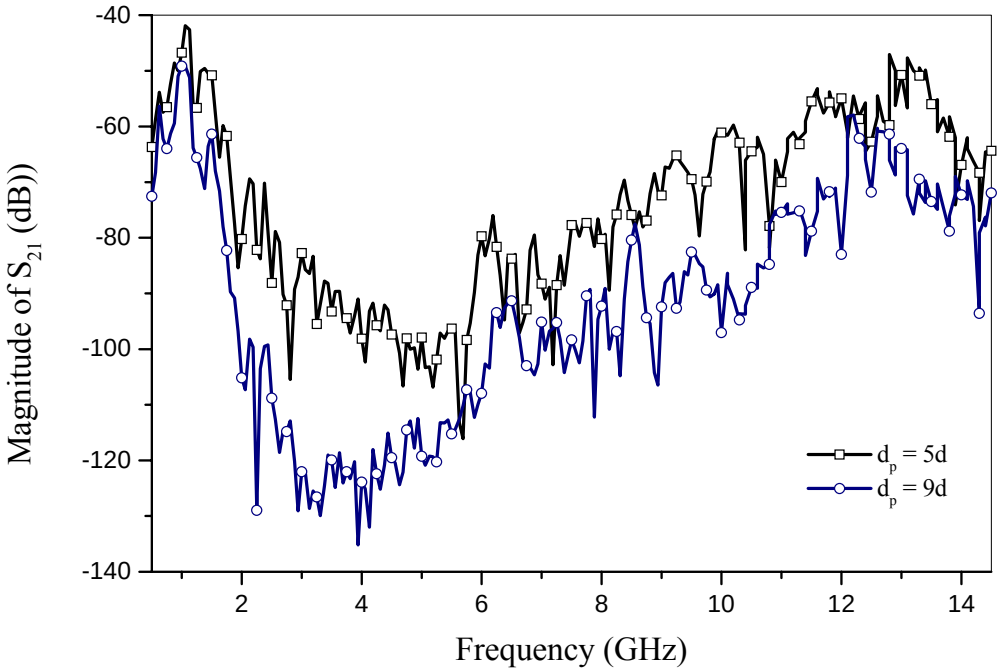

Figure 5.37. Magnitude of S_{21} between ports 1 and 2 in the single layer package under study for two different cases in test setup 2 (refer to Figure 5.36).

The efficacy of EBG patterning of the plane pairs in EMI and SSN noise suppression for through propagation was shown. In the next part of the study, we look at the radiation loss parameter (1- $|S_{11}|^2$ - $|S_{21}|^2$) to assess the possibility of interference due to outward radiation from plane pairs to surrounding media. Testing the performance of the other parts of a system with patterned layers is necessary to keep the functionality of a whole system. The radiation loss for the microprocessor package with the test setup 1 shown in Figure 5.34 is calculated and presented in Figure 5.38. For comparison purpose, the radiation loss from a single plane pair with two different materials of ε_r = 4.3 and tan δ = 0.02 providing low value embedded

capacitance and ε_r = 200 and tan δ = 0.0015 providing high value embedded capacitance are included in the same figure. The 20 dB suppression band of the EBG structure, from 1.9 GHz to 10.8 GHz, showing the effective operating frequency region is marked in that figure.

It is seen that for the low value embedded capacitance case the radition loss at low frequency regions is negligible. However, by increasing the frequency strong local peaks are appearing that may interfere with other levels or parts in the package. The high value embedded capacitance case has reduced peaks of interference in the whole frequency band compared to the low embedded capacitance case. However, we can obviously see that the local peaks are distributed in the entire frequency band. In the effective band of EBG patterned case, the level of radition loss compared to two other cases is negligible. Out of this band, strong local peaks are seen in the plot. Therefore, EBG structures are effective in suppressing noise in their band not only for through propagation but also for radiation to surrounding environment. The effect of those strong local peaks, in the patterened case, on the other parts should be assessed. We need to evaluate the performance of system for purposes of signal integrity especially in low frequency regimes.

Studies in Subsection 3.3.10 have shown that there are local peaks in the radiation loss diagram in the frequency bands compatible with the slow propagating modes of EBG pattern as shown in Figure 3.62. In those frequency regimes, shown in Figure 5.38, radiation exists. However, it is not strong enough to be clearly seen.

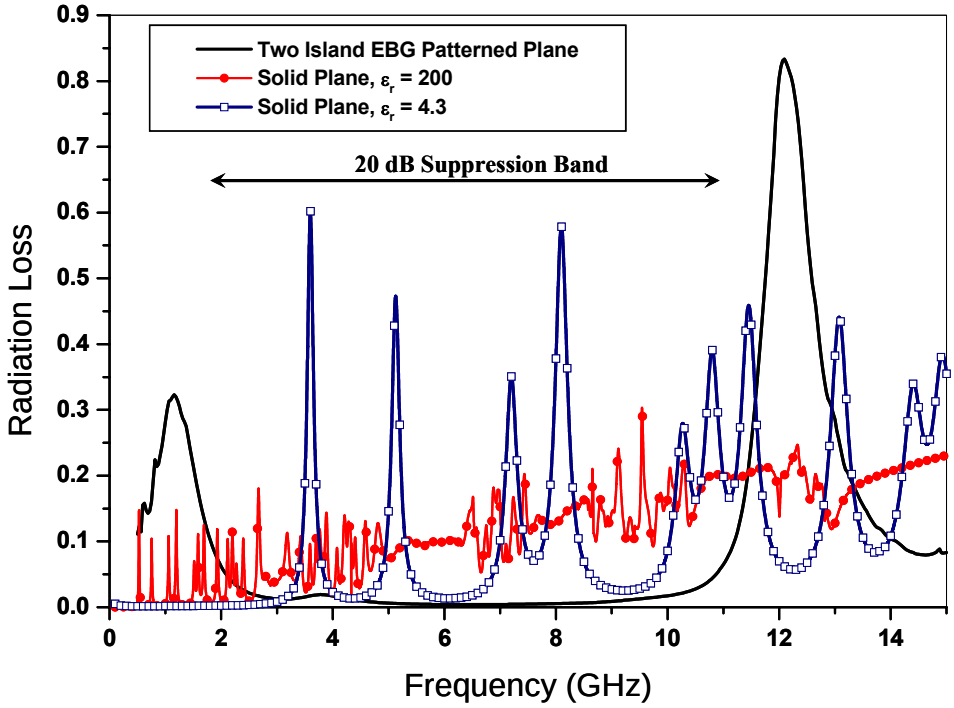

Figure 5.38. Radiation loss, $(1- |S_{11}|^2 - |S_{21}|^2)$, versus frequency for a single plane pair under study for three different scenarios. The first case shows the test setup 1 (refer to Figure 5.34). The second and the third cases show the embedded capacitance (refer to Figure 5.33)

This discrepancy may be attributed to different structural setups. In the package, the larger dimensions of the parallel planes are not populated with EBG patterns as reverse to those results in Figure 3.62 which are coming from fully EBG populated parallel planes with small dimensions. The EBG patterns are radiating waves in those bands, however, the solid parallel planes support propagating waves. Therefore, in the package case the power radiated out per unit area to surrounding environment (computational domain) from the EBG patterns is less than the second

case. As a general result, even by considering those peaks from slow modes, EBG patterning reduces radiating emissions to surrounding environment in the suppression bandgap.

5.2. Design of Low Profile Antenna

EBG structures show novel features which may not occur in nature such as in-phase reflection phase and surface wave suppression. These features have led EBGs to a wide range of applications including antennas. Due to their properties, it has been shown that EBG structures emulate good magnetic conductors, or high-impedance surfaces, in their bandgap when used as ground plane in the design of low profile antennas [72], [73]. This could be explained as follows. When an antenna placed closely on top of an EBG surface is radiating, the reflected waves from this surface will add up constructively to waves radiated from the antenna. Therefore, unlikely to an antenna system with perfect electric conductor (PEC) reflector, there is no need to have that distance of approximately $\lambda/4$ between antenna and reflector. These results can be justified by reflection coefficient of plane wave normally incident on surface defined by:

$$\Gamma = \frac{Z_s - \eta_0}{Z_s + \eta_0}$$

Equation 5-1

where Z_s is the surface impedance of the reflector and η_0 is the wave impedance in the media filling the space between reflector and antenna.

Previous EBG structures made of dielectric materials had desirable properties over a narrow frequency range, thus, their application was limited in design of narrow band low profile antenna. In this study, we have proposed novel EBG structures which make the design of low profile antennas viable.

5.2.1. Limitations in Design of Low Profile wideband Antennas

Previous EBG structures made of dielectric materials, however, had desirable properties over a narrow frequency range thus limiting their application in the design of low profile wideband antennas such as spirals. In [74]-[76], EBG structures were used as a ground plane to implement low profile spiral antennas, but in those works the frequency independent behavior of the spiral antenna was limited by the relatively narrow bandgap of the EBG surface. In [77], negative impedance converters which are active loads (capacitors and inductors having negative values) were inserted within the EBG structure leading to a significant increase in the bandgap. However, the implementation of active circuits adds complications and cost to the design.

Recently, magneto-dielectric substrates were used in several applications [78], [79]. In [78], magneto-dielectric substrates were used for miniaturization of antennas. In [79] it was demonstrated that using such substrates in woodpile EBG structures leads to an increase in its bandgap. Furthermore, [80] showed a method of synthesizing meta-ferrites with desired permeability using novel EBG structures which makes these materials available. In this study, our objective is to show that the effective bandgap in mushroom EBGs can be increased significantly due to the use of magneto-dielectric materials. This achievement opens the doors for designing low

profile wideband antennas. However, this proposed EBG structure is based on development in design and fabrication of low loss magneto-dielectric materials in the microwave region.

5.2.1.A. *Concept and Modeling of Mushroom-Type EBG Structures Using Magneto-Dielectric Substrates*

The square patch mushroom-type EBG structure and its design parameters shown in Figure 2.1 is redrawn in Figure 5.39 for convenience. The EBG structure has a HIS in its bandgap at normal incidence. This surface impedance can be modeled as an inductor in parallel with a capacitor close to the region that it is emulating a PMC surface[26]. The capacitance part is due to the gap between the adjacent patches and is equal to [81]:

$$C = \frac{D\varepsilon_0(\varepsilon_r + 1)}{\pi} \ln\left(\frac{2D}{\pi g}\right)$$

Equation 5-2

where $D = a + g$ is the period of unit cell. The inductance part is due to the adjacent vias and the metal backed substrate which can be calculated using transmission lines theory. The impedance of shorted transmission line while ignoring inductance of vias is calculated from:

$$Z_s = j\eta \tan(\beta h)$$

Equation 5-3

where η and β are the wave impedance and the phase constant in the substrate slab, respectively. When $h << \lambda$, and the substrate is lossless the above impedance

becomes purely inductive. λ is the wavelength in substrate slab. Therefore, L is given by:

$$L = \mu_0 \mu_r h$$

Equation 5-4

L is a monotonic function of h and μ_r up to the range governed by the tangent function in the impedance formula.

To use EBG surface as a ground plane in the design of low profile antennas, the operational frequency band is defined as the overlap of the input-match frequency band and surface wave frequency bandgap [72]. The in-phase reflection bandwidth is the range of frequencies over which the phase of the broadside reflected wave is bounded by ±45°. In this band, the antenna shows good return loss. In another words, the reflected wave from surface is in-phase with incident wave from the antenna. Therefore, the interaction of EBG surface with antenna is constructive. The surface wave frequency bandgap is the range of frequencies over which the surface wave is suppressed significantly. This band improves the radiation pattern of the antenna. These two bands for the square patch mushroom structure overlap completely providing an efficient operating frequency band.

It is well known, that bandgap for a parallel LC circuit is proportional to $\sqrt{(L/C)}$, while the resonance frequency is proportional to $1/\sqrt{(LC)}$. It can be seen that using magneto-dielectric materials with relative permeability $\mu_r > 1$ leading to increase of L has distinct advantage of increasing the bandgap besides the shifting down the lower edge of the bandgap. The increase in L, for a specific resonance frequency, has the added advantage of reducing the size of the patch as a smaller

capacitance would be needed to achieve the same resonant frequency. Thus, the bandgap increases more than before due to reduction of capacitance, *C*.

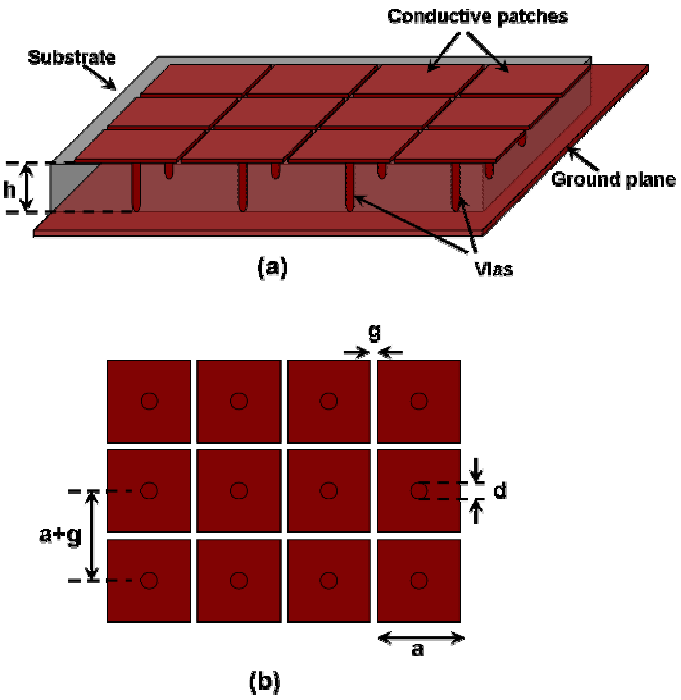

Figure 5.39. Square patch mushroom-type EBG structure (a) Perspective view. (b) Top view. Relevant design parameters are shown on the diagrams.

5.2.1.B. *Numerical Study of EBG Structures Made of Magneto-Dielectric Substrates*

To verify the concept, several square patch mushroom-type EBG structures with magneto-dielectric substrate of permeability higher than one are designed and compared with a conventional EBG structure (EBG with dielectric substrate). The antenna under study is a wideband spiral antenna operating between 8 GHz and18 GHz. Therefore, for low profiling this antenna our ultimate goal is design of an EBG structure which can cover this band of operation. According to the physical model

mentioned in Subsubsection 5.2.1.A and the study of effect of the design parameters in Section 2.3, we consider new structures with the following parameters: a = 0.5 mm, g = 0.15 mm (D = 0.65mm), h = 1.57 mm, d = 0.1 mm, ε_r = 2.51, and different values of relative permeability $1 < \mu_r < 9$. It is assumed that all the magneto-dielectric substrates have $tan\ \delta_m$ = 0.01. This is the lowest value of magnetic loss which has been achieved and reported in design of engineered magnetic materials [82]-[84]. Ansoft HFSS is used to extract in-phase reflection band for EBG structures. The setup is shown in Figure 5.40. For this purpose a unit cell of these structures is simulated using plane wave excitation with normal incidence. Periodic boundary condition is assigned around the cell to model an infinite EBG structure. The phase shifts between corresponding boundaries is equal to zero. Absorbing boundary condition is placed on the top of the cell. The reflected waves are recorded at an observation plane which is far enough from the EBG surface to make sure that evanescent modes are vanished. Using recorded field, the reflection phase is computed on the observation plane which is linearly transferred to the top surface of EBG structure [36]. The in-phase reflection band shows the range of frequencies in where the phase of broadside reflections on top of the EBG structure is bounded by ±45°. The center frequency shows the point at which the reflected phase on top of the EBG structure is equal to zero. The percentage bandwidth is defined as the ratio of the in-phase reflection bandwidth to the center frequency in percentage.

Figure 5.41 demonstrates the result of the simulation for structure with μ_r = 6 where the reflection phase is presented as a function of frequency. The in-phase reflection phase for this structure is 7.1 GHz to 14.6 GHz as marked on the figure. To

show advantages of using magneto-dielectric substrate as compared to dielectric substrate which is conventionally used to design EBG structures, one conventional sample is studied as a reference. The selected EBG which is designed and tested in [85] has the following specifications: a = 2.44 mm, g = 0.15 mm (D = 2.59 mm), h = 1.57 mm, d = 0.25 mm, μ_r = 1, and ε_r = 2.51. The reflection phase of this structure is also plotted in Figure 5.41. The in-phase reflection phase for this structure is from 12.1 GHz to 14.5 GHz as marked on the figure. Our EBG structure has same ε, g, and h as the conventional EBG structure, but its cell size is 4 times smaller. In addition the in-phase reflection band in the proposed EBG is 72.4% while this band is 18% for the conventional one. The result of simulations including in-phase reflection band, center frequency, and percentage bandwidth for EBG structures introduced earlier in this subsubsection are summarized in Table 5.II. It can be seen that the percentage bandwidth increases as the relative permeability increases.

Interested readers can follow the subject of design of low profile wideband antennas using magneto-dielectric EBG structures in [86]. This subject and design of magneto-dielectric materials in microwave frequency region is already under progress by members of other research groups.

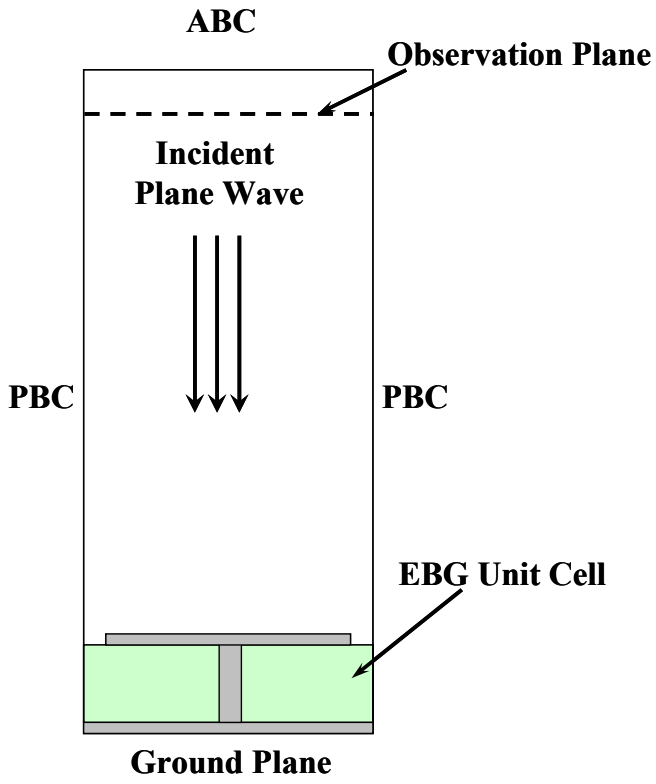

Figure 5.40. Setup used to extract the reflection phase of an EBG structure. The schematic shows the boundary setup for a unit cell. The unit cell is excited through normal incident plane wave. The reflected waves recorded at the observation plane are used to compute the phase.

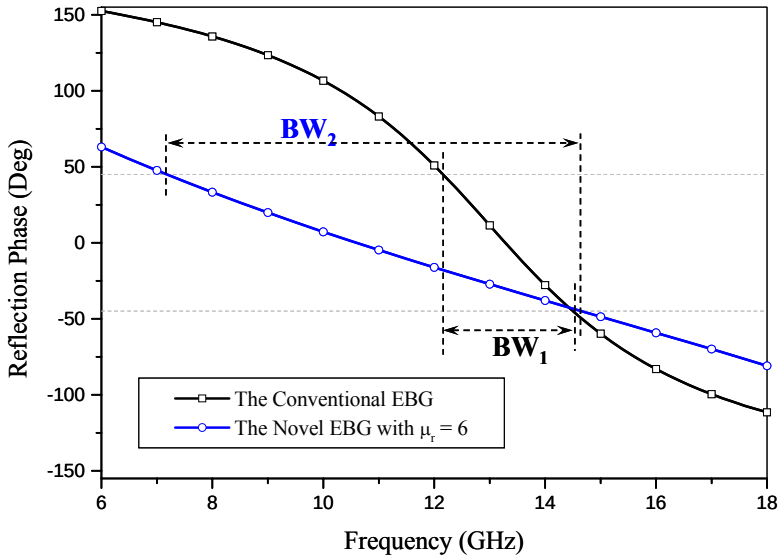

Figure 5.41. Reflection phase of EBG structures. The in-phase reflection phase is marked on each graph. The conventional EBG structure introduced in [85] is specified by: a = 2.44 mm, g = 0.15 mm, h = 1.57 mm, d = 0.25 mm, μ_r = 1, and ε_r = 2.51. The novel EBG structure is specified by: a = 0.5 mm, g = 0.15 mm, h = 1.57 mm, d = 0.1 mm, ε_r = 2.51, μ_r = 6, and $tan\ \delta_m$ = 0.01.

Table 5.II. In-phase reflection band obtained from numerical simulation for different EBG structures. The EBG structures have common specification of a = 0.5 mm, g = 0.15 mm, h = 1.57 mm, d = 0.1 mm, and ε_r = 2.51. The value of relative permeability, μ_r, is varying from 1 to 9. The magnetic loss tangent for material with $\mu_r > 1$ is equal to 0.01 ($tan\ \delta_m = 0.01$).

μ	In-phase Reflection Band (GHz)	In-phase Reflection Bandwidth (GHz)	Center Frequency (GHz)	Percentage Bandwidth
1	22 - 30	8	25.9	% 30.89
3	11.3 - 19	7.7	15	% 51.33
6	7.1 – 14.6	7.5	10.65	% 72.42
9	5.4 – 12.7	7.3	8.7	% 83.91

Chapter 6 : Conclusions and Future Work

6.1. Conclusions

The designs and analytical studies carried out through this work proved that EBG structures are strong contenders of EMI suppression in wide class of important problems where the EM wave interferes with the victim through surface wave or surface current, e.g., in applications where the source and victim share a common reference plane.

In this research, the mushroom-type EBG structures for open media applications were numerically characterized. The nonlinear relationship of the suppression bandgap versus the constituent materials and dimensions of structure was studied. Through the use of full-wave modeling commercial software based on finite element method, High Frequency Structure Simulator (HFSS), the efficacy of the mushroom-type EBG structures in two generic problems involving radiating structure sharing a common ground plane were demonstrated. In the first problem, we demonstrated that EBG structures can suppress EMI in the enclosures and chassis. In the second application, we showed the performance of those structures in the cavities as a part of cavity-backed antennas system. Also, we verified the efficiency of those structures through laboratory measurements. From the numerical and experimental results presented, we conclude that the numerical simulation setup discussed in this work provides a reliable methodology for predicting the suppression band of the generic class of simple EBG structures compromising square patches on the metal

backed dielectric substrates with a via connection in between. We anticipate that EBG structures with more complex topology can be treated in identical manner.

The EBG structures presented in this work were not optimized but rather arrived at using simple trial and error procedure coupled with educated guess. The optimization of EBG structures plays a strong role in more complex and sensitive applications where the radiators and victims are very close to each other and the higher EM noise suppression is required. In the antenna applications, it was shown that the design and implementation of EBG structures can amount to a balancing act between maintaining functionality and reducing coupling. Also, in the applications where several antennas are present in the same media such as array of cavity-backed antennas the spacing between antennas add up to mentioned trade off. Therefore, the entire multi antennas system with presence of EBG structure should be designed and optimized to satisfy the required performance.

Through study of the effect of presence of EBG structure on the performance of cavity-backed antenna system by assessing the gain pattern, it was demonstrated that the design of directive CBS antennas using EBG structure is possible. Also, the gain of antenna at the direction of maximum directivity can be increased.

In another study, we developed the concept of miniaturization of EBG structures using very high-k materials for mushroom- and planar-type structures. Also, we presented using very high value inductive bridges besides the high value effective capacitance made of very high permittivity dielectrics we could design miniaturized planar EBG structures providing wide suppression bands at the low frequency regions. Those novel EBG structures were numerically characterized. The

modeling of the proposed planar EBG structures was discussed. The effect of parameters in the model presenting the physical structure on the suppression band was studied. The developed model could provide a good initial guess for the EBG dimension and the structure as an initial starting point in the EBG design procedure. The miniaturized EBG structures presented in this study work were not optimized. Optimizing the structure may provide more effective ones.

Availability of the miniaturized EBG structures promotes another set of EMI/EMC applications which were impractical due to sizing issues. We studied the efficiency of proposed EBG structures in EMI and SSN noise suppression in IC packages. Modern electronic designs are requiring high level of isolation in the integrated high power density circuits which demands more efficient methods of noise suppression. To asses the performance of the EBG structures we studied the embedded capacitance method which is well known as an efficient method of EM noise suppression in packages operating in microwave region. We studied analytically and numerically the limitation of using the embedded capacitance method made of very high-k dielectric materials. It was shown how a thin slab of very high-k material decreases the peak of EMI; however, EM waves are still guided in the entire frequency band. The comparison results between the two methods show that in IC packages the method of EM noise suppression using EBG structures is very promising. The applicability of the embedded capacitance method depends on the defined noise tolerance level in a system.

The concept of design of novel wideband EBG structures using magneto-dielectric materials is developed. These novel EBG structures could be applied in the

design of low profile wideband antennas. It was shown that the designed mushroom-type EBG structures made of magneto-dielectric material are providing very wide bandgap compared to conventional designs made of only dielectric materials with smaller size patterns. This wide bandgap may extend from low frequencies.

6.2. Future Work

The development of the equivalent circuit-transmission line model of the proposed EBG structures in the two remainder regions of the irreducible Brillouin zone, X-M and M-Γ regions need to be completed. Completing that model can provide an initial start in design procedure with higher accuracy.

The miniaturized planar EBG structures made of very high-k material should be fabricated and the performance has to be measured. However, the fabrication process with high-k materials is in very early stages and it is hardly possible to find laboratories dealing with the fabrication as a research.

Also, time domain analysis of the proposed miniaturized EBG structures is necessary. The signal integrity with presence of these structures in packages should be assessed.

Finally, experiments and measurements of packages with presence of the proposed EBG structures in the real scenarios have to be assessed.

Appendix

The quasi-static value of the characteristic impedance Z_C for microstrip line shown in Figure A. 1 is given by [53]:

$$Z_C = \begin{cases} \dfrac{\eta}{2\pi\sqrt{\varepsilon_{re}}} \ln\left(\dfrac{8h}{w_e} + 0.25\dfrac{w_e}{h}\right) & \dfrac{w}{h} \le 1 \\ \dfrac{\eta}{\sqrt{\varepsilon_{re}}}\left[\dfrac{w_e}{h} + 1.393 + 0.667\ln\left(\dfrac{w_e}{h} + 1.444\right)\right]^{-1} & \dfrac{w}{h} \ge 1 \end{cases}$$

Equation A- 1

where η is the wave impedance in free space and $\eta = 120\pi$ ohms. The effective width of microstrip w_e is obtained from [53]:

$$\frac{w_e}{h} = \begin{cases} \dfrac{w}{h} + \dfrac{1.25t}{\pi h}\left(1 + \ln\left(\dfrac{4\pi w}{t}\right)\right) & \dfrac{w}{h} \le \dfrac{\pi}{2} \\ \dfrac{w}{h} + \dfrac{1.25t}{\pi h}\left(1 + \ln\left(\dfrac{2h}{t}\right)\right) & \dfrac{w}{h} \ge \dfrac{\pi}{2} \end{cases}$$

Equation A- 2

To simplify the modeling it is assumed that the conductor thickness is negligible (t = 0), therefore, $w_e = w$. The effective relative dielectric constant ε_{re} is given by [53]:

$$\varepsilon_{re} = \frac{\varepsilon_r + 1}{2} + \frac{\varepsilon_r - 1}{2} F\left(\frac{w}{h}\right) - C$$

Equation A- 3

where $C = \dfrac{\varepsilon_r - 1}{4.6} \dfrac{t/h}{\sqrt{w/h}}$. Therefore, in our modeling $C = 0$. Function F is given by [53]:

$$F\left(\frac{w}{h}\right) = \begin{cases} \left(1 + \dfrac{12h}{w}\right)^{-1/2} + 0.041\left(1 - \dfrac{w}{h}\right)^2 & \dfrac{w}{h} \le 1 \\ \left(1 + \dfrac{12h}{w}\right)^{-1/2} & \dfrac{w}{h} \ge 1 \end{cases}$$

Equation A- 4

A few points to improve modeling in Section 3.3:

- For small values of $\frac{t}{h}$, the effect of strip thickness on Z_C and ε_{re} is insignificant where we have good conductor. However, in applications such as IC packaging in which the dielectric thickness h, is shrinking by development in design and fabrication technology, for accurate modeling we need to take to account the metalic thickness (assuming $t = 0$ will introduce large error in modeling).
- If $\frac{h}{\lambda_{\min}} << 1$, the effect of dispersion on Z_C and ε_{re} is negligible. Yet, this is not the case when we are dealing with very high-k materials at high frequencies imperated by growing operating-speed in systems. Therefore, to get better compatibility with experimental results we need to consider the effect of dispersion on Z_C and ε_{re}.
- We need to remember that all the above mentioned formulas and the ones in the Section 3.3 are approximate. They are valid in certain ranges. For example, the accuracy of those expressions has not been confirmed for very high-k materials. However, those formulas are working accurate enough for quick analysis purpose as it is shown in our study.

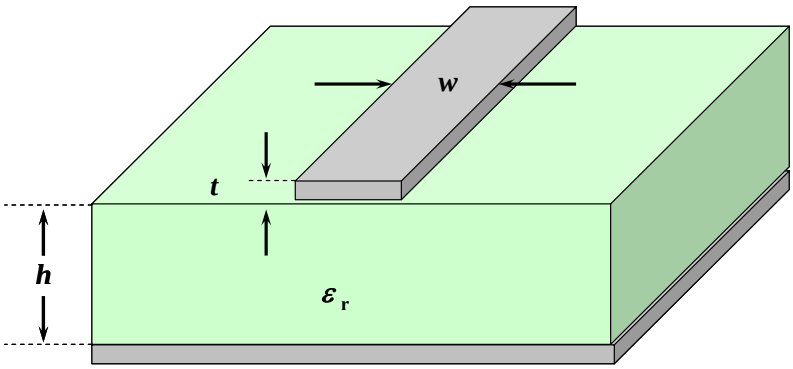

Figure A. 1. Microstrip line. Design parameters are shown in the figure.

Bibliography

[1] S. Van den Berghe, F. Olyslager, D. De Zutter, J. De Moerloose, and W. Temmerman, "Study of the ground bounce caused by power plane resonances," *IEEE Trans. Electromag. Compat*., vol. 40, no. 2 pp. 111-1119, May 1998.

[2] S. Chun, M. Swaminathan, L.D. Smith, J. Srinivasan, Z. Jin, and M.K. Iyer, "Modeling of simultaneous switching noise in high speed systems," *IEEE Trans. Adv. Packag*., vol. 24, no. 2, pp. 132-142, May 2001.

[3] S. Chun, M. Swaminathan, L.D. Smith, J. Srinivasan, Z. Jin, and M.K. Iyer, "Physics based modeling of simultaneous switching noise in high speed systems," *IEEE Proc. Electron. Compon. Technol. Conf.*, pp. 760-768, May 2000.

[4] J. Lee, H. Kim, and J. Kim, "High dielectric constant thin film EBG power/ground network for broad-band suppression of SSN and radiated emissions," *IEEE Microw. Wireless Compon. Lett., v*ol. 15, no. 8, Aug. 2005.

[5] R. Mahajan, K. Brown, and V. Atluri, "The evolution of microprocessor packaging," *Intel Technology Journal Q3*, vol. 4 issue 3, Aug. 2000, Available: http://www.intel.com/.

[6] E. Diaz-Alvarez and J. P. Krusius, "Package and chip-level EMI/EMC structure design, modeling and simulation," *Proceedings of the 49th IEEE Electronic Components and Technology Conference*, pp. 873-878, Jun. 1999.

[7] S.V. Georgakopulos, C.R. Birtcher and C.A. Balanis, "Coupling modeling and reduction techniques of cavity-backed slot antennae: FDTD versus

measurements," *IEEE Transactions on Electromagnetic Compatibility*, vol. 43, no. 3, pp. 261-272, Aug. 2001.

[8] J.F. Dawson, J. Ahmadi and A.C. Marvin, "Reduction of radiated emissions from apertures in resonant enclosures by the use absorptive materials," *8th International Conference on Electromagnetic Compatibility*, pp. 207-212, Sept. 1992.

[9] V. Adsure, H. Kroger and S. Weimin, "Improving signal integrity in circuit boards by incorporating embedded edge terminations," *IEEE Transactions on Advanced Packaging,* vol. 25 , no. 1, pp. 12-17, Feb. 2002.

[10] M. Li, J. Nuebel, J. L. Drewniak, T. H. Hubing, R.E. DuBroff and T.P. Van Doren, "EMI reduction from airflow aperture arrays using dual-perforated screens and loss," *IEEE Transactions on Electromagnetic Compatibility*, vol. 42, no. 2, pp. 135-141, May 2000.

[11] L. Li and O. M. Ramahi, "Analysis and reduction of electromagnetic field leakage through loaded apertures," *IEEE International Symposium on Electromagnetic Compatibility*, vol. 2, pp. 942-945, May 2003.

[12] I. Novak, "Reduction simultaneous switching noise and EMI on ground/power planes by dissipative edge termination," *IEEE Trans. Adv. Packag.*, vol. 22, no. 3, pp. 274-283, Aug. 1999.

[13] S. Van den Berghe, F. Olyslager, D. De Zutter, J. De Moerloose, and W. Temmerman, "Power plane resonances as a source of Delta-I noise and the influence of decoupling capacitors," *IEEE Proc. Int. Symp. Electromag. Compat.,* pp. 145-148, Aug. 1997.

[14] J. M. Hobbs, H. Windlass, V. Sundaram, S. Chun, G. E. White, M. Swaminathan, and Rao R. Tummala, "Simultaneous switching noise suppression for high speed systems using embedded decoupling," *IEEE Proc. Electron. Compon. Technol. Conf.*, pp. 339-343, 29 May-1 June 2001.

[15] I. Novak, "Lossy power distribution networks with thin dielectric layers and/or thin conductive layers, " *IEEE Trans. Adv. Packag.*, vol. 23, pp. 353-360, Aug. 2000

[16] T. Hubing, J. Chen, J. Drewniak, T. Van Doren, Y. Ren, J. Fan and R. E. DuBroff, "Power bus noise reduction using power islands in printed circuit board designs," *IEEE Proc. Int. Symp. Electromag. Compat.,* pp. 1-4, May. 1999.

[17] X. Ye, D. M. Hockanson, M. Li, Y. Ren, W. Cui, J. L. Drewniak and R. E. DuBroff, "EMI mitigation with multilayer power bus stacks and via stitching of reference planes," *IEEE Trans. Electromagn. Compat.,* vol. 43, no. 4, pp. 538-548, Nov. 2001.

[18] J. He, D. Zhong, S. Yun Ji, G. Ji, and Y._L. Li, "Study of package EMI reduction for GHz microprocessors," *IEEE Proceeding on Electrical Performance of Electronic Packaging Conference*, pp. 271-274, Oct. 2002.

[19] T. Kamgaing and O. M. Ramahi, "A novel power plane with integrated simultaneous switching noise mitigation capability using high-impedance surfaces," *IEEE Microwave and Wireless Components Letters,* vol. 13, no. 1, pp. 21-23, Jan. 2003.

[20] T. Kamgaing, High-impedance electromagnetic surfaces for mitigation of simultaneous switching noise in high-speed circuits, Ph.D. Dissertation, Department of Electrical and Computer Engineering, University of Maryland, College Park, MD, Oct. 2003.

[21] S. Shahparnia and O. M. Ramahi, "Electromagnetic interference (EMI) reduction from printed circuit boards (PCB) using electromagnetic bandgap structures," *IEEE Transactions on Electromagnetic Compatibility*, vol. 46, No. 4, pp. 580-587, Nov. 2004.

[22] T. Kamgaing and O.M. Ramahi, "Inductance-enhanced high-impedance surfaces for broadband simultaneous switching noise mitigation in power planes," *IEEE MTT-S International Microwave Symposium Digest*, vol. 3, pp. 2165-2168, June 2003.

[23] R. Abhari and G. V. Eleftheriadese, "Mtallo-dielectric electromagnetic bandgap structures for suppression and isolation of the parallel-plate noise in high-speed circuits," *IEEE Transactions on Microwave Theory and Techniques,* vol. 51, no. 6, pp. 1629-1639, June 2003.

[24] S. Shahparnia and O.M. Ramahi, "Simultaneous switching noise mitigation in PCB using cascaded high-impedance surfaces," *IEE Electronics Letters*, vol. 40, no. 2, pp. 98-100, 22 Jan. 2004.

[25] S. Shahparnia and O. M. Ramahi, "Miniaturized electromagnetic bandgap structures for broadband switching noise suppression in PCBs," *Electronic Lett*., vol. 41, no. 9, pp. 519-520, April 2005.

[26] D. F. Sievenpiper, High-impedance electromagnetic surface, Ph.D. Dissertation, Department of Electrical Engineering, University of California, Los Angeles, CA, 1999.

[27] D. Sievenpiper, L. Zhang, R.F.J. Broas, N.G. Alexopolous and E. Yablonovitch, "High impedance electromagnetic surfaces with a forbidden frequency band," *IEEE Transactions on Microwave Theory and Techniques,* vol. 47, no. 11, pp. 2059-2074, Nov. 1999.

[28] D. Sievenpiper and E. Yablonovitch, "Eliminating surface currents with metallodielectric photonic crystals," *IEEE MTT-S International Microwave Symposium Digest*, vol. 2, pp. 663-666, Jun. 1998.

[29] F. R. Yang, K. P. Ma, Y. Qian, and T. Itoh, "A uniplanar compact photonic-bandgap (UC-PBG) structure and its applications for microwave circuit," *IEEE Trans. Microw. Theory and Tech.*, vol. 47, no. 8, pp. 1509-1514, Aug. 1999.

[30] J. Choi, V. Govind, and M. Swaminathan, "A novel electromagnetic bandgap (EBG) structure for mixed-signal system application," *IEEE Proc. Radio Wireless Conf.*, pp. 243-246, Sept. 2004.

[31] T.-L. Wu, C.-C. Wang, Y.-H. Lin, T.-K. Wang, and G. Chang, "A novel power plane with super-wideband elimination of ground bounce noise on high speed circuits," *IEEE Microw. Wireless Compon. Lett.*, vol. 15, no. 3, pp. 174-176, March 2005.

[32] T. Kamgaing, J. He, and R. Hsu, "Package-level implementation of multiband electromagnetic band-gap structures," *IEEE MTT-S IMS*, pp. 598-601, June 2006.

[33] M. Li, J. Nuebel, J. L. Drewniak, R. E. DuBroff, T H. Hubing, and T. P. Van Doren, ”EMI from airflow aperture array in shielding enclosures-experiments, FDTD, and MoM modeling,” *IEEE Transaction on Electromagnetic Compatibility*, vol. 42, no. 3, pp. 265-275, Aug. 2000.

[34] T. Kamgaing and O. M. Ramahi, “Design and modeling of high-impedance electromagnetic surfaces for switching noise suppression in power planes,” *IEEE Transactions on Electromagnetic Compatibility*, vol. 47, no. 3, pp. 479-489, Aug. 2005.

[35] S. Shahparnia and O. M. Ramahi, “A simple and effective model for electromagnetic bandgap structures embedded in printed circuit boards,” *IEEE Microwave and Wireless Components Letters*, vol. 15, no. 10, pp. 621-623, Oct. 2005.

[36] R. Remski, “Analysis of photonic bandgap surfaces using Ansoft HFSS”, *Microwave Journal,* Sept. 2000.

[37] R. E. Collin, *Field Theory of Guided Waves*, Second Edition, John Wiley and Sons, Inc. 1991.

[38] HFSS, High Frequency Structure Simulator, Ansoft Co.

[39] L. Brillouin, *Wave propagation in periodic structures*, Electric Filters and Crystal Lattices, McGraw-Hill Inc., 1946.

[40] S. D. Rogers, “Electromagnetic-bandgap layers for broad-band suppression of TEM modes in power planes,” *IEEE Transaction on Microwave Theory and Techniques*, vol. 53, no. 8, Aug. 2005.

[41] S. Shahparnia and B. Mohajer-Iravani, O. M. Ramahi, "Electromagnetic noise mitigation in high-speed printed circuit boards and packaging using electromagnetic bandgap structures," *Proceedings of 54th Electronic Components and Technology Conference*, USA, June 2004.

[42] J. Qin and O. M. Ramahi, "Ultra-wideband mitigation of simultaneous switching noise using novel planar electromagnetic bandgap structures," to appear in *IEEE Microwave Wireless Component Letters*.

[43] Ramo, Whinnery, Van Duzer, *Fields and Wave in Communication Electronics*, 2nd ed., New York, John Wiley and Sons, 1984.

[44] M. Rahman and M. A. Stuchly, "Modeling and application of 2D photonic band gap structures," *IEEE Proceeding on Aerospace Conference*, vol. 2, pp.2/893-2/898, March 2001.

[45] R. E. Collin, *Foundation for Microwave Engineering*, Second Edition, McGraw-Hill, Inc., 1992.

[46] D. M. Pozar, *Microwave Engineering*. Addison-Wesley Publishing Company, Inc., 1990.

[47] Jia-Sheng Hong, M. J. Lancaster, *Microstrip Filters for RF/Microwave Applications*, John Wiley & Sons, Inc., 2001.

[48] K. C. Gupta, R. Garge, I. Bahl, and P. Bhartis, *Microstrip Lines and Slotlines*, 2nd Edition, Artech House, Boston, 1996.

[49] P. Benedek and P. Silvester, "Equivalent capacitances for microstrip gaps and steps," *IEEE Trans. Microwave Theory Tech.*, vol. MTT-20, no. 11, pp. 729-733, Nov. 1972.

[50] T. C. Edwards, *Foundations for Microstrip Circuit Design*, John Wiley and Sons, New York, 1992.

[51] H. M. Greenhouse, "Design of planar rectangular microelectronic inductors," *IEEE Transaction on Parts, Hybrids, and Packaging*, vol. PHP-10, no. 2, pp. 101-109, June 1974.

[52] B. C. Wadell, *Transmission Line Design Handbook*, Artech House, Boston, 1991.

[53] I. J. Bahl, *Lumped Elements for RF and Microwave Circuits*, Artech House, Inc., Boston, 2003.

[54] F. W. Grover, *Inductance Calculations,* Van Nostrand, Princeton, N.J., 1946; reprinted by Dover Publications, New York, N.Y., 1962.

[55] D. M. Krafcsik and D. E. Dawson, "A closed–form expression for representing the distributed nature of spiral inductor," *IEEE Microwave and Millimeter-Wave Monolithic Circuits*, vol. 86, no. 1, pp. 87-92, Jun. 1986.

[56] W. Hilberg, "From approximation to exact relations for characteristic impedances," *IEEE Trans. Microwave Theory Tech.,* vol. MTT-17, no. 5, pp. 259-265, May 1969.

[57] S. S. Bedair, "On the odd-mode capacitance of the coupled microstriplines," *IEEE Trans. Microwave Theory Tech.,* vol. MTT-28, no. 11, pp. 1225-1227, Nov. 1980.

[58] S. S. Bedair, "Characteristics of some asymmetrical coupled transmission lines," *IEEE Trans. Microwave Theory Tech.,* vol. MTT-32, no. 1, pp. 108-110, Jan. 1984.

[59] I. kneppo and J. Gotzman, "Basic parameters of nonsymmetrical coplanar line," *IEEE Trans. Microwave Theory Tech.,* vol. MTT-25, no. 8, pp. 718, Aug. 1977.

[60] T. Endo, Y. Sunahara, S. Satoh, and T. Katagi, "Resonant frequency and radiation efficiency of meander line antennas," *Electronics and Communications in Japan*, part 2, vol. 83, no. 1, pp. 52-58, 2000.

[61] T. Okoshi, Planar Circuits for Microwaves and Lightwaves, Springer-Verlag, 1985.

[62] N. Na, J. Choi, S. Chun, M. Swaminathan, and J. Srinivasan, "Modeling and transient simulation of planes in electronic packages," *IEEE Trans. Adv. Packag.*, vol. 23, pp. 340-352, Aug. 2000.

[63] J. Lee, M. D. Rotaru, M. K. Iyer, H. Kim, and J. Kim, "Analysis and suppression of SSN noise coupling between power/ground plane cavities through cutouts in multilayer packages and PCBs," *IEEE Trans. Adv. Package.*, vol. 28, no. 2, pp-298-309, May 2005.

[64] R. Ito and R. W. Jackson, "Parallel plate slot coupler modeling using two dimensional frequency domain transmission line matrix method," *IEEE Proc. Electrical Performance of Electronic Packaging*, pp. 41-44, Oct. 2004.

[65] I. Young, "Intel introduces chip-to-chip optical I/O interconnect prototype," *Technology@Intel Magazine,* April 2004, Available: http://www.intel.com/.

[66] Trans-Tech Inc., Available: http://www.trans-techinc.com/.

[67] F. Yang and Y. Rahmat-Samii, "Mutual coupling reduction of microstrip antennae using electromagnetic band-gap Structure," *Proceedings of the IEEE*

Antennae and Propagation Society International Symposium, vol. 2, pp. 478-481, July 2001.

[68] W.E. III. McKinzie III, R.B. Hurtado, B.K. Klimczak and J.D. Dutton, "Mitigation of multipath through the use of artificial magnetic conductor for precision GPS surveying antenna," *Proceedings of the IEEE Antennae and Propagation Society International Symposium*, vol. 4, pp. 640-643, Jun. 2002.

[69] K.M.K.H. Leong, A.C. Guyette, B. Elamaran, W.A. Shiroma and T. Itoh, "Coupling suppression in microstrip lines using a bi-periodically perforated ground plane", *IEEE Microwave and Wireless Components Letters*, vol. 12, no. 5, pp. 169-171, May 2002.

[70] R.F. Jimenez Broas, D.F. Sievenpiper and E. Yabolonovitch, "A high-impedance ground plane applied to a cell phone handset geometry," *IEEE Transactions on Microwave Theory and Techniques*, vol. 49, no. 7, pp. 1262-1265, Jul. 2001.

[71] S. Rogers, W. McKinzie and G. Mendolia, Artificial Magnetic Conductor (AMC) technology enables the coexistence of 802.11b and Bluetooth™, Technical literature Etenna Corporation.

[72] F. Yang and Y. Rahmat-Samii, "Reflection phase characterizations of the EBG ground plane for low profile wire antenna applications," *IEEE Transactions on Antennas and Propagation,* vol. 51, no. 10, pp. 2691–2703, Oct. 2003.

[73] Z. Li and Y. Rahmat-Samii, "PBG, PMC and PEC ground planes: A case study of dipole antennas," *IEEE Proc. Antennas Propagation Soc. Int. Symp.,* vol. 2, pp. 674–677, July 2000.

[74] J. M. Bell and M. F. Iskander, "A Low-Profile Archimedean spiral antenna using an EBG ground plane," *IEEE Antennas and Wireless Propagation Letters*, vol. 3, pp. 223-226, 2004.

[75] T. H. Liu, W. X. Zhang, M. Zhang, and K. F. Tsang, "Low profile spiral antenna with PBG substrate," *Electronic Letters*, vol.36, no. 9, pp. 779-780, April 2000.

[76] H. Nakano, M. Ikeda, K. Hitosugi, J. Yamauchi, and K. Hirose, "A spiral antenna backed by an electromagnetic band-gap material," *IEEE Proc. Antennas Propagation Soc. Int. Symp*., vol. 4, pp. 482-485, June 2003.

[77] D. J. Kern, D. H. Werner, and M. J. Wilhelm, ''Active negative impedance loaded EBG structures for the realization of ultra-wideband Artificial Magnetic Conductors," *IEEE Proc. Antennas Propagation Soc. Int. Symp.*, vol. 2, pp. 427-430, June 2003.

[78] R. C. Hansen and M. Burke, "Antennas with magneto-dielectrics," *Microwave and Optical Technology Letters*, vol. 26, no. 2, pp. 75-78, June 2000.

[79] H. Mosallaei and K. Sarabandi, ''Magneto-dielectrics in electromagnetics: concept and applications," *IEEE Transactions on Antennas and Propagation*, vol. 52, no. 6, pp. 1558-1567, June 2004.

[80] D. J. Kern, D. H. Werner, and M. Lisovich, "Metaferrites: using electromagnetic bandgap structures to synthesize metamaterial ferrites," *IEEE Transactions on Antennas and Propagation,* vol. 53, no. 4, pp. 1382-1389, April 2005.

[81] S. A. Tretyakov, *Analytical Modeling in Applied Electromagnetic,* Artech House, Inc., Boston, 2003.

[82] K. Buell, H. Mosallaei, and K. Sarabandi, "A substrate for small patch antennas providing tunable miniaturization factors," *IEEE Transactions on Microwave Theory and Techniques,* vol. 54, no. 1, pp. 135-146, Jan. 2006.

[83] S. Maslovski, P. Ikonen, I. Kolmakov, and S. Tretyakov, "Artificial magnetic materials based on the new magnetic particle: Metasolenoid," *Progress In Electromagnetic Research (PIER*), vol. 54, no. 9, pp. 61–81, Sept. 2005.

[84] J. B. Pendty, A. J. Holden, D. J. Robbins, and W. J. Stewart, "Magnetism from conductors and enhanced nonlinear phenomena," *IEEE Transactions on Microwave Theory and Techniques,* vol. 47, no. 11, pp. 2075-2084, Nov. 1999.

[85] M. A. Saville, "Investigation of conformal high-impedance ground planes", M.S. Thesis, Air force institute of technology Wright Patterson AFB, Ohio, March 2000.

[86] L. Yousefi, B. Mohajer-Iravani, and O. M. Ramahi, "Enhanced bandwidth artificial magnetic ground plane for low profile antennas," *IEEE Antennas and Wireless Propagation Letters*, vol. 6, pp. 289-292, 2007.